A DISSERTATION FOR THE DEGREE OF

DOCTOR OF PHILOSOPHY

Controlling Covalent Bond Dynamics of Epoxy Vitrimer Encapsulants for Enhancing Stress Dissipation in Semiconductor Packaging

에폭시 비트리머 포장재의 동적 공유결합 제어를 통한

반도체 패키징 응력 해소 향상 연구

Advisor: Hyun-Joong Kim

Jae-Ho Shin

PROGRAM IN ENVIRONMENTAL MATERIALS SCIENCE
GRADUATE SCHOOL
SEOUL NATIONAL UNIVERSITY

AUGUST, 2023

SEOUL NATIONAL UNIVERSITY

GRADUATE SCHOOL

PROGRAM IN ENVIRONMENTAL MATERIALS SCIENCE

WE HEREBY RECOMMEND THE THESIS BY
Jae-Ho Shin

ENTITLED

Controlling Covalent Bond Dynamics of Epoxy Vitrimer Encapsulants for Enhancing Stress Dissipation in Semiconductor Packaging

BE ACCEPTED IN FULFILLMENT OF THE REQUIREMENTS FOR THE DEGREE OF DOCTOR OF PHILOSOPHY

AUGUST, 2023

COMMITTEE ON FINAL EXAMINATION

Chairman
                                            Prof. Min-Sang Kwon

Co-Chairman
                                            Prof. Hyun-Joong Kim

Member
                                            Ph. D. Ick-Kyung Sung

Member
                                            Ph. D. Young-Min Kim

Member
                                            Ph. D. Dong-Won Kim

Abstract

Controlling Covalent Bond Dynamics of

Epoxy Vitrimer Encapsulants for

Enhancing Stress Dissipation

in Semiconductor Packaging

Jae-Ho Shin

Program in Environmental Materials Science

Graduate School

Seoul National University

With the advent of advanced packaging technologies such as fan-out wafer-level packaging or 3D-stack, the progress in upscaling and low-profiling of a semiconductor package drives a strong initiative for change in diverse aspects, including processing, architecture, integration strategy, and material selection. However, compared to developments in other areas, the innovation of packaging material itself seems to fall short. The packaging material usually comprises polymeric materials whose functions are to integrate an assembly, protect a chip or substrate, interconnect components, and dissipate heat or stress. Especially the role of dissipating stress, developed during packaging processes, has become of greater importance nowadays due to the intensive use of thin substrates, fragile components, and complex packaging designs. If the packaging material fails to suppress stress build-up, various stress-induced failures can occur, undermining quality and productivity. Among them, the warpage of an encapsulated substrate is a sore trial to production continuity, thwarting all efforts for chip assembly and packaging steps. Although using the encapsulant

with a low coefficient of thermal expansion has alleviated the problem so far, the matter has become more severe. It needs an innovative solution on the part of the material. In the meantime, a longing for a strong but flexible material also grows heavily in flexible hybrid electronics. Like the warpage issue, the heart of the solution is to develop a hard material capable of dissipating stress effectively.

In this study, we employed a material called vitrimer, a two-faced thermoset polymer capable of rearranging its crosslinked topology via a dynamic exchange reaction within covalent adaptable networks. During the topological rearrangement upon a trigger (e.g., heat, pH), a vitrimer attains freedom to flow despite the everlasting crosslinks and thus relaxes stress. The advantage of vitrimer can be further shone as it is combined with a strong epoxy material. Here, we developed epoxy vitrimers with tailored properties and controlled the dynamic exchange reactions within them to enhance their stress-relaxation capability and eventually address stress-induced problems.

Epoxy vitrimers were fabricated by formulating a commercial epoxy resin and a synthesized curing agent, called a dynamic curing agent, with various mixing ratios to achieve full re-processability upon melting and cooling. Using a commercial DGEBA resin and a special type of curing agent allows us to obtain very hard specimens at room temperature and melt-processable at high temperatures. Firstly, the effects of the types of dynamic curing agents according to their substituent and the compositions of epoxy networks with different fractions of dynamic/permanent linkages were investigated. The aromatic building block-based dynamic curing agent produced an epoxy vitrimer with a higher stress-relaxation capability than the epoxy vitrimer prepared by an aliphatic building block-based dynamic curing agent. This was attributed to the rapid transamination reaction via the stabilization effect of an aromatic neighboring group. In the same vein, the epoxy vitrimer with a higher fraction of dynamic linkage resulted in a higher stress-relaxation capability. However, since this characteristic would simultaneously decrease mechanical strengths and creep stability, great care must be taken in formulating to ensure that the resulting material has suitable properties for each application.

Secondly, we synthesized solvate ionic liquids, a relatively novel molten-metal complex. We introduced them into the epoxy vitrimers as a catalyst to accelerate the dynamic exchange reaction within the system. Unlike conventional metal powders, the solvate ionic liquid catalysts greatly enhanced the stress-relaxation characteristic of an epoxy vitrimer, even at a dosage of only 0.5-2 mol%. This is attributed to the compound's high miscibility and Lewis acidic character. With a wise choice of metal complexes and adequate dosage, high-performance epoxy vitrimers were fabricated, featuring a glassy modulus (over 10^9 Pa) at room temperature and an extremely short stress-relaxation time (about a few seconds) at 160°C. Thanks to the catalytic effect, the ability of stress dissipation of epoxy vitrimers was further improved without compromising mechanical properties (namely, storage modulus and tensile strengths) and viscoelastic performances (e.g., creep).

Lastly, we applied the developed epoxy vitrimer systems to both rigid (chip-on-wafer) and soft (chip-on-film) encapsulations. For this, each application's epoxy vitrimer with well-fitted properties (such as elastic modulus, stress-relaxation, creep, etc.) was selected. In the rigid encapsulation, the customized encapsulants were confirmed to be extremely effective in reducing warpage during assembly and cooling processes for silicon and glass wafers. Adding an inorganic filler and a solvate ionic liquid catalyst further suppressed the warpage almost to zero. In the soft encapsulation, the customized encapsulant also effectively reduced the warpage of a polyimide substrate while outperforming the reference soft encapsulant, a polydimethylsiloxane elastomer, regarding adhesion and conformability. For this case, rapidly deformable characteristics were required for the encapsulant to accommodate the ceaseless strain and stress from a flexible substrate. In addition, for both applications, the epoxy vitrimer encapsulants could be selectively removed from the packaged assembly at high temperatures without damaging the chip interconnection and substrates.

In conclusion, the above studies proposed several strategies to control:

1. The dynamic exchange reaction within crosslinked networks.

2. The ability of stress-relaxation without compromising mechanical properties.

3. The system's applicability to semiconductor packaging.

We believe the proposed approaches and prepared materials are novel and can be a game-changer in semiconductor packaging materials and flexible hybrid electronics.

Student Number: 2016-21467

Table of Contents

Chapter 2

Experimental Section

Vinylogous Urethane Epoxy Vitrimer System: Effects of Dynamic Curing Agents and Compositional Changes in Crosslinked Covalent Adaptable Networks

Chapter 4

Enhancing Stress-relaxation Capability of Epoxy Vitrimers : Solvate Ionic Liquid Catalysts for Accelerating Dynamic Exchange Reactions

Chapter 5

Application of Epoxy Vitrimers as Rigid and Soft Encapsulants

Chapter 6

Overall Conclusions

List of Tables

List of Figures

XVIII

Chapter 1

Introduction

1 Introduction

1.1 Semiconductor Packaging Adhesives and Encapsulants

Among the so-called eight core processes in semiconductor manufacturing, packaging is the final process for interconnecting the chip to internal electronic components and protecting the chip from the external environment. There are numerous polymeric products as the packaging solution inside the packaging or even constituting the packaging itself. The products are subsidized according to their applications, mainly (1) chip-to-board assembly and (2) chip-or-board protection. For assembly, underfill, conductive or non-conductive polymer pastes (films), film adhesives, surface mount adhesives, die-attach adhesives, and masking pastes are the frequently used adhesives in the packaging. For protection, conformal coatings, glob-top or dam-and-fill encapsulants, potting, gasketing, ruggedization, cornerbond, sealants, and molding compounds are the list of polymeric components.

Among them, the adhesive and encapsulant are vital subcomponents that cannot be omitted in any packaging design. Adhesives are widely adopted in assembling and packaging electronic devices, especially in assembling semiconductor dies, both in single-chip packages and multichip assemblies. As in pastes or solid films, they are also utilized in manufacturing high-density multilayer interconnection substrates, flexible printed circuits, panel displays, and other emerging applications, including optoelectronics and biomedical electronics. Since polymeric adhesives feature many advantages, including inexpensiveness, low processing temperatures, and re-workability, they replaced conventional interconnecting materials such as solder and eutectic alloys. Encapsulants are also applied in multiple spots on chips, leadframes, and substrates that need thorough protection from heat, moisture, and mechanical stimuli. Underfill, glob-top, and molding compounds are well-known names as an encapsulant. They are applied in the most sensitive parts that locate bonding wires, soldering balls, and downside-only-mounted integrated chips (IC). Epoxy molding

compound constitutes the final walls of the chip and electronic device packaging, enclosing the components and sub-structures into a single package. During molding, the melting characteristics and flowability of the encapsulant material are dominant parameters for covering the target area. After molding, the thermal stability, shrinkage, and moisture uptake are dominant parameters for its purpose.

From the viewpoint of material selection, only epoxy and silicone can satisfy the list of particular requirements for packaging materials. The use of acrylate, cyanoacrylate, and urethane, which are the favored materials for general adhesives, is limited in the field of semiconductor packaging because of many problems such as low modulus, need for ultraviolet exposure, poor heat resistance, and, most importantly, high moisture absorption, and severe corrosion (James J. Licari, 2005). In electronics and semiconductor packaging, three types of epoxy resin are widely used: diglycidyl ether (bisphenol A and F), phenolic and cresol novolac, and cycloaliphatic epoxides. The diglycidyl ethers of bisphenol A or F (DGEBA/F) are obtained from petrochemical derivatives and have low viscosity and good adhesion performance. The phenolic and cresol novolac exhibit superior thermal resistance and thus are used for molding compounds. The cycloaliphatic epoxides provide outstanding electrical insulation properties. In some cases, multifunctional and biphenyl resins can utilize their high glass-transition temperature, low stress, and low shrinkage properties (Haleh Ardebili, 2009). For a niche market, the use of a hybrid resin system such as epoxy-cyanate ester blend (Salunke, *et al.*, 2021) or phthalonitrile resin blend (Gu, *et al.*, 2022) can be found in very high-temperature working conditions (up to 300°C).

The polymerization of epoxy resin is achieved by the reaction of the glycidyl ether (epoxy) group with a curing agent (hardener). Epoxy resins are cured by curing agents with labile hydrogen atoms such as amine and acid anhydride molecules. The labile hydrogen attacks the alpha-carbon in the oxirane ring of the epoxy monomer, opening the ring structure to form dangling hydroxyl groups, which can consecutively react with neighbor epoxides until the epoxy resin is fully polymerized (cured or crosslinked). Amines and acid anhydrides are the most widely used curing agents. However, they are also prone to absorb moisture from

the ambient atmosphere and produce out-gassing, thus not favored for the packaging material. Imidazole derivatives and a complex of Lewis acid and bases, including boron trifluoride-amine complex, hexafluoroantimonate-imidazole complex, hexafluorophosphate salts, and organic acid hydrazide, are the better alternatives nowadays. Through the typical packaging process (wafer dicing, die attaching, electrical interconnection, molding, and final package inspection), each polymeric product, mounted or applied inside the package or dispensed around the borderline, is to be cured by either heat or ultraviolet (UV). The curing process turns flowable adhesives and encapsulants into a strong composite (chip-film-substrate). It provides the green strength to withstand shock and vibrations during the remaining processes and, eventually, the adhesion/cohesion strengths to the system. The choice of epoxy resin and hardener combination dominates the curing property such as cure temperature, cure duration, cure enthalpy, and cure-induced stress within the material. Also, it determines cured material's final properties, such as a crosslinking density, glass transition temperature (T_g), coefficient of thermal expansion (CTE), thermal conductivity, and elastic or flexural modulus. Those properties are reckoned and adopted as the material parameters during packaging processing and final inspection and hence must meet the requirements imposed on each packaging subcomponent.

However, the burden grows daily and changes according to new processes, designs, or building tactics for advanced packaging. Along with the progress in highly efficient device mounting and down-scaling, and also with the environmental drives such as the RoHS (Restriction of Hazardous Substances in Electrical and Electronic Equipment) directive, the changes in composition, design, and deployment of the subcomponents are rapidly happening. However, compared to the recent marvelous developments in processing, architecture, and chip integration strategy, the improvements or innovations of the material itself need to be improved on many fronts.

1.2 Trends in Advanced Packaging and Warpage

The semiconductor industry has been focused on designing electronics such as mobiles and displays to have a lower pitch and node size and a higher number of I/Os (input/output) and packaging density, following the guideline of the so-called Moore's Law. Numerous ideas and architectures for advanced packaging have been suggested to achieve higher functional density and performance. Developing interconnection and integration techniques, such as flip-chip, chip-scale-package, multi-chip-module, and system-in-package, has matured considerably over the last two decades. Nevertheless, the two-dimensional scaling-down techniques have reached the limit of the criterion of measuring circuit density, silicon packaging efficiency (SPE), which is the fraction of the total area of circuit elements versus the area of the substrate. Thus, it becomes challenging to maintain the trend in Moore's Law. One reasonable approach to attain higher SPE is stacking individual semiconductor elements in the Z-direction, called a 3D stack (see **Figure 1-1**). Nowadays, the smallest form factor, medium manufacturing cost, low interconnect-time-delay, and low crosstalk are the important reasons for adopting the concept of 3D packaging (Chanchani, 2009). In this vein, world-leading foundry companies have applied the technique to their latest line-ups, such as X-Cube (Samsung Electronics, 2020) and 3DFabricTM (TSMC, 2019).

Meanwhile, from the manufacturing outlook, wafer thinning, wafer alignment, and thru-silicon via (TSV) technologies are essential to fabricate 3D packaging. To reduce the length of TSV or other metal interconnections in the Z-direction, each wafer component should be thinned as much as possible so that the stacked architecture retains its low profile. However, as the silicon wafer is thinned to less than 50 μm, the wafer becomes very flexible and susceptible to weak forces such as interfacial bonding stress, the stress from the interfacial CTE mismatch, and die singulation force, which was negligible previously (Balde, 2003, Landesberger, *et al.*, 2001). Likewise, the requirement of precise alignment of dice within the 3D stacks also increases the technical hurdle. For highly dense circuitry, the alignment tolerance for each microchip is only about one μm. At this level, the internal stress from

packaging materials during bonding, curing, and thermal fluctuation could have negative effects, leading to inadequate stacks.
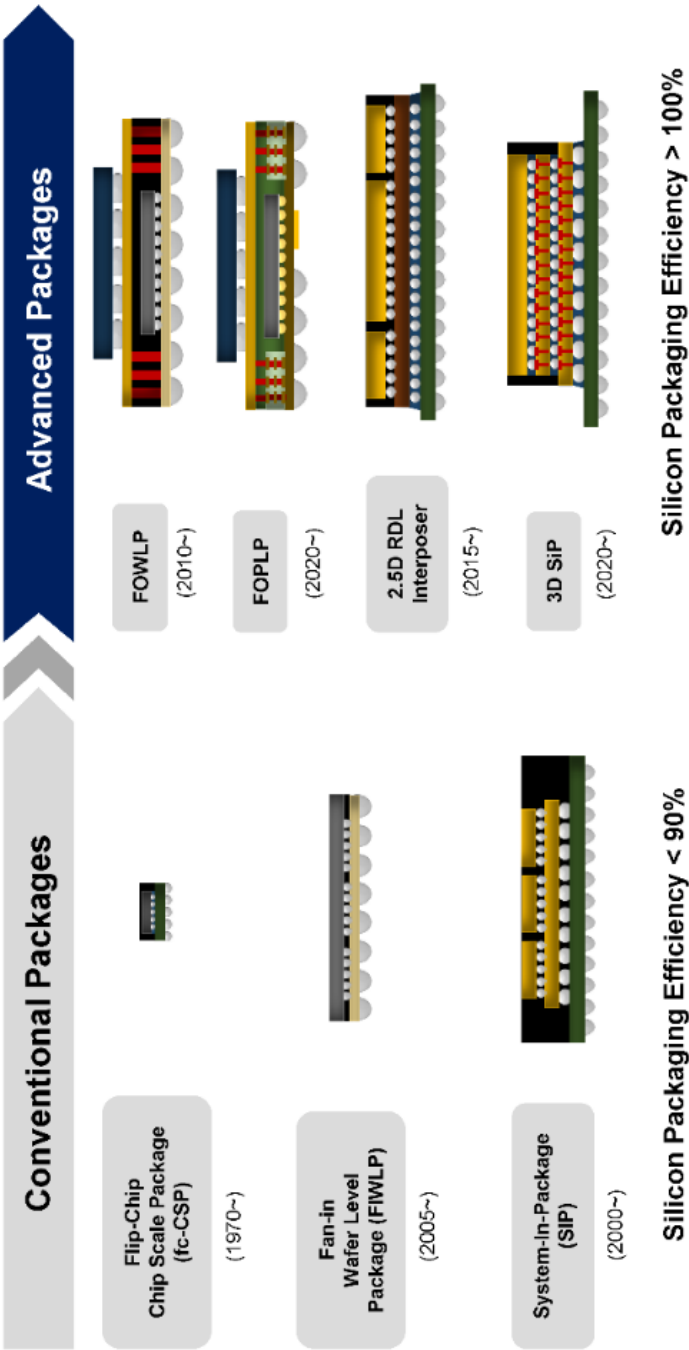
Figure 1-1. Progress in semiconductor packaging technologies.

The second mainstream of advanced packaging is fan-out wafer-level packaging (FO-WLP), which relieves time-consuming packaging steps and expensive materials used in conventional packaging structures. Since its debut by Infineon in 2001, the technology has continued to extend its application from the early stage of baseband, analog IC, and a radio frequency device to an application processor (AP) and a power management unit (PMU) nowadays (Watanabe, *et al.*, 2021). Noteworthy features of FO-WLP, such as substrate-less, low impedance, a high I/O number for the same chip size, lower package profile, short interconnection distance, improved board-level reliability, cost efficiency, and easier accessibility to the advanced packaging strategy such as system-in-package (SiP) or heterogeneous packaging, present it relative predominance over former processing technologies (Lau, 2020).

As the internal structure is simplified in FO-WLP, the role of epoxy molding compound and underfill material in forming the fan-out part becomes much more important in light of protection and interconnection. A known-good-die (KGD) is over-molded in a typical mold-first process by applying the EMC (liquid, pellet, and film type) on the temporary carrier. The structure is cured and grounded for depositing a redistribution layer (RDL) and bumps, which require molding underfill (MUF) support before chip singulation (**Figure 1-2a**). While the molding process generates high thermal and mechanical stresses within the architecture (**Figure 1-2b**), the location and alignment of subcomponents (die, carrier, solder ball, etc.) should remain constant during and after the packaging process to retain pitch interconnection. Hence, it is not an exaggeration that the performance and lifespan of the entire packaging rely on the reliability of the polymeric EMC and encapsulant materials.
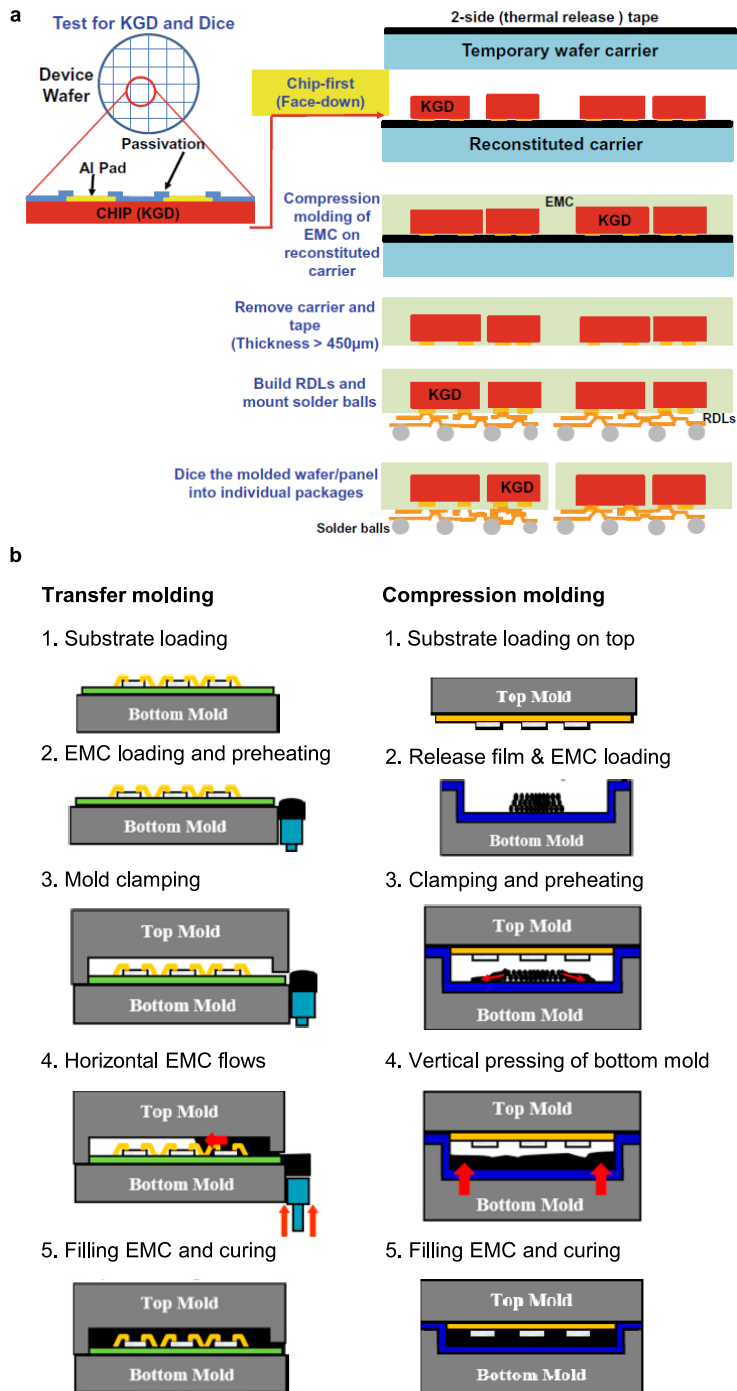
Figure 1-2. a Typical process of fan-out wafer-level packaging, (Lau, 2020) **b** Two different chip molding processes (Yeon*, et al.*, 2016).

The major weakness faced in FO-WLP is the issue of residual stress. Both sides of the adherend comprise heterogeneous materials: silicon chip and organic substrates (polyimide or cured epoxy-based composite, FR4) with different CTE, elastic modulus, and T_g values. When the encapsulant or adhesive is included in the system as a third component, a high degree of stress gradient develops, which can cause interfacial delamination and damage to the thin chip. The main cause of residual stress is the CTE mismatch between the adjacent materials, which leads to recurrent local interfacial failure and, eventually, crack propagation. The packaging downstream with successive heating and cooling loads often exerts an excessive force (**Figure 1-3a**) (Liao*, et al.*, 2017), especially on polymeric components, leading to misalignment of the cured adhesive or even vast dimensional deformation, called warpage (**Figure 1-3b**).

Warpage is an out-of-plane bending deformation whose modes can be concave, convex, and mixed, threatening the coplanarity within the package and frustrating subsequent assembly and packaging processes (**Figure 1-3c**). The stress level is proportional to the dimension of the chip size and becomes a critical issue with the trends of thinner and larger wafers in wafer-level packaging. The encapsulant materials are usually applied only to the top front, which unbalances the stress dissipation within the system during molding and post-mold curing. During cure, the viscous resin loses its free volume because of crosslinking, resulting in volumetric retraction called chemical shrinkage. Once the material is fully cured after post-mold curing, it shows a lower CTE value than one of the resins, resulting in a smaller dimensional change during cooling, leading to cold shrinkage and an irreversible deformation in size during the curing process. Additionally, the essential step for FO-WLP, the temporary carrier bonding and debonding procedure, adds another thermal stress to the interface between molding (CTE of 7-10 ppm °C^{-1}) and silicon (CTE of 2-3 ppm °C^{-1}), which further aggravates the warpage problem, especially in the FO-WLP process (Oi*, et al.*, 2018).

As a third mainstream, a recent thrust toward niche applications, such as optoelectronics, e-skins, biosensors, and electrical parts for autonomous driving, has encouraged non-traditional materials. These applications require an application-specific integrated circuit

(ASIC) and a packaging design. In many cases, for powerful functions, thinned silicon or GaAs die (or wafer), and larger-die devices are often used. To achieve two trade-off properties simultaneously - a small package size and an increase in the number of I/Os - the micro-bumps in flip-chip design become thin and very fragile. These changes all detrimentally affect the stability of the package. On the one hand, the greater use of flexible circuits and substrates drives the adoption of polyimide or polyester-based materials incompatible with conventional solder or other metallurgical options. Under these circumstances, a polymeric adhesive is the only component that can dissipate the concentrated stresses within the system. For this, a special type called low-stress adhesive has been gradually adopted for having a low modulus of elasticity and low cure-driven shrinkage.
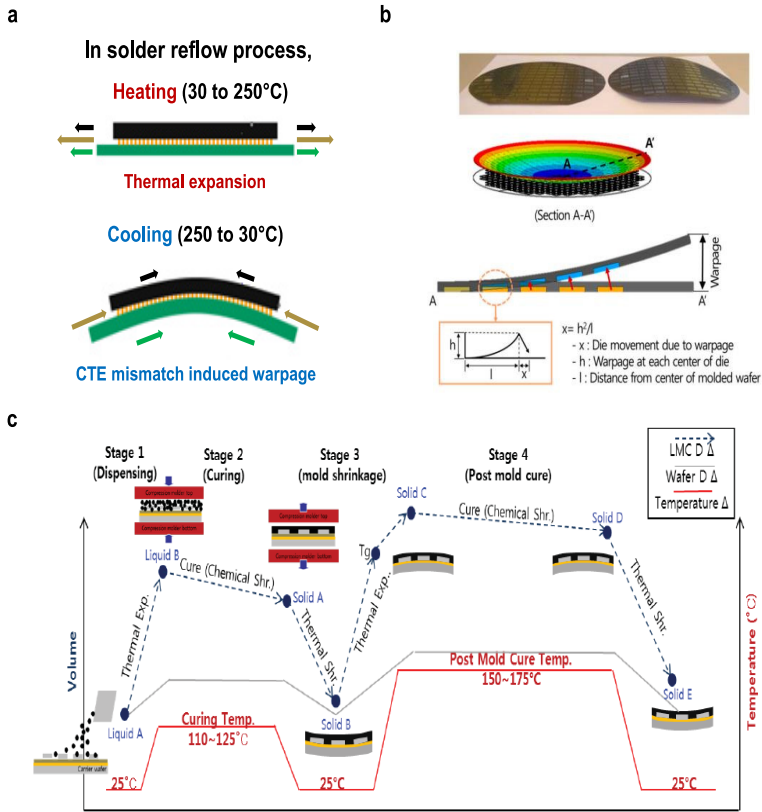
Figure 1-3. a CTE mismatch induced warpage of the chip-on-board structure (Liao*, et al.*, 2017), **b** Photographs of normal and warped wafer (up) and definition of warpage (down) (Yeon*, et al.*, 2016), **c** EMC curing and post-molding process (Kim*, et al.*, 2018).

1.3 Factors Contribute to Warpage

Initially, models of warpage pointed out the interfacial stress from CTE mismatch as the sole reason for warpage. Using a rigid and stiff adhesive to hold the interfaces, which have large differences in CTE values, inevitably brings about warpage. Generally, the most frequently used ceramic or metallic materials in semiconductor packaging have CTE values of about 3-20 ppm $°C^{-1}$, while the organic adhesives or encapsulants have CTE 1 values (before T_g) of about 30-100 ppm $°C^{-1}$ and CTE 2 values (after T_g) of about 70-300 ppm $°C^{-1}$ (Licari, *et al.*, 2011). Note that the CTE values of polymeric materials can vary significantly before and after their T_g point. As the material changes from a rigid glass state to a soft amorphous state, a degree of expansion abruptly soars, aggravating the CTE mismatch issue at the interface. Later models were expanded to cover other factors contributing to warpage, like the chemical shrinkage of polymeric materials (Kelly, *et al.*, 1996). During molding, curing, and post-curing, the epoxy encapsulant forms a three-dimensional crosslinking network, decreasing free volume between inter-chains. This is referred to as hot chemical shrinkage, whereas the difference between the specific volumes of the material before and after cooling is referred to as cold shrinkage (**Figure 1-4**) (Emst, *et al.*, 2006).
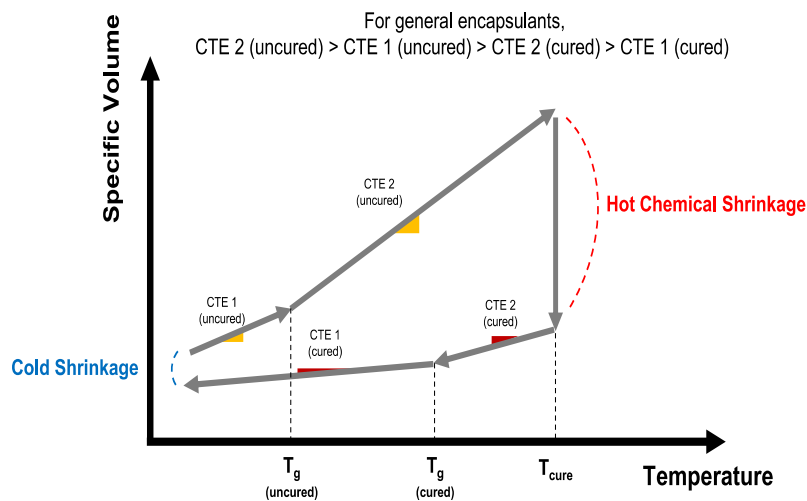
Figure 1-4. Encapsulant cure induced shrinkages during heating and cooling processes.

The following factors were also reported to contribute to the package warpage. (Chen, *et al.*, 2006, Konarski, 1999, Nguyen, *et al.*, 1991, Yang, *et al.*, 2005)

- ✓ Composition of an encapsulant: higher filler content leads to lower the warpage.

- ✓ Composition of an encapsulant: when modified with an elastomer, warpage is reduced.

- ✓ Stiffness of an encapsulant: higher stiffness of the encapsulant results in higher warpage.

- ✓ Encapsulant packing pressure: higher pressure causes higher warpage.

- ✓ Curing Temperature: longer the time of the encapsulant at high temperature, higher warpage.

- ✓ Curing Schedule: stepped curing (pre-gel + post-cure) reduces warpage.

- ✓ Package geometry: thicker and larger packages exhibit the higher warpage.

Encompassing all the factors, the most important determinant of warpage is the residual stress generated during post-encapsulation processes. Stress levels can vary significantly depending on the nature of the interfacial heterogeneous components (e.g., epoxy-polyimide, epoxy-silicon). Residual stress arises during the entire journey of hot chemical shrinkage and cold shrinkage. Its value can be indirectly quantified by measuring the dimensional change of a substrate (warpage) during the curing and cooling schedule. The first calculation method is to measure the bending stress from the radius of curvature where bonding stress, Sb, is defined as: (James J. Licari, 2005)

$$S_b = \frac{Eh}{2\gamma R} \qquad \text{(Equation 1-1)}$$

where E is Young's modulus, γ is Poisson's ratio, h is the thickness of adhesive, and R is the radius of curvature. As residual stress occurs in the bond-line, the substrate's radius of curvature decreases. This method is practical and straightforward in extracting the value of residual stress. However, in analyzing the warpage phenomenon, the equation has room to disentangle the hidden parameters. In a more theoretical approach, the stress buildup in a silicon wafer adhered to an adhesive was simply expressed in a one-dimensional model by the following equation: (Chung, *et al.*, 1990)

$$\sigma_{Si} = \varepsilon_{adh} \times E_{adh} = (\alpha_{adh} - \alpha_{Si}) \times E_{adh} \times \Delta T \qquad \text{(Equation 1-2)}$$

where σ_{Si} is the stress on the silicon substrate, ε_{adh} is the strain of the adhesive, E_{adh} is the storage modulus of the adhesive, α_{adh} is the CTE of the adhesive, α_{Si} is the CTE of silicon, ΔT is the temperature difference. The model reflects both the effects of CTE mismatch and the elastic modulus of the adhesive. Since the CTE of the adhesive is much larger than that of silicon, the residual stress works compressive on the silicon substrate and tensile on the adhesive. Another equation is obtained from a two-dimensional situation with three components (adhesive, substrate, and die), which yields a maximum stress as follows: (Kelly, 1999)

$$S_{max} = K(\alpha_{sub} - \alpha_{Si})(T_0 - T)\sqrt{\frac{E_{adh}E_{sub}L}{x}} \qquad \text{(Equation 1-3)}$$

where S_{max} is maximum stress within the package, K is a geometric constant associated with shape, α_{sub} is the CTE of the substrate, α_{Si} is the CTE of silicon, E_{adh} is the storage modulus of the adhesive, E_{sub} is the storage modulus of the substrate, L is length of the die, x is the thickness of adhesive, T_0 is the cure temperature and T is the application temperature. The equation attempts to capture the effects of CTE mismatch, elastic moduli of components, and geometrical parameters on residual stress. The above equations show that residual stress (and warpage) increases with the curing temperature, storage moduli of bonded components, difference in interfacial CTE values, dimension of the bonding area, and bond-line thickness. The relationship between the factors mentioned above and the warpage is summarized in **Table 1-1**.

Table 1-1. The relationship between the stress contributing factors and warpage.

Factors		Contribution to warpage
Adhesive material parameters	Glass transition temperature	Higher the T_g, lesser the CTE 2 region, hence lower warpage
	CTE 1 & CTE 2	Lower the CTE mismatch, lower warpage
	Elastic Modulus	Lower the elastic modulus, lower warpage
	Poisson's ratio	Higher the Poisson's ratio, lower warpage
Adhesive manufacturing parameters	Cure Temp.	Lower the curing temperature, lower warpage
	Cure Time	Shorter the curing time at maximum temperature, lower warpage
	Heating / Cooling speed	Slower the heating/cooling speed, longer the time to anneal, hence lower warpage
	Step cure	More the curing steps, lower warpage
	Packing Pressure	Lower the packing pressure, lower warpage
Packaging Dimensional parameters	Bonding area (Substrate, die, etc.)	Smaller the bonding area, lower warpage
	Bondline thickness	Narrower the bondline thickness, lower warpage

A recent study identified the stress index as the most relevant factor contributing to warpage. The stress index is defined as the product of CTE 1 and the flexural modulus of a material, as shown in **Figure 1-5a** (Mori, 2019). A simultaneous approach to reducing the encapsulant's CTE and flexural modulus value seems like a natural solution to address this issue. However, the CTE value of the encapsulant is typically controlled by adding inorganic fillers with a CTE value below one ppm °C^{-1} in the compound mixture, which results in a higher modulus for the composite. This design strategy assumes that the specific material and chosen adhesive will change in size at the same rate at a given temperature. Unfortunately, this approach often fails, and finding multiple substrates and adhesives with compatible CTEs can limit design freedom. In some cases, it may be impossible to match all the CTEs. Furthermore, even with matched CTEs, bond lines may fail under the stresses imparted by thermal cycles. A better approach to reducing residual stress should be discussed instead of solely focusing on CTE.
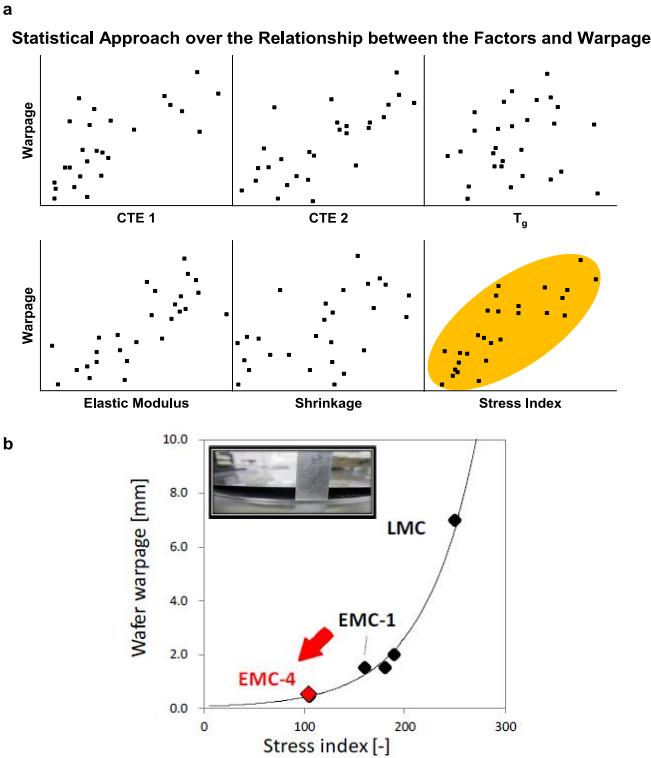
Figure 1-5. Relationship between the wafer warpage and the stress index (Mori, 2019).

1.4 Covalent Adaptable Networks and Vitrimers

The thermoset polymer, such as epoxy, attains a highly covalent crosslinked system after the cure reaction, rendering elasticity to the structure and providing high mechanical integrity and shape-set characteristics. While the behavior is highly appropriate for rigid packaging materials, it also has natural disadvantages in a lack of flexibility, stress dissipation and propagation, and irreversible processability. In addition, as mentioned in the previous section, the intrinsic high CTE of the matrix, compared to inorganic adherents, leads to the development of residual stress and damage to itself and its surroundings. Various innovative attempts to alter or attenuate the thermoset's adamancy have been widely implemented, introducing transient physical bonds such as hydrogen bonds (Feldman *, et al.*, 2009, Yepremyan *, et al.*, 2020), π- π stacking (Nakano, 2010, Vidal *, et al.*, 2019), ionic interactions (Hayashi *, et al.*, 2014, Wang *, et al.*, 2021), or molecular reformation within the crosslink (Hao *, et al.*, 2019, Seiffert, 2016). These materials demonstrate unique characteristics that adapt to varying conditions or stimuli and convert their responsibility to the applied stress, resulting in partial switching ability between thermosets and thermoplastics.

The recent emerging field of research utilizes a covalent adaptable network (CAN) in which the crosslinked chains within the thermoset can undergo reversible rearrangement reactions. The molecular rearrangements provide microscopic freedom to the tethered links to flow and relax shortly after reaching equilibrium. As the chain-reversible characteristics are combined with smart and stimuli-responsive concepts, these new materials are expected to be well-suited for materials used in custom-designed processes, or the material can be designed according to it. Although the historical origin of the CAN dates back to vulcanized rubbers with exchangeable disulfide bonds, the unique characteristics of the CAN have not been fully highlighted until the pioneering research of malleable epoxy by the Leibler group in 2011 (Montarnal *, et al.*, 2011). They sought materials that can undergo dynamic exchange reactions governed by Arrhenius behavior so that the exchange reaction enables stress-

relaxation at high temperatures. At the same time, the topology rapidly freezes upon cooling, and the system turns back to a rigid solid. By functionalizing diglycidyl ether of bisphenol A (DGEBA) epoxy with carboxylic acids, the cured epoxy composite behaved like an elastomer at the temperature of the transesterification exchange reaction, being elongated, twisted, melted, and even remolded (**Figure 1-6a**) while not losing the thermoset's network integrity. The material exhibited malleability, evidenced by the slower rate of increasing viscosity upon reaching T_g (cooling), similar to silica or strong glass formers (**Figure 1-6b**). This vitreous silica-like Arrhenius behavior gave the polymer the name "vitrimer," representing all the thermosets with similar thermal behavior. However, it should be noted that the vitrimer covers the materials with a group of CANs utilizing associative bond exchanges between adjacent polymer chains, in which the original bond is broken and a new bond is simultaneously formed. At its operating temperature, the vitrimer's network acts like a transient but ever-changing bridge, like the staircases in Hogwarts from the Harry Potter series.

On the other hand, a dissociative CAN undergoes temporary bond dissociation and suffers from a net loss of crosslinking density, resulting in a sudden drop in viscosity and material integrity, similar to thermoplastics (**Figure 1-6c**) (Denissen*, et al.*, 2016). The species and operating conditions for the stimuli-responsive systems utilizing the dissociative and associative CAN are both listed in **Table 1-2**. In the context of a manufacturing process, a material composed of a dissociative CAN only exist in the form of a dribbling liquid or a rigid solid, while an associative CAN (vitrimer) can possess a malleable form supported by a moderate degree of cohesion and hardness during the repeating heating and cooling stage. In short, vitrimers comprise covalently linked permanent networks with fixed numbers of connectivity at all operating temperatures, providing flexibility in their shape and processability tailored to each application.
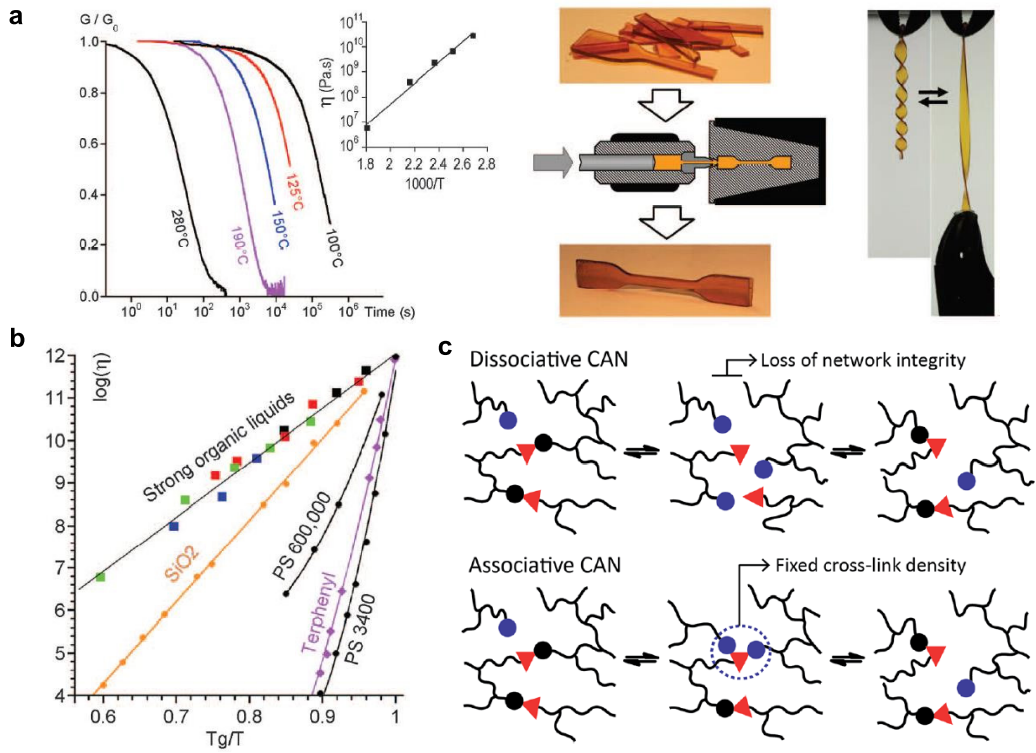
Figure 1-6. a Stress relaxation behavior of the epoxy vitrimer that can be reshaped. **b** Angell's fragility plots for thermoplastic (black and purple line), silica (orange line), and glass formers and vitrimers (square) (Montarnal, *et al.*, 2011). **c** Conceptual difference between a dissociative and an associative CAN (Denissen, *et al.*, 2016).

Table 1-2. Summary of stimuli-responsive dynamic covalent chemistries

(Kloxin*, et al.*, 2013).

Dynamic covalent chemistry	Type of reaction	Stimuli	Typical activation condition	Catalyst
Dies-Alder reaction	Dissociative	Temperature	Reversible at 90 ~ 150°C, mins to hours	Free
Thiol-Michael reaction	Dissociative	Temperature, pH	Reversible over 90°C, pH = 4 ~ 10	Bases, Nucleophile
Cycloaddition [4+4]: anthracene	Dissociative	Light	λ >300 nm forward, λ < 300 nm reverse	Free
Transesterification	Associative	Temperature	Reversible over 150°C for a couple of hours	Lewis acid, zinc acetate
Urea-amine exchange	Associative	Temperature	Reversible above 100°C for mins	Bases, Free amines
Transcarbonation	Associative	Temperature, strain	Reversible 150-180°C for mins	Stannous organocompounds
Vinylogous Urethane Transamination	Associative	Temperature	Reversible 100-150°C for mins	DBTL, pTsOH
Siloxane Exchange	Associative	Temperature	Reversible below 130°C	Sodium octanoate
Hydrazone formation and exchange	Dissociative / Associative	Temperature, pH	Dissociative: 25°C, pH 6.4 ~8.3 (condensation) Associative: >50°C, pH < 6	Lewis acid
Imine formation and exchange	Dissociative / Associative	Temperature, pH	Dissociative: 22°C, Associative: 50-110°C	Aniline/acid for condensation, acid for exchange
Boronic/borate ester-condensation/hydroxyl exchange	Dissociative / Associative	Temperature, pH	Dissociative: 25°C, pH < 7, Associative: ambient	*Cis*-diol concentration

What strikingly differentiates the vitrimer from polymers with transient bonds or thermoplastics is its viscoelastic behavior of having two different transition temperatures. The first is the glass transition temperature, describing the onset of long-range, coordinated molecular motion. The second transition temperature is the topology freezing transition temperature (T_v), derived from the dynamic exchange reactions between polymer chains. When the rate of bond exchange reaction is fast enough to be in the range of the timescale of the material's microscopic movement, the crosslinked system is accorded enough time and room for rearranging its topology.

As a viscoelastic solid passes through the point of T_v, conventionally chosen at the point where the viscosity is 10^{12} Pa s by Leibler (Montarnal*, et al.*, 2011), the constraint of its molecular arrangement is cleared up, transforming into a viscoelastic melt that can flow. To understand the stark difference, a comparative example is needed. A typical Angell's fragility plot of thermoplastics upon cooling shows rapid skyrocketing of viscosity in the vicinity of T_g, following the Williams-Landel-Ferry equation, resulting in a transition to the stage of reduced volumetric change from the Amorphous II to Amorphous I (**Figure 1-7a**).

On the other hand, when a vitrimer reaches the T_v upon cooling, the preposition of viscosity increase is rather slower, showing an Arrhenius behavior (**Figure 1-7b**) because the actions by micromorphic fluctuations during dynamic exchange reactions compete against the tendency of polymer segment freezing. What should be stressed is that the freezing topology transition is not a viscous-to-elastic gel transition. Since the vitrimer retains its connectivity and the network has been beyond the gel point, the system will not be soluble even above T_v. It will have the same material properties when returned to below T_g, making a vitrimer a perfect reversible engineering material.

a *Thermoplastic*

relative Volume →

Amorphous I

T_g

Amorphous II

Temperature →

T_g

log η →

$$\eta(T) = \eta_0 \cdot exp \left(\frac{C_1(T-T_r)}{C_2+(T-T_r)} \right)$$

Temperature →

b *Vitrimer*

relative Volume →

Amorphous I

T_g

Amorphous II

T_v

Amorphous III

Temperature →

T_v

log η →

$$\eta(T) = \eta_0 \cdot exp(E_a/k_B T)$$

T_g

Temperature →
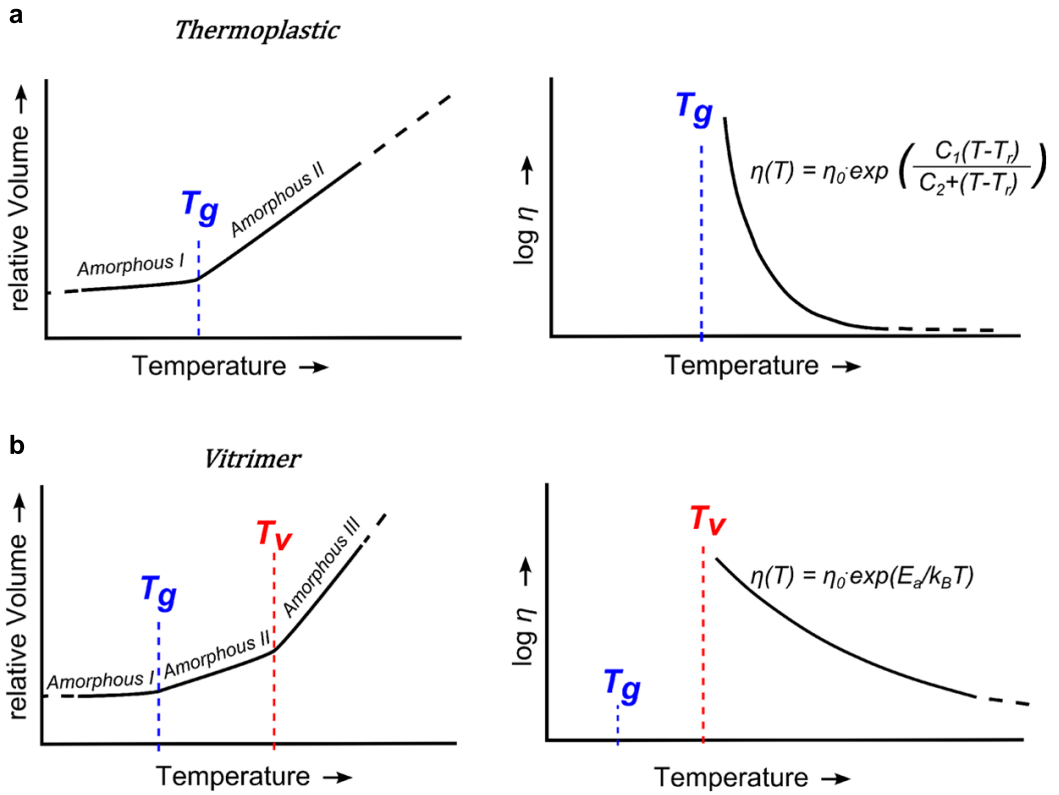
Figure 1-7. Volumetric transition and fragility plot for **a** thermoplastic and **b** vitrimer (Capelot, *et al.*, 2012).

1.5 Epoxy Vitrimer System via Transamination Reactions

In 2015, Filip E. Du Prez's group reported a vitrimer system that utilizes dynamic exchange reactions between vinylogous amides and free amines through transamination (Denissen*, et al.*, 2015). Compared to the former vitrimer system that utilized the Leibler group's transesterification, the system hallmarks several merits. Firstly, the amide group is thermodynamically more favorable than the ester counterpart, so the dynamic exchange reaction's activation energy (E_a) is much lower. The operating temperature of vinylogous amides and urethanes is about 100-120°C, even without a catalyst, while transesterification is usually activated above 150°C. Secondly, unlike ester-containing monomers, vinylogous amides are more hydrophobic and less susceptible to hydrolysis. Lastly, the prepared polyurethane-like material has superior mechanical properties without requiring any polymer backbone. The researchers synthesized the vinylogous urethane building blocks by mixing amines and acetoacetyl esters, while the ester was prepared by acetoacetylation for polyol building blocks in the beginning step. The bulk-polymerized poly(vinylogous urethane) network with a T_g of 87°C successfully exhibited stress relaxation behavior and re-moldability above 150°C. This satisfactory first step encouraged many researchers to consider using vinylogous urethane groups as a building block for a low-temperature-working vitrimer system.

Meanwhile, a recent study on epoxy vitrimers with vinylogous urethane linkage caught the material designer's eye for its unbounded strategy to introduce CANs to the epoxy system (Spiesschaert*, et al.*, 2020). A drawback of former research is that they were only viable with specific chemistry and niche monomers; hence, their high-volume bulk applications were restricted. In Spiesschaert's paper, the researchers used commercial epoxy resin instead of using the poly(vinylogous urethane) network as a building block or polymer's backbone. The amine-terminated vinylogous urethane molecules were oligomerized and utilized as a curing agent. The vinylogous urethane moieties were naturally inserted into the crosslinked networks via an epoxy-amine addition reaction during the epoxy-curing process. The

transamination between a vinylogous urethane molecule and an amine molecule occurs following a Michael-type pathway with an E_a of 102~112 kJ mol^{-1} (**Figure 1-8b**). Given this, the crosslinked epoxy system undergoes this dynamic exchange reaction between the vinylogous urethane moiety already included in the epoxy chain and the free or another chain-bounded amine moiety (**Figure 1-8c**). In such a system, the vitrimeric performance can easily be controlled by changing the dose of the curing agent and converting the curing agent's amine functionalities. The fully cured epoxy exhibited material properties comparable to the commercial epoxy and showed very short stress relaxation time and recyclability comparable to the former vinylogous urethane backboned polymers (**Figure 1-8d**). Although the authors did not emphasize this so much in the paper, the bypassing tactic of introducing CANs into a commercial epoxy resin is ingenious. It has enormous potential to let out the epoxy vitrimer to the application of industrial fields in dire need of strong, flexible, and reliable adhesives or encapsulants. Developing fabrication technologies that broaden the chemistry or the compositional design of epoxy vitrimers and improve their practical applicability is key to advancing this class of materials.
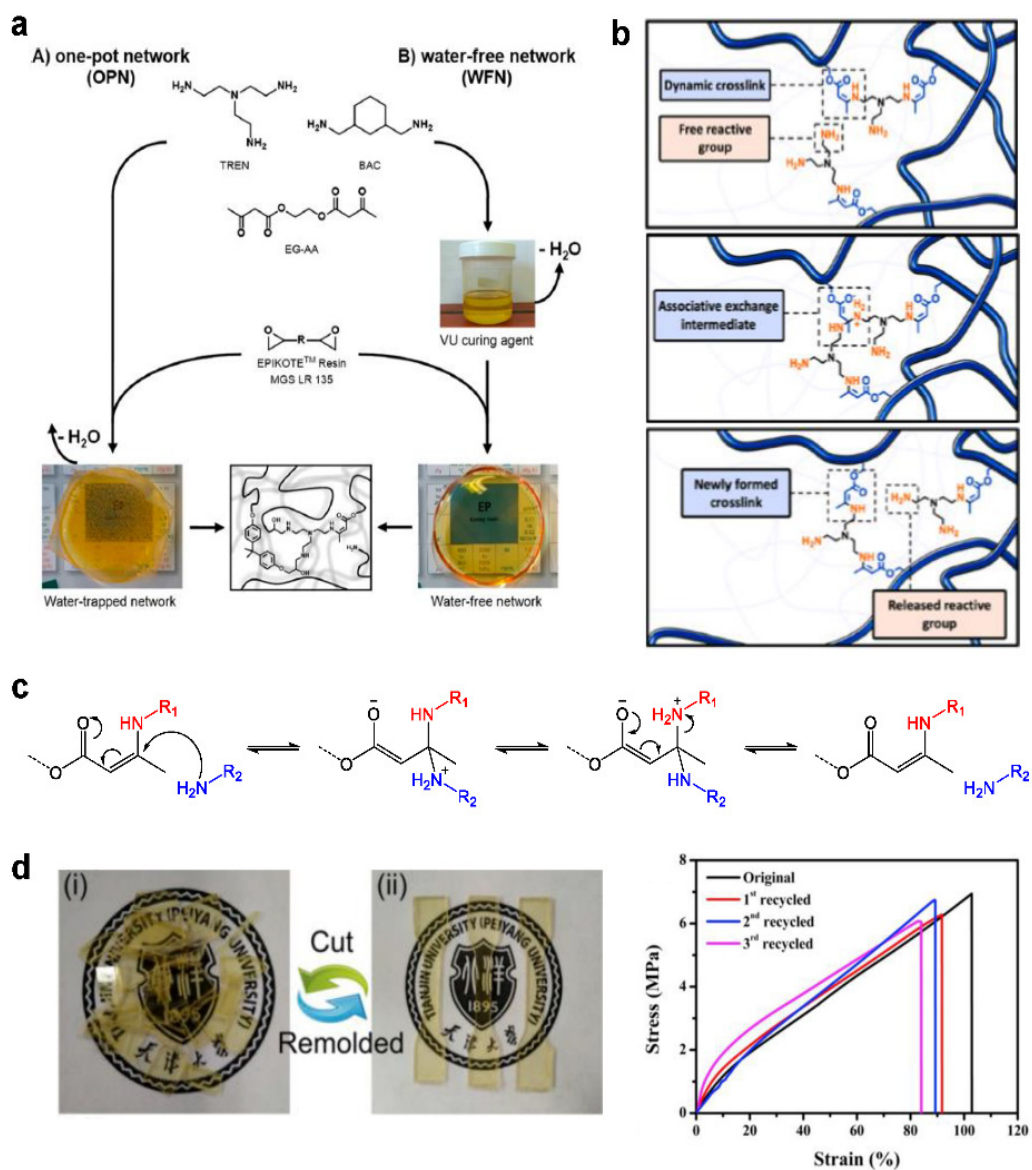
Figure 1-8. a A strategy to fabricate epoxy vitrimer using a vinylogous urethane-based curing agent along with a commercial epoxy resin (Spiesschaert, *et al.*, 2020). **b** Dynamic chain exchange reactions within the crosslinked network (Lessard, *et al.*, 2019). **c** Michael addition reaction pathway of the transamination between the vinylogous urethane and amine moieties. **d** Tensile properties and appearance of the pristine and recylced epoxy vitrimers (Bai, *et al.*, 2020).

2 Literature review

2.1 Materialistic Approaches to Reduce Stress in Chip Packages

There have been several researches and experiments to amend the residual stress induced within the packaging and reduce the warpage (Arayama, et al., 2019, Jansen, et al., 2013, Kikuchi, et al., 2018, Lau, et al., 2017, Mori, 2019, Oi, et al., 2018, Podpod, et al., 2019, Quirion, et al., 2020, Zhou, et al., 2015). The most effective way to reduce warpage is to use a two-step cure profile with careful control of heating and cooling rates based on the material's pre-measured gel-point temperature and CTE values. Pre-gelation at a lower temperature can help to lower cure-induced stress and CTE values by allowing sufficient time for polymer chains to anneal. However, the step cure process can add queueing time and space, hindering productivity. Altering wafer and EMC dimensions or packaging design is an effective solution without invoking material liability but may complicate the chipmaker and subcontractor's production chains. For those who want to mix chips from different processes, verification of the fully packaged chip design may need to be done using outsourced assembly and test (OSAT) outfits. Using a softer material as an encapsulant may reduce flexural modulus, anti-shock property, and reliability.

Introducing low-stress additives (Mori, 2019) and an additional polymer coating layer (Odashima*, et al.*, 2021) has significantly improved stress dissipation ability. However, it also suffers from additional processing, cost, compatibility, and interfacial adhesion problems between the heterogeneous chemicals. Thus, the best solution is to find a fundamental remedy for the stress-relaxation of the epoxy encapsulant and apply it to pre-set packaging processes like die-attach, molding, debonding, RDL building, and singulation. Epoxy encapsulants have been modified on many fronts, such as changing the resin backbone, curing agent selection, filler loading, and cure profile, to cope with the required characteristics on each occasion. Self-stress-relaxation will be the new objective for

thermoset epoxy in this case.

An encapsulant or adhesive is required to address the geometrically or thermally developed stress when facing heterogeneous interfaces, flexible substrates, or sensitive electronic components. Considering that epoxies exhibit excellent performances and reliability except for the ability of compliance related to flexibility, it is not surprising that almost desperate struggles have been conducted to search for ways to overcome its weakness. However, unfortunately, to individual researchers, the recipe or information about compositional changes in epoxy resin, crosslinker, and filler is often strictly confidential. Research on testing special epoxy products for final applications is mostly published in an abridged version by a few chemical corporations such as Henkel, Mitsubishi, and Sumitomo. They are normally classified and attributed to final users. Nonetheless, it is still worth learning from the published reports what efforts are devoted to utilizing epoxy adhesive/encapsulant in stress-sensitive applications.

In 2019, Mitsubishi Chemical reported a highly flexible epoxy film that survived a 10,000 times folding test without losing optical transparency and adhesion strength to the printed inks on the film (Noriyasu Yamane, 2019). The highly flexible epoxy films were prepared after being heat-cured by common amine-type crosslinkers by adjusting the high molecular weight varnish epoxy resin and multifunctional epoxy resin. One of the epoxy film products, tough hydrophobic units are included in the cured system and showed low water absorption (water vapor transmission rate for 24 hr of 30 g m^{-2}) and excellent dielectric property (Dk @ 10 GHz of 2.6, Df @ 10 GHz of 0.029). They successfully applied the epoxy film to a stretchable printed electronic and a conformable display (**Figure 1-9a**).

Also, in 2019, Sumitomo Bakelite reported a newly-developed epoxy molding compound or an underfill for FO-WLP to address the warpage issue on the wafer (Mori, 2019). As mentioned above, the stress index is the most critical parameter for developing warpage during epoxy curing and repetitive cooling and heating procedures. To lower the stress index, they mixed a special type of liquid, named a low-stress additive (LSA), with the pre-set EMC, yielding reduced elastic modulus at ambient temperature from 26 GPa to 15 GPa, and thus

reduced stress index from 182 to 105. The warpage of the 12 inches wafers encapsulated by the EMC with LSA was almost reduced by half (1.8 mm to 0.9 mm). Some LSA acted like a surfactant, providing the EMC with a higher chemical affinity to a PI-based RDL (**Figure 1-9b**). The difference in compatibility would also impact interfacial adhesion and stress dissipation behavior, leading to the prelude of stress-reduced encapsulation technology.

In 2021, Odashima et al. developed a new type of flexible hybrid electronics consisting of heterogeneous rigid chiplets embedded in 2D molded polymeric encapsulants composed of PDMS, parylene, and flexible epoxy (Odashima*, et al.*, 2021). They designed the 2D flexible encapsulants to endure the immense stress from the additional 3D molding required to obtain flexible 3D interconnect formation. The silicon chiplets were fixed on a temporary adhesive layer attached to the first carrier in the die-first FO-WLP fashion. After debonding the first carrier, a parylene layer was deposited on the chiplets/PDMS substrate, and subsequently, a flexible epoxy was spin-coated onto the parylene layer. Lastly, the 3D corrugated interconnections were deposited on the Ti/Au fan-out RDL, and the 2D-PDMS formation was completed. This 2D-PDMS with the embedded chiplets was remolded into a contact lens-shaped 3D-PDMS mold called a flexible 3D in-mold electronics (IME). After the fan-out RDL deposition, the system rapidly cools to room temperature, and the flexible epoxy layer significantly shrinks to produce corrugations in the Au interconnection.

The mechanism that produces the corrugations during cooling is mainly the CTE mismatch and modulus difference between the Au, epoxy, parylene, and PDMS. While the flexible epoxy greatly retracted during cooling (T_g of 45°C, In-plane CTE 1 of 86 ppm °C^{-1}, and CTE 2 of 197 ppm °C^{-1}), the stiff parylene will not yield (T_g of 75°C, CTE 1 of 49 ppm °C^{-1}, CTE 2 of 101 ppm °C^{-1}). Therefore, the shrinkage-induced stress left corrugation on the epoxy-Au layer (**Figure 1-9c**). The prepared 3D-PDMS almost retained a similar degree of resistance (0.3 Ω mm^{-1}) irrespective of wiring length from 20 ~ 40 mm and wiring width from 100 ~ 500 μm, which indicates the interconnection and encapsulation's dimensional stability (**Figure 1-9d**). The key point of the paper's fabrication strategy is that the flexible epoxy product finally gained its role even in soft encapsulation technology and

functioned as a stress-relaxing layer upon cooling. One can find strong evidence that stress-reduced epoxy adhesives or encapsulants are highly needed and managed to be applied in chip and electronics packaging through the literature.
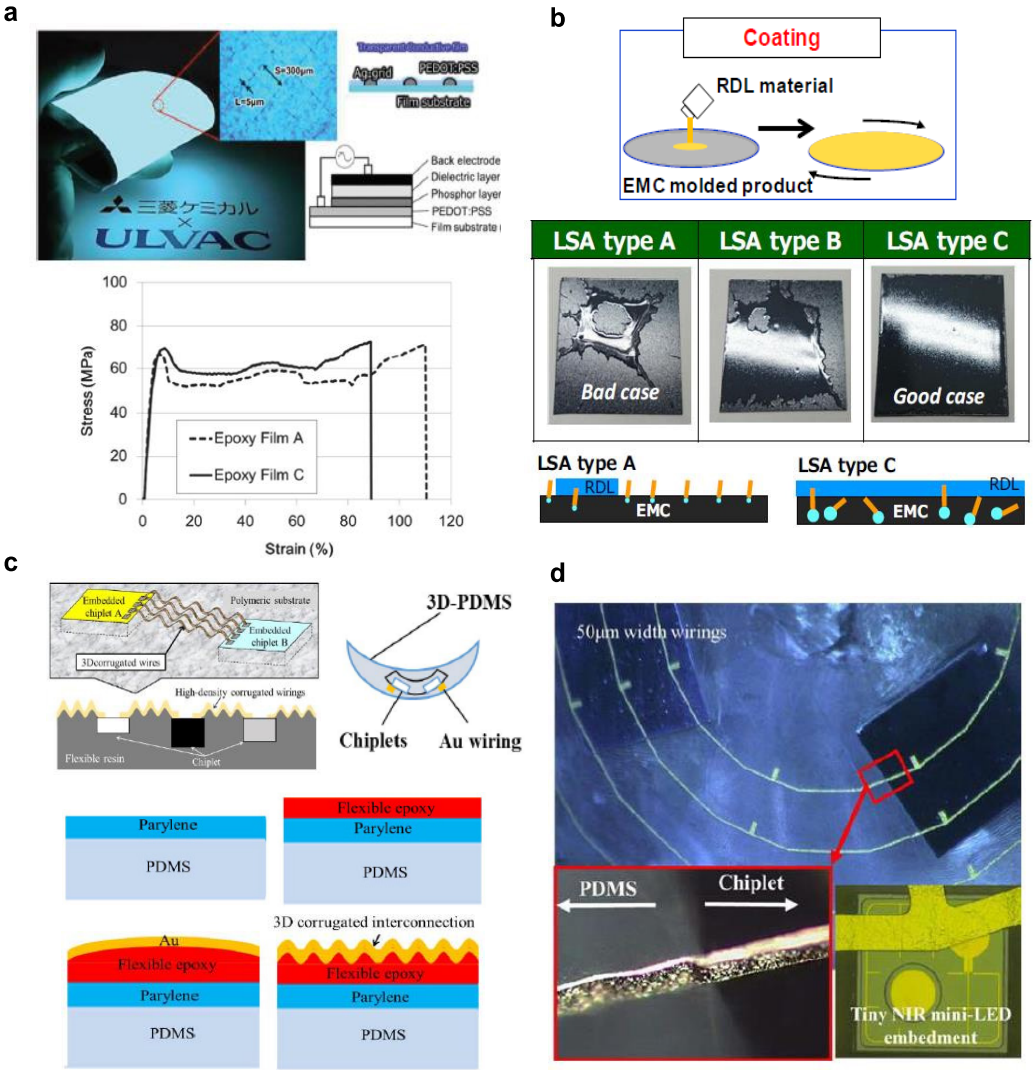
Figure 1-9. a Flexible epoxy film products applied on flexible electronics (Noriyasu Yamane, 2019), **b** EMC chemical modification by addition of a low stress additive (Mori, 2019), **c** Flexible 3D corrugated interconnections, 3D-remolded PDMS and corrugation formation mechanism (Odashima, *et al.*, 2021), **d** 3D-PDMS encapsulation with embedded chiplets (Odashima, *et al.*, 2021).

2.2 Designing an Epoxy Vitrimer System for Industrial Usage

Despite the unique characteristics of the vitrimer system - that it is easily controlled by heat and provides liberty of processing forms - there are barely any reports about the practical adoption of the vitrimer system in any industrial field. The interest in the vitrimer system remains at an academic level yet, and the development of the bulk use of epoxy vitrimer is still in its infancy. In the pursuit of applying the epoxy vitrimer to real-life industrial applications, the material with CANs should have enough mechanical strength, heat resistance, and endurance related to material reliability. Some recent reports are notable for considering these kinds of agenda, suggesting detailed approaches for addressing industrial itches such as (1) final material strength, (2) natural introduction of CANs in resin, and (3) permanency of vitrimeric performances.

Xiao Wu et al. designed a high-performance epoxy vitrimer based on siloxane equilibration by a simple approach (Wu, *et al.*, 2018). They synthesized a polysiloxane oligomer containing aminopropyl side groups and silanol end groups and used it as a curing agent for epoxy resins. As the curing agent reacted with the diglycidyl ether of ethoxylated bisphenol A, a stiff epoxy with a T_g of 83°C, Young's modulus of 2.2 GPa at room temperature, and yield stress of 46.6 MPa was obtained. The dynamic siloxane equilibration between the adjacent silanoates resulted in a relaxation time of 40.2 s at 170°C for the epoxy vitrimer system. The activation energy for the dynamic exchange reaction was calculated as 40 kJ mol^{-1}, far less than that of transesterification (130 kJ mol^{-1}) or transamination (100 kJ mol^{-1}) of former epoxy vitrimers. By adjusting the silanoates with potassium ions into the epoxy resin, the repeatability of recycling and its self-healing ability can easily be controlled (see **Figure 1-10a**). The paper showed a facile way of fabricating a high-performance epoxy vitrimer system. It provided a great demonstration of the self-healing property of the system, but it lacks consideration of potential applications.

Another study by Hanchao Liu et al. reported a weldable or repairable epoxy vitrimer based on dynamic imine bonds (Liu, *et al.*, 2019). Taking advantage of a highly reactive curing

agent, terephthalaldehyde and 3-aminobenzylamine, the preparation of the epoxy vitrimer is processed by a one-pot reaction without any separation or purification step. The dynamic imine linkage bestows malleability and shape reconfiguration ability to the epoxy vitrimer system. The welded and remolded epoxies exhibited a healing efficiency (a ratio of recovered property to initial property) above 75%. Meanwhile, the tensile stress and Young's modulus are higher than 70 MPa and 2.6 GPa, respectively, demonstrating superior mechanical properties. Additionally, the system is highly insensitive to water due to its hydrophobicity and high crosslinking density within the network. By the effect, the material maintained its tensile strength after 15 days of water-soaking (73 to 69 MPa). Along with its high thermal stability ($T_{d5\%}$ > 300°C), the water-resilient property is an extraordinary characteristic for CAN-based systems, highly desirable in many industrial fields. The research provides insights into designing a hydrophobic epoxy vitrimer but lacks a practical approach for potential applications.

Lastly, Spiesschaert et al. synthesized dynamic monomers consisting of a vinylogous urethane-based main chain and amine end-functionality. They used them as a curing agent in epoxy curing to form an epoxy vitrimer system (Spiesschaert, *et al.*, 2020). The prepared pristine epoxy vitrimer recorded almost 70 MPa of tensile strength and 1.7 GPa of Young's modulus, comparable to commercialized epoxies' values. The epoxy vitrimers were then chopped into small pieces and recycled using a hot press at 150°C. Some samples survived after four procedure cycles and maintained their tensile strength and stress-relaxation ability. What sets this research apart from the previous is that the researchers endeavored to find a real-life application for the material. They fabricated glass-fiber reinforced composites to fulfill the longing for recyclability. The vitrimer composite contained a fiber volume fraction of 53% and retained good adhesion between the resin and fiber while showing off its characteristic reshaping without damaging the matrix. The research presented a standardized procedure for preparing an epoxy vitrimer using a commercial epoxy resin and a dynamic curing agent. Further, it widened the material's applicability to numerous industrial fields by proving its mechanical and thermal reliability.
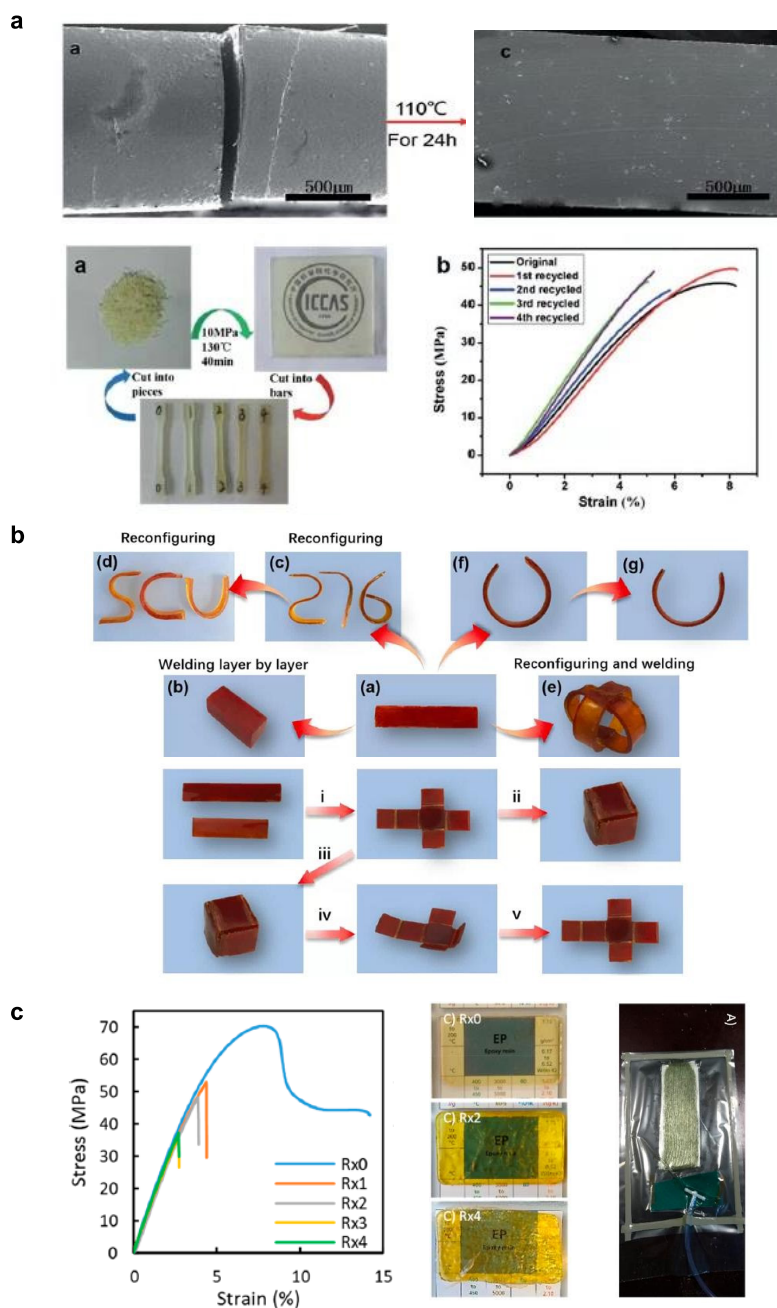
Figure 1-10. a (up) Crack healing of the cured epoxy vitrimer, (down) Recycling process of the dog-bone shaped epoxy vitrimers and the mechanical and chemical evaluations for proving reprocessability (Wu, *et al.*, 2018). **b** Deformation of welding epoxy vitrimer strips (Liu, *et al.*, 2019). **c** Mechanical strengths of reprocessed epoxy vitrimers and the hand-layered fiber-reinforced-resin using the epoxy vitrimer (Spiesschaert, *et al.*, 2020).

2.3 Controlling Stress-relaxation and Creep Behaviors of Epoxy Vitrimers

As the epoxy vitrimer takes steps toward becoming an engineering material, there comes the point when the most powerful advantage of a vitrimer turns into an Achilles heel: its enhanced viscoelasticity above T_g can invoke creep behavior and sagging, which threatens its re-processability. Creep is the tendency of a solid to deform continuously and permanently under external mechanical stresses. It is usually the main drawback of soft polymeric materials such as films, encapsulants, and adhesives in industrial fields. Many types of failure in semiconductor packaging, including die-shift, delamination, and loss of electrical interconnection, result from the creep property of the product used in the site. Additionally, considering the production line of semiconductor packaging consists of multiple recurrent steps of heating and cooling, the dislocation of polymeric components to the wrong place would eventually undermine the reliability of the packaging assembly. Thus, it is natural that the softened epoxy vitrimer's reliability should be questioned regarding whether it can replace conventional epoxy. Therefore, developing a simple method to suppress creep behavior, or more precisely, the loss of structural integrity in vitrimers, is of paramount importance. Research for vitrimer materials took a systemic approach, constructing groundwork regarding a quantitative relationship between vitrimeric characteristics and the amount of dynamic linkage within the vitrimer networks. Controlling creep behavior in the vitrimer material can be easily devised by strengthening the scientific basis.

Lingqiao Li et al. developed a theoretical approach to predict the threshold fraction of permanent links in a vitrimer system without sacrificing its re-processability (Li, *et al.*, 2018). The researchers adapted Flory and Stockmayer's famous gelation theory for the epoxy (permanent), thiol (permanent), and hexane thiol (dynamic) components. The main point of view in the research is that the incipient dose of components that will form a permanent link when cured should not percolate over the critical gelation threshold. The detailed derivation of the theory will be discussed in Chapter 3, Section 4.

Along with the theoretical construction, the researchers performed a melt-flow reprocessing test for samples containing 40% and 60% of permanent crosslinks within the system. As predicted in the theoretical threshold (below 50%), the sample with 40% of permanent crosslinks survived the test and maintained its mechanical properties, whereas the sample with 60% failed (**Figure 1-11a**). In the following stress-relaxation tests, the stress-relaxation abilities of the vitrimers with different compositions of permanent crosslinks varied and showed a linear relationship to each residual stress after the test (**Figure 1-11b**). Likewise, creep displacements varied according to the incipient amount of permanent links, where the creep deformation was greatly reduced from 10% to 3% in 12 hours of creep test as the vitrimer included 40% of permanent crosslinks within its network (**Figure 1-11c**). The gap of creep displacement between the sample with and without permanent crosslinks grew wider as the creep time increased. The result suggests that including permanent linkages within a vitrimer system would suppress creep behavior. The fundamental approach of deriving a theoretical threshold and adapting the theory to a specific chemistry guides the rational and systematic design of epoxy vitrimers.

On the other hand, Fanlong Meng et al. developed a continuum model of the mechanical response of vitrimers that experience dynamic exchange reactions simultaneously (Meng, *et al.*, 2019). At first, the researchers classified the three types of crosslinked chains in the networks: chains originally crosslinked at t=0, chains re-crosslinked at t=Δt, and chains newly crosslinked at t=Δ2t. The final newly crosslinked chains were assumed to be in the zero-force relaxed topology within the time interval that will contribute to the non-Newtonian part of the energy density of a vitrimer. The simplest neo-Hookean model was adopted for the continuum model to account for the large deformations in a vitrimer system. The researchers also designed vitrimer compositions with various fractions of dynamic linkages from a fully vitrimer network to a partially and permanently crosslinked network (**Figure 1-11b**). According to the model, the researchers constructed two types of expressions of internal stress σ(t) under tensile deformation and uniaxial stretching, respectively. The simple exponential decaying equation for stress-relaxation situations successfully predicted the residual stress of each system as a function of the fraction of

dynamic linkages (**Figure 1-11b**). The result also supports that the combinational or partial vitrimer composition effectively controls stress-relaxation and creep behavior. The simple model provides a quantitative description of how vitrimers with different dynamic fractions will react upon external load and serves as a guide for designing vitrimer systems.

Receiving the baton of developing engineering vitrimers, Filip van Lijsebetten et al. suggested a practical approach to suppress creep and promote reprocessing of vitrimers simultaneously (Van Lijsebetten*, et al.*, 2022). enerally, a vinylogous urethane-based vitrimer system requires additional free amines to provoke rapid dynamic exchange reactions. However, this excessive curing agent portion often induced unwanted creep deformation. In the paper, the researchers trapped the free amines within the polymer network by adding a dibasic ester, forming a transient dicarboxamide species. The trapped primary amine by esters was briefly liberated by a dicarboxamide dissociation (dissociative CAN) but instantaneously retrapped by a secondary pendant amine in the vinylogous urethane moiety, like a thermo-reversible regeneration. In this way, the vinylogous urethane system retained the exchanging amine moiety within the networks forever and used it as an internal catalyst. The researchers graded vinylogous urethane systems according to the content of exchangeable groups (-RNH$_2$). The amine-deficient sample (VU-95) showed good stress-relaxation behavior at 160°C while recording a low creep strain of 0.5% at 50°C. The paper proposed a novel method of introducing a small amount of dissociative CAN within a vitrimer network, simultaneously resulting in good control of stress-relaxation and creep performance. The result can promote the design of long-term dimensionally stable epoxy vitrimers without hampering their re-processability and mechanical properties. Nevertheless, the paper lacks the creep result at high temperatures and the following structural analysis, which are critical in designing the material for industrial usage. Literature about controlling stress-relaxation and creep behavior is incoherent and runs at peripheral ends. To grasp the designing factors of vitrimer materials and control them at our command, multi-level variables from the monomer selection, epoxy formulation, and compositions of dynamic fraction should be combined into a master batch and tested under the same test conditions.
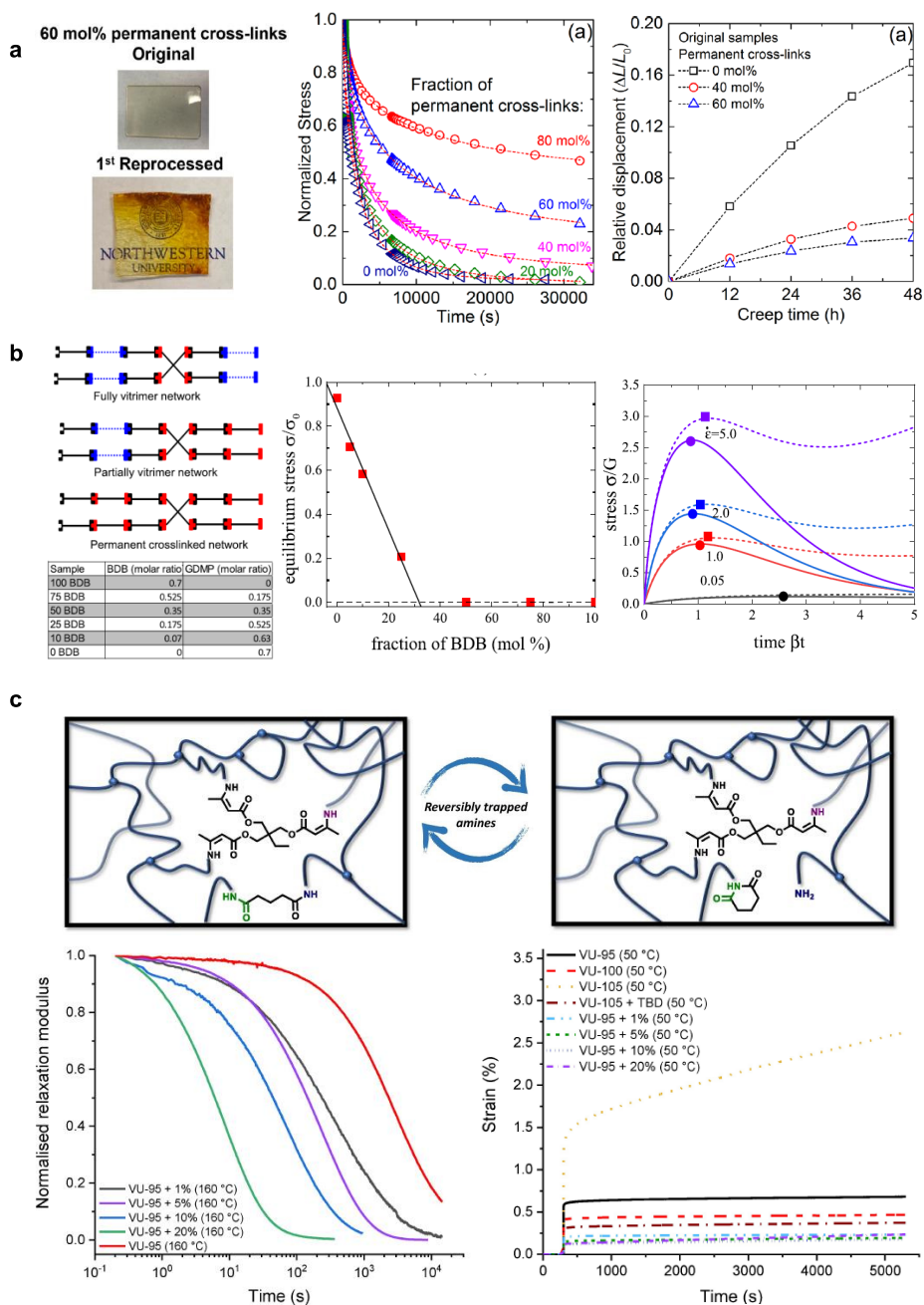
Figure 1-11. a Re-processability, stress-relaxation, and creep behaviors of the epoxy vitrimers with different compositions of permanent crosslinks. (Li*, et al.*, 2018) **b** Theoretical predictions and experimental results in stress-relaxation and uniaxial deformation tests for partial and fully vitrimer networks. (Meng*, et al.*, 2019) **c** Stress-relaxation and creep deformation of self-amine sufficient systems (Van Lijsebetten*, et al.*, 2022).

3 Objectives

Through the literature review, there is a great need for a hard but stress-relaxable epoxy material. Given the demanding requirements of the semiconductor packaging industry, any encapsulant material, including new designs, must have high thermomechanical properties (elastic modulus, yield stress, and elongation), favorable processing parameters (viscosity, flow, moldability), stability under environmental (temperature, humidity, pressure, shock) and operational (power dissipation, voltage, current, frequency) loads, and desirable geometric properties. To achieve reliability and novelty with a single material, we have formulated a commercial electric-grade epoxy resin blend and a dynamic curing agent that possesses both dynamically exchangeable groups and curable functionality.

The dynamic curing agent's chemistry must be common enough to use typical epoxy resins. Additionally, its operating system should be clear enough to assess the impact of the initial component's functions on the final product's properties, enabling the deliberate control of the epoxy vitrimer's performance. Among the dynamic exchange chemistries, the transamination reaction between a vinylogous urethane moiety and a neighboring amine is the most suitable candidate for the epoxy vitrimer encapsulant. This chemistry is well-studied and aligns well with the conventional epoxy-amine curing strategy. Furthermore, the transamination reaction's operating temperature perfectly aligns with the encapsulants' cure and cooling process in semiconductor packaging (200°C to r.t.).

In this study, we will investigate the design of epoxy vitrimer systems with vinylogous urethane-based dynamic curing agents and the control of stress relaxation and creep properties. Additionally, we will explore using soluble catalysts to accelerate the dynamic exchange reaction. Finally, we will apply the adjusted epoxy vitrimer system to semiconductor packaging for two encapsulation types: rigid (chip-on-wafer, CoW) and soft (chip-on-film, CoF) encapsulants.

In summary, this research will cover the formulation of epoxy vitrimers with dynamic

curing agents to control creep and stress relaxation performance, the acceleration of the dynamic exchange reaction using soluble catalysts, and the application of the modified epoxy vitrimer system to semiconductor packaging.

3.1 Formulating Epoxy Vitrimer Systems to Achieve High Stress-relaxation & Low Creep

As a first step towards the ultimate goal of applying the material in semiconductor packaging as an encapsulant, it is crucial to ensure its ability to dissipate stress and maintain re-processability at the packaging fabrication conditions. Therefore, we adopted a transamination dynamic exchange regime, working at medium temperatures (140~200°C), by introducing vinylogous urethane-based curing agents with amine end functionalities in a commercial epoxy resin. We synthesized four different types of dynamic curing agents (DCA) having either aliphatic or aromatic building blocks to compare their effects in eliciting enhanced performances of the prepared epoxy vitrimers (**Figure 1-1**2). Particularly, we used two species of acetoacetates, aliphatic and aromatic, respectively, as a reactant of the vinylogous urethane moiety. And we used three species of amines as reactants, both for amine-acetoacetate condensation reaction and amine-epoxy curing reaction. The first two species are bi-functional amines, aliphatic and aromatic, respectively. The last amine is tri-functional, forming 3D crosslinked networks in epoxy curing (**Table 1-3**). The epoxy vitrimers cured by the DCAs with aromatic building blocks showed faster stress-relaxation and lower creep strain at the same time.

Additionally, using the Flory-Stockmayer gelation theory, the epoxy vitrimer systems are designed to have compositions with different fractions of dynamic linkages, capable of dynamic exchange reactions within their crosslinked networks. Postulating that the composition of dynamic linkage affects the rate of dynamic exchange reaction, understanding its effect on the crosslinking structure is also of pivotal importance for the

design and control of the mechanical properties of epoxy vitrimers. Six compositions that have survived a reprocessing test (remolding) are selected for each DCA and compared in stress-relaxation and creep tests (**Table 1-3**). The higher the fraction of dynamic linkages in an epoxy vitrimer, the faster the stress-relaxation and the higher the creep strain that results. As we select an aromatic DCA and formulate it with an epoxy resin to have a low fraction of dynamic linkages, the prepared epoxy vitrimer results in fast stress-relaxation but low creep strain, albeit the properties are supposedly in a tradeoff relationship. The marriage of the two approaches presents a way of quantitatively controlling the degree of stress-relaxation and creep behaviors simultaneously.
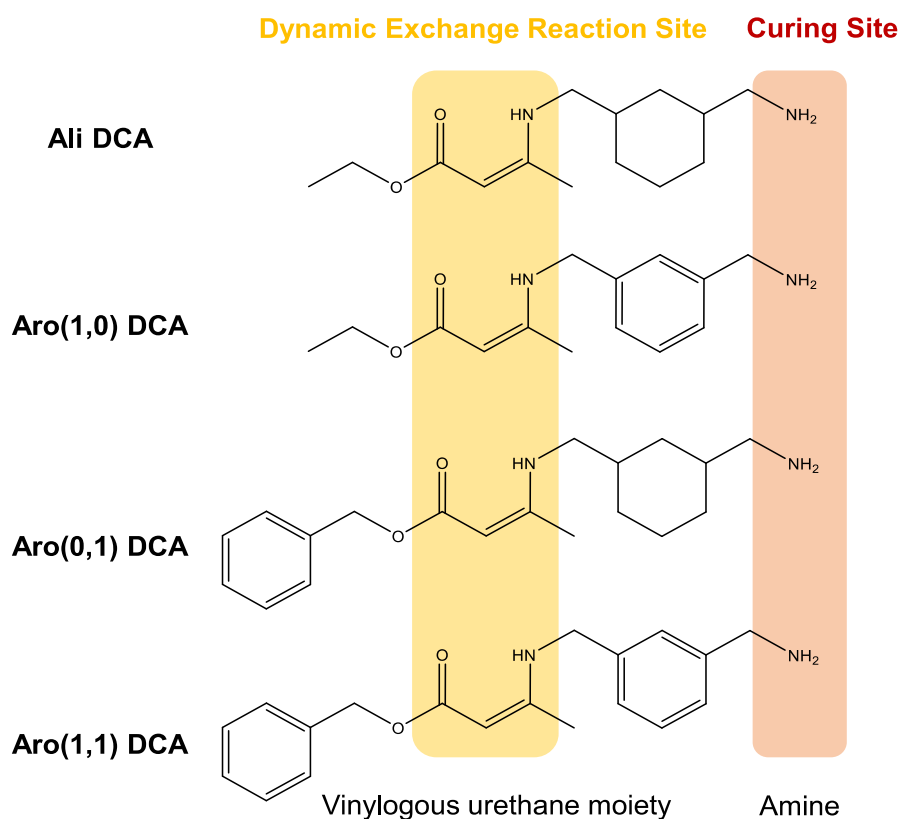
Figure 1-12. Four types of DCAs used in preparing epoxy vitrimers.

Table 1-3. Variables in designing epoxy vitrimer systems.

Variable I		Types of DCAs		
		Amines		
Nomenclature	Acetoacetates	Bi-functional	Tri-functional	**Expected Properties**
Ali DCA	Ethyl acetoacetate	1,3-bis(aminoethyl)cyclohexane		Low SR[*], Low Creep
Aro(1,0) DCA	Benzyl acetoacetate	1,3-bis(aminoethyl)cyclohexane	Tris(2-aminoethyl)amine	High SR, High Creep
Aro(0,1) DCA	Ethyl acetoacetate	*m*-xylylenediamine		High SR, High Creep
Aro(1,1) DCA	Benzyl acetoacetate	*m*-xylylenediamine		High SR, Low Creep
Variable II		**Compositions**		
Nomenclature	A ratio of dynamic / permanent links	A mix ratio of [epoxide] : [active hydrogen]		**Expected Properties**
D17	17 / 83			Low SR & Creep
D23	23 / 77			Low SR & Creep
D26	26 / 74	15% amine-rich system		Medium SR & Creep
D29	29 / 71	(off-stoichiometry)		Medium SR & Creep
D34	34 / 66			High SR & Creep
D40	40 / 60			High SR & Creep

[*]Stress-relaxation

3.2 Accelerating the Dynamic Exchange Reaction with Soluble Catalysts

In an attempt to maximize the stress dissipation ability of epoxy vitrimers, it is necessary to involve external components in the system. Previous studies have shown that accelerating dynamic exchange reactions requires internal or external catalysts. For the transamination reaction, Brønsted and Lewis acidic metal powders or complexes (such as zinc acetate, sulphuric acid, and dibutyltin dilaurate) have been reported to be effective in accelerating the dynamic exchange reaction and reducing the activation energy required for the reaction. However, metal powders were not as effective as expected due to their low solubility in epoxy resin and the need for additional mixing steps.

Therefore, we synthesized a novel type of liquid catalyst called a solvate ionic liquid, perfectly soluble in epoxy resin. The solvate ionic liquid, composed of a molecule called glyme consisting of multiple ethers, solvates a transition metal-cored complex into a liquid form even at near room temperature. Four species of solvate ionic liquid were prepared by combining two types of glymes and four types of metal powders (**Figure 1-13**).

Remarkably, a minimum dosage (0.5 mol%) of the soluble catalyst was sufficient to accelerate the dynamic exchange reaction and lower the activation energy in the cured epoxy vitrimers due to the high solubility of the catalyst. The center ion activated the carbonyl functionality of the vinylogous urethane moiety inserted in the epoxy vitrimer network. The catalyst induced a transition of the reaction pathway into a metal-catalyzed one with a lower energy barrier. As a result, the adapted epoxy vitrimer exhibited excellent stress-relaxation behavior.

1. [Li(G3)]OTf   **2. [Li(G3)]TFSI**   **3. [Zn$_{0.5}$(G4)]TFSI**   **4. [Mg$_{0.5}$(G4)]TFSI**
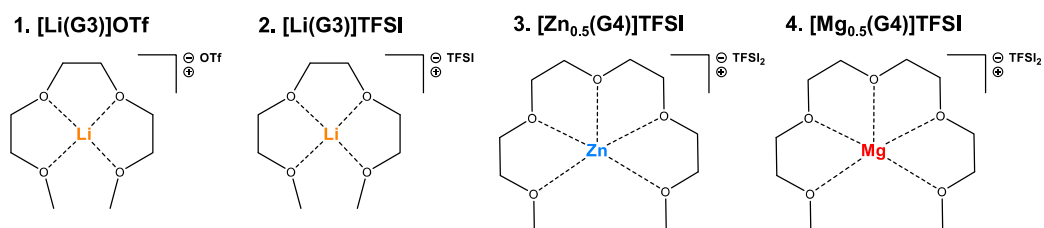
Figure 1-13. Four species of the synthesized solvate ionic liquid catalysts.

3.3 Applying Epoxy Vitrimers in Rigid and Soft Encapsulations

As a final step, we aim to find the proper combination of the developed epoxy vitrimer systems and SIL catalysts whose characteristics can be tailored to each rigid (CoW) and soft (CoF) encapsulation application.

For the rigid encapsulation innovation, the epoxy vitrimer encapsulants were designed to resolve the warpage issue of encapsulated substrates such as a silicon wafer, a glass wafer, and a polyimide film. There is still limited research on warpage during semiconductor packaging from a materialistic standpoint, let alone developing a material that can self-dissipate stress and reduce warpage altogether. Therefore, this chapter aims to experimentally explore the potential of various epoxy vitrimer encapsulants for warpage reduction during a wafer-level cure process. The previous chapters have proven that epoxy vitrimers with different compositions have wide variations in material properties. Thus, in addition to their diverse stress-relaxation capabilities, emphasis is also placed on the effects of their thermomechanical properties. The validity of the developed epoxy vitrimer encapsulants is verified by manual warpage measurement. Adding an inorganic filler and a SIL catalyst, an epoxy vitrimer encapsulant successfully dissipates thermal stresses, resulting in almost zero warpage on a silicon and glass wafer.

For the soft encapsulation innovation, the epoxy vitrimer encapsulants were designed to respond to the movement of a flexible polyimide substrate simultaneously. The epoxy vitrimer composition with high stress-relaxation capability is selected and further improved

to include a solvate ionic liquid catalyst so that the adapted system can extremely relax the interfacial stress between an encapsulant and a substrate and negate the interfacial strain, integrating the assembly. The epoxy vitrimer encapsulant is also applied to a flexible printed circuit board (FPCB), outperforming a silicone elastomer-based encapsulant regarding adhesion performance and conformability.

Lastly, we anticipate that the epoxy vitrimer system would bring both rigid and soft encapsulations reworkability. Due to their malleability at high temperatures, epoxy encapsulants can be completely removed from PCBs and FPCBs without damaging the chip and substrate. The rework characteristic significantly reduces the cost and waste of valuable resources, which will help save our planet.

Chapter 2

Experimental Section

1 Materials

1.1 Epoxy and Curing Agents

YD-128 (184 g eq^{-1} of equivalent epoxy weight) was obtained, courtesy of Kukdo Chemical Co. Ltd. (Republic of Korea). Ethyl acetoacetate (EAAc, 99%), 1,3-cyclohexane bis(methyl)amine (BAC, 98%), m-xylylenediamine (XDA), and tris(2-aminoethyl)amine (TREN, 98%) were purchased from Sigma-Aldrich. Benzyl acetoacetate (BAAc, 98%) was purchased from Alfa Aesar. All hygroscopic chemicals were stored in a desiccator under a nitrogen atmosphere. All solvents (GR grade) were used without further purification.
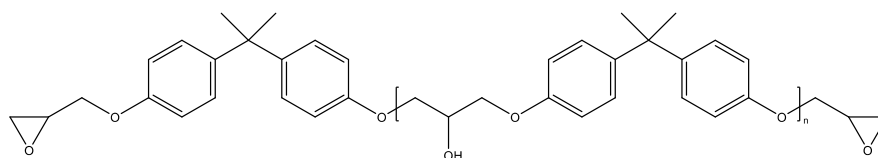
Diglycidyl Ether of Bisphenol A (YD-128)
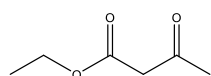
Ethyl acetoacetate (EAAc)
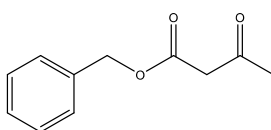
Benzyl acetoacetate (BAAc)
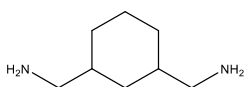
1,3-bis(aminomethyl) cyclohexane (BAC)
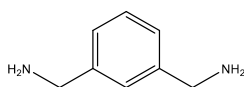
m-Xylylenediamine (XDA)
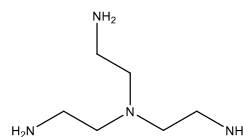
Tris(2-aminoethyl)amine (TREN)

Figure 2-1. The epoxy resin and chemicals for synthesizing curing agents.

1.2 Solvate Ionic Liquids

Zinc acetate (anhydrous), lithium bis(trifluoromethanesulfonyl)imide (99%), lithium trifluoromethane sulfonate (96%), and triethylphosphine oxide (97%) were purchased from Sigma-Aldrich. Triethylene glycol dimethyl ether (99%, triglyme, G3), tetraethylene glycol dimethyl ether (98%, tetraglyme, G4), zinc(II) bis(trifluoromethanesulfonyl)imide (98%) and magnesium(II) bis(trifluoromethanesulfonyl)imide (97%) were purchased from TCI. Octylamine (99.5%) were purchased from Daejung Chemical Co. Ltd. (Republic of Korea). All the hygroscopic chemicals were stored in a desiccator under N_2 atmosphere. All solvents (GR grade) were used without further purification.
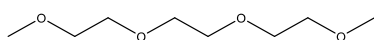
Triethylene glycol dimethyl ether (Triglyme, G3)
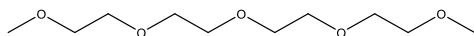
Tetraethylene glycol dimethyl ether (Tetraglyme, G4)
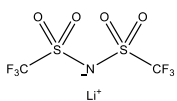
Lithium bis(trifluoromethanesulfonyl)imide
(LiTFSI)
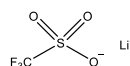
Lithium trifluoromethane sulfonate
(LiOTf)
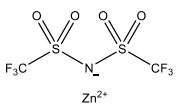
Zinc(II) bis(trifluoromethanesulfonyl)imide
(ZnTFSI)
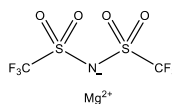
Magnesium(II) bis(trifluoromethanesulfonyl)imide
(MgTFSI)
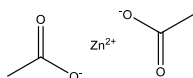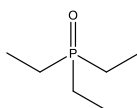
Zinc acetate   Triethylphosphine oxide   Octylamine
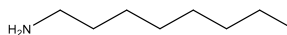
Figure 2-2. Chemicals used in Chapter 4.

1.3 Encapsulants, Additives, and Substrates

The previously prepared Ali D23_EV and Aro(1,1) D23_EV were selected as a rigid encapsulant. Loctite EO7021 was purchased from Henkel as a control group for a rigid encapsulant. Aro(1,0) D26_EV and Aro(0,1) D26_EV were selected as a soft encapsulant. Sylgard 184^{TM} was purchased from Dow for as a control of a soft encapsulant. The solvate ionic liquid catalyst, [Zn$_{0.5}$(G4)]TFSI was also adopted and added in the EV at the dose of 0.5 mol%.

For rigid substrates, 2-inch silicon wafer with a thickness of 280 μm and 2-inch EgleXG glass wafer with a thickness of 500 μm were used. For a flexible substrate, a sheet of polyimide film (HJA150) with a thickness of 150 μm was used.

2 Formation of Epoxy Vitrimers

2.1 Syntheses of Vinylogous Urethane-based Dynamic Curing Agents

2.1.1 Aliphatic Building Block-based Dynamic Curing Agent (Ali DCA)

The method used in Spiesschaert et al.'s study was employed (Spiesschaert, *et al.*, 2020). EAAc was added to a solution of BAC and TREN in a typical molar ratio of 9:14:4, although the mix ratio can be changed if necessary. To remove the water product, 1 g of $MgSO_4$ was added to the mixture. The mixture was then magnetically stirred and heated at 40°C for 24 h. Afterward, the mixture was centrifuged and dried in a vacuum oven at 90°C to eliminate any remaining water. The resulting yellow liquid was stored in an N_2 atmosphere desiccator before use. The prepared Ali DCA is a mixture of condensation products between EAAc-BAC (Ethyl 3-(((3-(aminomethyl)cyclohexyl)methyl)amino)but-2-enoate) and EAAc-TREN (Ethyl 3-((2-bis(2-aminoethyl)amino)ethyl)amino)but-2-enoate).
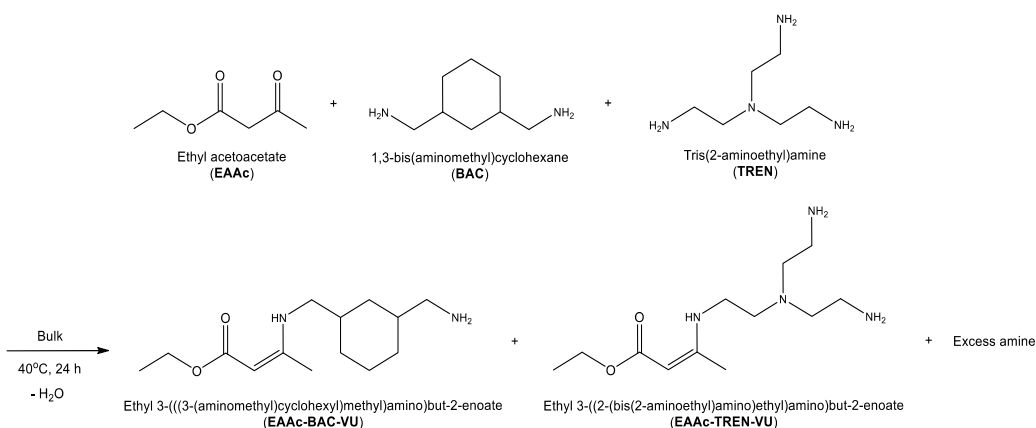
Figure 2-3. Reaction scheme for the synthesis of Ali DCA.

2.1.2 Aromatic Building Block-based DCAs (Aro DCAs)

2.1.2.1 One Aromatic Building Block DCAs (Aro(1,0)- and Aro(0,1) DCA)

Two types of DCA with one aromatic building block were prepared: Aro(1,0)- and Aro(0,1) DCA. The first number in the parenthesis represents the number of aromatic building blocks in the non-exchanging region (i.e., the dangling site after epoxy-amine curing reactions). In contrast, the second number represents the aromatic building blocks in the exchanging region (i.e., the intertwined site after epoxy-amine curing reactions).

To synthesize Aro(1,0) DCA, BAAc was added to a solution of BAC and TREN in a typical molar ratio of 9:14:4, although the mix ratio can be changed if necessary. To remove the water product, 1 g of $MgSO_4$ was added to the mixture. The mixture was then magnetically stirred and heated at 40°C for 24 h. After that, the mixture was centrifuged and dried in a vacuum oven at 90°C to eliminate the remaining water. Then, the yellow liquid was stored in an N_2 atmosphere desiccator before use. The prepared Aro(1,0) DCA is a mixture of condensation products between BAAc-BAC (Benzyl 3-(((3-(aminomethyl)cyclohexyl)methyl)amino)but-2-enoate) and BAAc-TREN (Benzyl 3-((2-bis(2-aminoethyl)amino)ethyl)amino)but-2-enoate).
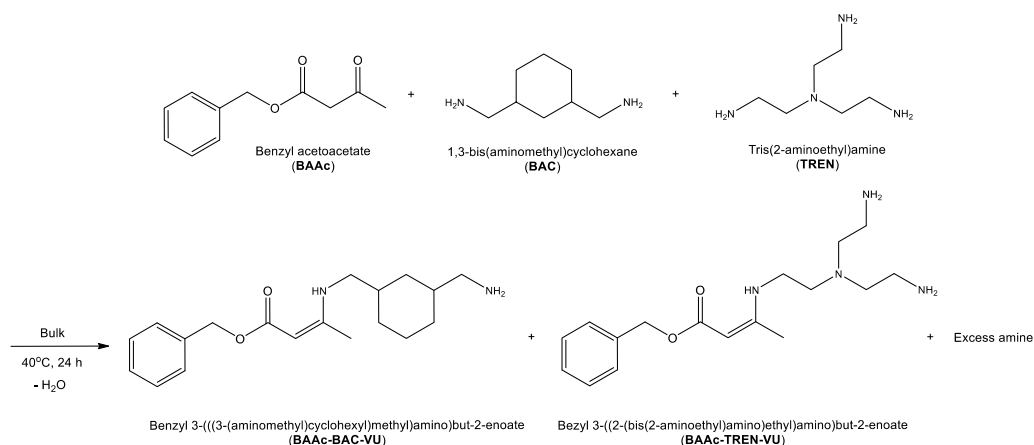
Figure 2-4. Reaction scheme for the synthesis of Aro(1,0) DCA.

For the synthesis of Aro(0,1) DCA, EAAc was added to a solution of XDA and TREN in a typical molar ratio of 9:14:4, although the mix ratio can be changed in necessary. To remove the water product, 1 g of MgSO₄ was added to the mixture. The mixture was then magnetically stirred and heated at 40°C for 24 h. After, the mixture was centrifuged and dried in a vacuum oven at 90°C to eliminate the remnant water. Then the yellow liquid was stored in an N_2 atmosphere desiccator before use. The prepared Aro(0,1) DCA is a mixture of condensation products between EAAc-XDA (Ethyl 3-(((3-(aminomethyl)benzyl)amino)but-2-enoate) and EAAc-TREN (Ethyl 3-((2-bis(2-aminoethyl)amino)ethyl)amino)but-2-enoate).
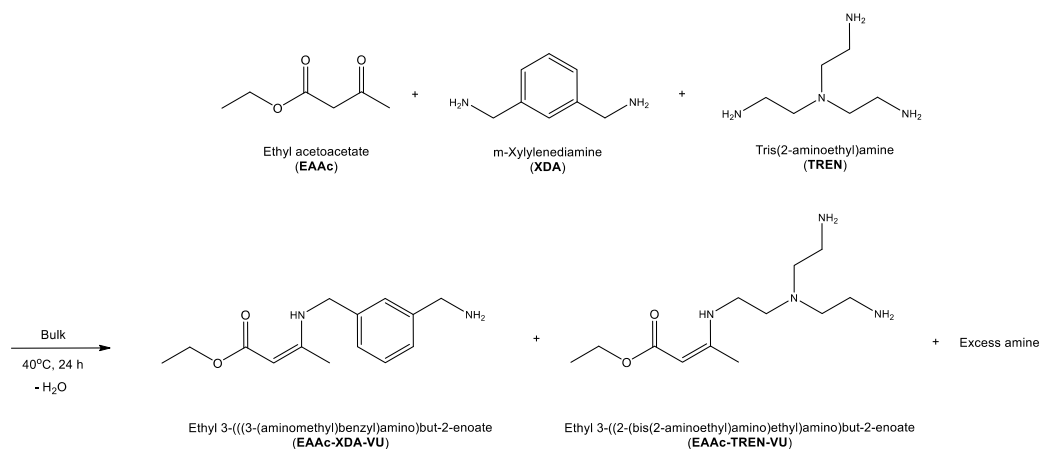
Figure 2-5. Reaction scheme for the synthesis of Aro(0,1) DCA.

2.1.2.2. Two Aromatic Building Blocks DCA (Aro(1,1) DCA)

BAAc was added to a solution of XDA and TREN in a typical molar ratio of 9:14:4, although the mix ratio can be changed in necessary. To remove the water product, 1 g of MgSO₄ was added to the mixture. The mixture was then magnetically stirred and heated at 40°C for 24 h. After, the mixture was centrifuged and dried in a vacuum oven at 90°C to eliminate the remnant water. Then the yellow liquid was stored in an N_2 atmosphere desiccator before use. The prepared Aro(1,1) DCA is a mixture of condensation products

between BAAc-XDA (Benzyl 3-(((3-(aminomethyl)cyclohexyl)methyl)amino)but-2-enoate) and BAAc-TREN (Benzyl 3-((2-bis(2-aminoethyl)amino)ethyl)amino)but-2-enoate).
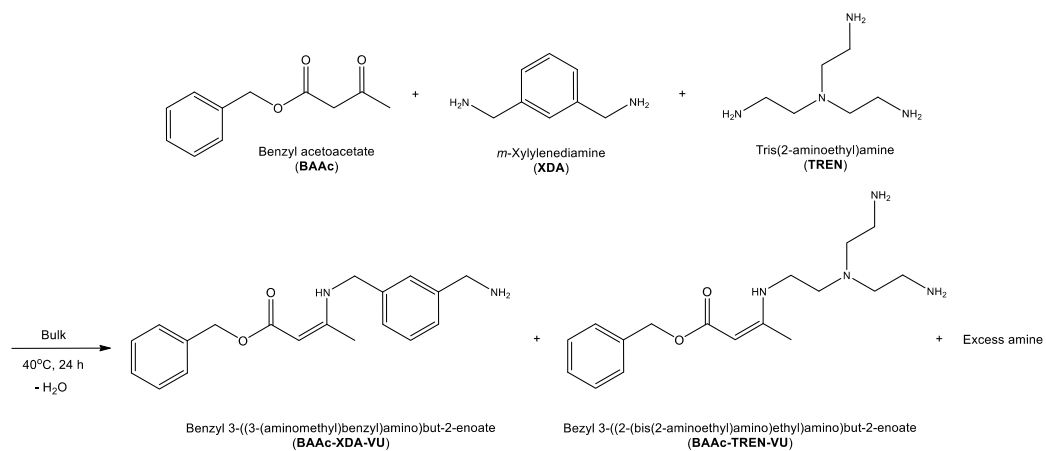
Figure 2-6. Reaction scheme for the synthesis of Aro(1,1) DCA.

2.2 Designing an Epoxy Vitrimer System (1) A ratio of Epoxy:Amine

Two criteria should be considered in advance to design epoxy vitrimers (EV) systematically. The first criterion concerns the system's initial fraction of -NH functionalities. This value critically determines the number of crosslinking points after the amine-epoxide reaction and, accordingly, the crosslinking density (the average distance between crosslinking points). If this parameter is changed, the resulting crosslinked network would have a completely different web structure, making it difficult to interpret the influence of sub-components or types of linkages. Therefore, our DCA-cured epoxy system should be designed according to a single value of the parameter "r" (an initial mole ratio between active hydrogen functionalities and epoxide + acetoacetate functionalities).

All commercialized epoxy resins use a parameter to measure the quantity of epoxide functionalities, called epoxy equivalent weights (EEW), which is the weight of resin per epoxy functionality. EEW is necessary for calculating the stoichiometric ratio of curing agents required to obtain a fully crosslinked structure. For example, with amine-curing agents, allocating one epoxy functionality for each active hydrogen of the amine species is customary. However, our DCA-cured epoxy system needs to be 15% off-stoichiometry since the dynamic exchange reaction (after curing) requires an excess of primary amines in the system.

Keeping the criterion in mind, we prepared a typical recipe for mixing the epoxy resin that releases 10.87 mmol of epoxide (input 2 g, EEW: 184 g eq^{-1}) and DCA that has 26.14 mmol of active hydrogen (input 1.58 g), which will yield a 15% amine-rich off-stoichiometric formulation. This ratio is consistently adopted in all cases of using Ali-, Aro(1,0)-, Aro(0,1)-, and Aro(1,1) DCA.

2.3 Designing an Epoxy Vitrimer System (2) Quantity of Dynamic Linkages

The second criterion concerns the quantity of dynamic linkage within the crosslinks. In accordance with Li's adapted version of Flory-Stockmayer theory (Li, *et al.*, 2018), our vinylogous urethane epoxy system is designed to have varying proportions of permanent linkages below their gelation threshold. **Figure 2-7** illustrates the typical components in the system before epoxy curing. A_3 is the trifunctional amine crosslinker (TREN, with three -NH_2 groups), while A_2 is the bifunctional amine (BAC or XDA, with two -NH_2 groups). B_2 is the bifunctional epoxy monomer (diglycidyl ether of bisphenol A unit). Finally, D_1 is the monofunctional acetoacetate monomer (EAAc or BAAc). In this design, A groups can only react with B or D groups, and vice versa. Analogous to the Flory-Stockmayer theory, all the same functionalities are assumed to have an equal probability of reacting, and no intramolecular reaction occurs. After the formation of crosslinking networks, the linkage between A and D groups can undergo an exchange reaction with other A functionalities; i.e., the A-D linkages are dynamic, while the A-B linkages are permanent.
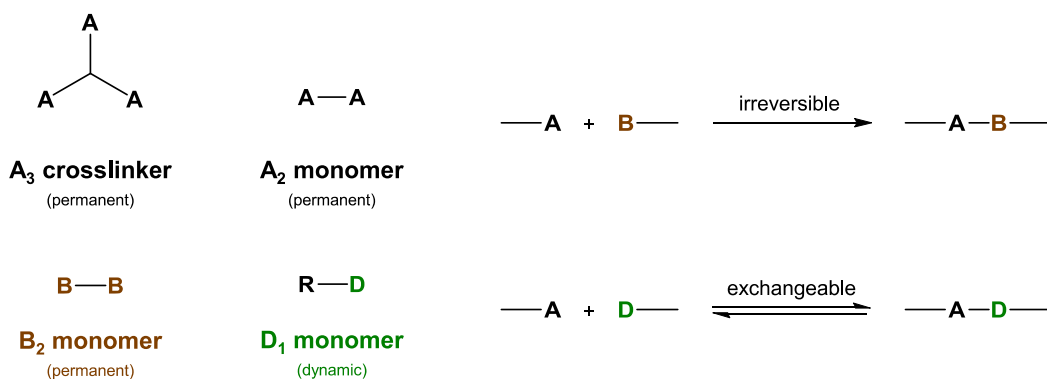
Figure 2-7. Possible linkages within the crosslinked networks; (upper) permanent and (lower) dynamic linkages.

Hereafter follows the parameter definitions that will be used in the calculation how much quantity of permanent network can exist in the EV without reaching percolation.

· r is the initial mole ratio between A functionalities and B + D functionalities, r = $N_{A, Init}$ / ($N_{B, Init}$ + $N_{D, Init}$) where $N_{A, Init}$, $N_{B, Init}$, and $N_{D, Init}$ are the initial molar quantity of A, B, and D functionalities, respectively.

· ρ is the fraction of A functionalities that initially belong to crosslinkers, hence ρ = 3 $N_{A3, Init}$ / ($3N_{A3, Init}$ + $2N_{A2, Init}$) where $N_{A3, Init}$ and $N_{A2, Init}$ are the molar quantity of A_3 and A_2 functionalities, respectively.

· S_B is the probability of A reacting with B, S_B = β × k / (k + 1) where β is a function of reactivity ratio, and k is the initial mole ratio between B and D functionalities: k = $N_{B, Init}$ / $N_{D, Init}$. If B and D functionalities equally reactive toward A, then β = 1.

· p_A is the fractional conversion of A and p_B is the fractional conversion of B. Accordingly, $N_{A, React.}$ is the amount of A functionalities reacted: $N_{A, React}$ = $N_{A, Init}$ × p_A and p_B = $N_{B, React}$ / $N_{B, Init}$.

The thoughtful consideration in Li's reverse Flory-Stockmayer gelation theory is that no permanent network should be percolated throughout the material, meaning that the linkages formed between A_3 or A_2 and B_2 must not react with each other above the gelation point. To determine the critical point of gelation, it is necessary to calculate the possibility of forming an A-B-A structure consisting only of permanent linkages. Based on the Flory-Stockmayer calculation (Flory, 1941, Stockmayer, 1944), the probability of a crosslinker leading to another crosslinker by a chain consisting of only permanent linkages, $α_p$:

$$α_p = [rp_A{}^2 ρ S_B^2 (k + 1)k]/[1 - rp_A{}^2(1 - ρ)S_B^2(k + 1)k] \quad \text{(Equation 2-1)}$$

In this context, the probability $α_p$ should be smaller than the critical gelation point, $α_c$, where $α_c$ = 1 / (f - 1), which is determined by the functionality of the crosslinker (f = 3).

$$[rp^2 ρ S_B^2(k + 1)k]/[1 - rp^2(1 - ρ)S_B^2(k + 1)k] < \frac{1}{f-1} \quad \text{(Equation 2-2)}$$

The equation 2-2 generally expresses the quantitative correlation between monomer compositions and the degree of conversion, which should be satisfied for an epoxy

containing both permanent and dynamic links to behave as a vitrimer.

In our case, all the system has excess of NH_2 in the network for the dynamic exchange reaction, then $r > 1$, and $p_A = N_{A,\,React} / N_{A,\,Initial} = (N_{B,\,Init} + N_{D,\,Init}) / N_{A,\,Initial} = 1 / r$ (assuming of full conversion of B and D). Then the S_B can be obtained via p_B since:

$$p_B = \frac{N_{B,React}}{N_{B,Init}} = \frac{N_{A,Init}\, p\, S_B}{N_{A,Init}\, \frac{k}{(k+1)}} = \frac{rpS_B(k+1)}{k} \;,$$

$$S_B = \frac{p_B k}{rp(k+1)} = \frac{k}{k+1} \qquad \text{(Equation 2-3)}$$

Inserting the $S_B = k / (k + 1)$ into the Equation 2-1,

$$\alpha_p = \frac{p\rho\frac{k}{(k+1)}}{[1-p(1-\rho)\frac{k}{(k+1)}]} \qquad \text{(Equation 2-4)}$$

Hence, in avoiding the formation of percolated permanent network, $\alpha_p < \alpha_{c,}$

$$\frac{[p\rho\frac{k}{(k+1)}]}{\left[1-p(1-\rho)\frac{k}{(k+1)}\right]} < \frac{1}{f-1} \qquad \text{(Equation 2-5)}$$

In our instance, a trifunctional crosslinker ($f = 3$) with 30 mol% of the fraction of the crosslinker and bi-functional amines ($\rho = 0.3$) is used; thus, the changes in k and p are only needed to be considered. For example, when we used the typical recipe of using the mix ratio of epoxy resin (10.87 mmol epoxide) and Ali-DCA composition (26.14 mmol active hydrogens) with a mix ratio of 4.5:2:7 = D:A_3:A_2, a 74 mol% fraction of permanent linkages and a 26 mol% fraction of dynamic linkages are obtained. In this case, $r = 1.15$, $p = 0.87$, and $k = 1.43$; thus, the $\alpha_p \sim 0.239$ is below the threshold $\alpha_c = 0.5$, which satisfies the criterion for the EV.

On the other hand, the Spiesschaert's calculation method differs from the traditional gelation theory in the light of determining the functionality of crosslinker (f). They calculated the functionality-averaged functionality of DCA: in a typical case, A_3 contains 6 NH groups and A_2 contains 4 NH groups. The mixture contains a molar quantity of 4 A_3 and 14 A_2, leading to f and resultant α_c:

$$f = \frac{4 \times 6 + 14 \times 4}{4 + 14} = 4.444, \quad \alpha_c = \frac{1}{f-1} = 0.29 \qquad \text{(Equation 2-6)}$$

They assumed that the primary amine and secondary amine react equally with epoxide. The result indicates that to avoid gelation of permanent linkages, the α_p should be lower than the threshold $\alpha_c = 0.29$. The point of the method is to calculate the ratio of A in DCA to B, which reflects the preferential reaction of A with D over B. In our typical 15% amine-rich formulation, 33.72 NH (5.90 × 4 + 1.69 × 6) moieties are present for 10.87 epoxides (2 g, EEW = 184 g mol^{-1}) functionalities. However, during the vinylogous urethane condensation, the 3.79 acetoacetates moieties heist 7.58 NH (3.79 × 2). Thus, a ratio of 26.14 NH to 10.87 epoxides is obtained as the calculation parameter, $1/r_{DCA}$:

$$\frac{1}{r_{DCA}} = \frac{10.87}{26.14} = 0.416 \qquad \text{(Equation 2-7)}$$

Hence, according to the second method, our typical formulation would not be re-processable since $1/r_{DCA} > \alpha_c$. Understandably, the method assumed the extreme case of equivalent reactivities of primary and secondary amines, so the threshold value overestimates the required quantity of dynamic linkages within the networks. Since our system uses a much more amine-excessive formulation than Spiesschaert's (5% excess), the deviation between the theoretical and actual situation is expected to be even greater.

Balancing Equations 2-5 and 2-7, we sorted and prepared six compositions with different fractions of dynamic linkages, all expected to exhibit vitrimeric performance. These compositions are listed in **Table 2-1**. To examine the validity of the reverse gelation theory, specimen preparation and testing for these compositions are required.

Table 2-1. Six compositions using Ali DCA with different dynamic linkage contents.

	A Ratio of Dynamic / Permanent Linkages	[Aceto acetates] [mmol]	r	ρ	k	p	α_p	α_c 1st Cal. Meth.	$1/r_{DCA}$	α_c 2nd Cal. Meth.
D40	40 / 60	70			0.74		0.15		0.40	
D34	34 / 66	60			0.95		0.18		0.41	
D29	29 / 71	50	1.15	0.3	1.24	0.87	0.22	0.5	0.41	0.29
D26	26 / 73	45			1.43		0.24		0.41	
D23	23 / 77	40			1.67		0.26		0.42	
D17	17 / 83	30			2.40		0.32		0.42	

2.4 Preparation of Epoxy Vitrimer Test Specimen

The following is the typical polymerization procedure using the synthesized Ali-, Aro(1,0)-, Aro(0,1)-, and Aro(1,1) DCAs. Each mixing ratio (epoxy to DCA) is adapted, corresponding to the composition list in **Table 2-2**. The epoxy resin was mixed with DCAs using a paste mixer for 5 × 2 min at 2000 rpm in an adapted ratio to ensure a 15% excess of primary amines. Then, the mixture was cast into a mold, left at 80°C for 12 h, and fully cured at 140°C for 8 h in a convection oven.

In chapter 4, the Ali D23 is consistently used as a dynamic curing agent in all formulations. YD-128 resin was mixed with the DCA using a paste mixer for 2 × 2 min at 2,500 rpm in an adapted ratio to ensure a 15% excess of primary amines. The additives (zinc acetate and solvate ionic liquid catalysts) were added at a fixed dose in this step. Then, the mixture was cast into a mold, left at 80°C for 12 h, and fully cured at 140°C for 8 h in a convection oven.

Table 2-2. EV Formulations of different dynamic fractions with Aro DCAs.

	DCA	Fraction of Dynamic Linkages	α_p	r
Aro(1,0) D40_EV		0.40	0.15	
Aro(1,0) D34_EV		0.34	0.18	
Aro(1,0) D29_EV	Aro(1,0) DCA	0.29	0.22	
Aro(1,0) D26_EV		0.26	0.24	
Aro(1,0) D23_EV		0.23	0.26	
Aro(1,0) D17_EV		0.18	0.32	
Aro(0,1) D40_EV		0.40	0.15	
Aro(0,1) D34_EV		0.34	0.18	
Aro(0,1) D29_EV	Aro(0,1) DCA	0.29	0.22	1.15
Aro(0,1) D26_EV		0.26	0.24	
Aro(0,1) D23_EV		0.23	0.26	
Aro(0,1) D17_EV		0.18	0.32	
Aro(1,1) D40_EV		0.40	0.15	
Aro(1,1) D34_EV		0.34	0.18	
Aro(1,1) D29_EV	Aro(1,1) DCA	0.29	0.22	
Aro(1,1) D26_EV		0.26	0.24	
Aro(1,1) D23_EV		0.23	0.26	
Aro(1,1) D17_EV		0.18	0.32	

3 Acceleration of Transamination via Solvate Ionic Liquids

3.1 Syntheses of Solvate Ionic Liquid Catalysts

3.1.1 Triglyme Solvated SILs

The lithium bis(trifluoromethanesulfonyl)imide, lithium trifluoromethane sulfonate salts, and triglyme were dried under a high vacuum at 140°C before use. The lithium salts were mixed with an equimolar amount of triglyme in a vial and magnetically stirred at 80°C overnight. All procedures (decanting, weighing, and mixing) were conducted in an N_2-filled glovebox with $[H_2O] < 100$ ppm. After the solvation of the metal salts, the solution was dried at 120°C in a convection oven overnight. The solvated ionic liquids became brownish after the removal of water molecules. In the current study, the glyme-metal X mixture of a 1:1 molar ratio is referred to as [M(G3)]X, respectively, which does not necessarily match the actual chemical formulation in the molten state. Rather, it represents the intended formula for the crystalline complexes.
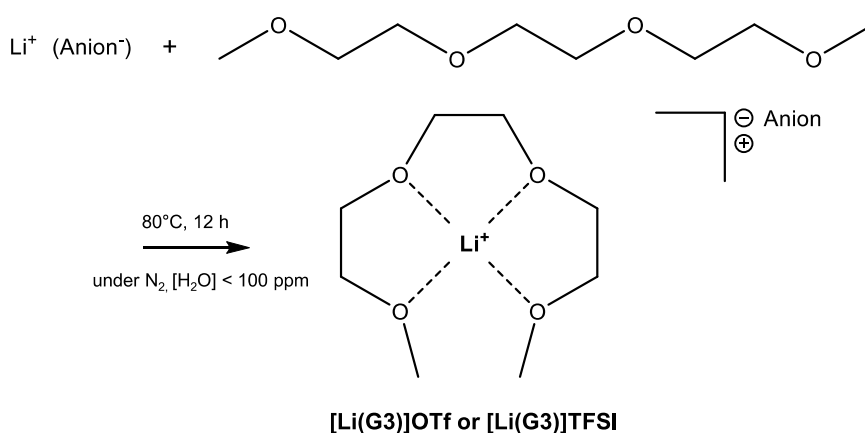
Figure 2-8. Synthesis of G3-solvated SILs.

3.1.2 Tetraglyme Solvated SILs

The magnesium bis(trifluoromethanesulfonyl)imide and zinc bis(trifluoromethanesulfonyl)imide salts and triglyme were dried under a high vacuum at 140°C before use. The metal salts were mixed with double the molar amount of tetraglyme in a vial and magnetically stirred at 80°C overnight. All procedures (decanting, weighing, and mixing) were conducted in an N_2-filled glovebox with $[H_2O] < 100$ ppm. After the solvation of metal salts, the solution was dried at 120°C in a convection oven overnight. The solvated ionic liquids turned brownish after the removal of water molecules. In the current study, the glyme-metal X mixture of 1:0.5 molar ratio is referred to as $[M_{0.5}(G4)]X$, respectively, which does not necessarily match the actual chemical formulation in the molten state. Rather, it represents the intended formula for the crystalline complexes.
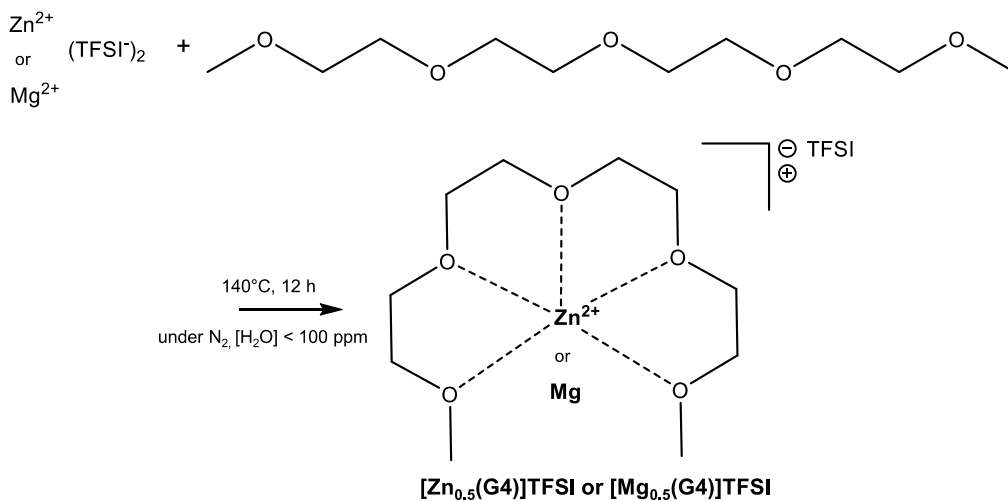
Figure 2-9. Synthesis of G4-solvated SILs.

3.2 Gutmann Acceptor Number of the Solvate Ionic Liquids

The Gutmann acceptor number measures the likelihood of a compound to coordinate with its environment and is used to evaluate the electrochemical properties of SILs (Eyckens, *et al.*, 2019). To determine this number, a solution containing the compound (2 mM) and triethylphosphine oxide in benzene-d_6 (0.67 mM) was analyzed using phosphorus-31 NMR measurements on a Bruker Avance 600. A proton-decoupled ^{31}P single-pulse spectrum was obtained, and the difference in chemical shift between the compound and triethylphosphine (δ_{adduct} - $\delta_{triethylphosphine}$ = $\Delta\delta_{adduct}$) was calculated. The Gutmann acceptor number was then calculated by multiplying this number by a factor (2.348) recommended by Gutmann (Mayer, *et al.*, 1975). The peak corresponding to the triethylphosphine/additive adduct in the ^{31}P NMR spectra was used for the calculations. The catalytic effects of the SILs on dynamic exchange reactions will be compared using this parameter.

3.3 A Model Study using a Small Molar Mass Compound

3.3.1 Synthesis of the Model Compound

Synthesis of Ethyl-3-((2-ethylhexyl)amino)but-2-enoate: The method was adapted from W. Denissen's study (Denissen, *et al.*, 2017). Ethyl acetoacetate (1.0 equiv.) and octylamine (1.1 equiv.) were vigorously mixed in 30 mL of chloroform and heated at 70°C for 24 h. When the formation of the vinylogous urethane was confirmed (by TLC and IR), the mixture was extracted four times with pH 4 brine and dichloromethane. The organic phase was dried with MgSO4 and evaporated, yielding a pale yellowish solution. Excess amine was further purified by passing through a silica gel 60-packed column using ethyl acetate as the eluent.
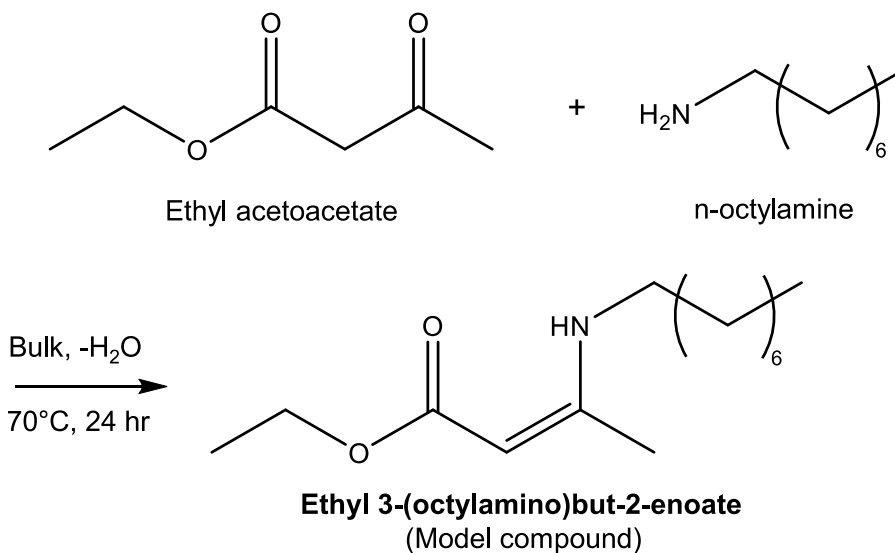
Figure 2-10. Synthesis of the Model Compound.

3.3.2 Tracing Transamination Reactions

The n-octyl vinylogous urethane compound (5 equiv.) was mixed with 2-ethyl-1-hexylamine (1 equiv.), dodecane (internal standard, 0.5 equiv.), and the additives (0.5 mol% in total) in a vial. The resulting mixture was heated in a heating bath, with temperatures set at 60°C, 70°C, and 80°C, respectively, and stirred at 200 rpm. The reaction was carried out at reasonably low temperatures for a vinylogous urethane-based system to suppress side reactions and evaporation. At specified intervals (0, 1, 5, 10, 30, and 60 minutes), 4 μl aliquots were taken and immediately diluted in dichloromethane. The ratio of 2-ethyl-1-hexylamine and octylamine was obtained by using GC-FID. The k-values for calculating activation energies were obtained by fitting the decaying curve. After the reference test without a catalyst, the catalytic effects of ethyl acetate and the SIL catalysts were compared through measurement.

4 Validation of Epoxy Vitrimer Encapsulants

4.1 Surface and Adhesion Properties

4.1.1 Surface Free Energy

The change in the surface chemistry of the EV was determined by analyzing the water contact angle (DSA100, KRUSS). The cured EV was hot-pressed to obtain a flat surface and then attached to a glass slide. At least ten drops (approximately 2 µL of volume) of water and diiodomethane (DIM) were placed randomly on each specimen, and the contact angle was measured after 10 seconds of equilibration time. The surface energy of the EVs was calculated according to Fowkes's theory, which defines both a dispersive and a non-dispersive component of the surface (Fowkes, 1962). The calculations for surface free energies of the substrates were conducted in the same manner.

4.1.2 Adhesion Performances

4.1.2.1 Die Shear Test

The epoxy mixture was poured onto the center of rigid substrates, including glass and a silicon wafer, to create a constant adhesion area of 5×5 mm^2. After being cured at 140°C for 6 hours, the substrate was firmly mounted on the testing stage of a Dage4000 Plus Bondtester (Nordson). The rectangular tip of the die shear jig moved at a speed of 100 µm s^{-1} and pushed the adhered sample to delaminate. The force profile was obtained as a function of time. The testing conditions were 23°C with 55% relative humidity.

4.1.2.2 T-peel Test

The T-peel test was performed to evaluate the interfacial adhesion property of the EVs with the flexible substrate. A polyimide film with a thickness of 150 μm was used as the substrate. The dimension of the adhesive bonding area was 115×25 mm^2, with an adhesive thickness of 50 μm. The thickness of the adhesive was controlled using a 3M cellophane tape attached at the point of 37.5 mm away from each end tip (half the size of the ASTM D1876). The specimen was cured at 80°C for 12 h and subsequently transferred to an oven at 140°C for 6 h to ensure sufficient curing. The cured specimen was then stored in a conditioning room at 23°C and 55% RH for three days. The test used a texture analyzer (TA.XT plus C, TA Instruments) with a crosshead speed of 112 mm min^{-1}.

4.2 Warpage Measurement for a Rigid Encapsulation

Warpage measurements of encapsulated 2-inch silicon and glass wafers were conducted using a manual height measure to determine where the maximum strain occurred. The process involved applying the same amount of epoxy mixture (2 g) to each wafer, placing the wafer on a non-sticking Teflon film, and transferring it to a convection oven preset at 200°C. After 6 hours of post-curing, the encapsulated wafer was cooled to ambient temperature. The fully cooled wafer showed concave warpage (in-plane direction), and the height at the tip of the boundary of the shrink wafer was considered as the value of the warpage.

4.3 Deformation Tests for a Soft Encapsulation

Bending and twisting tests were performed on encapsulated polyimide substrates by

manually applying multiple deformations. The samples were prepared using the same procedure as the 180° peel tests. The test was conducted on a heating block preset at 160°C. A simple structure of flexible hybrid electronics was also prepared by coating an NVE, EV, and PDMS encapsulant on a flexible printed circuit. Each soft package was deformed by bending, demonstrating the encapsulant's adaptability.

4.4 Rework Test

The Aro(1,0) D26_EV and Aro(1,1) D23_EV (with filler) encapsulants were applied onto a flexible printed circuit board and a rigid circuit board, respectively. The substrates were then heated at 180°C for 10 minutes to cure the encapsulants. After curing, the encapsulants were removed using tweezers.

5 Characterization of Materials

5.1 Validation of Chemicals

5.1.1 Nuclear Magnetic Resonance Spectroscopy

Nuclear magnetic resonance (NMR) analyses were conducted on a Bruker Avance 600 (600 MHz) for measuring proton spectra at 25°C. The NMR spectra were measured in $CDCl_3$, and chemical shifts (δ) are presented in parts per million (ppm) with respect to tetramethylsilane (TMS) as an internal standard. Data processing was carried out with MestReNova (ver. 9.0.1, Mestrelab Research S.L.)

5.1.2 Attenuated Total Reflectance-Fourier Transform Infrared Spectroscopy

Attenuated total reflection - Fourier-transform infrared spectroscopy (ATR-FTIR) spectra were obtained using a ThermoFisher Scientific Nicolet iS20, equipped with a PIKE GladiATR diamond ATR-accessory. The spectra were collected with a spectral resolution of 4 cm^{-1} in the range of 450-4000 cm^{-1}.

5.1.3 Raman Spectroscopy

Raman spectra were recorded on a Horiba LabRAM HR Evolution with a laser wavelength of 1064 nm. The SIL samples were sealed in a glass tube under a vacuum. The laser was focused onto the sample using a 50× (WD= 10.6 mm) NIR objective lens with a numerical aperture of 0.25. For the regions of interest, the data collection was made with a 1000 nm grating from 700 to 1000 cm^{-1} (1.5 cm^{-1} resolution) for 100 s and three accumulations.

5.1.4 Gas Chromatography-Mass Spectroscopy

Gas chromatography-mass spectroscopy (GC-MS) analyses were conducted on ISQ-LT GC/MS for measuring products of transamination reactions in the model study. During heating 25 to 150°C, the trace of exchange products of the model compound and n-octylamine were obtained by flame ion detector.

5.2 Mechanical / Viscoelastic Properties of Epoxy Vitrimers

5.2.1 Dynamic Mechanical Analysis

5.2.1.1 Storage and Loss Moduli

Dynamic mechanical analysis (DMA) was performed on a dynamic mechanical thermal analyzer (TA Q800) in a dual-cantilever mode. The specimen dimension was $35 \times 12.5 \times 3.0$ mm^3 (length × width × thickness). The oscillating amplitude was set at 15 μm. The storage modulus, loss modulus, and tan delta were measured at a frequency of 1 Hz and a heating rate of 3°C min^{-1} from 20 to 200°C. The glass transition temperature was taken at the peak point of the tan delta curve.

5.2.1.2 Stress-relaxation and Creep Tests

The creep and stress-relaxation tests were conducted using tension-film mode on the same DMA instrument. The typical specimen dimension was $10 \times 12.5 \times 1.2$ mm³ (length × width × thickness). Creep tests were performed at 160°C for 180 min under a constant pressure of 5 kPa. Creep-recovery experiments at different temperatures were also performed using a constant pressure of 5 kPa. At first, no tensile stress was applied for 300 s. Sequentially, a 5 kPa tensile stress was applied for 1500 s, and then the stress was removed for another 1500 s. Stress-relaxation tests were performed at 160°C for 180 min using a constant strain of 2% (within the range of linear viscoelastic region). The relaxation modulus was recorded, and the characteristic relaxation time (τ^*) was obtained at 36.8% of the initial relaxation modulus. Data processing was performed by Universal Analysis 2000 (ver. 4.5A, TA Instruments - Waters LLC).

In chapter 4, the stress-relaxation test used a constant strain of 3% (within the range of linear viscoelastic region) to rapidly obtain the relaxation time.
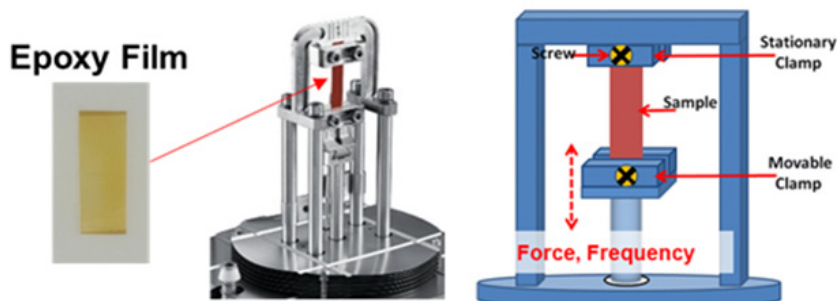
Figure 2-11. Schematic illustration of DMA creep and stress relaxation tests.

5.2.2 Rheology Analysis

An MCR 302e rheometer (Anton-Paar) with a disposable aluminum plate (diameter = 5 mm) was used to measure the rheological properties of the EVs. The cured sample was placed on the lower plate, and the gap between the upper and lower plates was set at 0.5 mm, which was kept constant during the test. The sample was frequency-scanned under a strain of 2% at 160°C.

5.2.3 Universal Testing Machine

The tensile properties of the cured epoxy specimens were measured using a Zwick/Roell Z050 universal testing machine (UTM) equipped with a 50 kN load cell at a speed of 10 mm min^{-1} and a preload of 0.05 N. The specimens were prepared as a dumbbell according to the ASTM D638 standard. Prior to each measurement, the specimen was gripped with an effective gauge length of 40 mm and equilibrated at the testing temperature for 10 minutes. At least five specimens were tested to obtain average values.

5.2.4 Thermomechanical Analyzer

The EV was cured in a mold, yielding a bulk cube whose size is $5 \times 5 \times 5$ mm^3. The prepared specimen was pressed by load of 100 kPa under heating from 30 to 200°C with a heating rate of 3°C min^{-1} (TMA 402 F3, Netzsch).

5.3 Properties Related to Encapsulant

5.3.1 Thermogravimetric Analysis

Thermogravimetric analyses (TGA) were performed with a PerkinElmer TGA4000 instrument under a nitrogen atmosphere (flow rate = 20 mL min^{-1}) at a heating rate of 10 °C min^{-1} from 40°C to 800°C for the dynamic mode. Isothermal measurements were conducted at 150°C for 60 min. About 5-10 mg of samples were weighed in a ceramic crucible.

5.3.2 Thermal Conductivity

The thermal diffusivities of the cured epoxies were measured by a laser flash method (LFA 457, Netzsch). The specific heat capacity was measured by a differential scanning calorimetry in the range of 20-200°C. The testing was conducted according to ASTM E1461.

5.3.3 Water Vapor Transmission Rate

The water vapor transmission rates (WVTR) of the epoxy samples were measured on a Permatran-W 3/61 MA (Mocon Corp.). The specimen dimensions were $10 \times 10 \times 0.1$ cm^2 (Length × Width × Thickness). The testing was conducted according to ASTM F1249, under $38 \pm 2°C$, 100% relative humidity.

5.3.4 Volume Resistivity

The direct-current volume resistivities of the encapsulants were measured using a 4-point probe meter (MCP-HT800, Mitsubishi) at 300 V. 5 discs were used for the measurement, and every specimen was measured 20 times to get an average value. The specimen dimensions were $10 \times 10 \times 0.1$ cm^2 (Length × Width × Thickness). The testing was conducted according to ASTM D257, under $23 \pm 2°C$, $45 \pm 5\%$ relative humidity.

Chapter 3

Vinylogous Urethane Epoxy Vitrimer System:

Effects of Dynamic Curing Agents and Compositional

Changes in Crosslinked Covalent Adaptable Networks

1 Introduction

There are four primary functions of adhesives used in semiconductor applications: mechanical attachment, electrical interconnections, thermal dissipation, and stress dissipation. The first function is the naturally expected action for adhesives: bonding heterogeneous surfaces and maintaining interfacial adhesion forces throughout various production and service conditions. The second function is required for adhesives that serve a special role: forming electrical connections between semiconductor devices and printed circuit boards or film-based hybrid microcircuits. The third function is about releasing the confined heat within the multi-component devices using a filled adhesive of high thermal conductivity. The last function – stress dissipation – is the most recently deemed important as the adherend substrate, such as dies and films, has become thinned and enlarged. Throughout the multi-component architecture of electronics assembly and packaging designs, adhesives are the only polymeric (or tidal) material to dissipate internally generated stress and relieve external vibration or shock. Due to major changes in the electronics production environment, the need to develop specialized adhesives capable of stress absorption and dissipation has greatly increased. Such changes expose vulnerable points to external or internal stresses: (1) the use of larger chip devices or substrates, (2) the use of fragile components (glass diodes, fiber optics, microelectromechanical systems (MEMS)), (3) the use of thinned silicon or GaAs wafer, (4) increased I/Os number and reduced line widths, and (5) the use of flexible circuitry (Lau, 2020, Yufeng Jin, 2011)

By far, elastomeric adhesives with a low modulus are occasionally adopted for these specific requirements. They are often called low-stress or no-stress adhesives and have tailored mechanical properties to reduce stress. The representative specialties are (1) a moderate curing temperature. (2) low cure-induced shrinkage (less than 3%). (3) a low modulus of elasticity. (4) a CTE value close to that of the adherend, and (5) a T_g value that lies outside the scope of its operating temperature (James J. Licari, 2005). However, the types of these materials are often limited, and their long-term reliability and fidelity are

questionable against the harsh and diverse processing environments of electronics or semiconductor production. Accordingly, the diverse development of materials capable of stress reduction is in dire need, whether based on elastomeric or not.

Epoxy resin has been the most important family of polymeric adhesives in the electronics packaging industry. The various formulations based on the epoxy material are extensively used in die and substrate attachment, surface mounting, underfill, solder replacement, and molding or potting. They are the best choice in component assembly, exhibiting excellent adhesion and mechanical strength, and in packaging material due to their insulation properties against solvents, moisture, and electricity. The epoxy materials earn these properties from crosslinked molecular networks formed during curing. However, this rigid architecture functions inversely when the situation demands coping with stresses. Because of the pre-fixed network structure, the material lacks macroscopic flowability or flexibility and thus fails catastrophically at the adhered interfaces, damaging the thin adherends and threatening continuous production. This puts a limitation on its application as a low-stress adhesive.

To circumvent these problems, we suggest introducing a vitrimer system that uses a conventional epoxy formulation or at least a similar one. Vitrimers are a subcategory of covalent adaptable networks that allow exchange reactions between adjacent crosslinks while keeping the number of crosslinks constant, resulting in a permanent, structurally rigid yet dynamic network that enables the material to topologically flow or relax its structure against stresses (Kloxin and Bowman, 2013) Ever since the pioneering study by Leibler and colleagues (Montarnal*, et al.*, 2011), vitrimers have attracted substantial interest from academia and industry for their thermoplastic-like behavior at high temperatures. There have been many attempts to use this new class of polymer as a self-healing coating, reusable material, or shape-converting thermoset (Bai and Zheng, 2020, Capelot*, et al.*, 2012, Lu*, et al.*, 2021, Snyder*, et al.*, 2018, Taplan*, et al.*, 2020) Despite the ample potential of vitrimers in electronics assembly and packaging applications due to their stress-relaxation character, practical approaches to exploit this feature have yet to be developed.

One major reason is well pointed out in a noteworthy review article by Du Prez and co-workers, disclosing vitrimer's inevitable drawback - susceptibility to creep (Denissen, *et al.*, 2016). For typical processing of epoxy adhesives, creep behavior is highly undesirable and can potentially undermine the material's dimensional stability against multiple thermal shocks and external complex stresses. A balance between stress-relaxation and creep properties should be conceived in advance to utilize the vitrimer system and its characteristics in semiconductor packaging production. Recently, Sumerlin and co-workers stated that incorporating permanent crosslinks (i.e., normal covalent links) could render structural integrity and reduce plastic deformation of the vitrimer system (Cash, *et al.*, 2018). However, the material ceases to be a vitrimer at some point, losing stress-relaxation properties even at high temperatures. The critical level of permanent crosslinks is related to the system's percolation threshold, and its limiting condition can be roughly determined by Flory's and Stockmayer's gelation theory (Flory, 1941, Stockmayer, 1944). Torkelson and co-workers derived a theoretical, quantitative prediction of the limiting fraction of permanent crosslinks that constitute vitrimers without sacrificing vitrimer's characteristics - melt-state re-processability in the case (Li, *et al.*, 2018). Their approach is the reverse direction of the Flory-Stockmayer gelation theory, which shows how a low quantity of permanent segments in the vitrimer can be permitted to retain infinite connectivity or a gelation state. From the calculation, they tuned the epoxy resin formulation just below the critical gelation point, which strongly suppresses creep without sacrificing the vitrimer's advantages. However, they regarded the reactivities of amine to epoxide and amine to acetoacetate as the same and ignored the possible reaction between the secondary amine and epoxide for simplicity of calculation. Hence, the suggested threshold of a required amount of dynamic linkage needed to be higher, where the material with minimum dynamic linkages turned out to be not re-processable.

As an alternative, Du Prez and co-workers devised both a theoretical and empirical calculation for constructing a re-processable epoxy vitrimer (EV) of low-creep-guaranteed but rapid stress-relaxation (Spiesschaert, *et al.*, 2020). They used vinylogous urethane chemistry, formed by an a priori condensation reaction between acetoacetates and primary

amines. Hence, the researchers took into consideration the required quantity of amine moieties for both the vinylogous urethane-forming reaction and the subsequent epoxy-amine curing reaction. Following the adapted Flory-Stockmayer theory, they designed the prepolymer's formulation - the molar ratio of epoxide and amine moieties, considering leaving excess free amines after curing. Meanwhile, they proposed a different calculation method, which assumes that (1) the reaction of amine to acetoacetate precedes (which was true, as they prepared the dynamic curing agent separately) and (2) the reactivities of primary amine and secondary amine to epoxide were the same (which is not true, as they stated). The assumption led the calculation to overestimate the necessary dynamic linkages for re-processability, which can severely aggravate the creep behavior of the material.

Here, we sought to determine the optimum range for the ratio of dynamic to permanent linkages within the vinylogous urethane-based EV to balance between the two abovementioned thresholds. Our systematic and empirical study of the EV provides us with various EV formulations that simultaneously exhibit decent stress-relaxation behavior and suppressed creep behavior. In our system, we adopted an excessive off-stoichiometric ratio (15% amine-rich to epoxide) to accelerate the dynamic exchange reaction when the amount of dynamic linkages within the network is comprehensively limited to suppress creep behavior.

Additionally, we examined the effect of substituents in the dynamic curing agents (DCAs), which possess the vinylogous urethane functionality and multi-amine end-groups. The rate of the dynamic exchange reaction strongly depends on the ambient population of the exchangeable moieties and the corresponding moieties' tendency to participate in the reaction (reference). When the DCA cures the commercial epoxy resin, the crosslinked networks can behave as an EV. Under this preset, we replaced the chemical component of DCAs to change the hydrophobicity of the resultant epoxies. The changes in substituents and nucleophilic reactivity of the curing agent greatly influence the formation of epoxy crosslink networks, thus determining the final product's mechanical strengths and surface characteristics. This defines the basis for the great chemical versatility of our approach. By

adopting different types of substituents for DCAs, we can produce various sets of EV adhesives that are well-suited for different types of substrates (e.g., silicon wafer, glass wafer, polyimide film) and corresponding applications.

2 Results and Discussion

2.1 Syntheses of DCAs

2.1.1 The Synthesis of Ali DCA

The yield of Ali DCA was 96%. Its chemical structure was defined by ^{1}H-NMR spectrum and FT-IR spectrum. In the FT-IR spectrum, the newly formed stretching vibrations of carbonyl and vinyl moieties at 1646 and 1600 cm^{-1}, respectively, denotes the formation of the vinylogous urethane linkage in the Ali DCA. Note that the stretching vibration of ester moieties of EAAc at 1737 and 1712 cm^{-1} was totally consumed after the condensation reaction. In the ^{1}H NMR spectrum, peaks of chemical shift around 4.8 ppm are attributed to the newly formed vinyl proton, which is not present in the reactants (EAAc, BAC, and TREN). The list of total peaks from the NMR analysis is as follows:

δ: 1.21 (m, H_{a-c}, H_{y-z}, $H_{w'-z'}$), 1.45 (m, H_{n-q}), 1.64-1.83 (m, H_{m-r}), 2.32 (m, H_{g-l}, $H_{g'-l'}$, H_{w-x}), 2.64 (m, $H_{s'-v'}$, $H_{m'-l'}$), 4.15 (q, J = 7.1 Hz, H_{d-e}, $H_{d'-e'}$), 4.28 (m, $H_{k'-l'}$), 4.85 (m, H_f, $H_{f'}$), 7.16 (s, C_6D_6), 9.07 (m, H_j, $H_{j'}$)

2.1.2 The Synthesis of Aro(1,0) DCA

The yield of Aro(1,0) DCA was 97%. Its chemical structure was defined by ^{1}H-NMR spectrum and FT-IR spectrum. In the FT-IR spectrum, the newly formed stretching vibrations of carbonyl and vinyl moieties at 1646 and 1600 cm^{-1}, respectively, denotes the formation of the vinylogous urethane linkage in the Aro(1,0) DCA. Note that the stretching vibration of ester moieties of BAAc at 1737 and 1712 cm^{-1} was totally consumed after the condensation reaction. In the ^{1}H NMR spectrum, peaks of chemical shift around 4.8 ppm are attributed to

the newly formed vinyl proton, which is not present in the reactants (BAAc, BAC, and TREN). The list of total peaks from the NMR analysis is as follows:

δ: 1.11 (m, $H_{ab\text{-}ac}$, $H_{ab'\text{-}ac'}$, $H_{z'\text{-}aa'}$), 1.38 (m, $H_{t\text{-}aa}$), 1.63 (m, $H_{r\text{-}s}$), 2.32 (m, $H_{j\text{-}l}$, $H_{j'\text{-}l'}$, $H_{p\text{-}q}$), 2.63 (m, $H_{p'\text{-}s'}$, $H_{t'\text{-}y'}$), 4.53 (s, $H_{n\text{-}o}$), 4.89 (m, H_i, $H_{i'}$), 5.28 (m, $H_{g\text{-}h}$, $H_{g'\text{-}h'}$), 7.16 (s, C_6D_6), 7.20 (m, $H_{a\text{-}f}$, $H_{a'\text{-}f'}$), 9.02 (m, $H_{m,m'}$)

2.1.3 The Synthesis of Aro(0,1) DCA

The yield of Aro(0,1) DCA was 92%. Its chemical structure was defined by ^{1}H-NMR spectrum and FT-IR spectrum. In the FT-IR spectrum, the newly formed stretching vibrations of carbonyl and vinyl moieties at 1646 and 1600 cm^{-1}, respectively, denotes the formation of the vinylogous urethane linkage in the Aro(1,0) DCA. Note that the stretching vibration of ester moieties of BAAc at 1737 and 1712 cm^{-1} was totally consumed after the condensation reaction. In the ^{1}H NMR spectrum, peaks of chemical shift around 4.8 ppm are attributed to the newly formed vinyl proton, which does not present in the reactants (EAAc, XDA, and TREN). The list of total peaks from the NMR analysis is as follows:

δ: 1.11 (m, $H_{ab\text{-}ac}$, $H_{ab'\text{-}ac'}$, $H_{z'\text{-}aa'}$), 1.38 (m, $H_{t\text{-}aa}$), 1.63 (m, $H_{r\text{-}s}$), 2.32 (m, $H_{j\text{-}l}$, $H_{j'\text{-}l'}$, $H_{p\text{-}q}$), 2.63 (m, $H_{p'\text{-}s'}$, $H_{t'\text{-}y'}$), 4.53 (s, $H_{n\text{-}o}$), 4.89 (m, H_i, $H_{i'}$), 5.28 (m, $H_{g\text{-}h}$, $H_{g'\text{-}h'}$), 7.16 (s, C_6D_6), 7.20 (m, $H_{a\text{-}f}$, $H_{a'\text{-}f'}$), 9.02 (m, $H_{m,m'}$)

2.1.4 The Synthesis of Aro(1,1) DCA

The yield of Aro(1,1) DCA was 94%. Its chemical structure was defined by ^{1}H-NMR spectrum and FT-IR spectrum. In the FT-IR spectrum, the newly formed stretching vibrations of carbonyl and vinyl moieties at 1646 and 1600 cm^{-1}, respectively, denotes the formation of the vinylogous urethane linkage in the Aro(1,1) DCA. Note that the stretching vibration of

ester moieties of BAAc at 1737 and 1712 cm^{-1} was totally consumed after the condensation reaction. In the ^{1}H NMR spectrum, peaks of chemical shift around 4.8 ppm are attributed to the newly formed vinyl proton, which does not present in the reactants (BAAc, XDA, and TREN). The list of total peaks from the NMR analysis is as follows:

δ: 0.91 (s, H$_{v-w}$), 1.45 (m, H$_{ab'-ac'}$, H$_{z'-aa'}$), 2.14 (m, H$_{j-l}$, H$_{j'-l'}$), 2.52 (m, H$_{p'-s'}$, H$_{t'-y'}$), 2.73 (m, H$_{n'-s'}$), 3.64 (m, H$_{n-o}$, H$_{p-q}$), 4.76 (m, H$_i$, H$_{i'}$), 5.25 (m, H$_{g-h}$, H$_{g'-h'}$), 7.16 (s, C$_6$D$_6$), 7.20 (m, H$_{a-f}$, H$_{a'-f'}$, H$_{r-u}$), 7.87 (m, H$_{v-w}$), 9.02 (m, H$_{m,m'}$)

Figure 3-1. a IR spectrum and **b** ^{1}H spectrum of the synthesized Ali DCA.
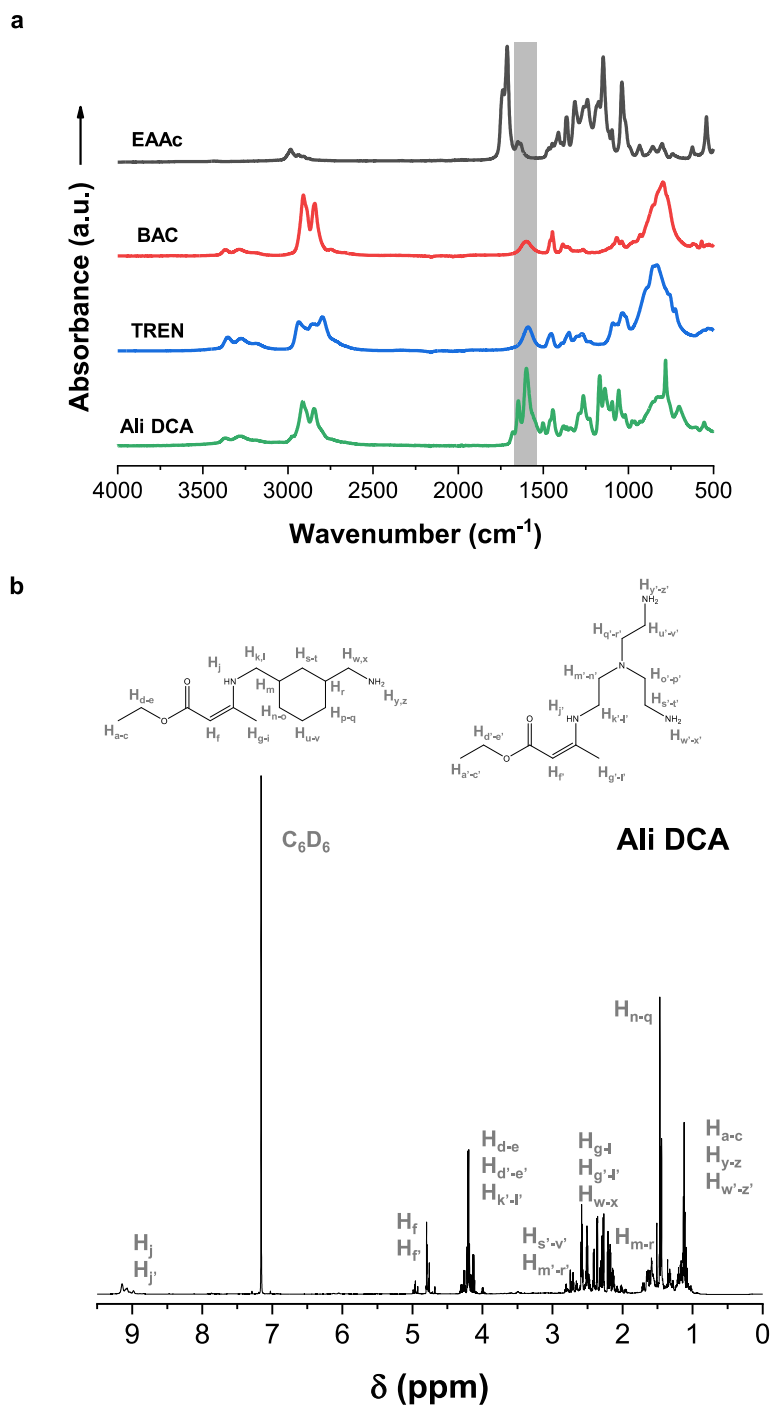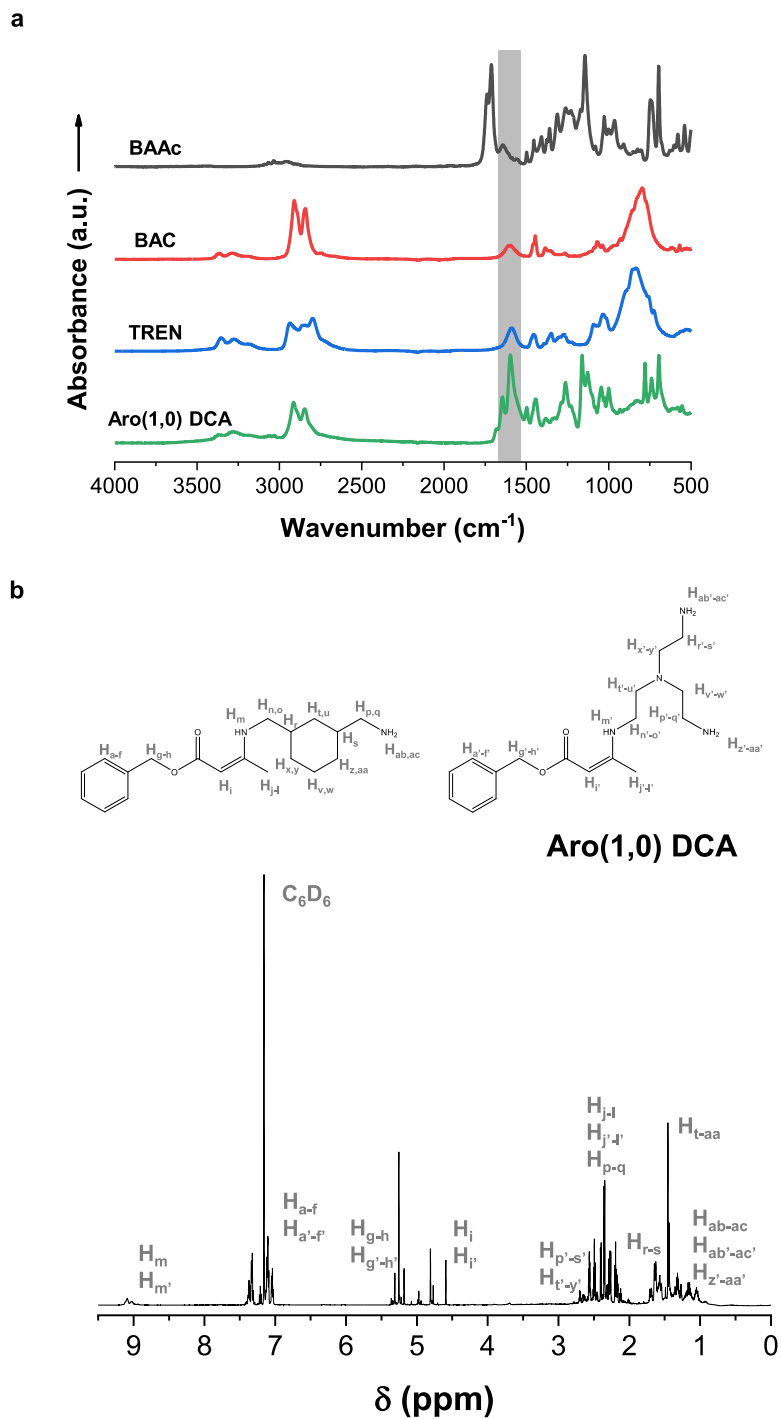
Figure 3-2. a IR spectrum and **b** ^{1}H spectrum of the synthesized Aro(1,0) DCA.

a

EAAc

XDA

TREN

Aro(0,1) DCA

Absorbance (a.u.)

Wavenumber (cm^{-1})

4000 3500 3000 2500 2000 1500 1000 500

b

Aro(0,1) DCA

C$_6$D$_6$

H$_j$
H$_{j'}$

H$_{o-r}$

H$_f$
H$_{f'}$

H$_{d-e}$
H$_{d'-e'}$

H$_{k-l}$
H$_{m-n}$

H$_{p'-s'}$
H$_{t'-y'}$

H$_{y'-z'}$
H$_{w'-x'}$

H$_{g-i}$
H$_{g'-i'}$

H$_{a-c}$
H$_{a'-c'}$

H$_{s-t}$

δ (ppm)

9   8   7   6   5   4   3   2   1   0
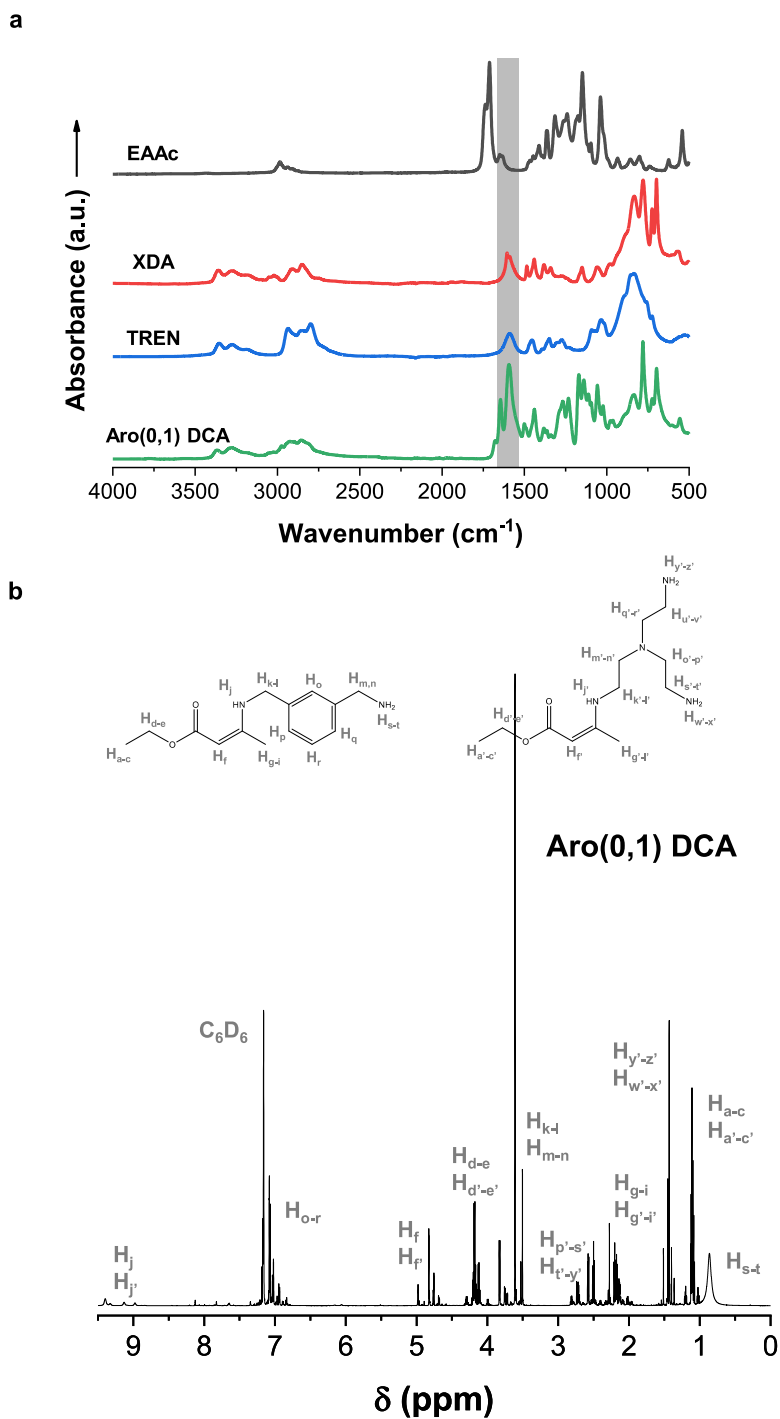
Figure 3-3. a IR spectrum and **b** ^{1}H spectrum of the synthesized Aro(0,1) DCA.
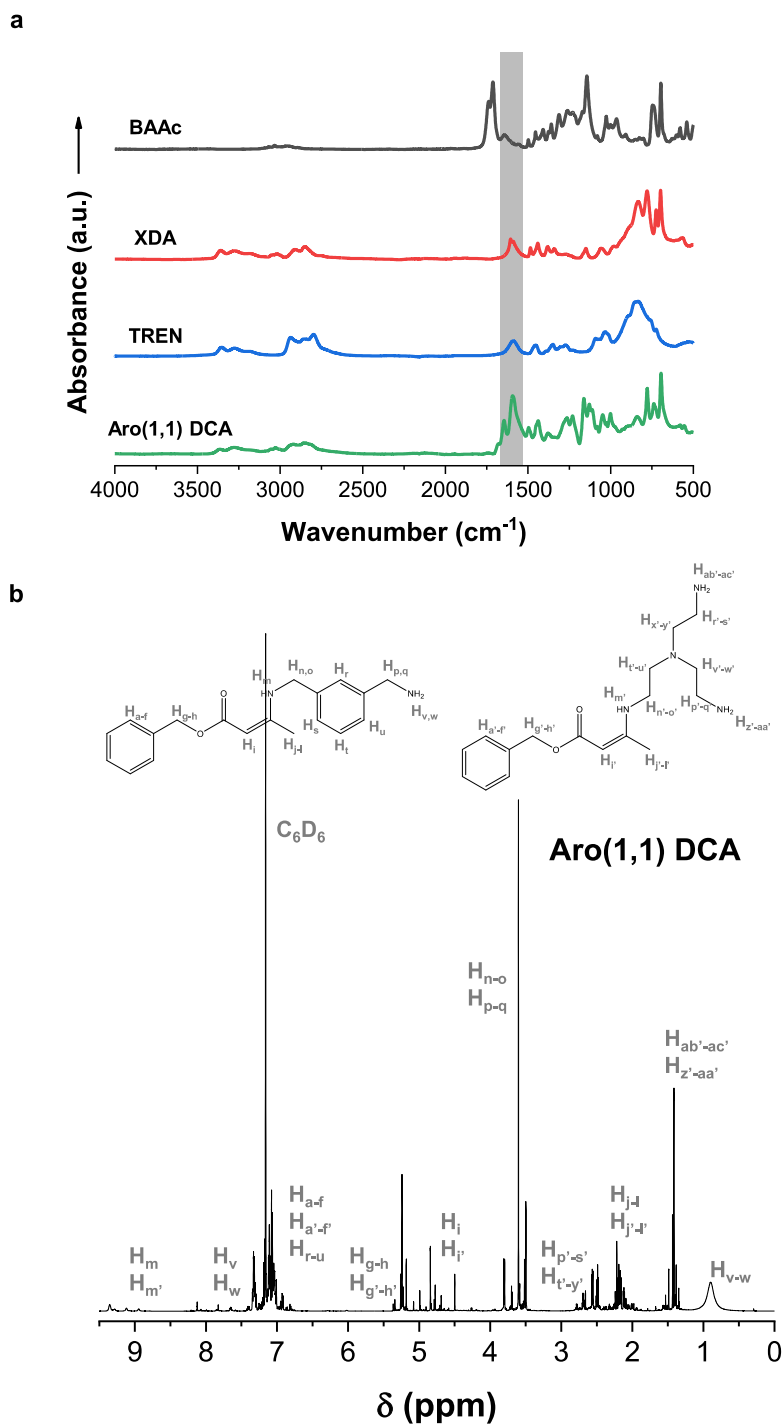
Figure 3-4. a IR spectrum and **b** ^{1}H spectrum of the synthesized Aro(1,1) DCA.

2.2 Verifying the Formation of Epoxy Vitrimer Systems

2.2.1 Superiority of an Off-stoichiometric System on Vitrimer Performances

Prior to analyzing the effects of composition, we attempted to verify that the off-stoichiometric system is superior to the stoichiometric system in terms of stress-relaxation and creep properties. We aim to design an EV system with good stress-relaxation properties while keeping its creep properties as low as possible. In the vinylogous urethane-based EV, stress-relaxation of the networks occurs when a secondary amine at the vinylogous urethane is exchanged with a neighboring primary amine. Thus, the amine exchange reaction rate is highly dependent on the concentration of primary amines in the system. When an EV system adopts a stoichiometric formulation, all the primary amines are consumed during epoxy curing, so the transamination reaction is unavailable throughout the system. Under these circumstances, transamination occurs only when the primary amine functionality at the end of dangled chains survives curing due to incomplete condensation, steric hindrance, or regional rheological differences. In contrast, an off-stoichiometric formulation provides plenty of free primary amines even after epoxy curing, allowing the crosslinked networks to access and react with them readily.

Here, we prepared four different systems and compared their stress-relaxation and creep properties at 160°C. NVE is non-vitrimer epoxy, cured by BAC and TREN (without EAAc) with a stoichiometric ratio. The r(1.0)_Ali D35_EV stands for an EV cured by the Ali D35 DCA with a stoichiometric ratio (r = 1.0). The r(1.15)_Ali D26_EV and r(1.15)_Ali D29 stand for EVs, cured by the Ali D26 and D29 DCA, respectively, with an off-stoichiometric ratio (r = 1.15). All the EV samples showed higher stress-relaxation and creep strain than the NVE. The stoichiometric EV showed a stress-relaxation ability in the middle of those of r(1.15)_Ali D26_EV and D29_EV (**Figure 3-5a**). The earlier stage of the stress-relaxation curve of the stoichiometric EV was even closer to that of the r(1.15)_Ali D26. As stated above, the D34 DCA contains higher contents of dynamic linkages than the D26 or D29

DCAs. The result denotes that the stoichiometric system is much less efficient and requires a much higher composition of dynamic linkages to achieve a similar degree of stress-relaxation ability compared to the off-stoichiometric system. Moreover, this kind of increase in dynamic links would inevitably lead to a rise in creep deformation. The creep results show that the r(1.0)_Ali D35_EV recorded the highest strain, above 8%, whereas the off-stoichiometric systems recorded a medium range of strain, below 5% (**Figure 3-5b**). Considering their stress-relaxation abilities were comparable, the higher insertion of dynamic links within each system only begets negative effects on creep performance. Additionally, since the thermomechanical degradation of the EVs due to changes from a stoichiometric to an off-stoichiometric formulation seems minor (**Table 3-1**), adopting the off-stoichiometric system should be more sensible.

Table 3-1. Thermomechanical properties of EVs cured by Ali-DCAs with mixing ratios of r = 1.0 and r = 1.15.

	T_g (DMA) [°C]	Max. storage modulus [MPa]	$T_{d5\%}$ [°C]	Tensile strength [MPa]
r(1.0)_Ali D34_EV	75	825	268	74
r(1.15)_Ali D26_EV	78	810	261	72
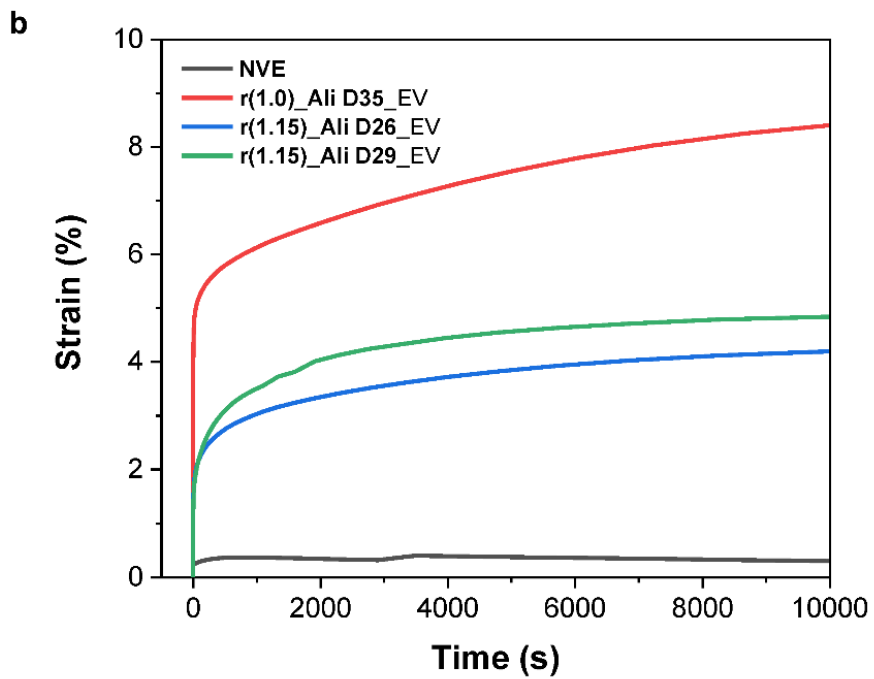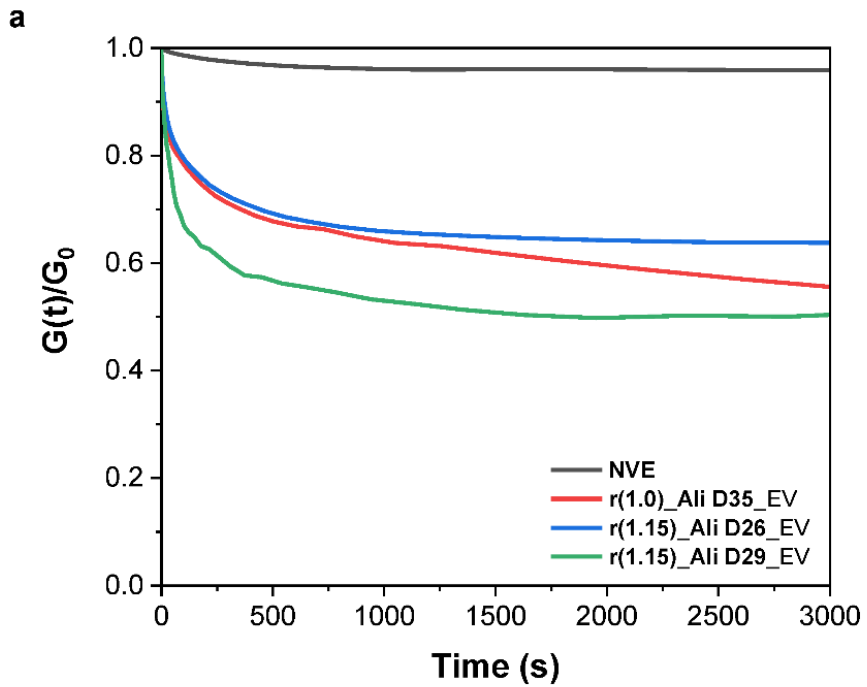
Figure 3-5. a Stress-relaxation and **b** creep strain curves obtained from the NVE, r(1.0)_Ali D35_EV, r(1.15)_Ali D26_EV, and r(1.15)_Ali D29_EV.

2.2.2 Verifying the Formation of Re-processable Cured Epoxy Vitrimers

According to the reverse approach of the Flory-Stockmayer theory, we designed formulations for an EV system possessing different amounts of dynamic linkages within the network. To this end, we used different kinds of DCAs, named after their dynamic fraction ([acetoacetate]/[amines]), to cure each EV. For example, if we used Ali D26 DCA as a curing agent, the cured epoxy would be named Ali D26_EV. By adapting the mix ratios between the DCA and the epoxy monomer, the resultant crosslinked network would possess as many dynamic linkages as it has been named. Then, each EV system is differentiated by the two gelation parameters, $1/r_{DCA}$ (a ratio of epoxides and remnant amines in a DCA) and αpermanent (i.e., a probability of percolation of permanent crosslinks). Meanwhile, all EV systems will have constant values for the basal parameters, ρ (a fraction of crosslinker amines in a DCA) and r_{total} (a ratio of amines in the system). We tested the formation of cured EVs under ten formulations (D0, D6, D11, D17, D23, D26, D29, D34, D40, and D46) using four types of DCAs (Ali-, Aro(1,0)-, Aro(0,1)-, and Aro(1,1) DCA) (**Figure 3-6**). Regardless of the type of DCA, the formulations named D0, D6, D11, and D46 were not fully cured after the curing schedule. The formulations were assumed to have too little or too much curing agent to fit the parameters. Except for the case of using Aro(0,1) DCA, all the other formulations from D17 to D40 were confirmed to be successfully cured and sustained during the characterization. However, Aro(0,1) D34_EV and Aro(0,1) D40_EV were unavailable for such tests due to their low hardness and high stickiness, even at room temperature.

The six EV formulations (D17, D23, D26, D29, D34, and D40) survived a re-processing test (chipped and remolded at 180°C for 6 h), exhibiting no significant change in appearance, and E' at the glassy state almost maintained, compared to that of the corresponding pristine samples (**Figure 3-7a, b**). The result is notable since their dynamic fractions are not expected to be re-processable according to the reported thresholds (Li*, et al.*, 2018, Spiesschaert*, et al.*, 2020). In the report of Spiesschaert, the required quantity of dynamic linkages within the EV network is about 42 mol% to be fully re-processable when they use a 5% primary amine-

87

excessive system. It appears that the 15% amine-excessive formulation of our system contributed to providing the ready-to-exchange environment and lowering the hurdle of dynamic linkages within the networks. The low-dynamic fraction-but-fully-re-processable formulations would be a great boon to the EVs for having the resilience to multiple thermal shocks and low creep behaviors at high temperatures.

Nomenclature	Not being cured (Too less curing agents)			Fully Cured (Re-processable)						Not being cured (Too much substances)
	D0	D6	D11	D17	D23	D26	D29	D34	D40	D46
Dynamic fraction	0	6	11	17	23	26	29	34	40	46
Parameters										
r_{total} ([f$_{amine}$]/([f$_{epoxide}$]+[f$_{Acetoacetate}$]))				1.15 (15% off-stoichiometric)						
ρ ([f$_{amine,\ crosslinker}$]/[f$_{amine,\ total}$])				0.3						
$\alpha_{permanent}$ (a probability of percolation of permanent crosslinks)	1	0.51	0.40	0.32	0.26	0.24	0.22	0.18	0.15	0.12
α_c (critical gelation point, according to the Li's calculation)		**0.5** Li's threshold								
$1/r_{DCA}$ ([f$_{epoxide}$]/([f$_{amine}$]-[f$_{Acetoacetate}$]))	0.43	0.43	0.43	0.42	0.42	0.41	0.41	0.41	0.40	0.39
α_c (critical gelation point, according to the Spiesschaert's calculation)									**0.29** Spiesschaert's threshold	

Not re-processable (if, $\alpha_{permanent} > 0.5$) (Underestimation of a required dynamic fraction)

Not re-processable (if, $1/r_{DCA} > 0.29$) (Overestimation of a required dynamic fraction)

Figure 3-6. Formulations and resulted parameters for various EV systems

89
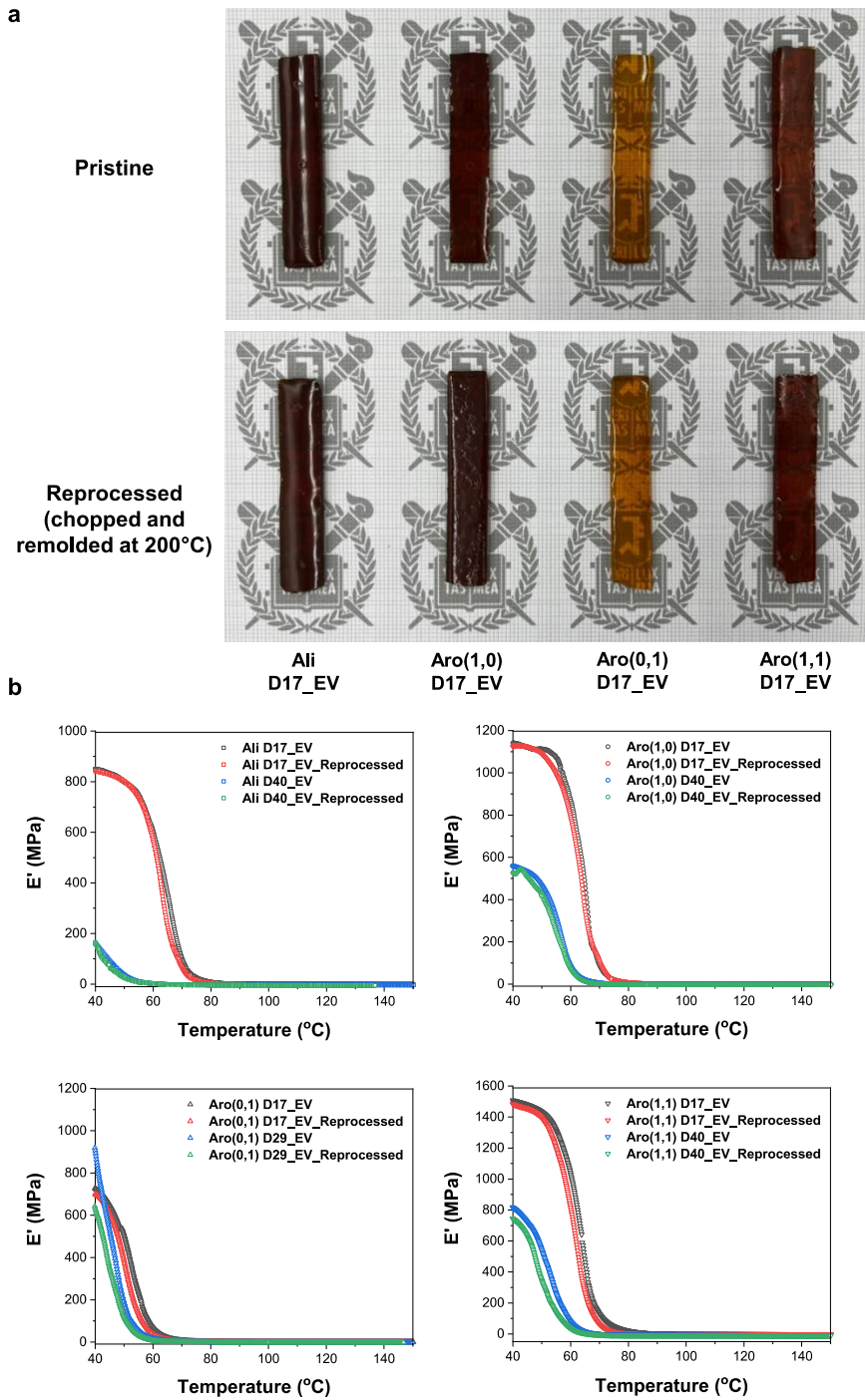
Figure 3-7. a Photographs of pristine and reprocessed EVs, cured by four different types of DCAs. **b** Comparisons for storage moduli of the pristine and reprocessed EVs.

2.3 Effects of Dynamic Linkage Compositions

The effect of fabricating a hybrid vitrimer network, consisting of both dynamic (reversible) and permanent (irreversible) linkages, has been documented so far (Li*, et al.*, 2018, Meng*, et al.*, 2019, Taplan*, et al.*, 2020). Nevertheless, few papers cover materials like our EV system, with a high off-stoichiometric composition and high mechanical strength, meticulously designed for industrial usage. It would be beneficial for us to explore changes in various properties of EV systems in accordance with their compositional deviations.

2.3.1 Storage modulus at a Glassy State and T_g

Firstly, we measured storage moduli (E') and tan(δ) for the prepared 6 (compositions) × 4 (types of DCAs) EVs (**Figure 3-8**). All the cured samples exhibited storage moduli > 10^8 Pa at 30°C, which are very high for the vitrimer materials whose typical E' at room temperature are about $10^4 \sim 10^7$ Pa (Bai and Zheng, 2020, Haida*, et al.*, 2020, Reisinger*, et al.*, 2021). From the result, the storage moduli at the glassy state first increased and then decreased as the dynamic fraction included in each network increased. In designing DCA composition, the inclusion of dynamic linkage was enabled by the addition of acetoacetates (EAAc, BAAc) into the mixture of bi-functional amine (BAC, XDA) and tri-functional amine (TREN). The higher the fraction of dynamic linkage in a DCA, the lower the amine functionalities left after forming vinylogous urethane moiety. Thus, EVs with high dynamic linkages require a higher input of the corresponding DCA to compensate for the amine loss. The vinylogous urethane moiety in a DCA would act as a chain extender between the crosslinked sites (i.e., amine end functionality). Thus the higher inclusion of dynamic fraction lowers the crosslinking density of the epoxy network during curing. Hence, the cured EVs with higher dynamic fractions like D29, D34, and D40 showed a linear degradation of E' and recorded below almost half of the highest value obtained from D17 or

D23. Nevertheless, the cured samples were hard and non-sticky at room temperature, similar to other commercial plastics. Notably, regardless of the types of DCAs, the samples cured with DCA D23 recorded the highest E' in each DCA series. The obtained E' values are above 10^9 Pa, comparable to an amine- or polyamine-cured commercial epoxies. This high level of hardness would render the EVs the mechanical stability and reliability required in industrial fields.

Meanwhile, the results for tan(δ) indicate that an increase in dynamic linkages leads to a reduction in the glass transition temperature (T_g) of the EV. The T_g values of Ali D17_EV, Aro(1,0) D17_EV, and Aro(1,1) D17_EV were above 80°C, while the T_g value of Aro(0,1) D17_EV was 68°C. These T_g values were relatively low compared to amine-cured commercial epoxies, which typically have a T_g around 90~140°C (Licari and Swanson, 2011). Even considering the effect of off-stoichiometric composition, the degree of reduction in T_g seems severe, which requires an explanation from another point of view. It can be attributed to the dynamic exchange reaction within the network during heating. The potential amine-exchanging reaction is responsible for intra- or intermolecular polymer chain rearrangement, which advances the onset of the glass-to-rubber transition. Transamination was observed even below the T_g point (81°C) of Ali D17_EV by monitoring the changes in its IR spectrum as a function of time, measured at 60°C (**Figure 3-9**). The intensities of stretching and vibration bands corresponding to amine and vinyl moieties of the DCA increased as the reaction proceeded. Additionally, the reduction of T_g was aggravated as the dynamic fraction increased (**Table 3-2**). It appears that the properties related to material stability (namely, E' and T_g) were in inverse proportion to the tendency of chain rearrangement.

Table 3-2. Maximum E' and T_g of the Ali DCA_EVs with different fractions of dynamic linkage.

	Ali DCA		Aro(1,0) DCA		Aro(0,1) DCA		Aro(1,1) DCA	
	Max E'	T_g	Max E'	T_g	Max E'	T_g	Max E'	T_g
	[MPa]	[°C]	[MPa]	[°C]	[MPa]	[°C]	[MPa]	[°C]
D17	866	81	738	82	777	68	1538	87
D23	1126	80	1150	77	1270	67	1632	79
D26	792	78	1156	74	953	66	938	75
D29	740	74	817	72	1231	65	1268	73
D34	697	73	685	67	-	-	1167	70
D40	292	64	573	66	-	-	862	68
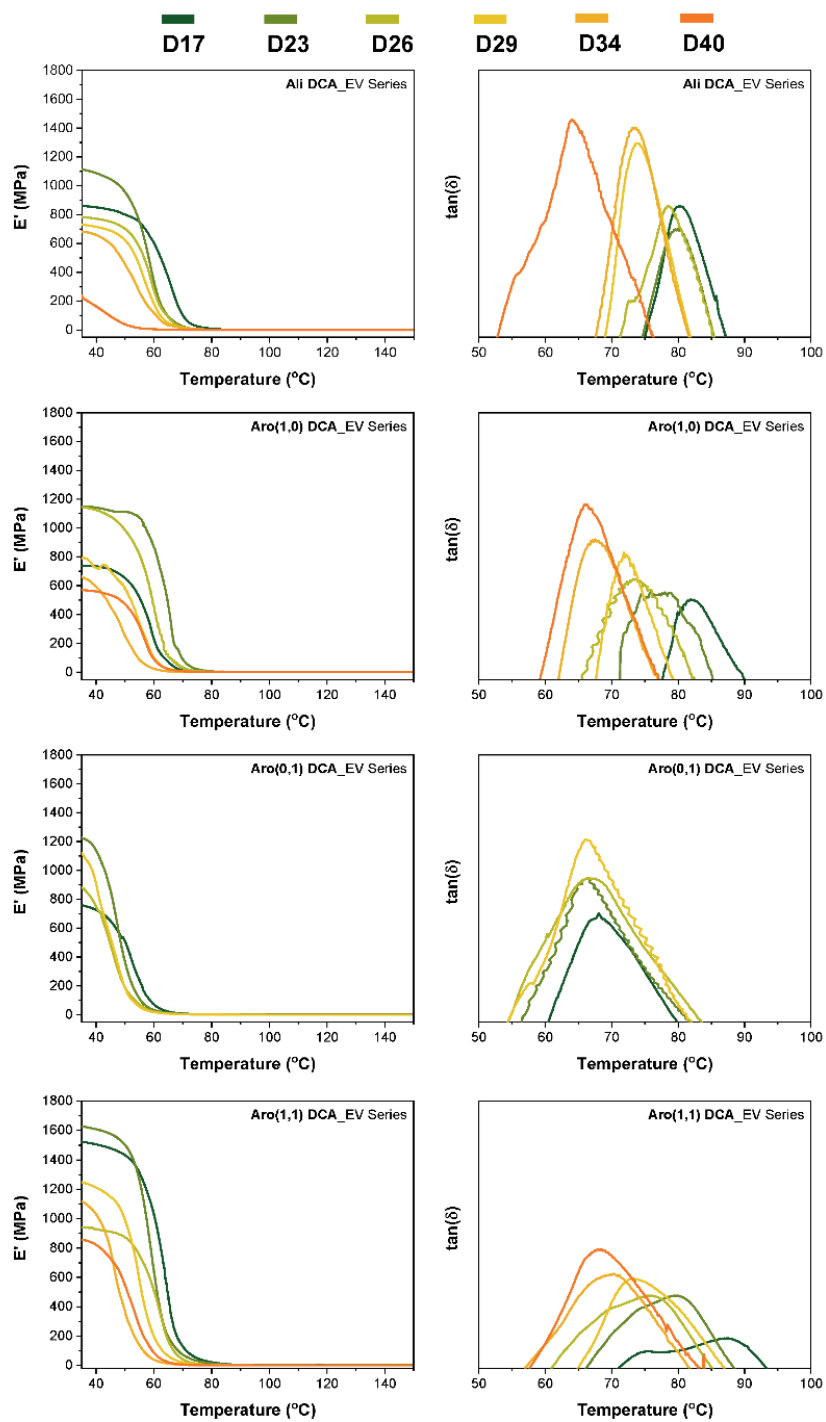
Figure 3-8. E' and tan(δ) of the cured EV with different fractions of dynamic linkages.
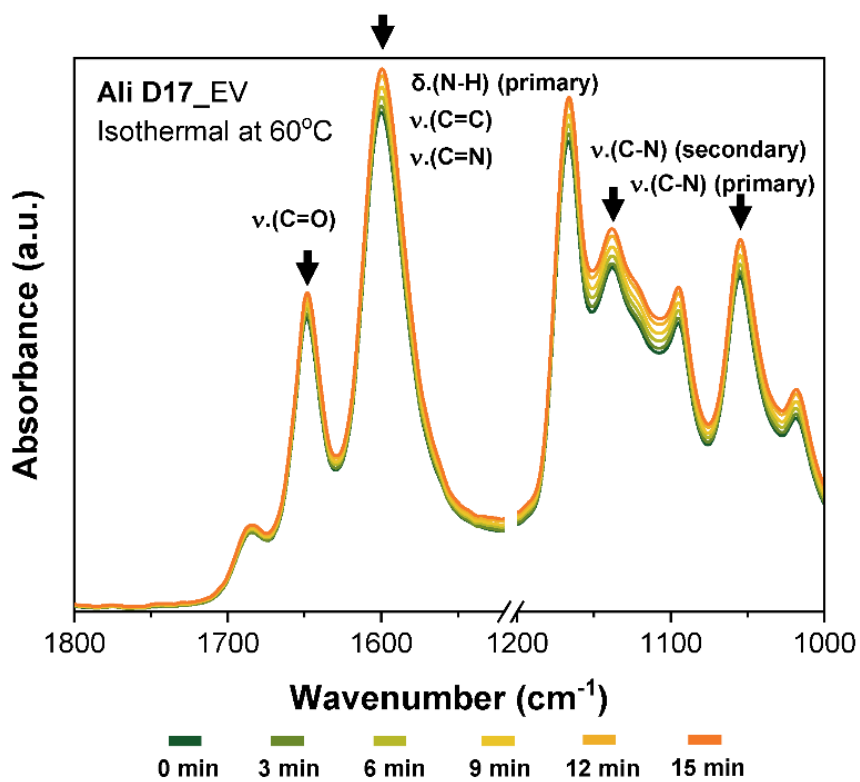
Figure 3-9. Monitoring IR spectra of Ali D17_EV for 15 min at 60°C in the range of 1000-1800 cm⁻¹.

2.3.2 Stress-relaxation and creep behaviors

The stress-relaxation curves of the cured EVs with different fractions of dynamic linkages were obtained from the DMA stress-relaxation tests at 160°C (**Figure 3-10**). All series showed a consistent tendency that samples with higher dynamic fractions resulted in lower residual stress values at the final testing time. However, the obtained relaxation curves included a distinctive soaring shape for some samples, denoting an unequilibrated state at the end of the tests. In the Ali DCA_EV series, the D17_EV sample reached the lowest point of the residual stress of 0.908 as it was stretched, and then the value went back up to 0.95 after 3000 s. Likewise, the Aro(1,0) D17_EV reached the residual stress to unity. The stress-relaxation at an early stage occurred because of the chain rearrangement within the vitrimer network. However, at the later stage of the test, the measured stress increases if the material shows a high elastic response against the direction of deformation. This behavior was also reported in hybrid vitrimer networks (Meng, *et al.*, 2019).

In general, the viscoelastic flow behavior of polymers, such as stress-relaxation, is analyzed using various mathematical models. The Maxwell model, with a serial connection of a spring and a dashpot, traditionally well-represents the time-dependent stress relaxation function of viscoelastic liquids, formulated as follows:

$$\tau(t) = \gamma_0 \cdot G \cdot \exp(-t/\tau^*) \qquad \text{(Equation 3-1)}$$

where $\tau(t)$ is the time-dependent stress, γ_0 is the initial constant strain, G is related to the spring constant, and τ^* is the relaxation time, which corresponds to the time constant determining the system's time-dependent behavior of the serially connected components of the Maxwell model. Given the concept of a vitrimer is coined after vitreous liquids, the interpretation of the stress-relaxation behavior of a vitrimer is also rooted in the Maxwell model; hence τ^* is important.

In the Ali DCA_EV series, none of the samples reached the relaxation modulus point of $1/e$ (= 0.368), which denotes the characteristic relaxation time (τ^*) of the system. On the

contrary, in the other three EV series with aromatic DCAs, half of the samples (D29, D34, and D40) successfully reached the point and recorded their τ^*. It can be assumed that the transamination reaction and subsequent chain rearrangement are more vigorously activated when aromatic DCA is present within vitrimer networks. The faster transamination due to an aromatic building block in a vinylogous urethane molecule has already been reported (Haida and Abetz, 2020). A detailed discussion of the effect of types of DCA will be presented in section 3.4.

Notably, the residual stresses (after relaxation) were sequentially decreased upon increasing the dynamic fractions from D17 to D40, regardless of the type of DCAs. A higher degree of stress-relaxation can be achieved as the system secures more dynamic components within its network. In addition, the decreasing slope of relaxation curves at the initial stage decreases much faster as the dynamic linkage fraction increases. This sudden decrease is not only due to the accelerated exchange reaction but also to the viscoelastic response of the epoxy matrix. As already stated, the elastic moduli of the EVs with a high dynamic fraction are low (**Table 3-2**). This is attributed to the increased dose of acetoacetates ([acetoacetates]/[epoxide]), which does not participate in crosslinking. As bulky pendants are inserted between crosslinks, the node density decreases, so the network secures a large free volume to rearrange and dissipate stress (**Figure 3-11**). The interpretation of crosslinking density and stress-relaxation is consistent with other vitrimer systems (Fortman*, et al.*, 2017, Yu*, et al.*, 2014).
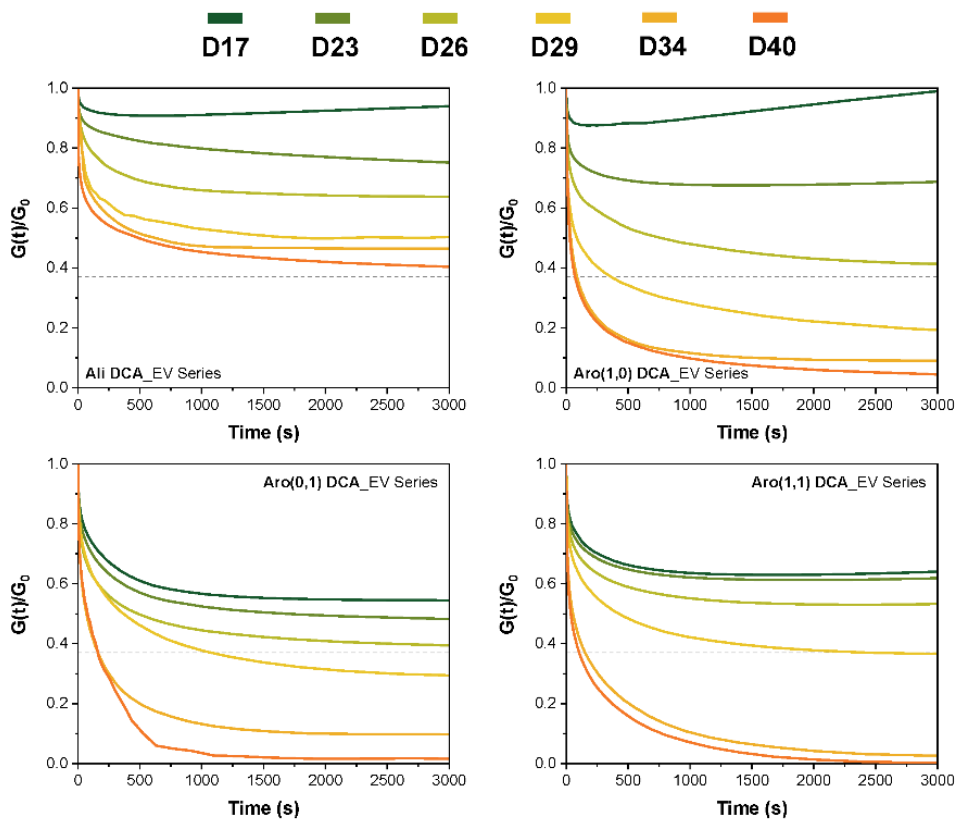
Figure 3-10. Stress-relaxation curves (at 160°C) obtained from Ali-, Aro(1,0)-, Aro(0,1)-, Aro(1,1) DCA_EV Series with different fractions of dynamic linkages.
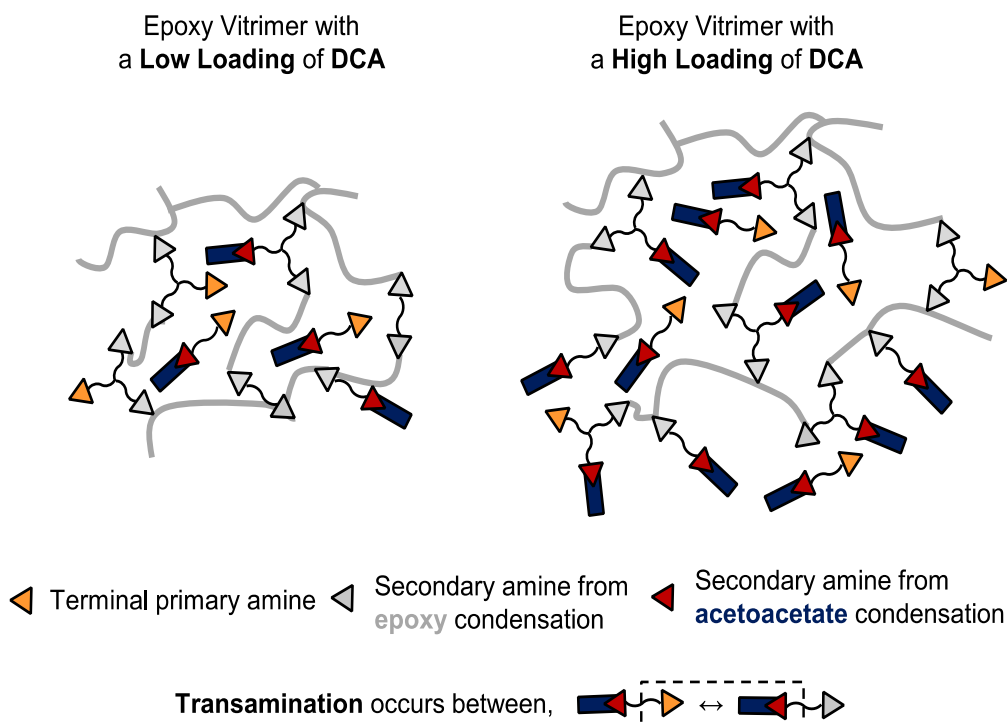
Figure 3-11. Schematic crosslinking networks of EVs with a low (left) and a high (right) fraction of dynamic linkages, respectively.

Regarding describing the stress-relaxation curve of vitrimer, a single-exponential decay is not fully applicable. Instead, a Kohlrausch-William-Watts (KWW) stretched exponential decay model is reported to be much useful to describe the curve of amorphous materials (Fancey, 2005, Williams, *et al.*, 1970); which is:

$$\frac{G(t)}{G_0} = \frac{G_{perm.}}{G_0} + \left(1 - \frac{G_{perm.}}{G_0}\right) \exp\left[-\left(\frac{t}{\tau^*}\right)^{\beta}\right] \qquad \text{(Equation 3-2)}$$

where $G(t)/G_0$ represents the normalized relaxation modulus at time t, while τ^* is the characteristic relaxation time. The fraction of residual stress, $G_{perm.}/G_0$, is expected to be zero if the material is non-percolated polymer. The parameter β, which ranges between 0 and 1, determines the shape of the stretched decay curve, with $\beta = 1$ denoting a single exponential decay and $\beta = 0$ denoting a very wide distribution of relaxation times (Li, *et al.*, 2018).

We applied equation 3-2 to the stress-relaxation curves obtained from the D29, D34, and D40_EV samples that had reached the point of $G(t)/G_0 = 1/e$. The parameter values in **Table 3-3** were obtained by best-fitting the stress relaxation data in **Figure 3-12** with adjusted R^2 values greater than 0.95. Notably, the stress-relaxation curves of the D34 and D40_EV samples, regardless of the type of DCAs, were well-fit to the stretched decay model when their $G_{perm.}/G_0$ values were close to zero (ranging from 0.002 to 0.096). Given that the testing time of 3 hours was short, we believe these values will converge to zero as the testing time approaches infinity. Therefore, the good fit of equation 3-2 to the data indicates that the chain rearrangement within the vitrimer network, at the high portion of dynamic linkages, makes the epoxy matrix behave like an amorphous melt fluid.

On the contrary, the stress-relaxation curves of the D29_EV series, regardless of the types of DCAs used, failed to fit the KWW model. This may be due to a larger portion of permanent linkages within the network, which can induce regional percolation of permanent linkages, enhancing the elastic response and suppressing overall chain rearrangement through the matrix. This result is consistent with a previous report, which found that the presence of 60 to 80 mol% of permanent crosslinks results in a discrepancy between the data and the stretched decay fitting curve (Li, *et al.*, 2018). Given that the D29_EV samples showed a large distribution of relaxation ($\beta < 0.3$), it can be assumed that EVs with lower fractions of dynamic linkages (such as D17, D23, and D26) would behave much more like percolated thermosets.

Table 3-3. Parameters obtained from fitting stretched decay curves to experimental data (at 160°C) in Figure 3-12 according to the equation 3-2.

	Aro(1,0) DCA			Aro(0,1) DCA			Aro(1,1) DCA		
	D29	D34	D40	D29	D34	D40	D29	D34	D40
$G_{perm.}/G_0$	0.171	0.088	0.033	0.292	0.096	0.014	0.366	0.026	0.002
τ^*	365	88	72	1079	163	161	2477	152	105
β	0.3	0.51	0.39	0.2	0.66	0.72	0.15	0.48	0.43
Adjusted R^2	-	0.992	0.967	-	0.969	0.985	-	0.976	0.980
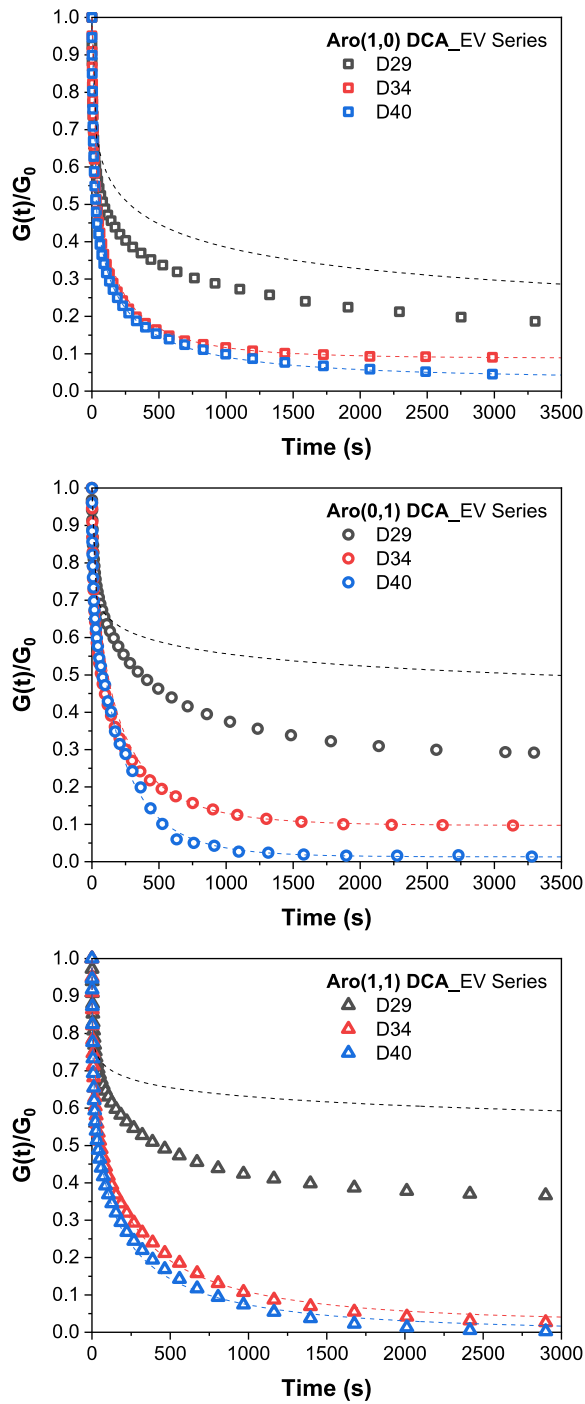
Figure 3-12. Stress-relaxation data (hollow symbols) and best fitting curves (dotted line) obtained from the stretched decay model.

A nemesis of vitrimer is the tendency to creep, which is related to stress-relaxation behavior. Unlike normal thermosets, EVs are prone to creep when heated above their T_g since topological rearrangement makes the material flow macroscopically and unhinges the crosslinked lock points. Especially at elevated temperatures like those found in semiconductor packaging, the creep behavior of polymeric materials can cause severe problems such as die shift, loss of electrical contact, and contamination. Therefore, it must be contained as much as possible. It has been reported that the hybridization of dynamic and permanent crosslinks can suppress the degree of plastic deformation (Li, *et al.*, 2018). Herein, we have designed the formulation of EVs to endow them with two oppositional characteristics, namely fast exchange reactions and a high amount of permanent linkages simultaneously, in accordance with technological needs. Thus, the creep resistance of the material was characterized at 160°C, which is a very high testing temperature, especially for epoxy vitrimers when their creep properties have been reported around 40-120°C (Spiesschaert, *et al.*, 2020, Van Lijsebetten, *et al.*, 2022).

Figure 3-13 shows the creep behavior of all the prepared EVs with four different DCAs having six compositions of dynamic fraction. During 10,000 s, a constant 2 kPa stress was applied to each sample at 160°C, which is about 80°C higher than its T_g points. From the viewpoint of dynamic fraction, the degrees of creep strain were minimal for the lowest ones (D17_EV samples), about 1-2%. However, they became more significant (2-5%) as the fraction of dynamic linkage increased from D17 to D29. What was worse, soaraway values of creep strain (10-300%) were obtained for the D34 and D40_EV samples, except for the case of using Aro(1,1) DCA. Along with the fast exchange reaction, the low mechanical strength exacerbated creep resistance of D34 and D40 samples. No matter how good the stress-relaxation capabilities of the D29 ~ D40_EV samples are, the amounts of irreversible deformation would not be acceptable in real-life applications. It would be much wiser to compromise the selection criteria of the fraction of dynamic linkage between stress-relaxation capability and creep resistance.
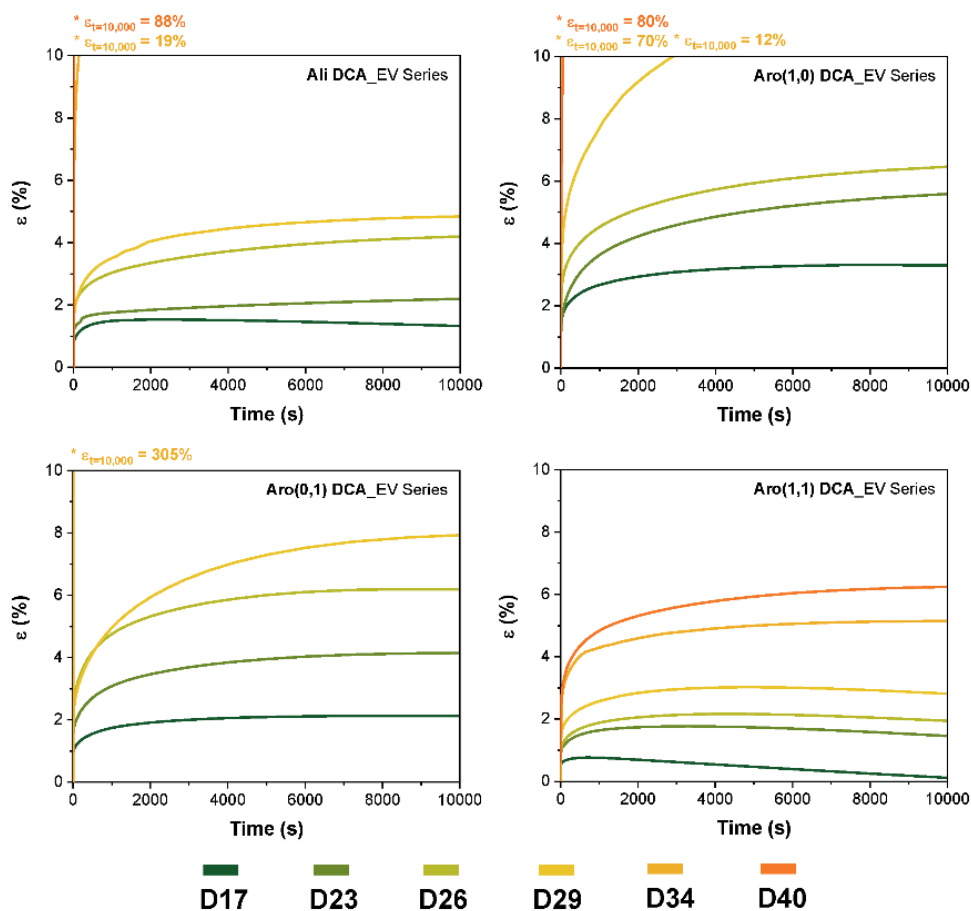
Figure 3-13. Creep strain measured at 160°C for the Ali-, Aro(1,0)-, Aro(0,1)-, and Aro(1,1) DCA_EV Series with different fraction of dynamic linkages.

Notably, the degrees of creep strain from the samples with the same dynamic fraction greatly differed according to the DCA types. The lower creep strains of the Ali_EV series can be attributed to the slow exchange reactions between aliphatic components, as verified by their lowest stress-relaxation capabilities compared to those of the samples prepared with aromatic DCAs (**Figure 3-10**). For the same reason, the low creep resistances of Aro(1,0)- and Aro(0,1)_EV series were attributed to their fast exchange reactions. Interestingly, Aro(1,1)_EV series showed the highest creep resistance at every dynamic fraction and recorded a creep strain of only 6%, even for the D40_EV sample. What is controversial is

that the stress-relaxation capabilities of the Aro(1,1)_EV series were fair as compared with those of the Aro(1,0)- and Aro(0,1)_EV series. The result requires more explanation and will be discussed in session 2.4.

2.4 Effects of the Functionality of DCAs

In designing EV systems, we deliberately used four types of DCAs, formed by chemically or sterically different amines and acetoacetyl esters. Ali DCA is the representative product of a vinylogous urethane vitrimer (Spiesschaert, *et al.*, 2020), composed of aliphatic components (EAAc, BAC, and TREN). In contrast, Aro DCAs are newly synthesized compounds with at least one aromatic building block. Aro(1,0) DCA possesses an aromatic ring at the BAAc end functionality, where the site becomes a dangling chain end when cured with epoxy chains. On the other hand, Aro(0,1) DCA possesses an aromatic ring at XDA, where the site becomes the extension of the epoxy main chain when cured. Finally, Aro(1,1) DCA possesses two aromatic rings at both sites (**Figure 3-14**).
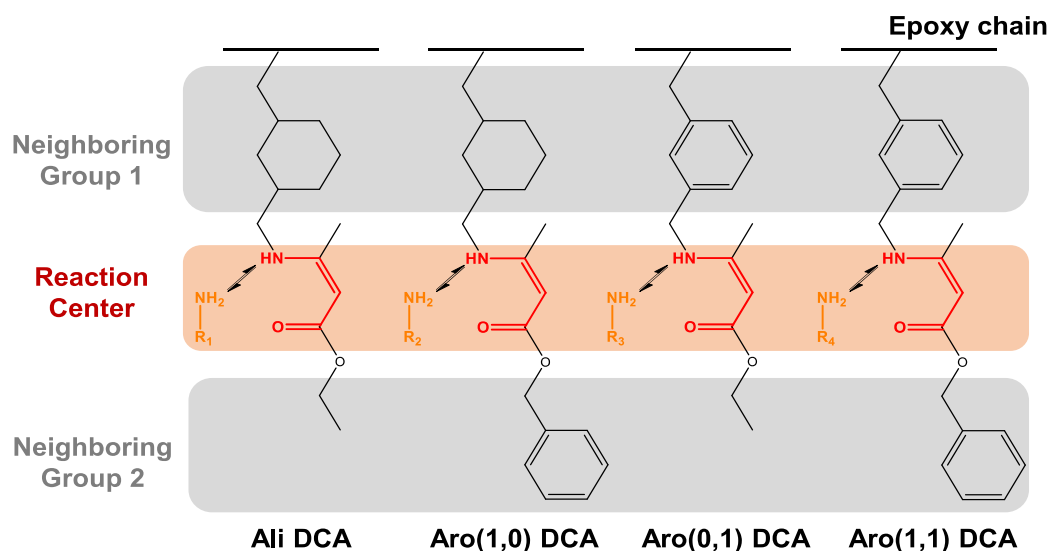
Figure 3-14. Schematic comparison for neighboring groups of Ali-, Aro(1,0)-, Aro(0,1)-, and Aro(1,1) DCA (the TREN-linked structures are omitted).

The employment of chemically modified dynamic components to alter the kinetics of the exchange reaction relies on the effect of neighboring group participation (NGP). NGP is defined as the substituent effect of enhancing the rate of exchange reaction by stabilizing its transition state, wherein the substituent is tethered to the reaction center, prompting internal proton transfer within the molecule (Cuminet, *et al.*, 2021, Guerre, *et al.*, 2020). In an elaborate and fundamental article by Hamzehlou and Ruiperez (Hamzehlou and Ruipérez, 2022), the effects of NGP on the kinetics of transamination in vinylogous urethane and acyl compounds were studied at the level of electrons using density functional theory calculations. According to the research, a protic mechanism of transamination involves four transition states (TS1~TS4) and three intermediates (Int1~3). As the protonated guest (free) amine commences attacking enamine, the proton transfer from the guest ammonium to the vinylic α-carbon forms a stable complex between the vinylogous urethane and the guest amine (TS1). Next, the subsequent electron transfer forms an iminium (host) cation (Int1), where the site is nucleophilic-attacked by the guest amine (TS2). As the second protonation is done (Int2), the protonated host amine is about to be eliminated (TS3) and turned into a new iminium cation (Int3). Lastly, a proton transfer occurs from the vinylic α-carbon to the former guest amine (TS4) to receive it as a new host (product). The entire process is given in **Figure 3-15** (data from Hamzehlou, *et al.*, 2022, Denissen, *et al.*, 2017).

In their results comparing the use of n-butyl amine and tert-butyl amine in a vinylogous urethane, the steric hindrance effect of the bulky tert-butyl group reduces the distance between -NH and O=C (carbonyl), thus allowing the fortified hydrogen bond to stabilize the formation of Int1. At the elimination stage (TS3), the significant steric hindrance facilitates the exchange process. Hence, the presence of bulky functionality lowers the energy barrier for the transamination reaction. Another result comparing benzylamine and phenylamine emphasizes three advantages of aromatic components: (1) low basicity of leaving amine, (2) intermolecular interaction, and (3) constrained planar arrangement. An aromatic compound is less basic due to the delocalization of the nitrogen lone pair. Thus the conjugated acid is much stronger, making protonation to α-vinylic carbon easier (a step of forming TS1) than when using an aliphatic compound. TS1 is then greatly stabilized to Int1 due to the π-π

interactions between the aromatic ring and the carbonyl (C=O) or iminium (C=N) double bonds in vinylogous urethane. Finally, due to the strong restraint wielded by aromatic compounds, the vinylogous complex undergoes molecular rearrangement into a planar conformation, which further promotes a stronger intramolecular hydrogen bond between the iminium N-H and the carbonyl O=C.

In our system, the structural differences (1) between Ali DCA and Aro(1,0) DCA and (2) between Aro(0,1) DCA and Aro(1,1) DCA will be an example demonstrating the indirect effect of steric hindrance, although the functionality is not located at the site that can meddle in the reaction center. Meanwhile, the structural differences (3) between Ali DCA and Aro(0,1) DCA and (4) between Aro(1,0) DCA and Aro(1,1) DCA will demonstrate the direct effect of aromaticity as they can interfere with the proton exchange reaction within the reaction center. Herein, we investigated the changes in EVs according to the types of DCAs from a materialistic perspective, particularly through rheological interpretation.
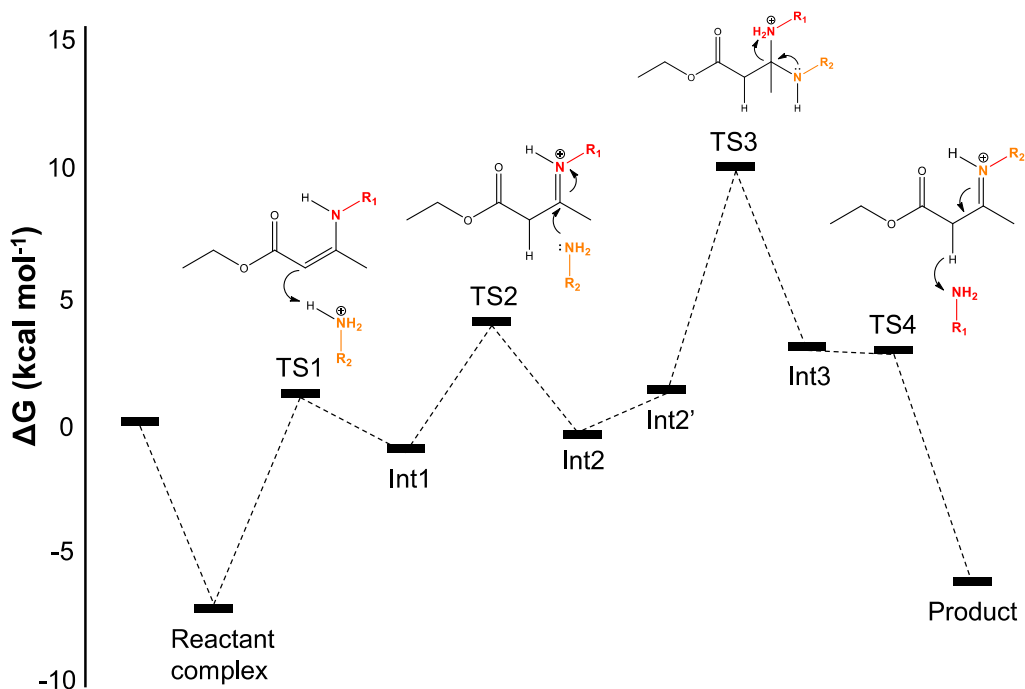
Figure 3-15. Changes in potential energy of the transamination of vinylogous urethane via a protic pathway (Hamzehlou, *et al.*, 2022).

2.4.1 Activation Energies of Transamination in the Epoxy Vitrimers

Reportedly, in associative exchange reactions like transamination, the temperature dependence of the characteristic relaxation time (τ*) follows the Arrhenius law (Capelot, *et al.*, 2012):

$$\tau(T) = \tau_0 \exp(E_a/RT) \qquad \text{(Equation 3-3)}$$

According to equation 3-3, we plotted ln(τ*) against temperature using the stress-relaxation data of Ali-, Aro(1,0)-, Aro(0,1)-, and Aro(1,1) D34_EV samples obtained at different temperature ranges. In all cases, a perfect linear relationship was obtained in the Arrhenius plots, indicating the vitrimeric nature of the materials. The calculated activation energies (E_a) are shown in **Figure 3-16**. The E_a of Ali D34_EV was 51 kJ mol^{-1}, quite low for uncatalyzed vinylogous urethane systems whose typical E_a are around 60-90 kJ mol^{-1} (Denissen, *et al.*, 2015, Haida and Abetz, 2020, Spiesschaert, *et al.*, 2020). This can be attributed, in part, to the effect of hydroxy groups from the amine and epoxide condensation reactions, which autocatalyze the protonation of vinylogous urethane (Spiesschaert, *et al.*, 2020). Additionally, thanks to the 15% amine-rich formulation, abundant free primary amines are readily available to nucleophilic-attack the protonated vinylogous urethane.

Surprisingly, after substituting Ali DCA with Aro(1,1)-, (1,0)-, and Aro(0,1) DCAs, the corresponding E_a values were further decreased to 45.2, 34.6, and 25.6 kJ mol^{-1}, respectively. The additional reductions in E_a are attributed to the effect of substitution with aromatic compounds that facilitate dynamic exchange reactions via a protic mechanism. This paper will not cover a detailed investigation at the atomistic level. Rather, we assessed that the rheological comparison of the prepared EVs provides a practical interpretation for understanding the impact of dynamic components at the crosslinked network level.
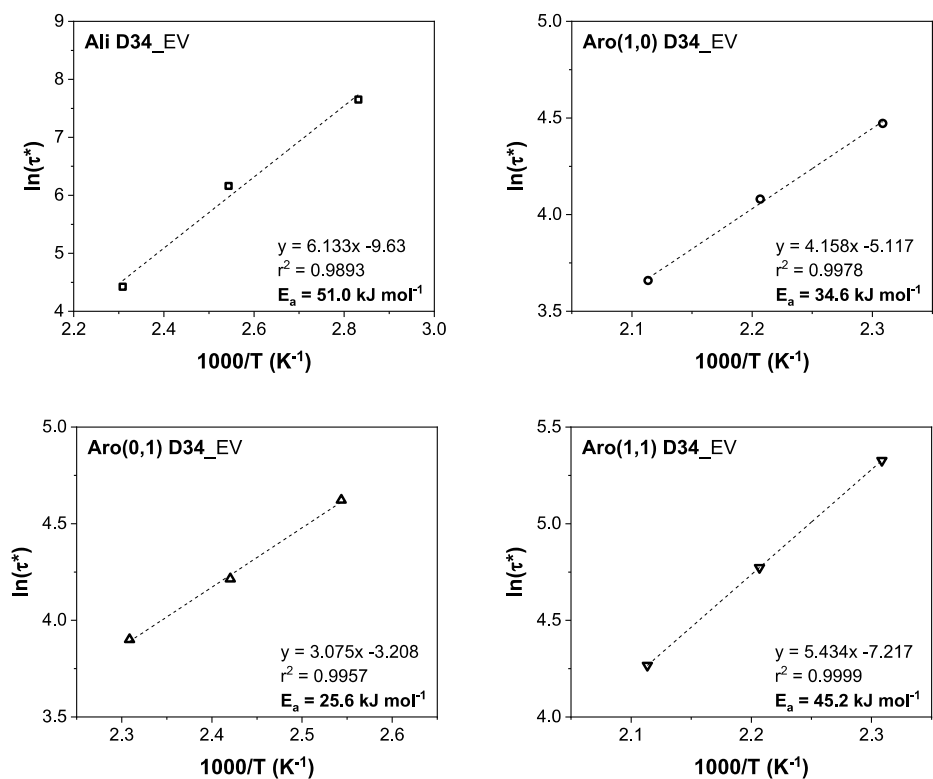
Figure 3-16. Calculation of activation energies of the EVs with different types of DCAs.

2.4.2 Viscoelastic Properties of the Epoxy Vitrimers at Rubbery State

Since numerous factors affect the final mechanical properties of polymers during and after processing, especially in the case of thermosets, the effect of the composition should be discussed in detail under specific testing conditions. Unlike typical thermosets, vitrimers show temperature- and time-dependent characteristics, making them a fruitful subject for rheological studies. As shown in **Figure 3-8**, the change in E' of EVs as a function of temperature shows a large difference between thermosets and thermoplastics. At low temperatures, E' values were retained for a very short period, so the material barely demonstrated its glassy plateau. After the T_g point, E' drastically decreased, as if it were an amorphous thermoplastic. Notably, at high temperatures above $T_g + 60°C$ (i.e., over 120°C), E' values were kept steady at a rubbery plateau, as in the textbook case of crosslinked polymers. At this temperature range, dynamic exchange reactions persistently occur, freeing the crosslinked network from the effect of entanglement or regional differences in crosslinking density. Thus, a much more straightforward comprehension of the average chain movement can be made at the rubbery state.

Figure 3-17 emphasizes partial data from **Figure 3-8**, displaying the E' values obtained between 120 and 160°C. As already noted, in all samples, the storage moduli are almost constant upon heating, indicating the material's thermoset-like characteristics. More importantly, the degree of E' differs greatly according to the type of DCAs used. For all dynamic compositions, Aro(1,1)_EV records the highest E' values between 0.5 (at D40) and 1.55 (at D17), while Aro(0,1)_EV records the lowest E' values between 0.1 (at D29) and 0.6 (at D17). The high-temperature stiffness might be the determining factor of viscoelastic responses in vitrimers. It appears that the order of E' at the rubbery state complements the materialistic interpretation for the effect of substituting residues of DCAs.
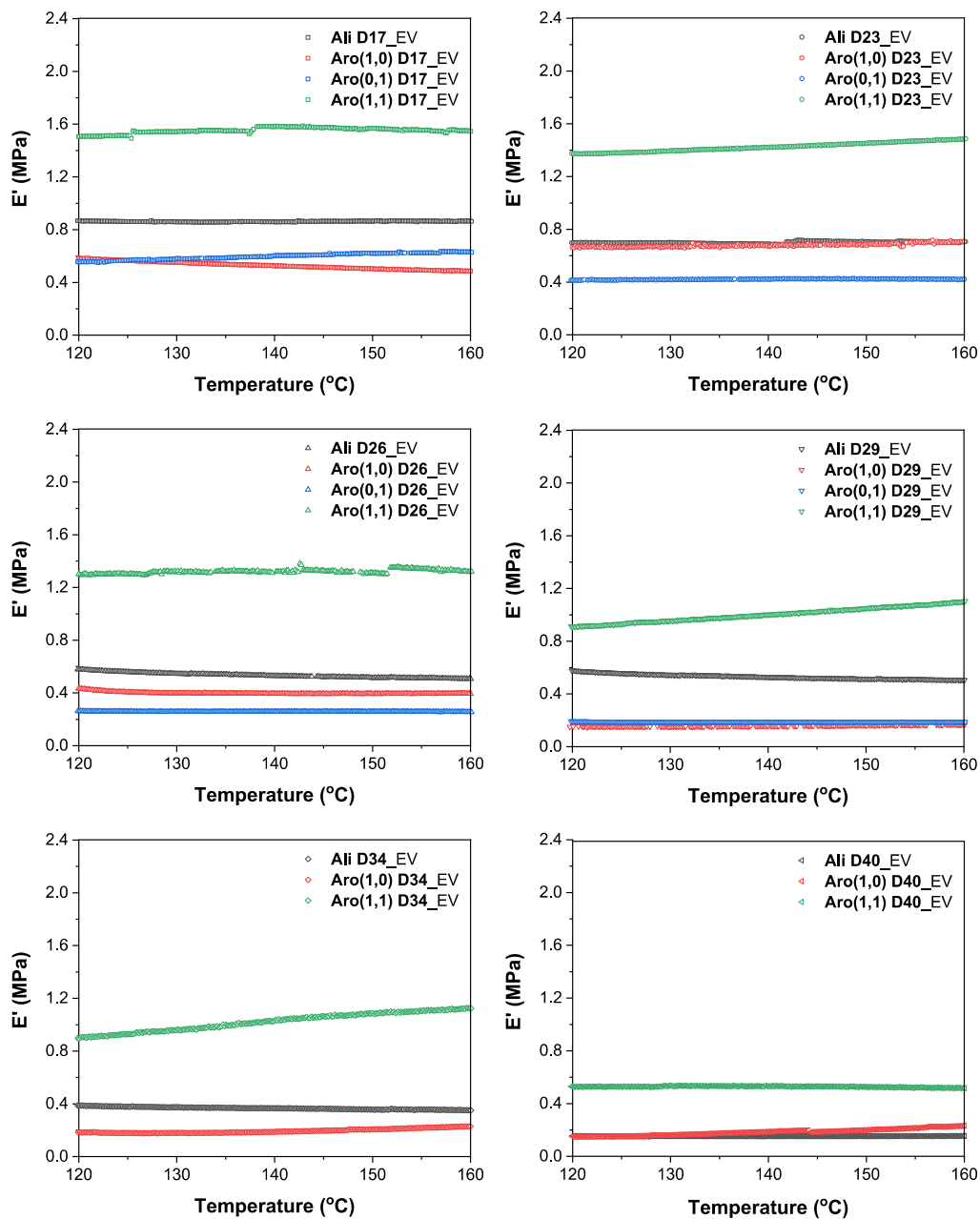
Figure 3-17. Storage moduli of the cured Ali-, Aro(1,0)-, Aro(0,1)-, and Aro(1,1) DCA_EV series with different fractions of dynamic linkage, measured between 120 and 160°C.

We implemented a rotational rheometer in a frequency-sweep mode to assess the viscoelastic properties of the cured EVs. The samples had been slightly melted in advance and sandwiched between the lower and upper rotation plates. Upon shear strain of 2% (within the linear viscoelastic range), the shear moduli (G') and loss moduli (G") of D26 and D34 compositions were obtained at 160°C as a function of angular frequency (ω) from 0.1 to 100 rad s^{-1} (**Figure 3-18a, b**).

In D26_EV compositions, all the samples recorded a higher G' value than G" at the same frequency, which denotes the characteristic of highly crosslinked thermosets. In D34_EV compositions, on the contrary, the Aro(0,1) D34_EV sample showed lower G' than G" below the frequency of 4 rad s^{-1} and then recorded higher G' than G" above the frequency of 4 rad s^{-1}, leaving the crossover gel point (G'=G"). The rheological behavior is typical of amorphous thermoplastics. Along with the higher fraction of dynamic linkages, the usage of Aro(0,1) DCA, which has very low activation energy for transamination, extremely attenuated the epoxy's cohesive feature, resulting in the weak strength and sagging problem at the condition.

What is noteworthy is that for both the D26 and D34_EV compositions, the order of complex viscosity of the EVs with different types of DCAs is consistent with the order of E' at 160°C measured by DMA: Aro(1,1) DCA_EV > Ali DCA_EV > Aro(1,0) DCA_EV > Aro(0,1) DCA_EV. Plus, the order matches with that of the E' of D34 EV compositions. It seems that the viscoelastic information at a targeted temperature is a prerequisite to studying the matrix deformation as well as the activation energies of the system's exchange reaction.

Within the flowing polymer melts, the molecules or strands exhibit relative motion between each other, and this action/reaction invokes internal frictional force, resulting in flow resistance. In the case of thermoplastics, numerous materialistic factors determine their melt viscosity, such as molar mass, polydispersity index, intra- or intermolecular interaction, chain packing, free volume, softening point, etc. Analogous to these, several factors can be responsible for the complex viscosity of EVs since the material under incessant exchange reactions would behave like the hot-melt polymer with a minimum margin of crosslinking

networks.

The potential factor responsible for the high viscosities of Aro(1,1)- and Aro(1,0) DCA_EV is the presence of an aromatic building block (XDA) in the chemical structure of the curing agent. Conventionally, aromatic amine-type curing agents are favored over aliphatic amine-type curing agents in light of the cured epoxy's high T_g, high modulus, and high thermal resistance. The substitutional effect is first aroused from the difference in the packing behavior of the polymer during the initial stage of chemically controlled epoxy-amine reaction kinetics. Reportedly, an aromatic structure shows better packing efficiency and thus results in higher crosslinking density in the cured epoxies (Lv, *et al.*, 2021). The planar and bulky structure on the opposite side of the epoxy backbone (Neighboring group 2 in **Figure 3-14**) would provide a larger space to accommodate other molecules to approach, leading to better intrachain packing than in the case of using aliphatic (ethyl) end group (Xu, *et al.*, 2004). The effect is evidenced by the higher E' and T_g values of the epoxies cured with the Aro(1,1) and Aro(1,0) DCAs than those of the epoxy cured with Ali DCA (**Table 3-2**).

Secondly, at the final stage of epoxy-amine reaction kinetics (namely, diffusion-controlled), the steric hindrance induced by aromatic building blocks much more effectively deters the diffusion of other low molar mass species, enhancing the internal resistance to flow and reduces the curing reaction rate at the same time (Karkanas, *et al.*, 2000).

Finally, for the melt state of a fully cured EV, there can be an additional effect of intramolecular interactions. From the DFT calculation of the transamination between a vinylogous urethane moiety and aniline, the phenyl ring of aniline and the vinylogous compound were positioned in parallel, showing a π-π interaction between the aromatic ring and the carbonyl (C=O) or iminium (C=N) double bonds (Hamzehlou and Ruipérez, 2022). Although the research only suggested an intramolecular stabilizing effect, the same effect can be present within chain-packed epoxy networks where the nearly located aromatic building blocks interact with each other and adjacent carbonyl (C=O) functionalities via the transient π-π interaction. The preference of Aro-DCAs for a planar conformation and intramolecular hydrogen bonds in vinylogous urethane moieties can contribute to reinforcing

such π-π stackings over several chain folds in a polymer (Burattini, *et al.*, 2010). In this circumstance, it would not be counterintuitive that the loosely intertwined chain segments impart additional cohesion to the matrix, resulting in high viscosity.

In contrast, the Aro(0,1) DCA recorded the lowest viscosity, despite an aromatic building block (XDA) at neighboring group 1, where the block is attached to the epoxy side. It appears that the location of the aromatic building block is too close to the epoxy main chain to influence the intramolecular packing at the opposite acyl-end group. Rather, the packing-enhancement effect seems to be nullified by fierce chain rearrangements via an accelerated dynamic exchange reaction due to the presence of the aromatic building block, as already mentioned in the stress-relaxation tests.

Figures 3-18c and **d** show the shear-thinning behavior of D26 and D34 compositions, respectively. Note that all the EVs' zero shear viscosities are above 10^5 Pa s at $\omega = 0.1$ s^{-1} (except for the Aro(0,1) D34_EV), where the values are between those of typical high-density polyethylene (HDPE) or polypropylene ($10^4 \sim 10^5$ at 150~170°C) (Chen, *et al.*, 2021, Nichetti, *et al.*, 1998) and that of thermoplastic polyurethane (TPU) for 3D Printing (10^6 Pa s at 175°C) (Wang, *et al.*, 2020). Given the resemblance to thermoplastics at the testing temperature, the macromolecules trapped between the transient crosslinks are prone to be oriented in the shear direction, so the flow resistance will be lowered according to high shear. The decreases in the complex viscosity of each EV as a function of shear rate were tremendous; for instance, the 630-fold decrease in Ali D26 between the angular frequency of 0.1 and 100 s^{-1}, recording a complex viscosity of only 520 Pa s at 100 s^{-1}. In contrast, the decrease in the complex viscosity of NVE (i.e., non-vitrimer epoxy) as a function of shear rate was not severe, recording only a 26-fold decrease (**Figure 3-18e**). The very difference between them is the presence of dynamic linkages within the network. It can be assumed that the dynamic exchange reactions that occur in the vicinity of crosslinking points would (temporarily) enhance partial disentanglements of the macromolecule on the one hand and disrupt re-entanglement to the originally-linked position on the other hand.

114
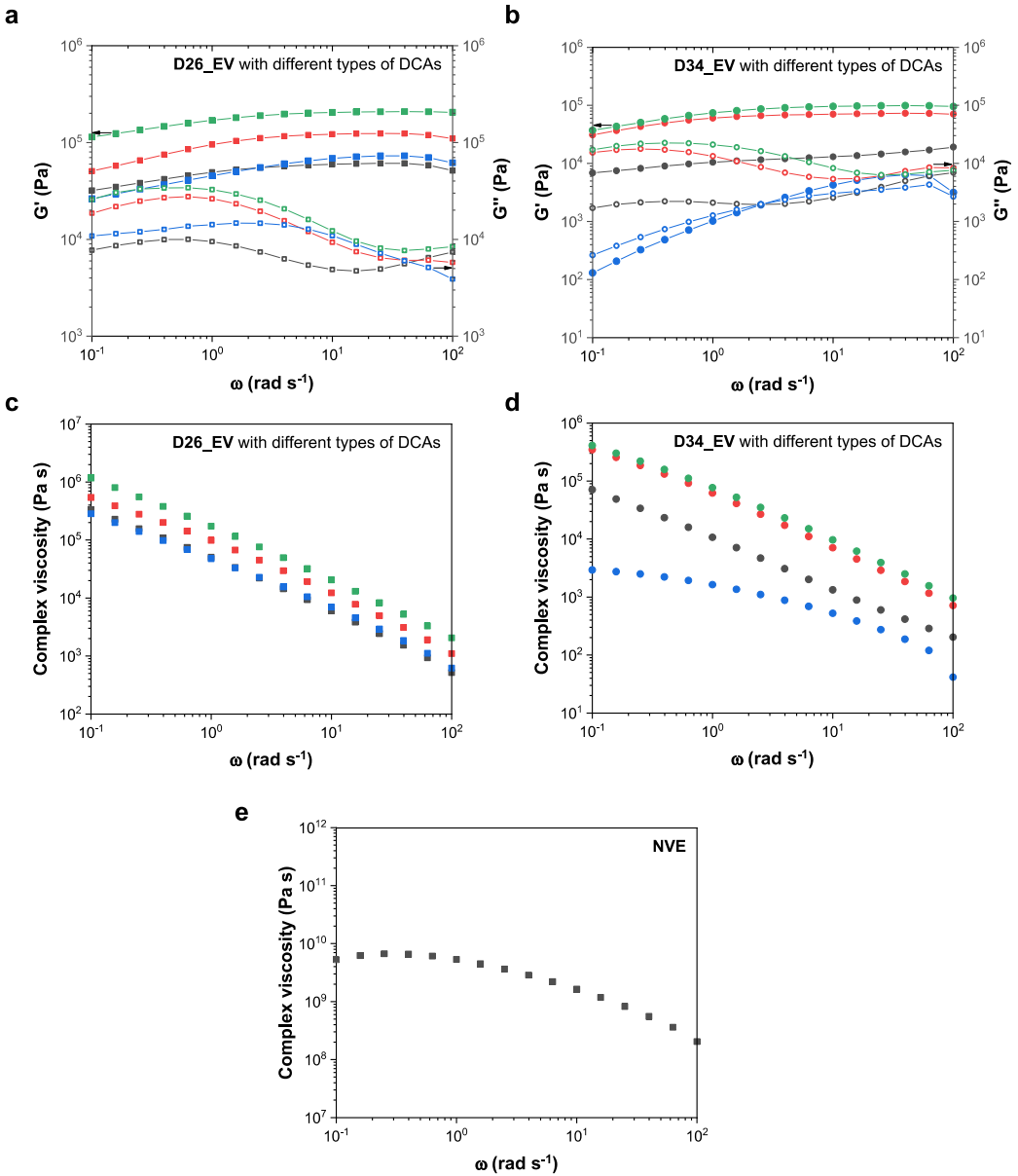
Figure 3-18. G' and G'' of **a** D26_EV and **b** D34_EV; and complex viscosities of **c** D26_EV and **d** D34_EV with different types of DCAs.

Considering the order of complex viscosities of the EVs, we conducted several creep tests using DMA (ε deformation), with different constant creep stress values (σ) preset for each test. To interpret the creep deformation of a viscoelastic material with orthodox mechanical models, the material should be maintained within the linear viscoelastic (LVE) region range. In principle, the creep compliance as a function of time ($J(t)$) is independent of the preset stress value if the testing condition falls within the material's LVE range. Therefore, plotting the time divided by creep compliance against time ($t/J(t)$ vs. t) can determine whether the steady-state behavior is achieved for the testing condition. **Figure 3-19** shows the plots obtained from different creep stresses (1, 2, 3, and 5 kPa) for the EVs with different types of DCAs. For all EVs, the curve obtained at the creep stress of 3 kPa exhibits linear variations as a function of time (i.e., a steady-state). In contrast, the curves obtained at the creep stresses of 1 or 5 kPa show significant upward or downward fluctuations, indicating non-linear viscoelastic behavior outside the LVE range. Therefore, the creep tests were conducted at creep stress of 3 kPa.
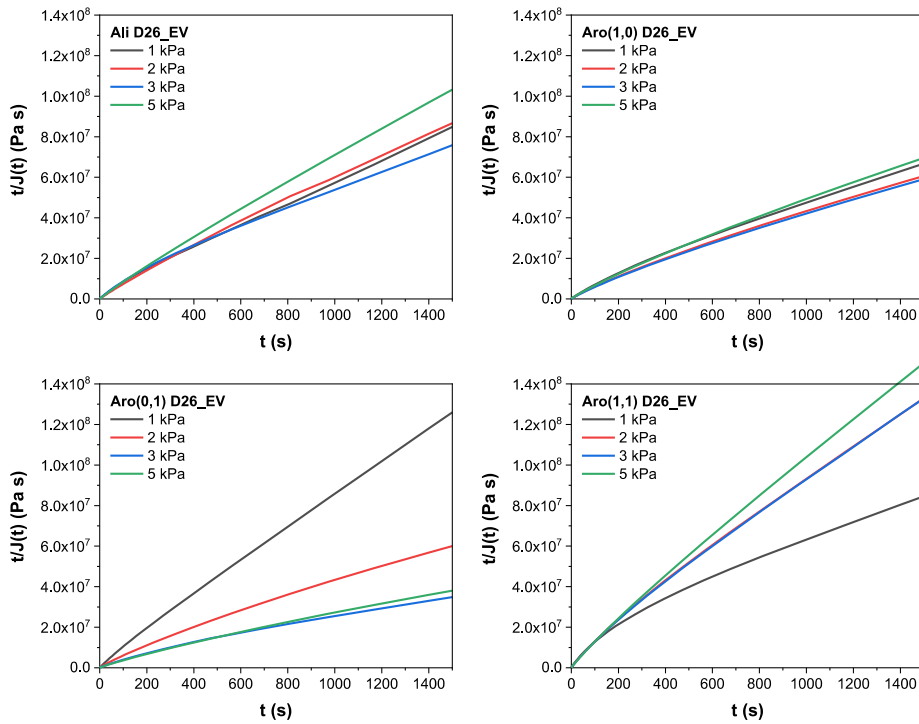
Figure 3-19. Plot of time divided by creep compliance as a function of time for the EVs with different types of DCAs, measured at creep stresses of 1~5 kPa.

When analyzing a viscoelastic material within its LVE range, the time-dependent properties like strain and stress can be expressed by a mechanical model composed of springs and dashpots as elastic and viscous components, respectively. The stress experienced by each spring proportionally increases with the increase in strain (Hooke's law), whereas the stress experienced by each dashpot is proportional to the strain rate (Newton-Stokes' law). The combination and arrangement of these components in each model differ, determining the model's accuracy to mimic or predict the time-dependent behaviors. For analyzing a specialized case of creep, the well-known Burgers model (Burgers, 1935), which consists of a spring 1 (S_1), a spring 2 (S_2) and a dashpot 2 (D_2) (in parallel), and a dashpot 3 (D_3) (**Figure 3-20**), represents the creep strain follows:

$$\varepsilon(t) = \frac{\sigma_0}{G_1} + \frac{\sigma_0}{G_2}(1 - e^{-t/\tau_2}) + \frac{\sigma_0}{\eta_3}t \qquad \text{(Equation 3-4)}$$

where $\varepsilon(t)$ is the strain at measured time, σ_0 is the creep stress, G_1 and G_2 are the shear modulus of S_1 and S_2, respectively, τ_2 is the retardation time of D_2, and η_3 is the viscosity of D_3 component.

1 at creep, Instant elastic deformation   **2** at creep, Delayed viscoelastic deformation   **3** at creep, Constant viscous deformation
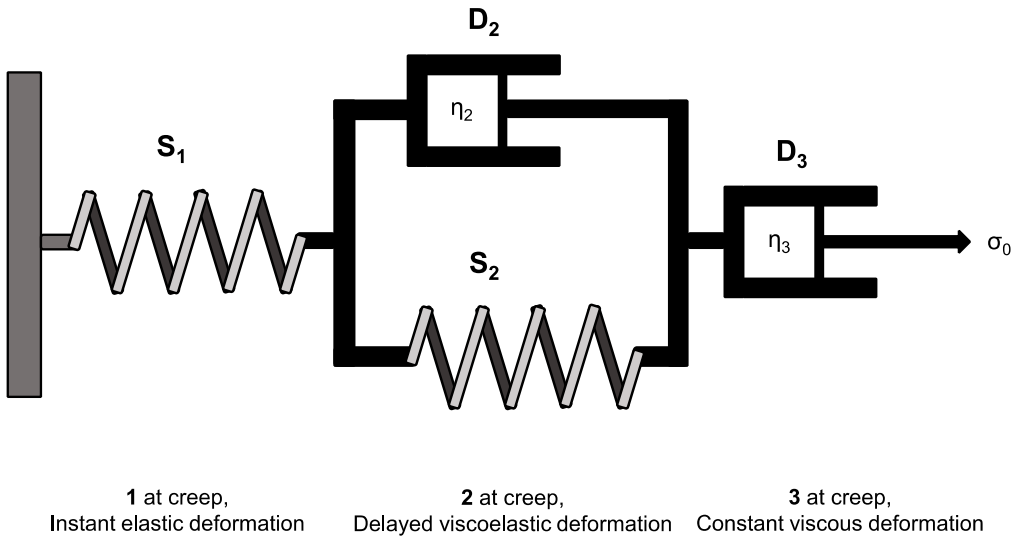
Figure 3-20. The Burgers model describing a creep phenomenon.

Figure 3-21a depicts the creep curves of D26 compositions with various types of DCAs, measured at 160°C. Upon applying creep stress, all curves exhibit delayed viscoelastic deformation for an initial 300 seconds, with the degree of delay varying depending on the type of DCA. Subsequently, each curve enters a steady-state region of purely viscous deformation. In this sufficiently large time range (i.e., $e^{-t/\tau_2} \rightarrow 0$) when the material shows steady-state behavior (i.e., time-independent), equation 3-4 simplifies to:

$$\varepsilon(t) = \frac{\sigma_0}{G_1} + \frac{\sigma_0}{G_2} + \frac{\sigma_0}{\eta_3}t = const. + \dot{\varepsilon}_3 t \qquad \text{(Equation 3-5)}$$

where the $\dot{\varepsilon}_3$ is the time-independent, constant strain rate obtained from the slope value within the linear region of each creep curve.

Meanwhile, according to the Burgers model, the behavior of the dashpot D_3 captures the zero-shear viscosity (η_0), which is the limiting value of the deformation rate-dependent viscosity function at a very low strain rate. The value of η_0 can be determined at the end of the creep phase as:

$$\eta_0 = \sigma_0 / (\varepsilon_3/\Delta t) = \sigma_0 / \dot{\varepsilon}_3 \qquad \text{(Equation 3-6)}$$

Thus, the creep rate and zero-shear viscosity values were calculated from the constant creep slopes and are demonstrated in **Figure 3-21b**. The order of $\dot{\varepsilon}$, rated from highest to lowest, is Aro(0,1)-, Ali-, Aro(1,0)-, and Aro(1,1) D26_EV. On the contrary, the order of $\eta0$, rated from highest to lowest, is Aro(1,1)-, Aro(1,0)-, Ali-, and Aro(0,1) D26_EV. Note that the order of η_0, derived from the creep analysis by DMA, is consistent with the order of E' at the rubbery state (**Figure 3-17**) and the complex viscosities measured by a rheometer (**Figure 3-18c**). The result suggests that the EV at the rubbery state (T > T_g + 60°C) can be regarded as a melt thermoplastic and be analyzed using rheometric studies. According to the interpretation using the Burgers model, even for the EV, its creep behavior can depend on the material's intrinsic viscoelastic response, no matter what other factors may contribute.

In other words, under the tested conditions for stress-relaxation and creep tests in the chapter, it was possible to achieve an EV system with very high stress-relaxation capability and high creep resistance simultaneously, as long as the material maintains a high viscosity

(flow-resistivity) above its T_g or T_v due to a high crosslinking density and some intra- or intermolecular interactions. This seemingly contradictory phenomenon has also been reported in recent papers using vitrimer materials (Van Lijsebetten*, et al.*, 2022, Wang*, et al.*, 2022), although these studies lack mechanistic interpretations. We attribute this discrepancy to the gap between the regions of interest in stress-relaxation and creep tests. The former observes the testing material within an elastic region (i.e., no actual deformation), while the latter induces plastic deformation of the testing material during long-term observations. However, a detailed discussion of this topic will not be included in the paper and will be a future subject of study.

In summary, the substitution effect of DCA residues produced changes in both (1) the rate of dynamic exchange reaction via neighboring group participation and (2) the cohesiveness within the matrix via chain packing and noncovalent intermolecular interactions. The compositional effect corresponding to a portion of dynamic linkages within each EV system resulted in wide variations in both E' at glassy and rubbery states, critically influencing the elastic and viscoelastic responses, respectively. Combining the effects, we procured a set of EVs with different degrees of stress-relaxation (SR) and creep behavior (**Figure 3-22**). Based on the degree of these two properties, we divided the EVs into four groups: thermoset-like EVs with low SR and low creep; medium SR and low creep; medium SR and medium creep; and flexible EVs with high SR and high creep. Among them, we selected the medium SR and low creep groups as the reference material for the next chapter.
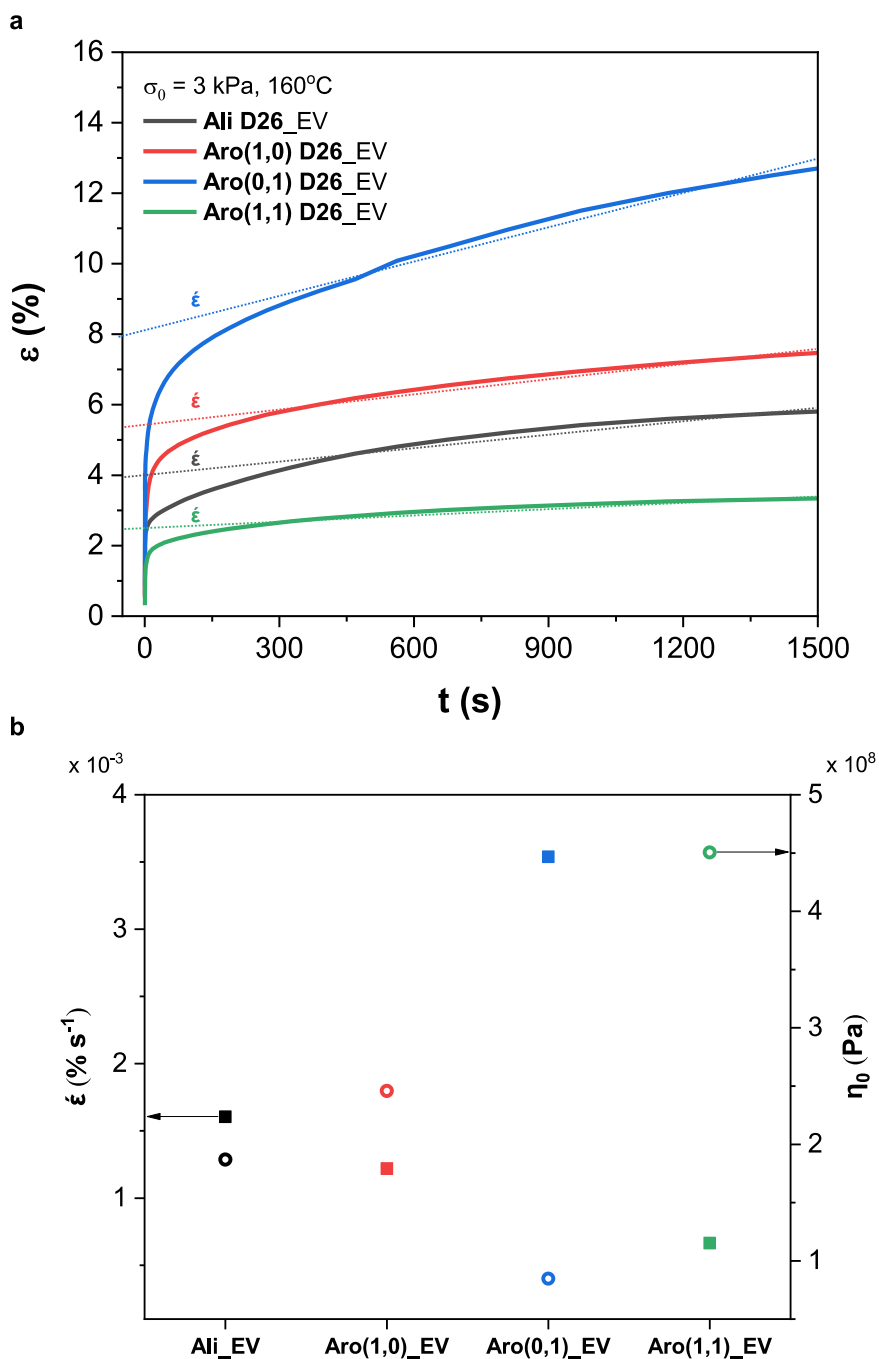
Figure 3-21. a Creep curves of EV_D26 compositions obtained at creep stress of 3 kPa. **b** Calculated creep rates (left column) and zero-shear viscosity values (right column) of the samples.
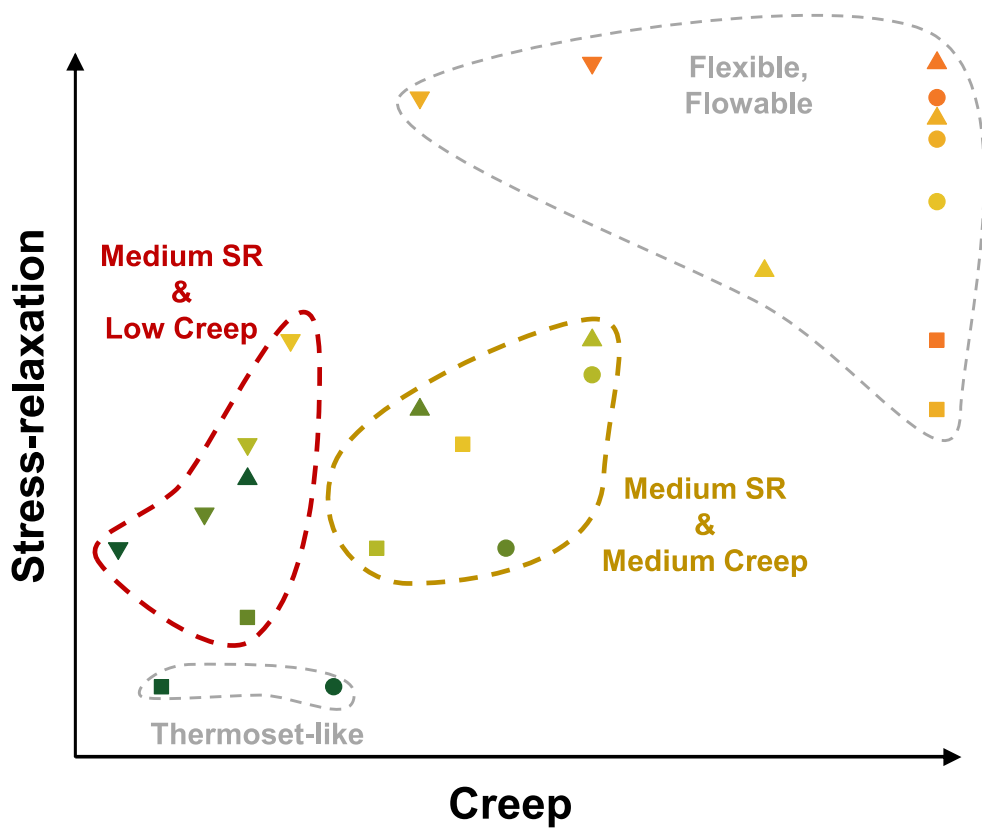
Figure 3-22. Comparison of viscoelastic behaviors of overall EV formulations.

3 Conclusion

Here, we synthesized four types of DCAs with different substituents and prepared six compositions of EVs with different fractions of dynamic linkages to secure viable EV formulations. Through comprehensive comparison, we studied the effects of substituents and dynamic linkages on the material properties, including re-processability, E', T_g, and, most importantly, stress-relaxation and creep performances. The ability to tune the characteristics with the designed formulations opens the possibility for EVs to respond to various requirements in practical applications.

Firstly, we experimentally uncovered that the required value of the non-gelled threshold for a partial vitrimer to be re-processable was lower (17 mol% of dynamic linkages) than the value (50 mol%) expected by the former criterion, Li's adaptation of the Flory-Stockmayer theory. This was attributed to the facilitated dynamic exchange reaction in the 15%-amine rich environment. Additionally, it was possible to control the EV's mechanical, thermal, and viscoelastic properties as a function of the dynamic fractions within the EVs. As the dynamic fraction increased, the obtained vitrimer's E' and T_g were reduced, while its stress-relaxation ability and creep strain were increased accordingly.

Meanwhile, the substitution of DCA with aromatic-building blocks resulted in a great deal of acceleration of transamination and reduction in activation energies for the reaction; inversely, E_a: 51, 35, 26, and 45 kJ mol^{-1} from the stress-relaxation results of Ali D34-, Aro(1,0) D34-, Aro(0,1) D34-, and Aro(1,1) D34_EV, respectively. Surprisingly, the tendency was inconsistent with the creep deformations obtained from the same composition. The aromatic components of Aro DCAs seem to contribute to a rise in the matrix's viscosity, dragging a viscoelastic fluid deformation. Through this effort, we were able to secure several practicable formulations: Aro(0,1) D17-, Aro(1,1) D17, 23, 26, and 29_EVs, demonstrating decent stress-relaxation ($G_{final}/G0 < 0.7$) and low creep deformation (strain < 2%) at the same time.

Chapter 4

Enhancing Stress-relaxation Capability of Epoxy
Vitrimers:

Solvate Ionic Liquid Catalysts for Accelerating
Dynamic Exchange Reactions

1 Introduction

The term "Vitrimers," which was first introduced by Leibler and his co-workers in 2011 (Montarnal*, et al.*, 2011), refers to a class of advanced polymeric materials capable of rearranging their crosslinked topology through associative dynamic exchange reactions while maintaining a constant number of networks in the system at service temperature. Upon activation of the dynamic exchange reaction, the vitrimer undergoes a characteristic transition from an elastic solid to a viscoelastic liquid in an Arrhenius-like manner (Capelot*, et al.*, 2012). On closer examination, the dynamically exchangeable moieties rapidly reach thermodynamic equilibrium and undergo degenerate reactions within a percolated system, allowing the network to flow (Denissen*, et al.*, 2016). During the topological rearrangement, the material self-relaxes stresses while preserving its structural fidelity, which is a key attribute of vitrimers and the primary reason why these materials have garnered considerable interest from industries seeking innovative polymeric materials to address stress-induced issues.

In this perspective, an epoxy vitrimer (EV) represents a promising category of materials that combines epoxy's high mechanical strength and excellent adhesion properties with the (re)processability and stress-relaxation abilities of vitrimers. Various dynamic chemistries have been explored in recent years to develop EVs, including transesterification (Altuna*, et al.*, 2019, Altuna*, et al.*, 2020, Capelot*, et al.*, 2012, Demongeot*, et al.*, 2016, Fang*, et al.*, 2020, Liu*, et al.*, 2019), transamination (Bai and Zheng, 2020, Denissen*, et al.*, 2015, Guerre*, et al.*, 2018), and imine metathesis (Haida and Abetz, 2020, Lei*, et al.*, 2020), etc. Nevertheless, while expanding and enriching the domain of EVs, many researchers have encountered deviations from existing epoxy formulations, necessitating non-commercial resins and hardeners with different formulations from conventional ones. Due to these constraints, the adoption of EVs in industrial applications remains premature, with the most significant progress thus far being the exploration of multiple-processability or self-healing abilities in published studies. Therefore, to expand the potential applications of EVs, it is

imperative to develop more facile and robust designs to overcome these challenges.

Regrettably, attaining sufficient dynamic exchange reactions for epoxy-based vitrimers necessitates high temperatures and extended reaction times. Attempts have been made to modify the time-temperature scale, including developing tailored polymer systems (Han, *et al.*, 2018, Lessard, *et al.*, 2019) or altering the composition of exchangeable moieties (Altuna, *et al.*, 2019, Haida and Abetz, 2020, Van Lijsebetten, *et al.*, 2021). However, from the industrial users' perspective, using a catalyst with a 1K resin is more practical than utilizing unstandardized resins and undefined recipes. Zinc acetate has traditionally been widely used as a catalyst in EV systems (Bai and Zheng, 2020, Capelot, *et al.*, 2012, Capelot, *et al.*, 2012, Demongeot, *et al.*, 2016). Zinc ions interact with carboxylates, generating O-ligand/Zn(II) complexes that serve as junctions for the dynamic exchange reaction (Yue, *et al.*, 2020). Nonetheless, the utilization of metal salts inevitably engenders adverse effects, such as low solubility of inorganic powders in epoxy resins, which necessitates additional mixing efforts, and high loading (>5%) requirements, resulting in detrimental effects on the material's properties. Thus, a novel type of miscible catalyst capable of accelerating the dynamic exchange reaction in EVs is urgently needed at this juncture.

In this study, we propose a novel approach to address the limitations of using conventional zinc acetate ($Zn(OAc)_2$) as a catalyst in EV systems. To this end, we introduce solvate ionic liquids (SILs) as an alternative additive to accelerate the dynamic exchange reaction in EVs. SILs, termed by Angell (Austen Angell, *et al.*, 2012), consist of oligoethers (glymes) and metal salts that form a new complex $[M(glyme)]^+$ through coordination. The neutral glyme (Lewis base) allows the multidentate sequestration of metal ions, thereby enabling their dissolution in a liquid medium. SILs offer remarkable properties such as non-flammability, negligible vapor pressure, and a low melting point below 100°C, with some species remaining liquid even at room temperature (Ueno, *et al.*, 2012). Furthermore, SILs have high ionic mobility and can act as a reaction medium in various reactions, including epoxy curing (Hameed, *et al.*, 2020), Diels-Alder, and [2+2] diene cycloaddition (Eyckens and Henderson, 2019). One of the most attractive features of SILs is their versatility in composition, where

their physicochemical properties and reactivity can be readily tailored by modifying the combinations of metal cations, solvates, and anion types (Eyckens and Henderson, 2019).

In the selection process of the SIL composition, it was focused on exhibiting activities in both an epoxy curing and a dynamic exchange reaction, suitable as an additive in an epoxy vitrimer system. The earlier study of Zhang and Wong discovered that the metal acetoacetates were effective in epoxy curing (Zhang, *et al.*, 2002). The metal ions' coordination behavior to epoxide strongly depends on which group a metal core belongs to, resulting in stark contrasts in curing reactivities. Accordingly, we employed lithium (alkali metal, monovalent), magnesium (alkaline earth metal, divalent), and zinc (transition metal, filled d_{10}) cations whose crystal field stabilization energies are zero (e.g., readily exchanges ligands according to their surroundings). For the selection of anions, we adopted two famous anions, trifluoromethanesulfonate (OTf-) and bis(trifluoromethanesulphonyl)imide (TFSI-), whose anionic charge is strongly delocalized by the sulfur flanking groups and hence easily be detached (Eyckens and Henderson, 2019). Collaterally, the anion's hydrophobicity confers air- and moisture-resistivities to SIL. As for solvates, we selected triglyme (G3) for lithium salts because the ionic radius of Li^+ cation matches the cavity size of G3, and the resulting solvate structure is stable (Brouillette, *et al.*, 2002). Considering their higher charge density, we selected tetraglyme (G4) for zinc and magnesium salts. Using these combinations, we also aimed to maximize the stress relaxation performance of the vinylogous urethane-based EV. To the best of our knowledge, only a few papers reported magnesium and zinc-based SILs (Shterenberg, *et al.*, 2015), and this is the first report of applying any SILs into a vitrimer system. In our blueprint, we utilize SILs for the three following objectives at the same time:

1. Obsoleting of metal salt mixing processes that might invoke unwanted pre-gelation or compromise mechanical strengths.

2. Resolving metal cations' catalytic activity during epoxy curing.

3. Accelerating the dynamic exchange reaction in cured EV with a minimum catalyst dose.

2 Results and Discussion

2.1 Validation of SIL Syntheses

The synthesized G3- and G4-solvated SILs ([Li(G3)]TFSI, [Li(G3)]OTf, [Mg$_{0.5}$(G4)]TFSI, and [Zn$_{0.5}$(G4)]TFSI) were homogeneous liquids even after being cooled to room temperature, and no phase separation was observed as depicted in **Figure 4-1a**.

The G3 and G4-solvated SILs that were synthesized had structures that were similar to those reported in previous crystallographic and spectroscopic studies, (Henderson*, et al.*, 2003) despite the differences in the types of anions used (as shown in **Figure 4-1b**). In the G3-SILs, the Li$^+$ core was coordinated with four adjacent ethylene oxides and one oxygen atom from the SO$_2$ group of the TFSI anion, resulting in a 12-crown-4 ether-like coordination geometry, as reported by Tsuzuki in 2015 (Tsuzuki*, et al.*, 2015). On the other hand, in the G4-SILs, the Mg^{2+} or Zn^{2+} core was coordinated with five adjacent ethylene oxides and one oxygen atom from the SO$_2$ group of the TFSI anion, forming a 15-crown-5 ether-like coordination geometry (Henderson*, et al.*, 2003, Watkins*, et al.*, 2015).

2.1.1 IR Analysis

In order to investigate the chemical interaction between metal salts and solvating species in SILs, IR spectra were collected and compared with those of pristine glymes and prepared SILs. The focus was on the two main bands in the glymes: the OCCO asymmetric stretching at 1100 cm^{-1} and a combination of OCCO symmetric stretching and CH$_2$-rocking vibration at 850 cm^{-1} (**Figure 4-1c**), as reported by Seneviratne (Seneviratne*, et al.*, 2004). The IR spectra of SILs showed that both bands split into two, with higher and lower wavenumbers. This was attributed to the coordination between the metal cations (Li$^+$, Mg^{2+}, and Zn^{2+}) and

ethylene oxides in the glymes, which induced a torsional change in the glymes' backbone conformations. Similar observations were made previously in the presence of Na^+ and Li^+. The characteristic bands of the anionic species also confirmed the solvation of metal salts, resulting in a liquid form. The band appearing at 1348 and 1330 cm^{-1} corresponded to the SO_2 asymmetric stretching modes (TFSI$^-$), while the band appearing at 1230 and 1162 cm^{-1} corresponded to the CF_3 stretching modes (OTf^{-1}).
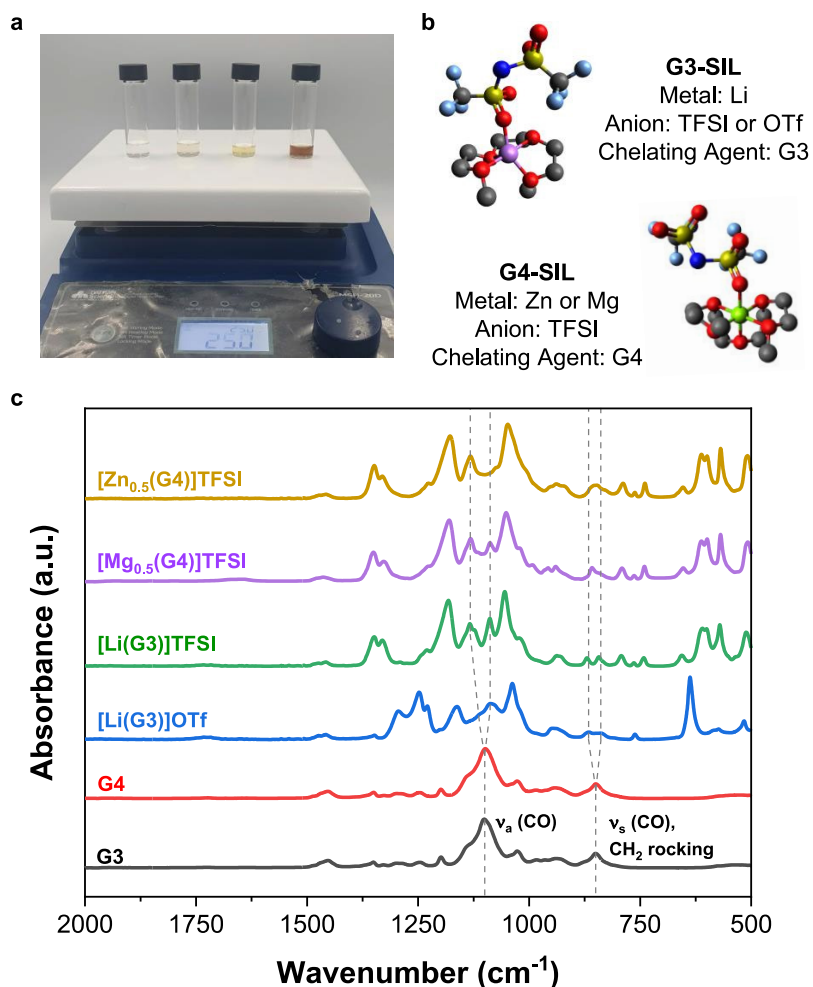
Figure 4-1. a Photographs of the synthesized SILs; (from left to right) [Li(G3)]OTf, [Li(G3)]TFSI, [Zn$_{0.5}$(G4)]TFSI, and [Mg$_{0.5}$(G4)]TFSI. **b** Geometry-optimized structures of G3- and G4-solvated SILs. **c** IR spectra of pure G3, G4, and the synthesized SILs (Shin*, et al.*, 2022).

2.1.2 Raman Analysis

To find other evidence of metal-to-glyme coordination, Raman spectroscopies of SILs were gathered (**Figure 4-2**). The characteristic Raman bands, assigned to the intermolecular vibration modes (CH$_2$ ¬rocking and C-O-C symmetric stretching) of the ligand glymes, appear within the range 800-900 cm^{-1} (Brouillette, *et al.*, 2002). Here we closely examined these bands to conjecture the coordination states of SILs in the light of the glyme side. Pure G3 and G4 showed similar spectra in this region with three bands at 797, 820, and 843 cm^{-1}, which were assigned to the vibrations of free ethylene oxide chains with trans (t), gauche plus (g), gauche minus (g') conformational arrangements. (Ueno, *et al.*, 2015) In contrast, for SILs, the region of interest has been shifted to 860-890 cm^{-1}, ascribed to the "ring breathing mode" of ethylene oxide via the metal ion complexation. (Mandai, *et al.*, 2013) Thus, the Raman spectrum in the region is indicative of the coordination structure of the glyme-metal salts complexes. The spectrum of [Li(G3)]OTf shows two major bands at 851 and 865 cm^{-1}, originating from its helical (tg't)$_3$ conformation structure, calculated from its crystal structure. (Henderson, 2006) The [Li(G3)]TFSI also exhibits a strong band at 865 cm^{-1}, assigned to the breathing mode, along with weaker bands at 803 and 832 cm^{-1}. Hence the result suggests that both the G3-based SILs form a metal-triglyme complex structure, where G3 molecules adopt a crown-ether-like conformation to form a monomeric [Li(G3)]$^+$ complex in the liquid state. (Ueno, *et al.*, 2015) The broad Raman bands were attributed to the multi-vibrational modes from the diverse conformations. The Raman spectra of G4-based SILs showed a much larger frequency downshift since the multi-valence metal ion forms a much tighter complex with tetraglyme whose viable oxide number is 5. While the pure G4 spectrum showed a characteristic (tgt)$_4$ conformational sequence with a couple of lines from 843 to 797 cm^{-1}, the [Mg$_{0.5}$(G4)]TFSI complex's spectroscopic signature is found at 886 cm^{-1}. This denotes the coordination manner, resulting in a G4 conformation completely changing to tgt-tg't-tg't-tgt as a result of the newly formed complex. (Grondin, *et al.*, 2004)

On the one hand, tracing the Raman band assignable to each anion can also be an effective way to examine the ionic interaction between the metal cation and glymes. When the metal cation forms a complex with the ethylene oxide in glymes, there should be changes in the electron density and internal force constant of the anion. This is especially well-reflected in the case of TFSI- whose normal mode, associated with the expansion and contraction of the entire anion, is very susceptible to polarization and ionic coordination. (Brouillette, *et al.*, 2002) Here we looked upon these bands to speculate the coordination states of SILs in the light of anion sides. It was reported that the TFSI anion's Raman spectra, demonstrating the wavenumber was downshifted from 748 cm^{-1} to 742 cm^{-1} as the lithium-coordinated TFSI- became "free", meaning the anion is not strongly associated with any cations. Therefore, the Raman shift is intuitive proof that the original coordination of metal cation and TFSI anion becomes altered. In our case, the G3 or G4 glyme intervenes between the original complex and heists the metal cation to form a new complex. At the moment TFSI anion becomes "free", or more likely, solvent-separated ion pairs (SSIP) state (Ueno, *et al.*, 2012) and the Raman downshift occurs. The bands appeared at 735 cm^{-1} in [Li(G3)]TFSI, 733 cm^{-1} in [Mg$_{0.5}$(G4)]TFSI, and 731 cm^{-1} in [Zn$_{0.5}$(G4)]TFSI. The spectral downshift order seems to be how much each metal cation pulls the glyme solvent out of the TFSI anion and vice versa, which is proportional to the metal cation's ability to form coordination with ethylene oxide in glymes. The result was consistent with the previous result for electrolytes containing the OTf anion (Monti, *et al.*, 2014),   explaining the high charge density to size ratio of the [M]$^{+}$ determines the degree of interaction of [M]$^{+}$ with the external electron-donating species. Only a few studies research the interaction between Mg^{2+} or Zn^{2+} and TFSI, focusing on the Raman band of the TFSI anion. Giffin et al. reported three frequency components located at 752, 746, and 742 cm^{-1} in Mg(TFSI)$_2$-based electrolytes with two high components corresponding to the Mg^{2+}-coordinated TFSI and one lowest component corresponding to the "free" TFSI anion. (Giffin, *et al.*, 2014) Similarly, Bakker and colleagues described the case of poly(ethylene oxide) Mg(TFSI)$_2$, where the absence of higher frequency peaks in the Raman spectra indicated that the coordination of Mg^{2+} ions by the poly(ethylene oxide) significantly reduced their interaction with TFSI^{-} (Bakker, *et al.*, 1995). They also observed

a larger frequency downshift for the TFSI- band released from the divalent Mg^{2+} compared to that released from alkali monovalent ions.

In contrast, our study found that both $[Mg_{0.5}(G4)]TFSI$ and $[Zn_{0.5}(G4)]TFSI$ produced a single sharp band at low frequency in the Raman spectra of the TFSI anion alone. This suggests that $TFSI^-$ exists in the unassociated SSIP state and that the glyme molecule fully chelates the metal cation, leading to solvation. While we did not assign all the spectral bands to determine the exact conformation or coordination structure of the SILs, we were able to confirm the formation of a new $[M]^+$ [glyme] complex and the solvation of metal salts resulting from it.
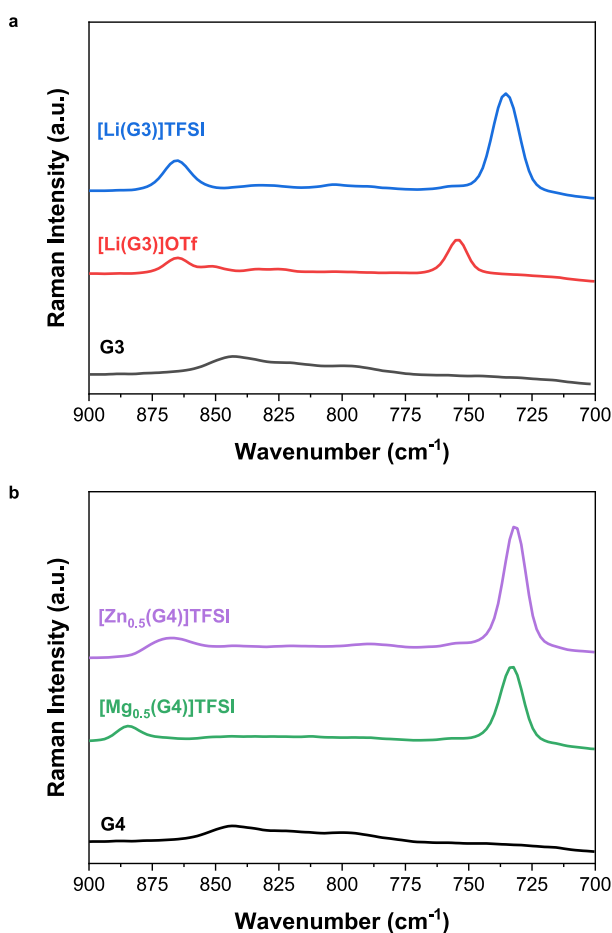
Figure 4-2. Raman spectra of **a** pure G3 and G3-based SILs and **b** pure G4, and G4-based SILs (Shin, *et al.*, 2022).

2.2 Material Characterizations of the SILs

2.2.1 Thermal Properties of the SILs

The thermal stability of the SILs was investigated to determine their suitability for use in EVs under working conditions. The $T_{d5\%}$ values of all SILs were significantly higher than those of pure G3 and G4 molecules (which were around 110°C) due to the formation of metal-glyme complexes. The thermogravimetric curves showed multi-phase degradation in weight, with the first phase attributed to the volatilization of the glymes, the next phases to further evaporation of the coordinated glymes ($[M^+(glyme)]$), and finally to the decomposition of the metal salts. The $T_{d5\%}$ varied based on the type of anions, glymes, and metal cations used, indicating that the thermal stability varied with the metal-glyme coordination structures. However, the order of the thermal stability of the SILs was not directly determined by the order of $T_{d5\%}$. [$Mg_{0.5}$(G4)]TFSI and [$Zn_{0.5}$(G4)]TFSI had a higher fraction of uncoordinated glymes, which made their weight loss in the earlier phase appear magnified. Despite this, all the SILs showed improved thermal stability due to the ion-dipole interactions between the glymes and the metal cations, confirming their suitability as additives in both epoxy processing and use conditions.

DSC profiles of the SILs revealed that all the SILs have melting below 40°C. (**Figure 4-3b**). At the temperature of epoxy processing, the SILs would be in liquid form.
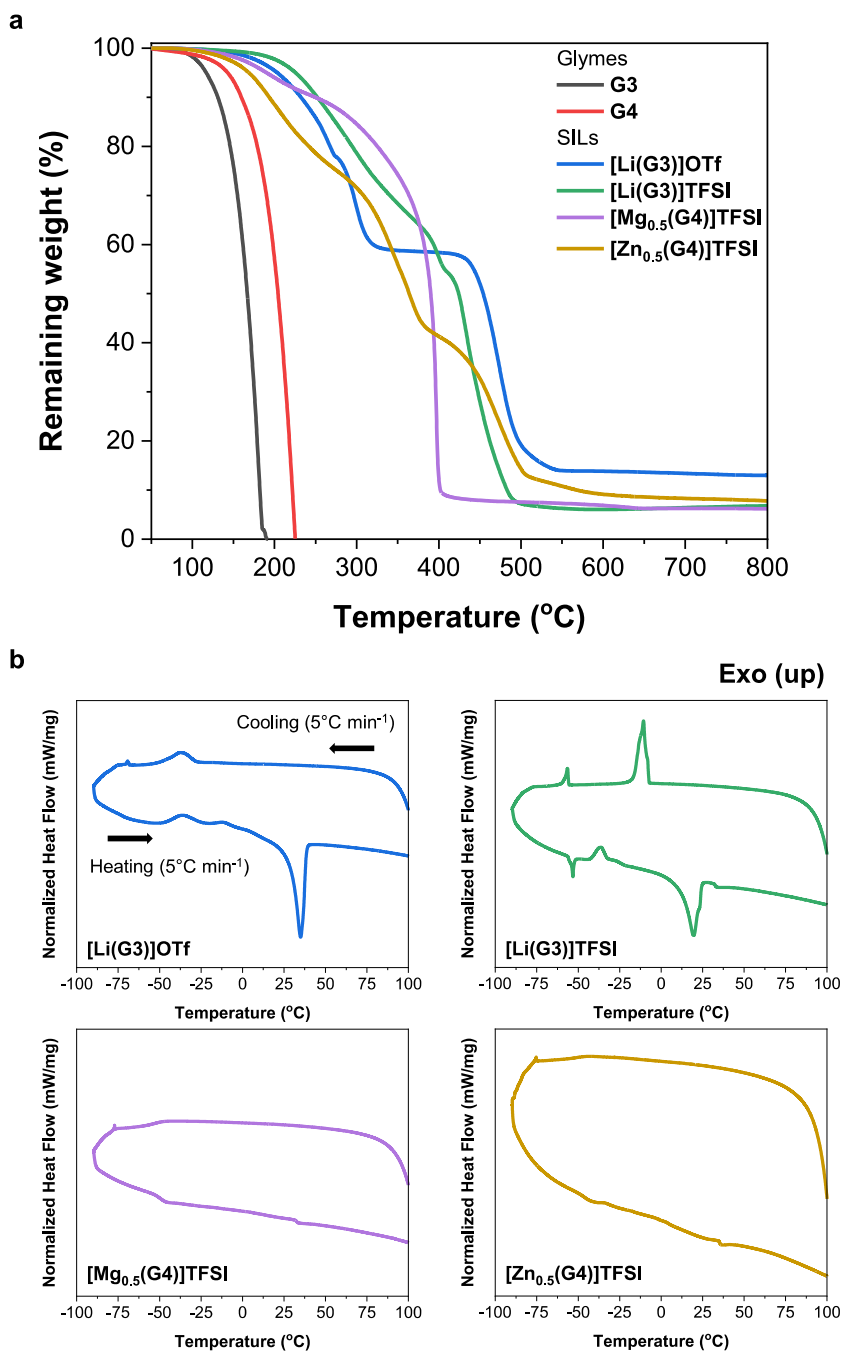
Figure 4-3. a Thermal degradation curves of pure G3, G4, G3-SILs, and G4-SILs. **b** Heat flow curves of [Li(G3)]OTf, [Li(G3)]TFSI, [Mg$_{0.5}$(G4)]TFSI, and [Zn$_{0.5}$(G4)]TFSI (Shin, *et al.*, 2022).

2.2.2 Gutmann Acceptor Number of the SILs

The comparison of Gutmann acceptor numbers between the SILs and other well-known catalysts in dynamic exchange reactions revealed that all the SILs recorded high values above 14, surpassing even the good Lewis acid, DBTL (**Table 4-1**). By the solvation of glymes (i.e. chelating species) within the aprotic solvent (i.e. benzene), the naked metal cations freely withdraw the lone pair electrons of triethylphosphine oxide (Eyckens and Henderson, 2019). Based on these results, it can be inferred that the SILs would be highly coordinative in electron-exchanging reactions within both the hydrophobic model reaction media or the epoxy polymer melt.

Table 4-1. Gutmann acceptor number for the listed compounds (Shin*, et al.*, 2022).

Compounds	$Et_3P=O$		Acceptor Number
	$\delta(^{31}P)$	$\Delta\delta(^{31}P)$	
None	46.69	-	-
THF	47.27	0.58	1.36
Triglyme	46.44	0.5	0.59
Tetraglyme	46.52	0.17	0.4
DBTL	53.02	6.33	14.86
$Zn(OAc)_2$	- (not dissolved in d_6-benzene)	-	-
[Li(G3)]OTf	52.81	6.12	14.56
[Li(G3)]TFSI	56.97	10.28	24.47
[Mg$_{0.5}$(G4)]TFSI	64.54	17.85	42.48
[Zn$_{0.5}$(G4)]TFSI	71.62	24.93	59.33

2.3 Tracing Transamination Reactions on Model Study

2.3.1 Validation of the Model Compound Synthesis

The Model Compound, ethyl-3-(octylamino)but-2-enoate, was obtained with a yield of 88%. R_f = 0.6 (EtOAc:Hexane=1:3); IR spectra confirmed that the conjugated C=O stretching (1654 cm^{-1}) and C=C stretching (1608 cm^{-1}) bands were newly found, which evidenced the formation of vinylogous urethane linkage in the model compound. 1H NMR (600 MHz, CDCl$_3$, 25°C, TMS): δ = 8.52 (s, 1H), 4.38 (s, 1H), 4.04 (q, J = 7.1 Hz, 2H), 3.16 (dd, J = 13.0, 6.8 Hz, 2H), 1.87 (s, 3H), 1.5 (m, 2H), 1.36 (m, 2H), 1.20 (t, J = 7.2 Hz, 3H), 0.89 (t, J = 7.3 Hz, 3H).
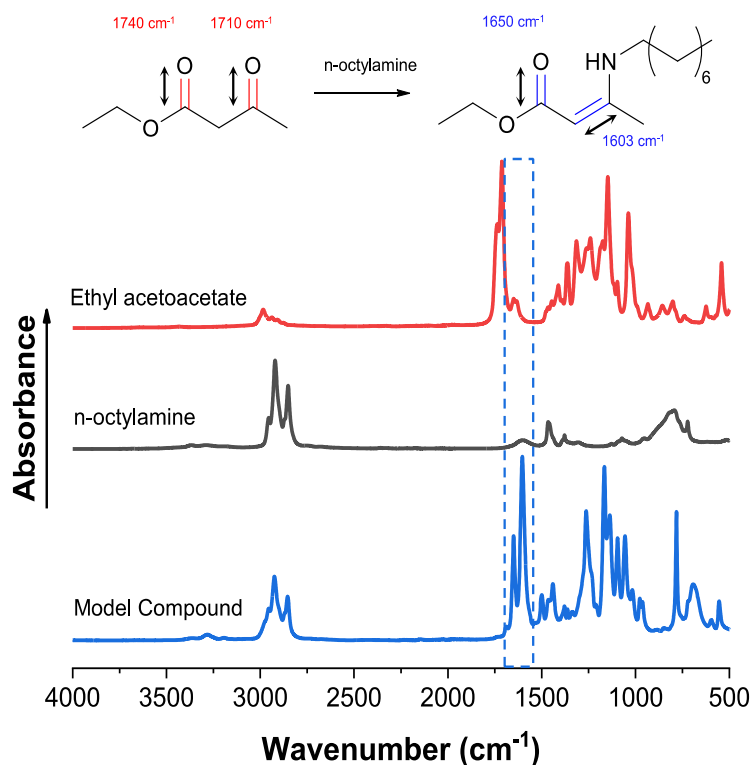
Figure 4-4. IR spectra of ethyl acetoacetate, n-octylamine, and the Model Compound (Shin*, et al.*, 2022).

136

Figure 4-5. ^{1}H NMR Spectrum of the Model Compound (Shin*, et al.*, 2022).

2.3.2 Acceleration of Transamination by the Introduction of SILs

We investigated the ability of the synthesized SILs to catalyze transamination using a model system based on the work of Denissen et al (Denissen*, et al.*, 2017). The transamination reaction involved the conversion of the model compound (R1, elution time of 20.09 min) to ethyl-3-((2-ethylhexyl)amino)but-2-enoate (P1, elution time of 19.00 min), and 2-EHA (R2, elution time of 9.50 min) to octylamine (P2, elution time of 10.31 min). The conversion ratio of R1 to P1 was determined using GC-FID analysis, with a lower limit of 0.8 for the [R1] fraction at the point of [R2] depletion due to the use of a five-fold excess of R1. After a reaction time of 60 minutes at 70°C, a conversion of 13% of [R1]/([R1]+[P1]) was achieved, whereas the theoretical maximum conversion was 20%. These results confirmed the occurrence of dynamic exchange reactions in the model system (**Figure 4-6**).
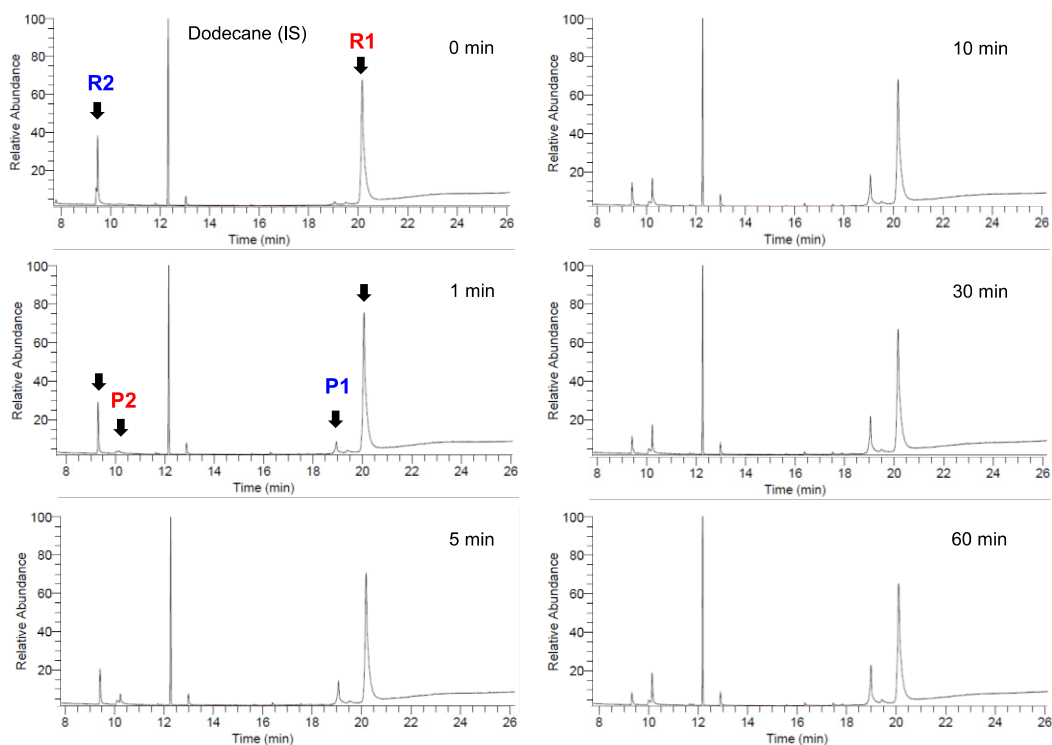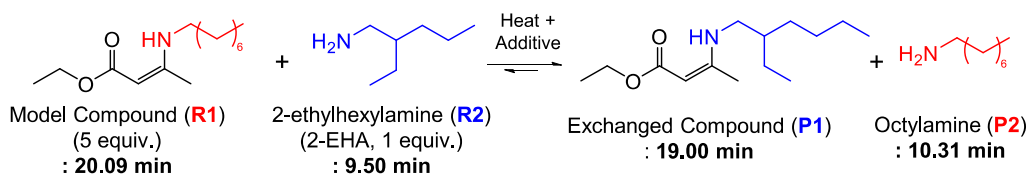
Figure 4-6. GC-traces for a representative transamination reaction (between the Model Compound and 2-ethylhexylamine) at 70°C, without additive (Shin, *et al.*, 2022).

The catalytic activity of various catalysts, including $Zn(OAc)_2$ and SILs at a dose of 0.5%, was investigated in the model reaction system, referring to a previous study by Denissen et al. In dynamic exchange reactions, Lewis acids have been known to increase the reaction rate by facilitating proton transfers between protonated primary amines and secondary amines (Denissen*, et al.*, 2017). Therefore, $Zn(OAc)_2$, a well-known catalyst for various dynamic exchange reaction systems (Capelot*, et al.*, 2012, Demongeot*, et al.*, 2016, Yue*, et al.*, 2020), was analyzed as the reference additive. The transamination reaction was expected to have a similar catalytic effect by chelating with Zn^{2+}-chelated carbonyl or carboxyl functionalities, which increases the partial charge on sp^3 carbon atoms (Demongeot*, et al.*, 2016). However, even with the use of 2 mol% (vs. [R1]) of $Zn(OAc)_2$, the system did not reach equilibrium even after 60 min, possibly due to its poor solubility in the medium. On the other hand, the SIL-introduced systems exhibited much higher reaction rates and reached equilibrium rapidly (<10 min) with a lower catalyst dosage (0.5 mol%) (**Figure 4-7**). This is attributed to the miscibility of the glyme-solvated compounds with the liquid media, enabling the system to utilize the high proton transfer ability of metal cations fully. Based on the model reactions, the molten metals resulting from the solvation can indeed be responsible for the accelerating effect. This confirms the earlier statement that the Lewis acidic characteristic of metal compounds can be utilized as long as they become soluble in a liquid media (Denissen*, et al.*, 2017).
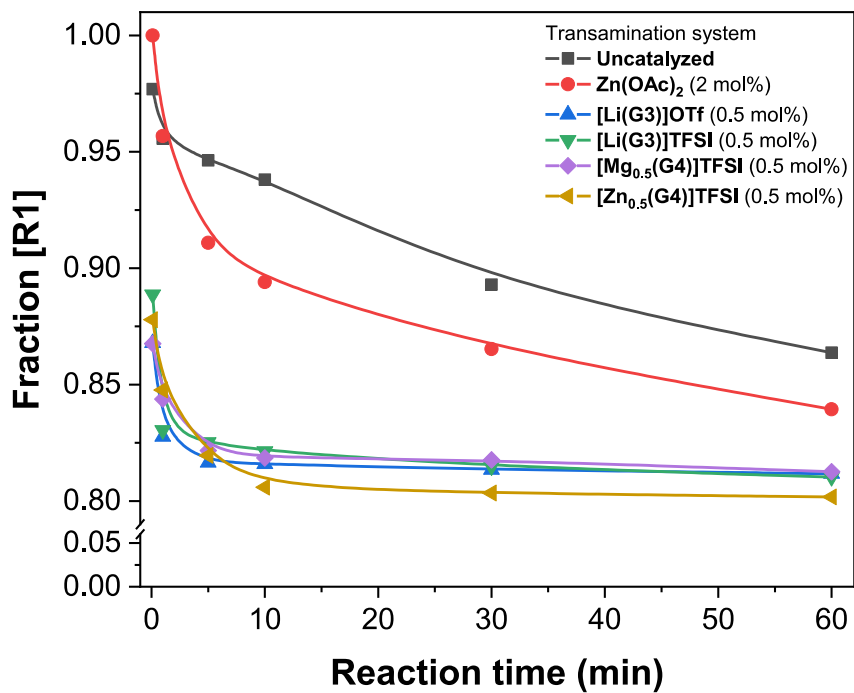
Figure 4-7. Decrease in the fraction of the Model Compound as aa function of time at 70°C, in the presence of various additives (Shin, *et al.*, 2022).

Further, we calculated the activation energies of transamination systems with and without additives. Following the Arrhenius law, the decrease in [**R1**], the concentration of the Model Compound, as a function of time can be expressed as:

$$[\textbf{R1}] = 1 - C_{eq} + C_{eq} \cdot e^{-kt/C_{eq}} \qquad \text{(Equation 4-1)}$$

Where C_{eq} = equilibrium fraction of the product = 0.8, k = initial rate constant (the first 4 points were fitted), and t = reaction time.

After obtaining k values at 3 different testing temperature (**Figure 4-8**), *k* values were fitted and the activation energy was calculated by plotting ln *k* against 1000/T. (**Figure 4-9a**)

$$\ln k = -\frac{E_a}{RT} + const. \qquad \text{(Equation 4-2)}$$

The model study exhibited pseudo-first-order linear decay kinetics at low conversions and reached an equilibrium plateau (**Figure 4-9a**). The kinetic curves showed the temperature dependence of typical dynamic exchange reactions. For example, the activation energy of the Model Compound can be obtained by multiplying the slope of the function (-7.435) and gas constant (-8.315); E_a = 61.8 kJ mol^{-1}. Subsequently, an activation energy of 62 ± 3 kJ mol^{-1} was calculated for the transamination of the uncatalyzed model system (**Figure 4-9b**), which is consistent with previous reports (59–73 kJ mol^{-1}). (Denissen*, et al.*, 2015, Haida and Abetz, 2020)

According to calculations by Du Prez et al. for vinylogous urethanes (Denissen*, et al.*, 2015), our model system proceeded via a protic iminium pathway, even though no additive had been used. In contrast, markedly different temperature dependences were observed in systems with additives. The activation energy of the Zn(OAc)$_2$-added system was = 50 kJ mol^{-1}, indicating a slight catalytic effect. Furthermore, the SIL-loaded systems significantly reduced the enthalpic barriers (E_a), which were almost half that of the uncatalyzed system. SIL's effect on transamination has never been reported so far for any vinylogous urethane system and thus deserves closer scrutiny. According to Denissen's previous study, acid-catalyzed transamination systems have an activation energy of 47 kJ mol^{-1} (Denissen*, et al.*,

2017), attributed to a shift in the reaction pathway to a more direct one. However, in our study, the G4-solvated multivalent SILs showed notably lower activation energies of 31 and 26 kJ mol^{-1} for [Mg$_{0.5}$(G4)]TFSI and [Zn$_{0.5}$(G4)]TFSI systems, respectively, as shown in **Table 4-2**. This is because the exchange reaction did not involve any Brønsted acid or protic solvent that would have followed an accelerated protic imine metathesis pathway dominated by the active protonated amine or imine species. (Haida and Abetz, 2020) Instead, the reaction commenced with metal complexation similar to Michael addition, following activating carbonyl sites of vinylogous urethanes that stabilized the resultant zwitterionic intermediates via conjugation. Moreover, the reduction in activation energies matched the order of the Gutmann acceptor numbers of each SIL, manifesting that the additive's ability to accept electron pairs strongly influenced the carbonyl complexation.

Table 4-2. Activation energies calculated from the model study with and without additives (Shin, *et al.*, 2022).

Catalysts	E_a from the model study [kJ mol^{-1}]
Uncatalyzed	62 ± 3
Zn(OAc)$_2$ (2 mol%)	50 ± 2
[Li(G3)]OTf (0.5 mol%)	35 ± 17
[Li(G3)]TFSI (0.5 mol%)	32 ± 16
[Mg$_{0.5}$(G4)]TFSI (0.5 mol%)	31 ± 10
[Zn$_{0.5}$(G4)]TFSI (0.5 mol%)	26 ± 12
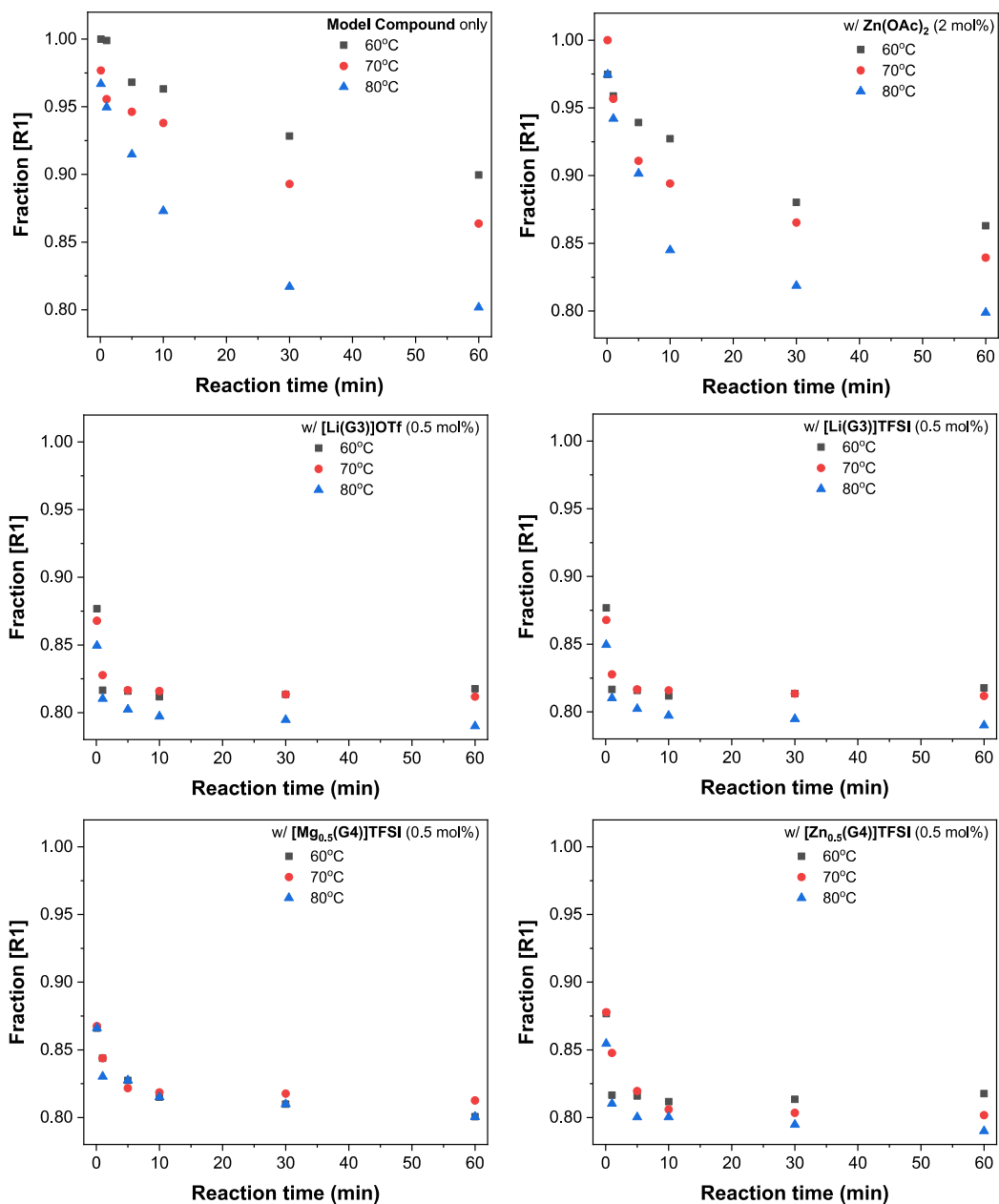
Figure 4-8. Progression of the transamination reaction of Model Compound, 2-ethylhexylamine, and additives at 60, 70, and 80°C; without additive, $Zn(OAc)_2$, [Li(G3)]TFSI, [Li(G3)]OTf, [Mg$_{0.5}$(G4)]TFSI, and [Zn$_{0.5}$(G4)]TFSI (Shin*, et al.*, 2022).
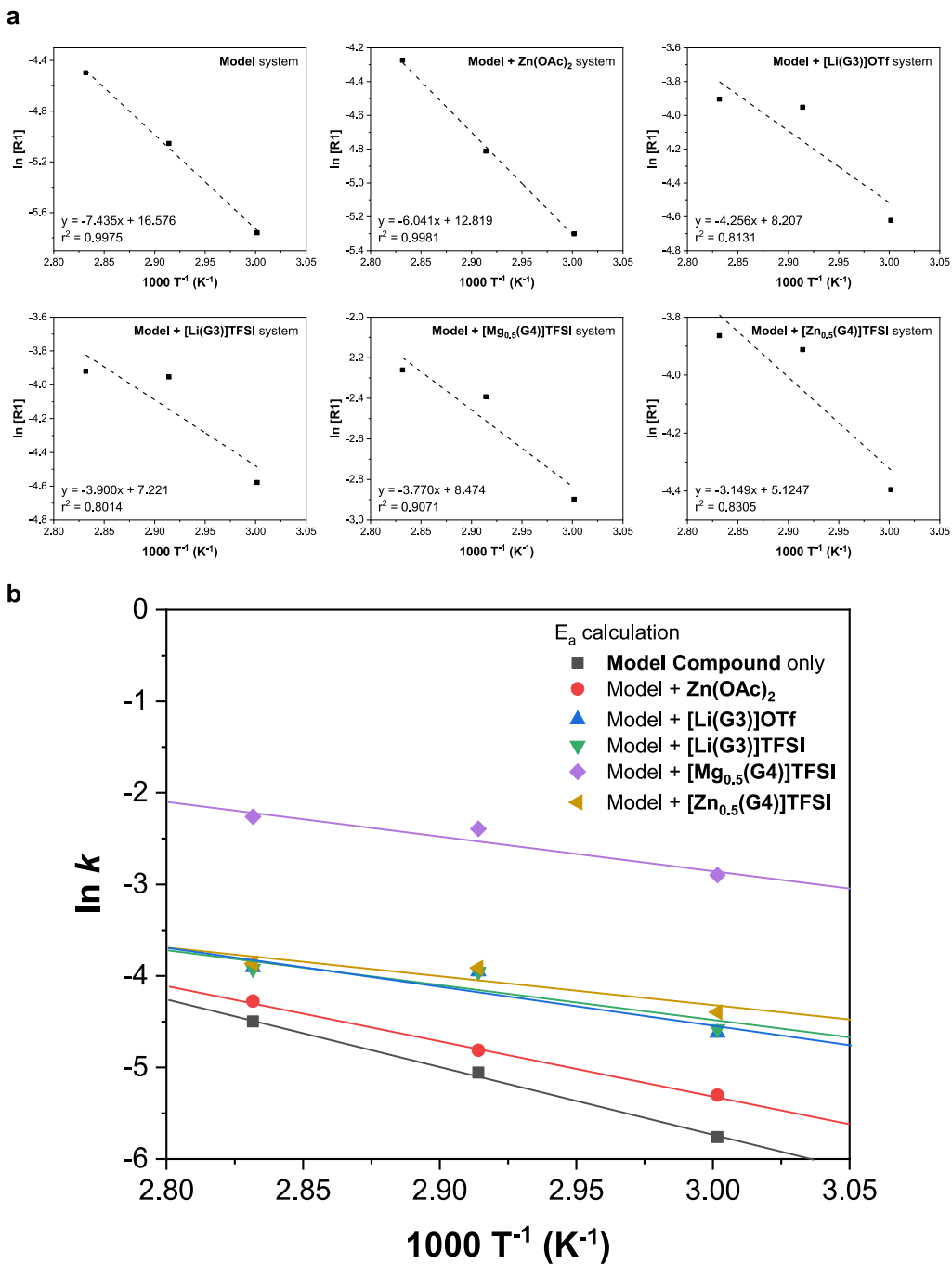
Figure 4-9. Calculation of **a** k values and **b** activation energies of transamination reaction with and without additives (Shin, *et al.*, 2022).

2.4 Accelerations of Transamination Reactions on Epoxy Vitrimers

2.4.1 Thermomechanical Properties of the Cured Epoxy Vitrimers

After confirming the effectiveness of SILs on model compounds, we investigated their impact on cured EV networks. The obtained EVs exhibited glassy elastic moduli ($>10^8$ Pa @ 25°C) and high thermal stabilities (<1.5% mass loss at 150°C for 1 h) regardless of with or without additives (**Figure 4-10** and **Figure 4-11**).

Next, to conduct tensile tests, dog-bone-shaped EV specimens with and without additives (0.5 mol%) were fabricated (**Figure 4-12a**). The mechanical properties of EVs were evaluated, and the representative stress-strain curves obtained at room temperature and 80°C are shown in **Figure 4-12b**, with the results summarized in **Table 4-3**. Notably, a small amount of $Zn(OAc)_2$ substantially reduced the tensile strength (30 MPa) at room temperature, which was less than half that of the reference EV (69 MPa), due to the interphase between the epoxy matrix and metal powder being vulnerable to crack propagation. However, the use of SILs as additives (0.5 mol%) yielded significantly higher tensile strengths (> 50 MPa) at room temperature, and their continuous networks had advantageous effects on the final storage moduli of cured EVs, compensating for the T_g-reduction effects on tensile strength (**Table 4-4**). At 80°C, all SIL-containing EVs exhibited similar or higher elongations (30-40%) than those obtained in the uncatalyzed and $Zn(OAc)_2$-catalyzed samples. These results demonstrate the potential of SIL-containing EVs as engineering materials and their ability to achieve excellent properties in both target temperatures.
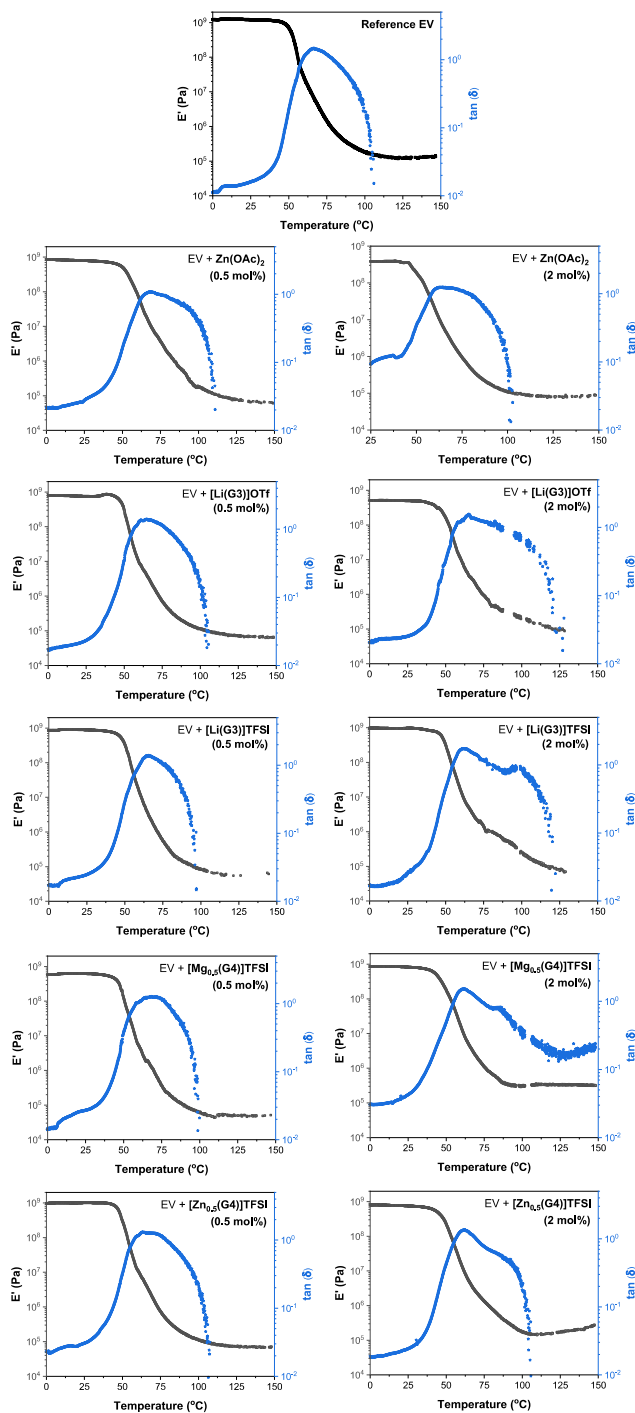
Figure 4-10. E' and tan(δ) of EVs with and without catalysts (Shin, *et al.*, 2022).
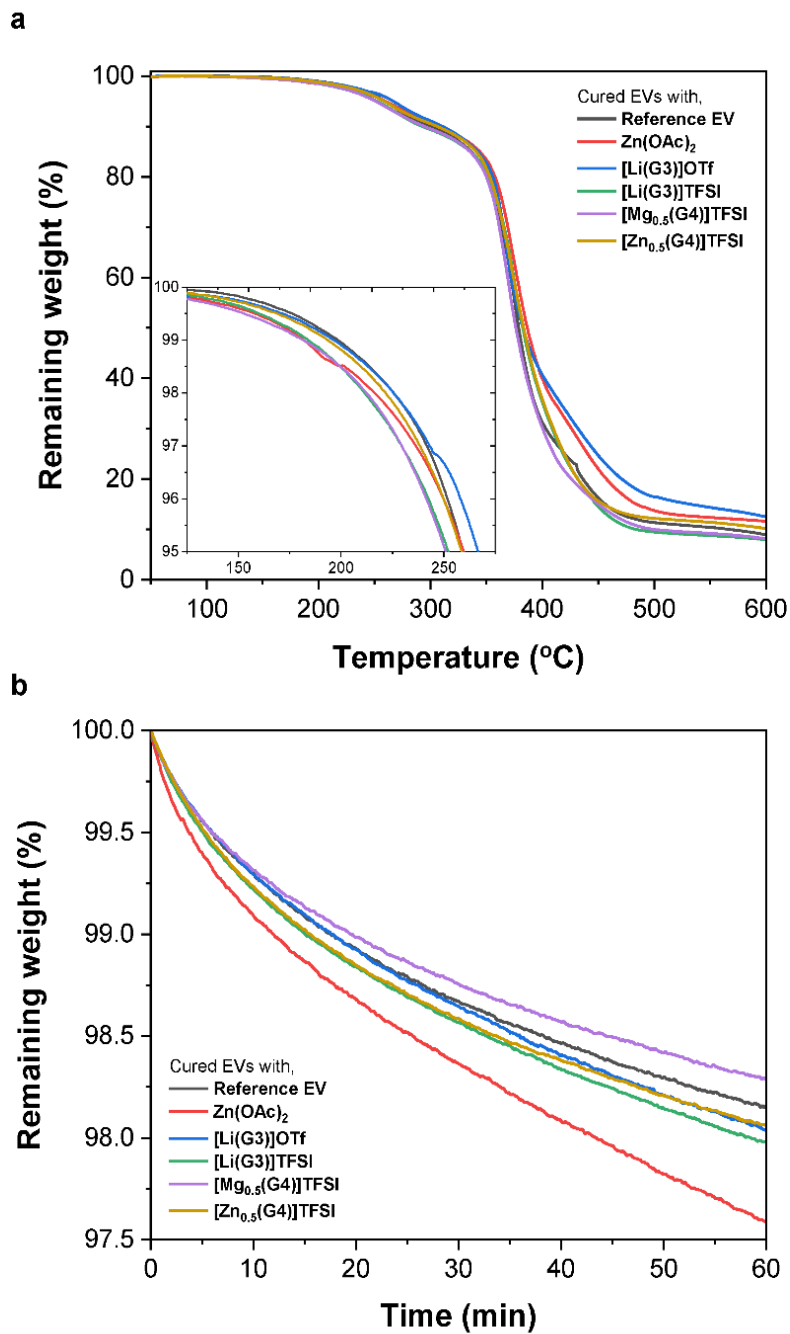
Figure 4-11. a Temperature ramp curves (10°C min⁻¹) of the cured EVs with and without catalysts. **b** Isothermal thermograms of the cured EVs at 160°C (Shin, *et al.*, 2022).
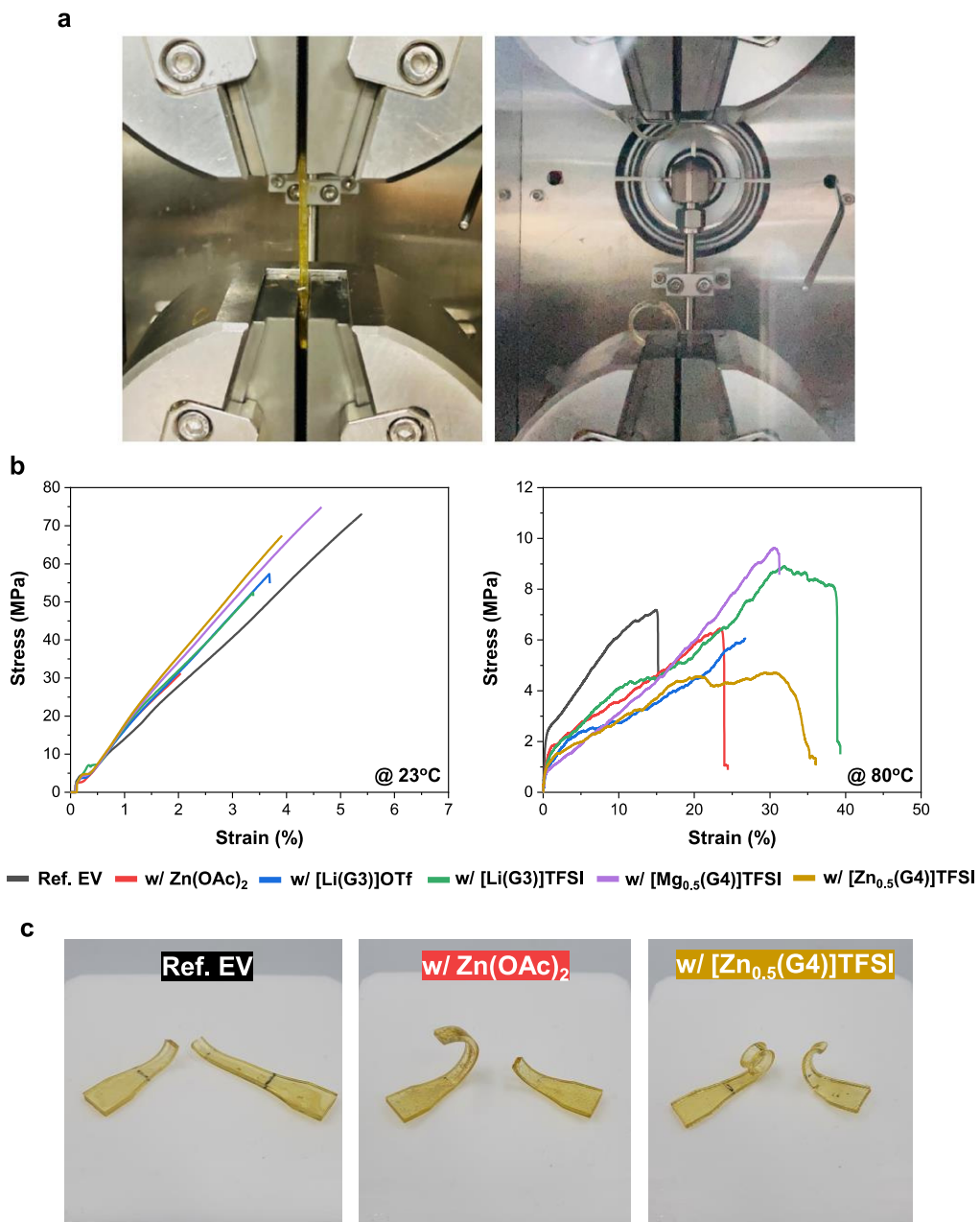
Figure 4-12. a An EV specimen loaded in tensile grip; before (left) and after (right) test. **b** Tensile properties of EVs with and without catalysts, measured at 23°C (left) and 80°C (right). **c** EV specimens with and without additives after the tensile test (Shin*, et al.*, 2022).

Table 4-3. Thermal and mechanical properties of EVs with and without catalysts. (Shin, *et al.*, 2022).

Entry	Dose [mol%]	$T_{d5\%}$ [°C]	T_g [°C]	ε at 25°C [%]	ε at 80°C [%]	σ at 25°C [MPa]	σ at 80°C [MPa]
Reference EV	0	259	66.2	5.3	15.0	68.7	8.5
w/ Zn(OAc)$_2$	0.5	260	68.2	3.2	29.7	29.8	8.4
	2	-	62.8	-	-	-	-
w/ [Li(G3)]OTf	0.5	267	64.3	3.8	27.9	55.8	6.1
w/ [Li(G3)]TFSI	0.5	252	65.6	3.6	43.2	46.1	8.3
w/ [Mg$_{0.5}$(G4)]TFSI	0.5	251	64.5	4.1	25.1	56.4	7.5
	2	-	61	-	-	-	-
w/ [Zn$_{0.5}$(G4)]TFSI	0.5	259	63.3	4.1	30.8	55.7	5.9
	2	-	61.6	-	-	-	-

2.4.2 Stress-relaxation Properties of the cured Epoxy Vitrimers

Through stress-relaxation experiments (**Figure 4-13**), we investigated the dynamic nature of EVs, specifically focusing on the efficacy of SILs. We observed that the stress-relaxation behavior of the EVs followed the Maxwell model, which resulted from the percolation of dynamic reversible bonds in the system (**Figure 4-14a**), consistent with previous studies on EV systems (Li*, et al.*, 2018).

We also found that an increase in temperature from 130 to 160 °C led to a decrease in relaxation time (τ^*), according to the Arrhenius law, for all EVs, regardless of the presence of additives. By comparing the relaxation curves of the catalyzed system at 140°C (**Figure 4-14b**), we observed that the addition of 2 mol% $Zn(OAc)_2$ reduced the τ^* from 2000 s (reference network) to 1500 s, as previously reported (Demongeot*, et al.*, 2016). In contrast, with SILs as catalyst (0.5 mol%), the τ^* was further reduced to 1000 s ([Li(G3)]OTf), 462 s ([$Mg_{0.5}$(G4)]TFSI), 405 s ([Li(G3)]TFSI), and 344 s ([$Zn_{0.5}$(G4)]TFSI), indicating that SILs exhibit substantially better catalytic activities for transamination in EVs compared to $Zn(OAc)_2$. Although the catalytic activity did not follow a linear order, we observed that its effect varied with the type of metal and counter anion, as indicated by the model study. In summary, our findings demonstrate the dynamic behavior of EVs and highlight the potential of SILs as efficient catalysts for transamination in EVs.

In order to investigate the effect further, EVs with a higher concentration of SILs (2 mol%) were prepared and tested at 160°C (**Figure 4-14b**). Surprisingly, an increase in the amount of SILs resulted in a further acceleration of the dynamic exchange reaction, resulting in τ^* values of 19 s and 26 s for systems containing 2 mol% of [$Mg_{0.5}$(G4)] TFSI and [$Zn_{0.5}$(G4)] TFSI, respectively. This is an unprecedently low dosage of an external catalyst for EV systems. The significant acceleration (about 38 or 28-fold, respectively) in comparison to the reference EV (with a τ^* of 730 s at 160°C) was attributed solely to the catalytic effect of the SILs, as there was no change in composition. The acceleration was concluded not to have originated from rheological differences such as chain mobility or cross-linking density, as

no significant difference in T_g or storage and loss moduli was observed within the temperature range (**Table 4-3**).

An Arrhenius plot was used to analyze the data obtained from relaxation times at various temperatures, and a linear relationship between $\ln(\tau^*)$ and $1000\,T^{-1}$ was established (**Figure 4-14c**). The activation energies were then calculated from the slopes. The measured activation energies for the reference EV and $Zn(OAc)_2$-catalyzed systems were 71 ± 4 and 70 ± 18 kJ mol^{-1}, respectively, which are consistent with those for the transamination system via a neutral iminium pathway (Denissen*, et al.*, 2017). With the addition of SILs, the systems showed apparent downward shifts in $\ln(\tau^*)$ and slower grades in the corresponding slopes, resulting in significantly lower activation energies, even below 50 kJ mol^{-1}, as listed in **Table 4-4**. Although the activation energies obtained from a model study and a stress-relaxation test were almost equal, a rise in the absolute values was observed for the latter. This significant change in a reaction pathway due to the SIL was evident, even though all systems, with or without additives, shared the same ratio of free primary amines and vinylogous urethane secondary amines. Denissen et al. reported a metal-catalyzed pathway using 1.9 mol% of dibutyltin dilaurate as an additive, reducing the thermal barrier of the transamination reaction to only 30 kJ mol^{-1} (Denissen*, et al.*, 2017).
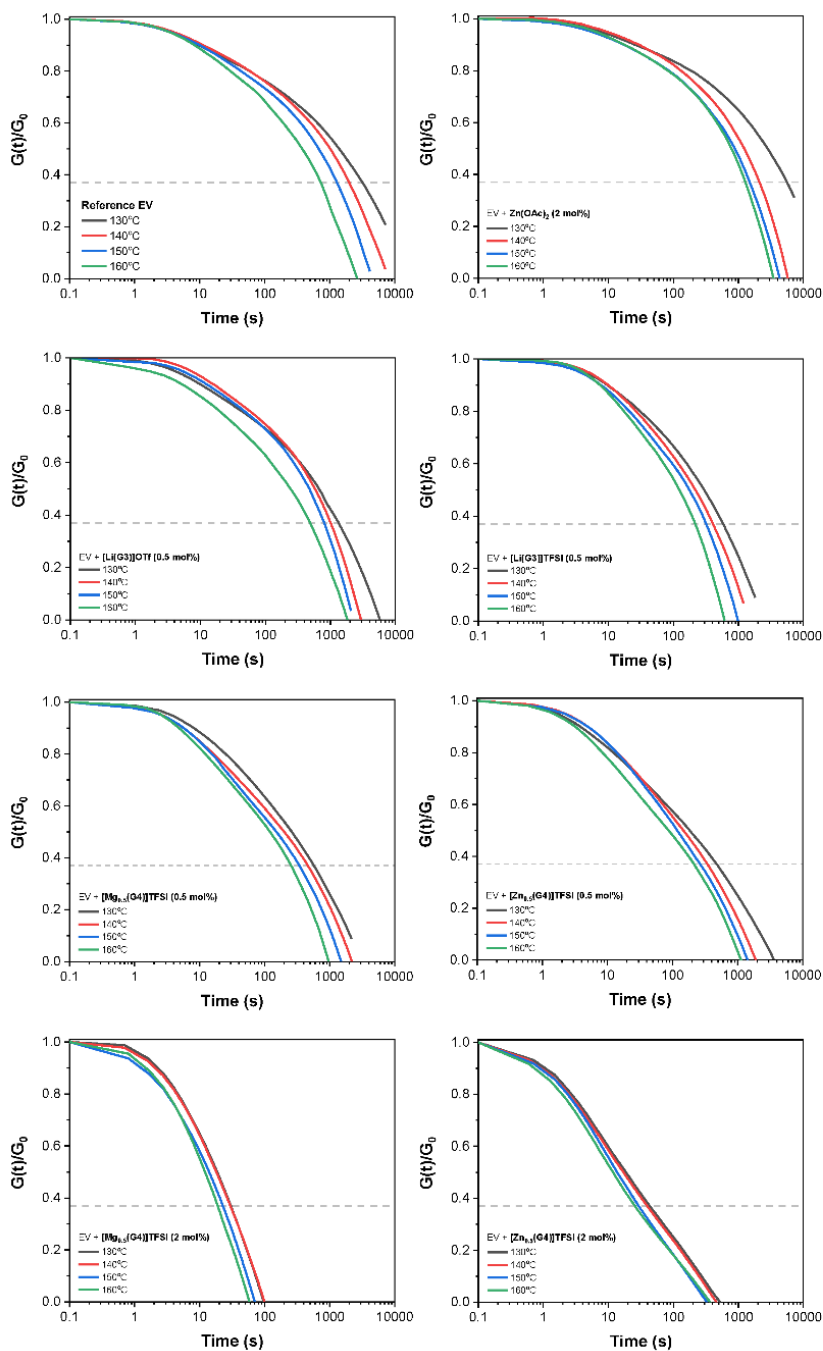
Figure 4-13. Normalized stress relaxation curves of the EVs without additive, with Zn(OAc)$_2$ (2 mol%), with SILs (0.5 mol%), and with SILs (2 mol%) under the temperature range from 130 to 160°C (Shin, *et al.*, 2022).
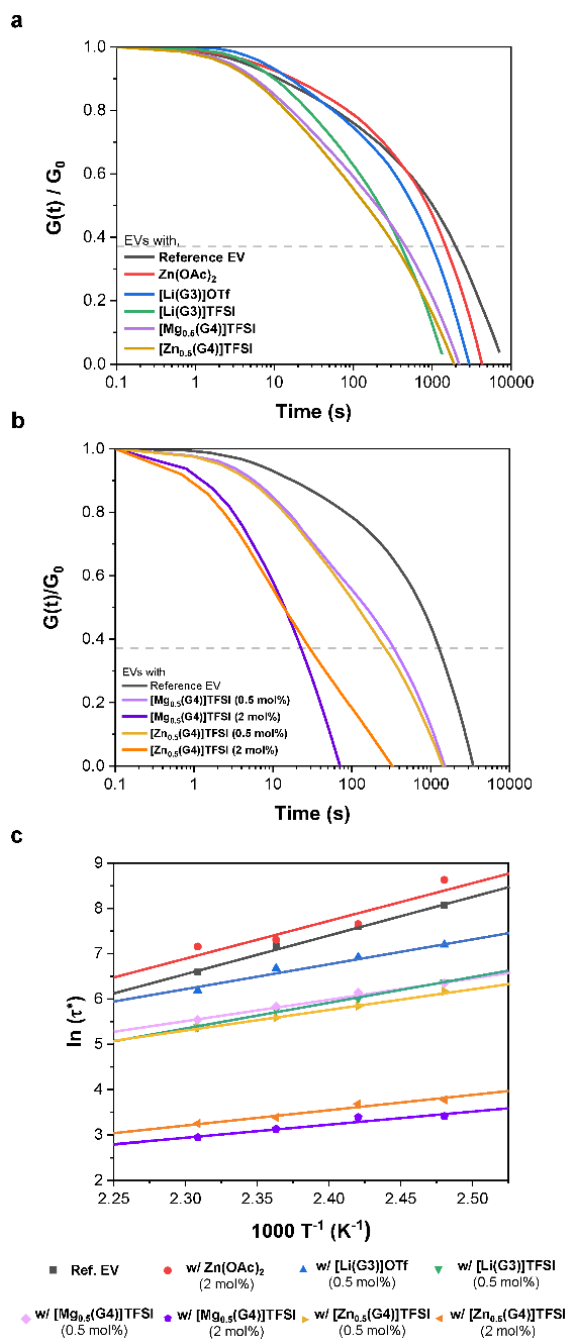
Figure 4-14. a Stress-relaxation curves of EVs without catalyst and with 0.5 mol% of catalysts. **b** Stress-relaxation curves of EVs containing [Mg$_{0.5}$(G4)]TFSI and [Zn$_{0.5}$(G4)]TFSI (dosages: 0.5 or 2 mol%). **c** Arrhenius curves of the EVs (Shin, *et al.*, 2022).

Table 4-4. Activation energies calculated from the stress relaxation tests with and without catalysts (Shin, *et al.*, 2022).

Catalysts	E_a from the stress-relaxation test [kJ mol^{-1}]
Uncatalyzed	71 ± 14
Zn(OAc)$_2$ (2 mol%)	70 ± 18
[Li(G3)]OTf (0.5 mol%)	47 ± 6
[Li(G3)]TFSI (0.5 mol%)	47 ± 3
[Mg$_{0.5}$(G4)]TFSI (0.5 mol%)	39 ± 3
[Mg$_{0.5}$(G4)]TFSI (2 mol%)	24 ± 5
[Zn$_{0.5}$(G4)]TFSI (0.5 mol%)	39 ± 2
[Zn$_{0.5}$(G4)]TFSI (2 mol%)	27 ± 4

2.4.3 Creep Behavior of the Catalyzed Epoxy Vitrimers

In the former chapter 3, we aimed to achieve two goals simultaneously: to enhance the stress-relaxation of EV compositions and minimize creep deformation. Adding SILs can accelerate the transamination and chain rearrangements for stress-relaxation; the concomitant increase in creep deformation might undermine the original intention. Therefore, we investigated the effect of the accelerated transamination on the creep performance of Ali D23_EV and Aro(1,1) D23_EV samples (see **Figure 4-15**). For the Ali D23_EV group, adding 2 mol% of $[Zn_{0.5}(G4)]TFSI$ did not significantly increase the creep strain compared to the uncatalyzed sample (max. strain of 1.5% for the uncatalyzed and 1.6% for the catalyzed). The high percentage of permanent crosslinks in the composition seems to contribute to the retarded deformation.

Similarly, for the Aro(1,1) D23_EV group, adding 0.5 mol% of the catalyst only slightly increased creep strain compared to the uncatalyzed sample (max. strain of 1.7% for the uncatalyzed and 1.8% for the catalyzed). However, adding an amount of the catalyst (2 mol%) to the Aro(1,1) D23_EV system rapidly increased the creep strain, reaching almost 6% at the end of the test. As discussed in Section 2, EVs with aromatic neighboring groups around a vinylogous urethane moiety undergo much faster transamination and have lower activation energy for the dynamic exchange reaction. Therefore, the exchange-acceleration effect of SILs can be much stronger for those samples. To minimize creep deformation, we recommend adopting lower dynamic fractions within the crosslinks or using lower doses of the catalyst for the EVs prepared by Aro DCAs.
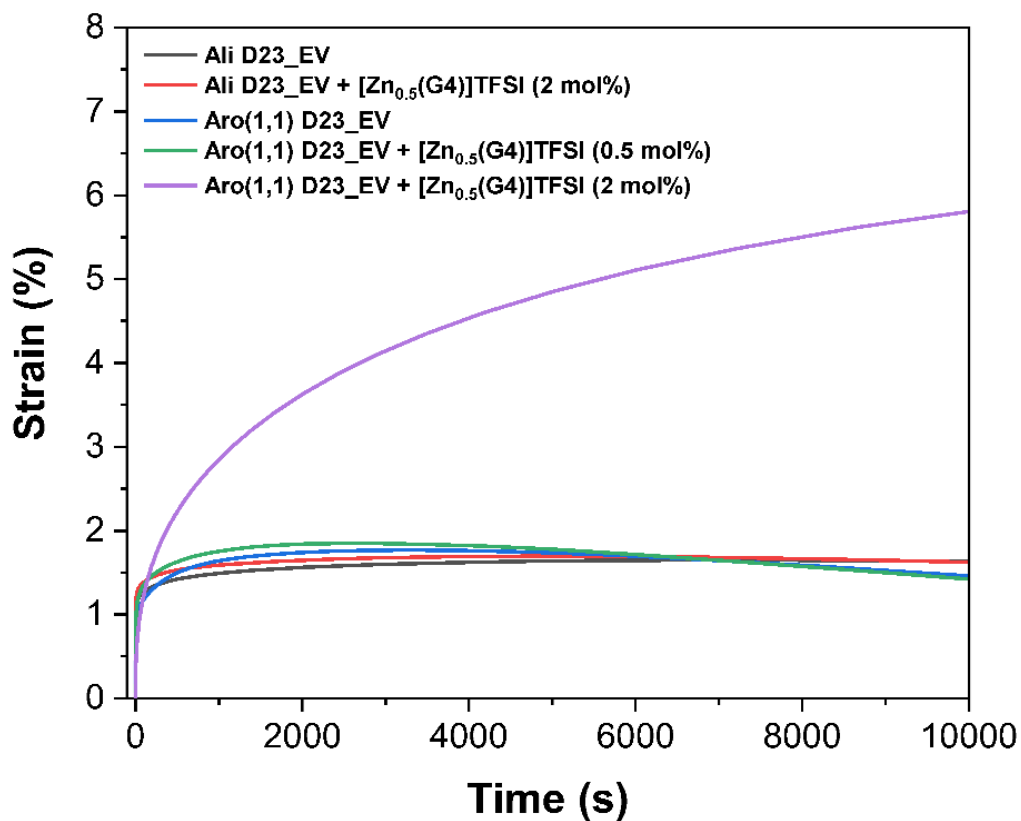
Figure 4-15. Creep strains of the uncatalyzed and catalyzed Ali D23_EV and Aro(1,1) D23_EV series with different doses of $[Zn_{0.5}(G4)]TFSI$ as a function of time.

2.4.4 Proof of the SIL's Activation on a DCA Carbonyl Moiety

We expected that the molten-metal cations of SILs would act as Lewis acids and create O-ligand/Metal complexes with the oxygen atom found in the carbonyl groups in the epoxy vitrmer system. As we gradually added SILs to the DCA medium, the characteristic IR band at 1645 cm^{-1}, corresponding to the carbonyl stretching vibration, decreased in intensity due to metal coordination (**Figure 4-16**). Adding SILs to DCA also resulted in significant reductions in the intensity of bands assigned to amines, such as the N-H stretching of primary amine at 3372 cm^{-1}, N-H stretching of secondary amine at 3279 cm^{-1}, N-H bending at 1599 cm^{-1}, and N-H out-of-plane wagging at 781 cm^{-1}. Notably, the spectral positions assigned to the stretching vibration of primary amine's N-H were down-shifted to 3367 cm^{-1} and 3358 cm^{-1} after adding 5 mol% [Mg$_{0.5}$(G4)]TFSI and [Zn$_{0.5}$(G4)]TFSI, respectively. On the other hand, the bands related to the stretching vibration of N-H secondary amine were up-shifted to 3287 cm^{-1} and 3295 cm^{-1}. These frequency shifts indicate that SILs form complexes with the amine moiety (Allen*, et al.*, 1967). Ideally, we would have observed the preferential coordination behavior of SILs to epoxide over DCA. However, obtaining precise IR spectra of epoxide and primary amine was impossible due to the curing reaction.

According to Bai and Zheng (Bai and Zheng, 2020), a similar shift was observed in the vinylogous urethane acrylate system when zinc chloride was added. In this system, the absorbance bands attributed to −NH2 also decreased in intensity, indicating the coordination of SILs with primary amine species. As a result, the protonated amine species became deactivated, and the reaction followed the metal-catalyzed mechanism with a significantly lower enthalpic barrier. This metal-catalyzed transamination pathway was previously unknown due to the medium's low solubility of metal salts. Interestingly, it demonstrated excellent efficacy for the dynamic exchange reaction, as SILs could be easily introduced into the vitrimer resin mixture.

Once the EV was fully cured, the SILs had a different function and greatly accelerated transamination reactions in model compounds and cross-linked epoxy networks. The

molten-metal cations of SILs acted as Lewis acids, creating a direct carbonyl activation pathway, significantly reducing the enthalpic barriers for transamination reactions (**Figure 4-17**). This allowed the prepared EVs to behave like normal glassy epoxies at room temperature and showed complete stress-relaxation over a short period at higher temperatures. Tensile tests conducted at room temperature and 80°C indicated that the SIL-containing samples maintained their mechanical strength and showed higher elongations, surpassing both the uncatalyzed and $Zn(OAc)_2$-containing EVs. Incorporating SILs into the EV allowed for rapid curing and stress relaxation in a moderate temperature range without deviating significantly from standard epoxy formulations, making it widely applicable in conventional epoxy industries. Since the complexation of SILs for activating epoxide or carbonyl moieties does not require specific chemistry, this strategy is expected to be used in a broader range of epoxy curing or dynamic exchange systems.
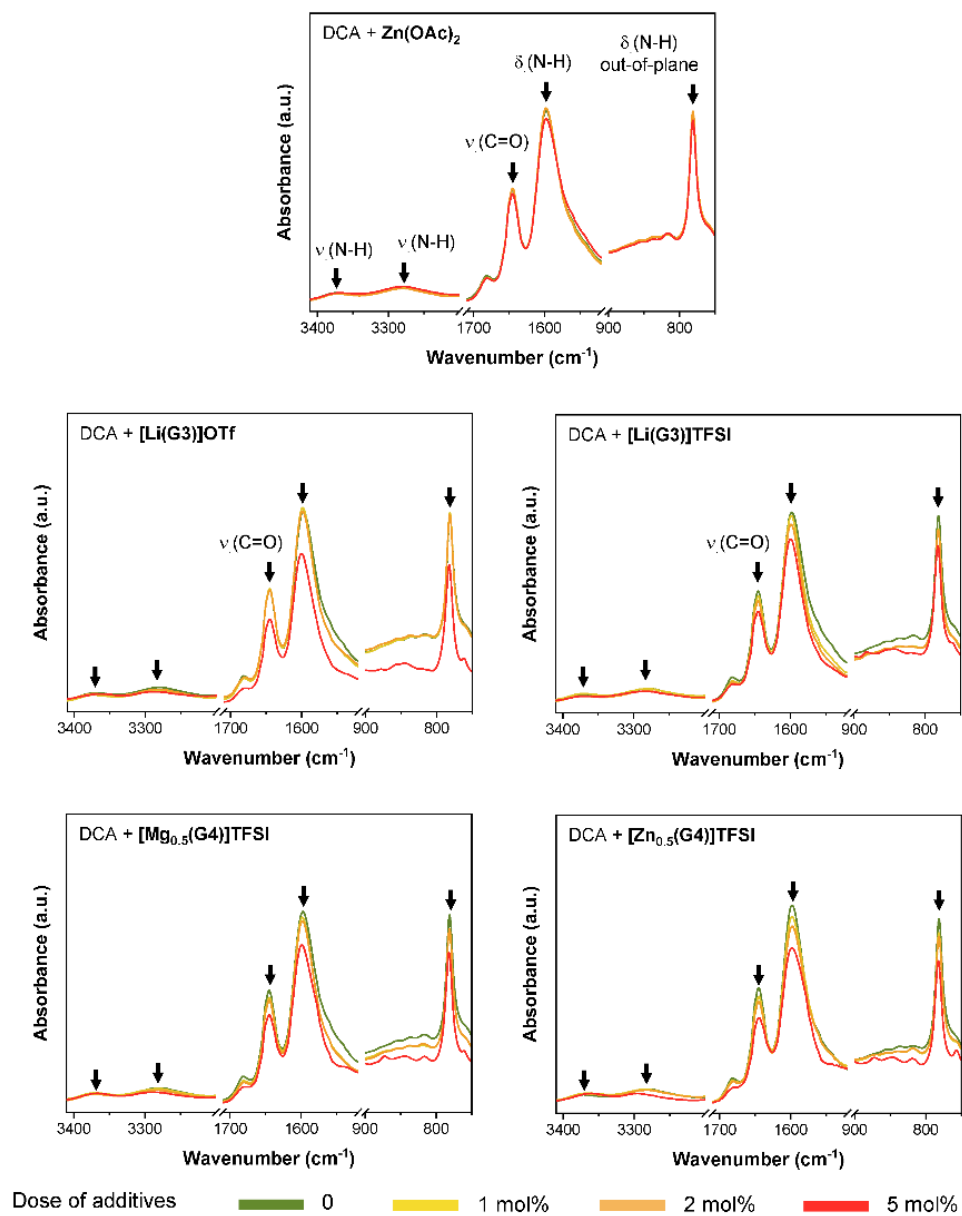
Figure 4-16. IR spectra of a DCA with different types and doses of additives in the range of 1750-700 cm^{-1} (the scales of y-axis are uniformized) (Shin, *et al.*, 2022).
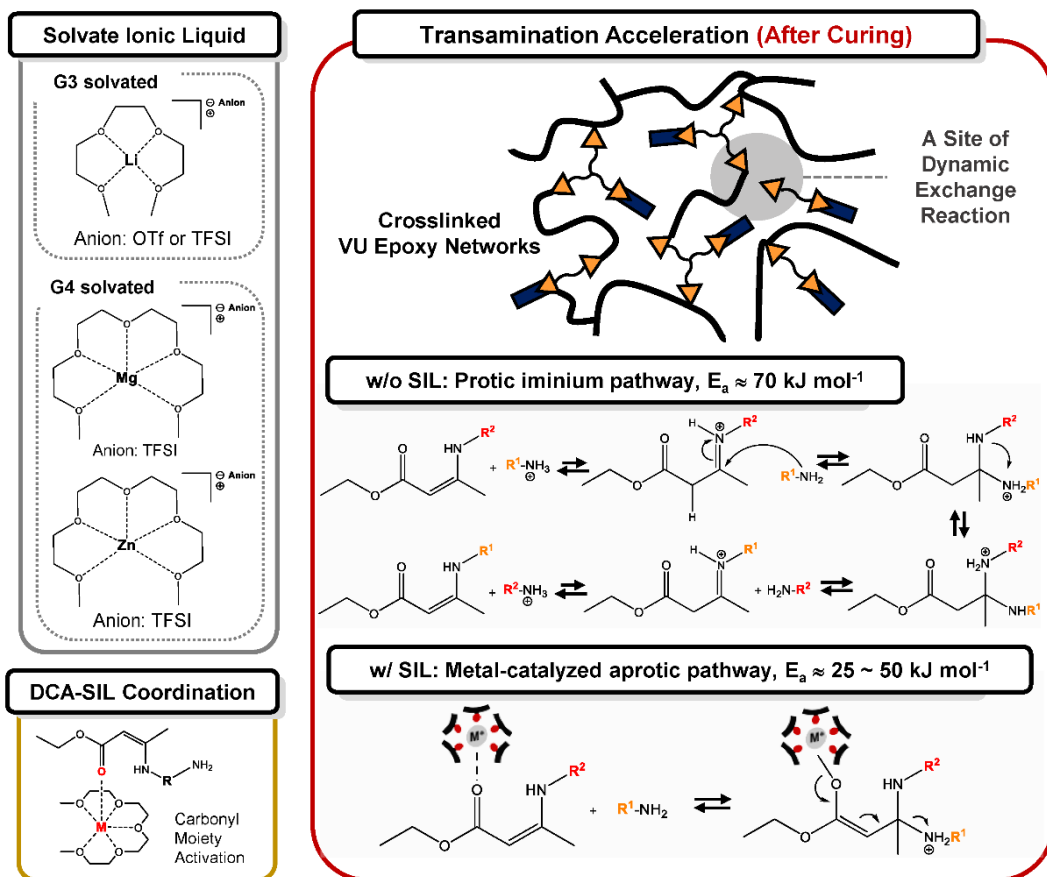
Figure 4-17. Mechanism of SIL catalysis on the transamination via metal-catalyzed aprotic pathway (Shin*, et al.*, 2022).

3 Conclusion

We demonstrated the acceleration of transamination reactions in an EV by adding low amounts of various types of SILs, including [Li(G3)]OTf, [Li(G3)]TFSI, [Mg$_{0.5}$(G4)]TFSI, and [Zn$_{0.5}$(G4)]TFSI. The catalytic effect can be easily adjusted by changing the dose of SILs (0.5~2 mol%). We anticipated that the catalytic performance of the SILs would be determined by their Lewis acidity (namely, Gutmann AN), and we discovered that they were indeed correlated. The role of the SILs was verified, manifesting that they accelerated transamination reactions in both model compounds and cross-linked epoxy networks. The molten-metal cation in the SILs acted as a Lewis acid, mediating the reaction pathway of transamination via direct carbonyl activation, significantly reducing the required enthalpic barriers for transamination reactions from 71 kJ mol^{-1} (uncatalyzed) to 24 kJ mol^{-1} (with 2 mol% of [Mg$_{0.5}$(G4)]TFSI).

Meanwhile, the prepared EVs behaved like ordinary glassy epoxies at room temperature (E' > 10^8 Pa) and exhibited complete stress relaxation (i.e., no residual stress) over a short time scale at 160°C. Tensile tests conducted at room temperature and 80°C showed that the SIL-catalyzed specimens had undamped tensile strengths and even higher elongations, outperforming both the uncatalyzed and the Zn(OAc)$_2$-catalyzed EVs. Thus, incorporating SILs into EV facilitated dynamic exchange reactions and stress relaxation within a wide temperature range without diverging from the customary epoxy formulations. Since the complexation of SILs activating carbonyl moieties worked well with the vinylogous urethane chemistry, we envisaged that the strategy could apply to a broader range of vinylogous urethane-based vitrimers. In fact, the [Zn$_{0.5}$(G4)]TFSI catalyst was also effective when included in Aro(1,1) D23_EVs with a 0.5 mol% loading without significantly increasing the creep deformation of the material (**Figure 4-18**).
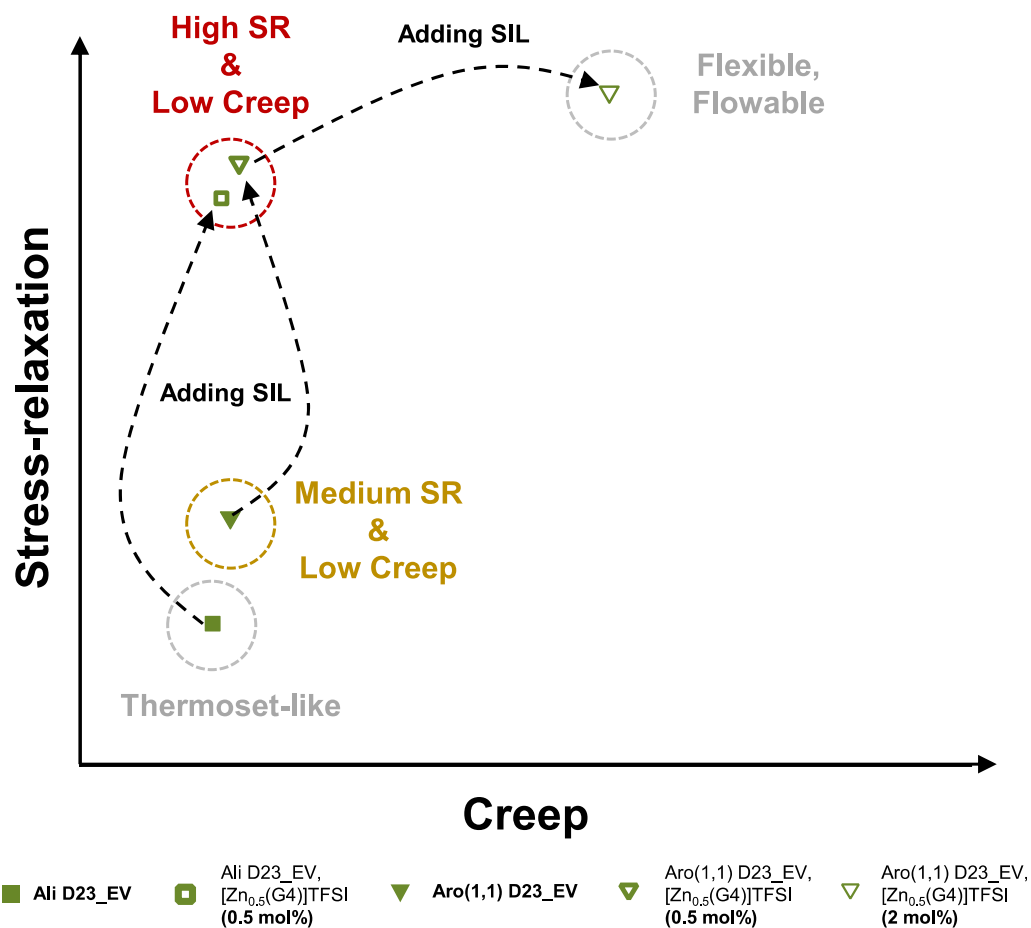
Figure 4-18. Comparison of viscoelastic behaviors of the EVs with and without a SIL catalyst.

Chapter 5

Application of Epoxy Vitrimers as Rigid / Flexible Encapsulants

1 Introduction

"More than Moore" is the new directive for this era, referring to the fact that the improvement in semiconductor performance is no longer solely dependent on the scaling-down strategy but on the complex integration of single dies (chiplet), each having a characteristic function, through several advanced packaging technologies. Among these technologies, fan-out wafer level packaging (FO-WLP) is considered the core foundation that reconciles multiple applications, such as system-in-package (SiP), 2.5/3D stack, and system-in-chip (SiP), owing to its structural versatility, high integration capability, and cost-effectiveness (Lau *, et al.*, 2018). Generally, for high-density FOWLP technology, the critical dimension in line/space limit is below 5 μm/5 μm, effectively enabling the encapsulation of the latest architecture for memory chips (Liu *, et al.*, 2019). In the design, the epoxy molding compound (EMC) covers and protects a core known good die (KGD) and the peripheral spaces of redistribution layers (RDL) and solder balls. However, with this level of critical dimension and the soaring ratio of packaging area/wafer thickness, the problem of wafer warpage is becoming increasingly serious. If the wafer warpage occurs to a certain degree, the wafer cannot be handled further due to severe misalignments, line size control, and handling problems in subsequent operations (Cheng *, et al.*, 2019).

There have been intensive trials for defining warpage in FOWLP by modeling the situation and optimizing process mechanics in compliance with actual processing parameters (Wang *, et al.*, 2021). In addition, the effects of cure-dependent volumetric shrinkage and interfacial material properties (modulus, CTE, heat release, etc.) mismatch were examined to suggest material selections for substrates and molding compounds (Qin *, et al.*, 2020, Wu *, et al.*, 2019). Although numerous guidelines for manufacturers regarding warpage reduction have been proposed, efforts to convert conventional packaging materials to improve their ability of stress-relaxation still need to be made. Moreover, adopting novel materials with a stress-relaxation characteristic is rarely considered because only some candidates have met the stringent qualification standards of the chip packaging industry so far. Thus, the deficiency

in the liberty of material choice forced the manufacturer to find detours to repress the stress development within interlayers (i.e., reducing CTE mismatch) and optimize geometric or processing parameters in packaging procedures. The understanding of practical stress dissipation by polymeric encapsulants is still in its infancy, not to mention their effects on the cure or cooling-induced warpage for semiconductor packaging. Besides, a new venture to innovate a functional polymer in lieu of conventional packaging materials is lacking.

Thus, the main goals of the study are to examine the applicability of the epoxy vitrimers (EV) as chip-on-wafer (CoW) and chip-on-film (CoF) encapsulants and elucidate the effect of stress-relaxation of a polymer on reducing warpage of the substrates through empirical encapsulation tests. During the encapsulation process, two successive deformations should be caused by: 1) volumetric shrinkage at the chemical crosslinking during the curing process and 2) the thermal stress from the CTE mismatch upon cooling to ambient temperature. There are many processes in a practical chip packaging procedure that might induce additional deformation to the encapsulant and wafer; RDL construction, carrier detaching, de-taping, lapping, ball mounting, back-grinding, and wafer dicing. Nonetheless, this paper will not discuss the effect of these additional processes. Rather, a simple situation (curing-and-cooling) and focus on discussing what brings the difference in the evolution of warpage as a function of materialistic factors.

Generally, encapsulation materials can be subcategorized according to the site where the material should function correspondingly, such as molding compounds, underfill, glob-top, dam-and-fill, potting, and conformal coatings (**Figure 5-1**) (Haleh Ardebili, 2009). The required material properties are largely varied depending on their specific functions in each application. For example, the representative hard chip-level encapsulant, EMC, is charged with the important mission of passivating the vulnerable chip/circuit inner systems from external stress or environmental factors. Therefore, the material has an extremely high storage modulus of over 10 GPa and a high T_g of over 150°C (Haleh Ardebili, 2009). Meanwhile, rigid board-level encapsulants, such as dam-and-fill and glob-top, are required to protect circuit components from external chemicals or electric stimuli without inflicting

too much stress on them. Hence, a bit softer material with a medium range of storage modulus (about a few MPa to a few GPa) was favored for these applications, such as epoxy, acryl, and polyurethanes. (Yao, *et al.*, 2015) However, all the conventional line-ups must compromise on either mechanical endurance or the low-stress property. Choosing either an ever-soft elastomer or an ever-hard thermoset would peg the innate characteristic of the chosen material, irrespective of various working temperatures. The elastic moduli of normal polymers follow the Williams-Landel-Ferry behavior upon heating above T_g, so the property change would not be large enough to make a difference in response to stress. In contrast, the vitrimer-based materials strongly show Arrhenius-like temperature dependency above their T_g, exhibiting a drastic change in modulus or viscosity while the matrix experiences internal chain rearrangements. We believe our EVs can satisfy both performances en route to remedy stress-induced warpage.

On the other hand, there are also requirements for soft encapsulation materials in the special field of semiconductor packaging. These soft encapsulation materials are represented by silicone gel or silicone elastomers and UV-curable acrylate or urethane resins. They possess very low Young's moduli (below 1 MPa) and very high CTEs (300-1000 ppm K^{-1}) (Gao, *et al.*, 2022). Soft materials are occasionally adopted for filling, conformal, power module, and optoelectronic applications (Gao and Liu, 2022), which demand high thermal resistance or optical transparency. Especially in the fields of flexible and wearable electronics, the use of fortified PDMS as a soft encapsulant for flexible circuits has been extensively studied in recent years (Li, *et al.*, 2019, Qi, *et al.*, 2021, Xu, *et al.*, 2017). All the while, the use of silicone-based elastomers for the substrate has been extensively studied so that the stress from the deformation of the substrate should be instantaneously dissipated through the soft matrix of the encapsulant. Unfortunately, such silicone-based elastomer shows very low adhesion toward PI substrate (peel strength < 0.1 N mm^{-1}) (Hoang, *et al.*, 2016) and experiences a great amount of thermal stress upon repeated heating & cooling because of high CTE mismatch (PDMS ~ 300 ppm K^{-1}; PI ~ 35 ppm K^{-1}), which can cause chip misalignment or even delamination (Ouyang, *et al.*, 2022). Additionally, the material suffers from a lack of long-term assurance owing to its weak gas and water vapor tightness (Qi, *et*

al., 2021). Our EV system can demonstrate rapid deformation to respond amply in harmony with the deformation of a flexible PI substrate while outperforming both fronts of adhesion and endurance over PDMS.

In this section, we selected two species of EVs for a rigid encapsulation application, which showed high E' and medium grades of stress-relaxation, along with low creep strains; Ali D23_EV and Aro(1,1) D23_EV. We adopted two kinds of wafers, silicon, and glass, as rigid substrates. Recently, a glass-type interposer (for example, an electrical routing interface in a 2.5D packaging) has attracted attention as a potential alternative to conventional silicon interposers owing to its relatively low cost, flatness, and high electrical resistivity (Shih*, et al.*, 2021). Thus, it would be beneficial to test the new substrate's response to rigid encapsulation and warpage and compare the results. On the other hand, we selected two species for a soft encapsulation application, which showed low E' and high grades of stress-relaxation, along with medium creep strains; Aro(1,0) D26_EV and Aro(0,1) D26_EV. We used a polyimide film as a soft substrate. Polyimide film is a favored substrate in mobile display and healthcare applications, in the form of flexible hybrid or printed electronics, due to its excellent conformability (Tong, 2022). While a complete mechanistic study will be the focus of future works, we conducted preliminary experiments to address the most outstanding question: whether the EV effectively reduces stress-induced deformations.
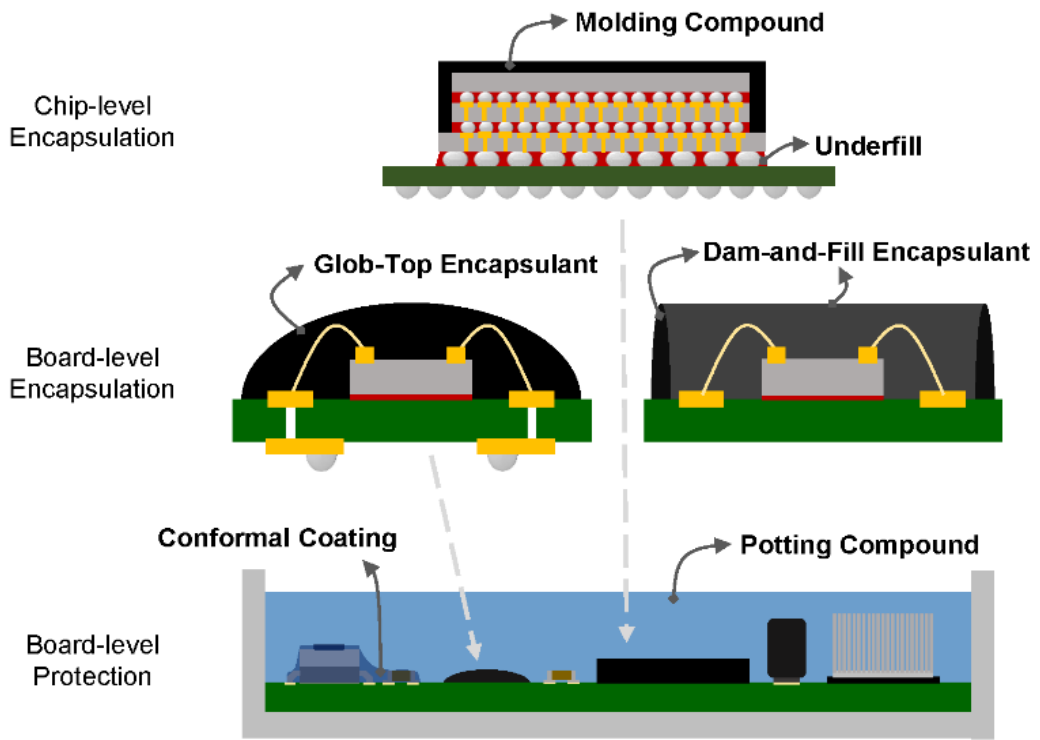
Figure 5-1. Types of encapsulants used in various levels of semiconductor packaging.

2 Results and Discussion

2.1 Surface and Adhesion Properties

2.1.1 Surface Free Energies of Substrates and Encapsulants

Firstly, the substrates' surface free energies (SFE) were evaluated according to the Fowkes equations, where the contact angle values were obtained from a sessile drop method (**Table 5-1**). The total SFEs (σ_{total}) of the substrates were similar, while that of the glass wafer was slightly higher: σ_{total} of 67.9, 56.0, and 53.3 mJ m^{-2} for the glass wafer, silicon wafer, and polyimide film, respectively. However, their subcomponent shares differed by each substrate. The polar component (σ_p) of the silicon wafer's SFE was 16.4 mJ m^{-2}, while the dispersive component (σ_d) was 39.6 mJ m^{-2}. For a much polar substrate, the glass wafer, its σ_p was higher at 28.5 mJ m^{-2}, while its σ_d was almost equal (39.4 mJ m^{-2}) to the silicon wafer. In contrast, the σ_p of the polyimide film was only 6.1 mJ m^{-2}, while the σ_d was 47.2 mJ m^{-2}, denoting the substrate's higher hydrophobicity compared to the other two substrates.

Likewise, we evaluated the surface characteristics of the prepared EVs. All the EVs were slightly hydrophilic ($\theta_{water} < 90°$), and their surface free energies were lower than the range of SFEs of the substrates: σ_{total} of 55.2, 48.7, 48.0, and 49.2 mJ m^{-2} for the Ali D23-, Aro(1,1) D23-, Aro(1,0) D26-, and Aro(0,1) D26_EV, respectively (**Table 5-2**). Since their SFEs were lower than those of substrates, the EV mixture resins were expected to be well-wetted on those substrates before cure and form a homogeneous adhesion interphase after cure. Especially the high ratio of σ_d/σ_p would result in a stronger adhesion to polyimide film and silicon wafer, which also have a higher fraction of the dispersive component.

Table 5-1. Measured contact angles and calculated surface free energies of silicon wafer, glass wafer, and polyimide film substrates.

Contact Angle (°)					
Silicon Wafer		**Glass Wafer**		**Polyimide Film**	
θ_{water}	θ_{DIM}	θ_{water}	θ_{DIM}	θ_{water}	θ_{DIM}
49.8	40.0	27.7	40.4	64.4	22.0
($\pm$ 2.6)	($\pm$ 0.5)	($\pm$ 1.3)	($\pm$ 1.4)	($\pm$ 4.9)	($\pm$ 2.1)

Surface Free Energy [mJ m^{-2}]								
Silicon Wafer			**Glass Wafer**			**Polyimide Film**		
σ_p	σ_d	σ_{total}	σ_p	σ_d	σ_{total}	σ_p	σ_d	σ_{total}
16.4	39.6	56.0	28.5	39.4	67.9	6.1	47.2	53.3

Table 5-2. Measured contact angles and calculated surface free energies of EVs.

Contact Angle (°)							
Ali D23_EV		**Aro(1,1) D23_EV**		**Aro(1,0) D26_EV**		**Aro(0,1) D26_EV**	
θ_{water}	θ_{DIM}	θ_{water}	θ_{DIM}	θ_{water}	θ_{DIM}	θ_{water}	θ_{DIM}
61.4	18.8	72.7	27.4	70.1	32.7	71.3	27.3
($\pm$ 1.5)	($\pm$ 1.0)	($\pm$ 1.8)	($\pm$ 1.1)	($\pm$ 1.8)	($\pm$ 2.6)	($\pm$ 1.4)	($\pm$ 0.8)

Surface Free Energy [mJ m^{-2}]											
Ali D23_EV			**Aro(1,1) D23_EV**			**Aro(1,0) D26_EV**			**Aro(0,1) D26_EV**		
σ_p	σ_d	σ_{total}	σ_p	σ_d	σ_{total}	σ_p	σ_d	σ_{total}	σ_p	σ_d	σ_{total}
7.1	48.1	55.2	3.4	45.3	48.7	4.9	43.1	48.0	3.9	45.3	49.2

2.1.2 Adhesion Performances of EV Encapsulants on the Substrates

Next, we evaluated the adhesion strengths of the EVs, which were used as an encapsulant, on the rigid substrates (silicon and glass wafer) using a die-shear method (MIL-STD-883). During the test, the tip of the instrument moved linearly and removed the adhered encapsulant from the substrate (**Figure 5-2a, b**). For the glass wafer, the EV encapsulants recorded lower die shear strength than that of Loctite Eccobond EO 7021, which is a filled epoxy encapsulant material. The adhesion strength of the commercial encapsulant was 19 N mm^{-2}, while the adhesion strengths of Ali D23_EV and Aro(1,1) D23_EV were 1.2 and 5 N mm^{-2}, respectively (**Figure 5-2c**). All the encapsulants showed adhesion failure, and no residue was left on the glass wafer after delamination (**Figure 5-2e**).

On the other hand, for a silicon wafer, the Aro(1,1) D23_EV recorded the highest adhesion strength of 12 N mm^{-2}, while the commercial encapsulant recorded an adhesion strength of 5.6 N mm^{-2} (**Figure 5-2d**). After the shear travel, the fracture surface of the Aro(1,1) D23_EV encapsulant ran along the silicon wafer, exposing detached layers of the silicon wafer (**Figure 5-2f**). The substrate failure of the silicon wafer is concrete evidence that the encapsulant can be a suitable material for a CoW application. Even though the surface of the silicon wafer became susceptible to shear force after mirror polishing, the other two encapsulants were unable to accomplish the substrate failure. This manifests the superior adhesion property of the Aro(1,1) D23_EV encapsulant towards a silicon wafer.
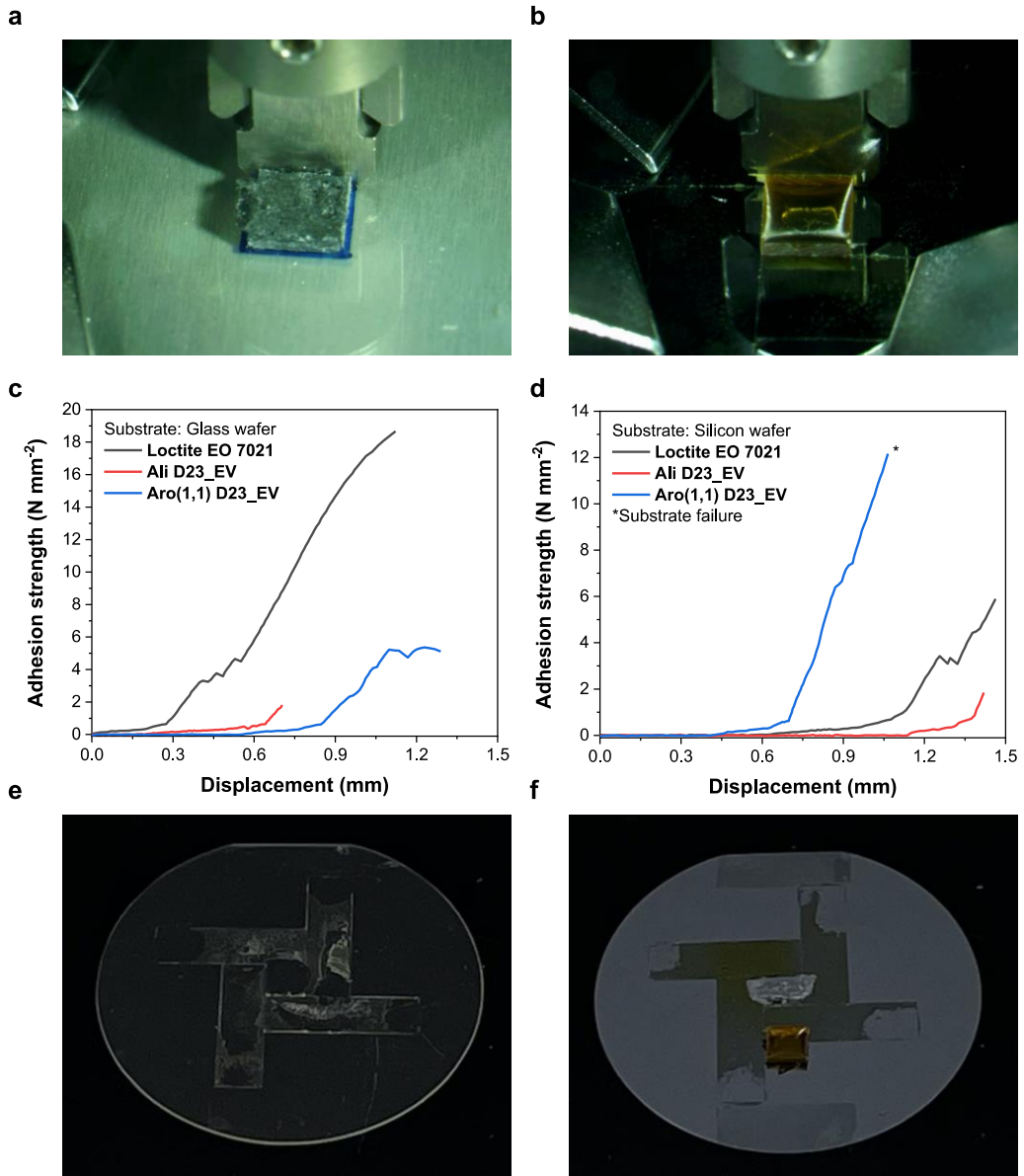
Figure 5-2. a Loctite Eccobond EO 7021 specimen on a glass wafer before the test. **b** Aro(1,1) D23_EV specimen on a silicon wafer. Die shear profiles of the encapsulants on a **c** glass wafer and **d** silicon wafer. **e** Ali D23_EV detached glass wafer after the test. **f** Aro(1,1) D23_EV sample detached silicon wafer after the test.

Additionally, we tested other EVs' adhesion performance on the substrates in the same manner (**Figure 5-3**). The Ali_EVs recorded higher adhesion strengths on a glass wafer and showed adhesion failures regardless of the type of substrate. The high fraction of σ_p of the Ali_EV (i.e., hydrophilicity) led to better adhesion to the polar glass substrate. Still, the recorded values were around 1-3 N mm^{-2}, which is not strong enough as a rigid encapsulant. In contrast, Aro(1,1)_EVs recorded higher adhesion strengths on a silicon wafer, and Aro(1,1) D17 and D23_EV encapsulants showed substrate failure on a silicon wafer. Moreover, the glass wafer with the Aro(1,1) D17_EV encapsulant did splinter after the test, which suggests a higher degree of adhesion strength than in the case of Aro(1,1) D23_EV. Some of the encapsulants (Aro(1,1) D26_EV and Ali D17_EV) left a partial residue on each substrate, denoting an interfacial failure (**Figure 5-3b, c**). In summary, the Aro(1,1) D17_EV and Aro(1,1) D23_EV encapsulants were best-fit for the CoW application.
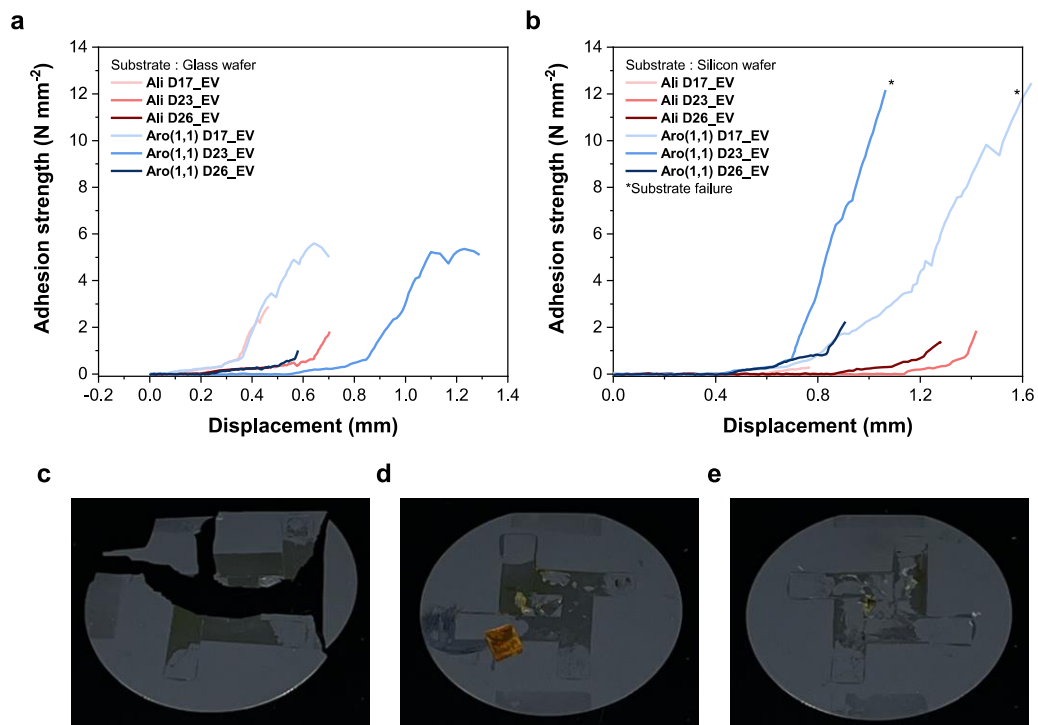
Figure 5-3. Die shear profiles of Ali D17-, 23-, and 26_EVs, and Aro(1,1) D17-, D23-, and 26_EVs on **a** a glass wafer, and **b** a silicon wafer. **c** Aro(1,1) D17_EV sample detached silicon wafer. **d** Aro(1,1) D26_EV sample detached silicon wafer. **e** Ali D17_EV sample detached silicon wafer.

For the soft encapsulation of the CoF application, it was unable to conduct the same die shear method because the polyimide substrate slipped upon shear stress. Instead, we performed T-peel tests to evaluate the adhesion properties of the soft encapsulants on a polyimide film. Each encapsulant was evenly coated on the flexible substrate with fixed bond-line dimensions: a width of 25 mm, a length of 114.5 mm, and a thickness of 50 μm. The representative T-peel profiles exhibited characteristics of micro-cracks, so the peak values along the bond-line length were averaged to obtain the peel strength (**Figure 5-4**). The calculated average peel strength of the PDMS encapsulant was below 0.1 N mm^{-1}, while the EV encapsulants recorded much higher values: Aro(1,0) D26_EV: 1.0 N mm^{-1}; Aro(1,0) D26_EV + cat.: 1.3 N mm^{-1}; Aro(0,1) D26_EV: 1.6 N mm^{-1}; Aro(0,1) D26_EV + cat.: 1.3 N mm^{-1}. All the encapsulants showed adhesive failures while leaving patchy strips on the substrate. The Aro(0,1) D26_EV, which has a larger portion of σ_d over σ_p than that of the Aro(1,0) D26_EV, recorded a higher adhesion strength towards the hydrophobic polyimide substrate. It appeared that the addition of the catalyst did not bring any harmful effects on the encapsulant's adhesion property. In summary, the Aro(0,1) D26_EV and Aro(0,1) D26_EV + cat. encapsulants showed better adhesion performance for the CoF application.
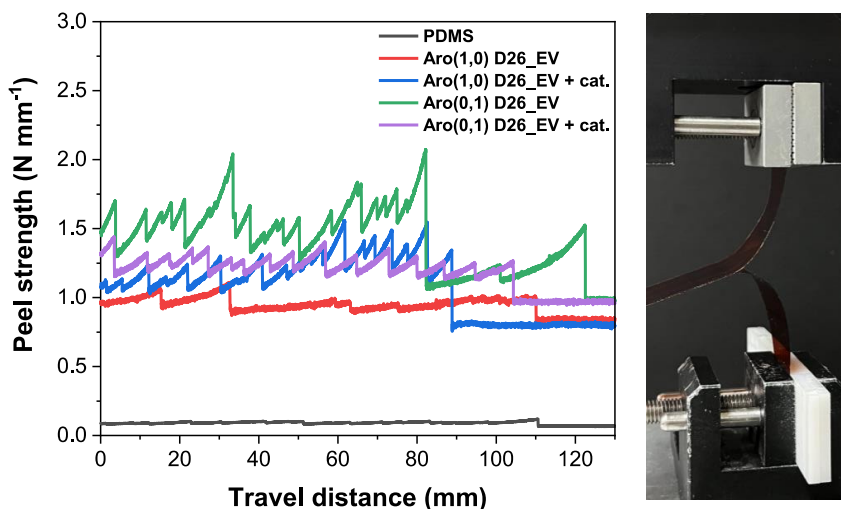
Figure 5-4. Representative T-peel profiles of the soft encapsulants on a polyimide film.

2.2 Warpage Reduction by the Rigid Epoxy Vitrimer Encapsulation

2.2.1 Warpage Tests

In the previous sections, we presented EV systems capable of rapid stress-relaxation by dissipating external stimuli via crosslink rearrangements. However, like other research on vitrimers, it needs to be fully verified whether the material makes a real difference in practical applications, such as in semiconductor packaging production, which is the case for our research. One of the critical issues in wafer-level packaging technology is substrate warpage development, which mainly originates from the stress of shrinkages of packaging materials during curing and cooling. Among the many materialistic factors contributing to warpage, the elastic modulus of a packaging material and the CTE mismatch between a polymeric material and an inorganic substrate are decisive. Under the guidance of material characteristics, manufacturers adopt a packaging material with a low degree of CTE (< 30 ppm K^{-1}) to prevent process-driven shrinkage as low as possible. However, in concept, the approach only minimizes the impending stresses from both the curing and cooling stages, which also has limitations and contributes little to reducing the warpage that has already taken place by numerous external stimuli.

Moreover, packaging processes inflict thermal or mechanical stresses on an assembly. Hence, to validate a new material's usefulness in the semiconductor packaging process, the material shall be designed to confront all sorts of stress squarely, no matter where the stress may come from during production. Bearing this purpose in mind, we envisioned that EV encapsulants fall into the functional material category, capable of stress-relaxation by themselves, and thus initiatively reduce warpage.

To demonstrate the superiority of the developed encapsulant, we designed a simple warpage-inducing test on three types of substrates: a silicon wafer, a glass wafer, and a polyimide film (**Figure 5-5a**). After coating a liquid encapsulant mixture on a substrate, it

generates shrinkage stresses through curing (at 180°C) and cooling (from 180 to 25°C) steps, which induce a concave warpage in the end (**Figure 5-5b**). Then, we measured local height values from 17 spots on the warped substrate and plotted a contoured surface to manifest warpage (**Figure 5-5c**). In the test design, we only measure the final deformation in the *z*-axis without differentiating whether the strain originates from curing shrinkage or cooling shrinkage.

For example, we selected a reference rigid encapsulant called DICY-cured (namely, DGEBA cured by dicyandiamide) and tested it on the three substrates in the same manner. As a result, the DICY-cured encapsulant induced a significant degree of warpage regardless of the substrate types (**Figure 5-5d, e**). This indicates that the DICY-cured rigid encapsulant could not dissipate the applied stresses during chemical and hot shrinkages. The substrate that was most warped was a polyimide film (maximum warpage of 5.98 mm), which is to be expected due to its low modulus and thickness compared to the other substrates. Warpage occurs more easily for substrates with low flexural moduli and thin profiles (Lau, *et al.*, 2017). Considering the moduli and thicknesses of the silicon and glass wafers (**Table 5-3**), it is natural that the maximum warpage decreased in the silicon wafer (3.83 mm) and further in the glass wafer (1.27 mm). Additionally, it should be noted that the obtained warpage profiles of the substrates showed a single-axisymmetric or asymmetric distribution. This can be attributed to various factors such as an encapsulant's dispensing uniformity, flowability at a high temperature, and non-uniform degree of conversion throughout the material on a substrate.

In wafer-level-packaging, a warpage value below 0.5 mm after a post-mold-curing process is tolerable for a 300 mm wafer to proceed with subsequent RDL fabrication (Lau, *et al.*, 2018). Since we use 50 mm wafers in our assembly production, the tolerable warpage limit should be much lower in our design.

Table 5-3. Geometric and mechanical properties of the molded substrate assembly.

	Thickness	Density	E' at r.t.	Poisson's ratio	CTE
	[mm]	[g cm^{-3}]	[GPa]	[-]	[ppm K^{-1}]
Substrates					
Silicon wafer[a]	0.3	2.4	110	0.28	3
Glass wafer[a]	0.5	4.5	200	0.3	10
Polyimide film[a]	0.15	1.4	3	0.35	35
Encapsulants					
DICY-cured	0.2	1.2	2.5		
NVE	0.2	1.13	1.2	0.5[b]	See **Figure 4-9**
Ali D23_EV	0.2	1.17	1.1		
Aro(1,1) D23_EV	0.2	1.21	1.6		

[a]The substrates' properties are given by the supplier.

[b]For unfilled thermosets, the value was assumed to 0.5 as like an incompressible rubber.

a Silicon wafer (T = 0.3 mm) Glass wafer (T = 0.5 mm) Polyimide film (T = 0.15 mm)

b Coating → Curing → Cooling

"Concave Warpage" (smiling face)

c Height measuring spots

2.5 cm
1.25 cm

d

e
DICY-cured, Silicon wafer
DICY-cured, Glass wafer
DICY-cured, Polyimide film

Z-height (mm)

Max. Warpage: 3.83 mm Max. Warpage: 1.27 mm Max. Warpage: 5.98 mm
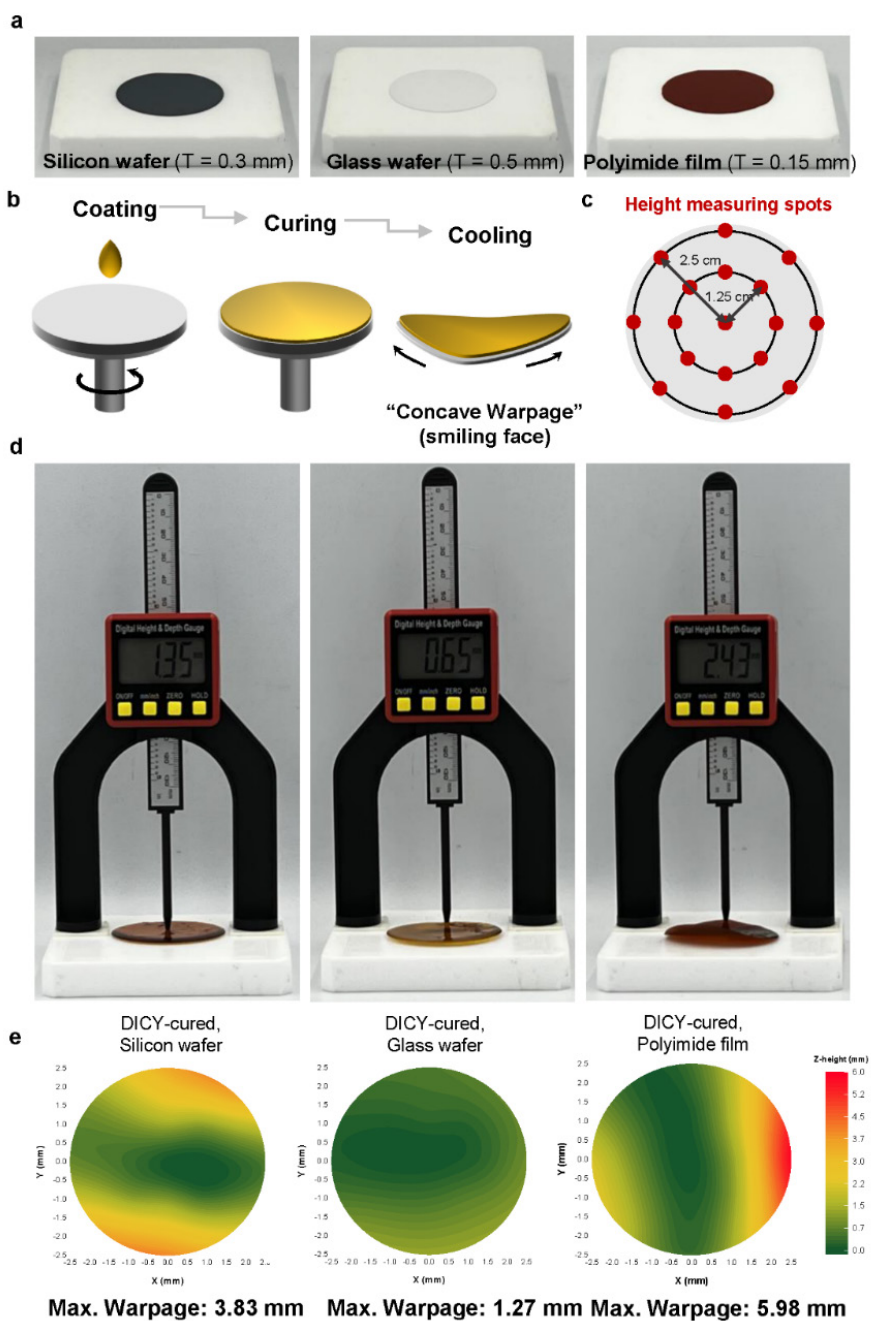
Figure 5-5. a Substrates before encapsulating. **b** A warpage test procedure. **c** Height measuring spots for testing specimens. **d** Photographs of warpage measuring for each encapsulated substrate; silicon wafer (left), glass wafer (middle), and polyimide film (right). **e** Contour plots of warped surfaces, encapsulated by DICY-cured epoxy.

Similarly, we tested seven encapsulants, including EV encapsulants, on the three substrates. The NVE encapsulant resulted in the highest z-strains for all substrates, and the maximum height value was set as the leveling standard for each substrate. The NVE-encapsulated silicon wafer deformed into a symmetrical concave surface with a maximum warpage of 1.38 mm (**Figure 5-6b**). On the contrary, when we applied the EV encapsulants to the silicon wafer, the maximum warpage values were immensely reduced to 1.05 (Ali D23_EV) and 0.11 (Aro(1,1) D23_EV) (**Figure 5-6c, f**). Since the NVE and Ali D23_EV share almost the same chemical composition except for a dynamic component (i.e., ethyl acetoacetates), the reduction in warpage can be attributed to the stress-relaxation characteristic of the covalent adaptable networks. Therefore, it is also understandable that the Aro(1,1) D23_EV encapsulant, which shows better stress-relaxation capability than the Ali D23_EV, resulted in a much lower warpage and better planarity. Moreover, the higher adhesion performance of the Aro(1,1) D23_EV encapsulant over Ali D23_EV toward a silicon wafer might contribute to the substrate's evenness and flatness.

The epoxy encapsulants containing 10 wt% of inorganic filler resulted in much lower warpage values compared with the ones without filler; maximum warpage: 0.67 mm (Ali D23_EV + filler) and 0.07 mm (Aro(1,1) D23_EV + filler) (**Figure 5-6d, g**). This is the conventional approach to reduce warpage, curtailing the CTE mismatch between the packaging material and the substrate. In fact, by the addition of the filler, the CTE values of Ali D23_EV and Aro(1,1) D23_EV were reduced by 33% and 27%, respectively, at the same temperature (**Figure 5-10c, d**). Additionally, the stress-relaxation properties of the filled encapsulant seemed to be unchanged by the introduction of the filler (**Figure 5-9a, b**). Thus, the reductions in warpage for the filled encapsulant can solely be ascribed to the effect of the CTE decrease of the material. Meanwhile, the additional administration of 0.5 mol% of a SIL catalyst showed further decreased warpages to 0.35 and 0.05 mm for the assembly using Ali D23_EV + filler + cat. and Aro(1,1) D23_EV + filler + cat. encapsulants, respectively (**Figure 5-6e, h**). As stated in chapter 4, the SIL catalyst accelerates dynamic exchange reactions within the network, facilitating crosslinked network reorganization. By the effect, the inclusion of the catalyst enhances the stress-relaxation capability of the EV

encapsulants (**Figure 5-9a, b**), which, in turn, contributes to effectively dissipating the developed stress within the assembly. Considering an exaggerated thick profile (0.5 mm) of the coating layer compared to a layer thickness of a practical encapsulant (a few dozen μm), the assembly using Aro(1,1) D23_EV + filler + cat. encapsulant has the potential to accomplish zero warpage when applied in a proper thickness.
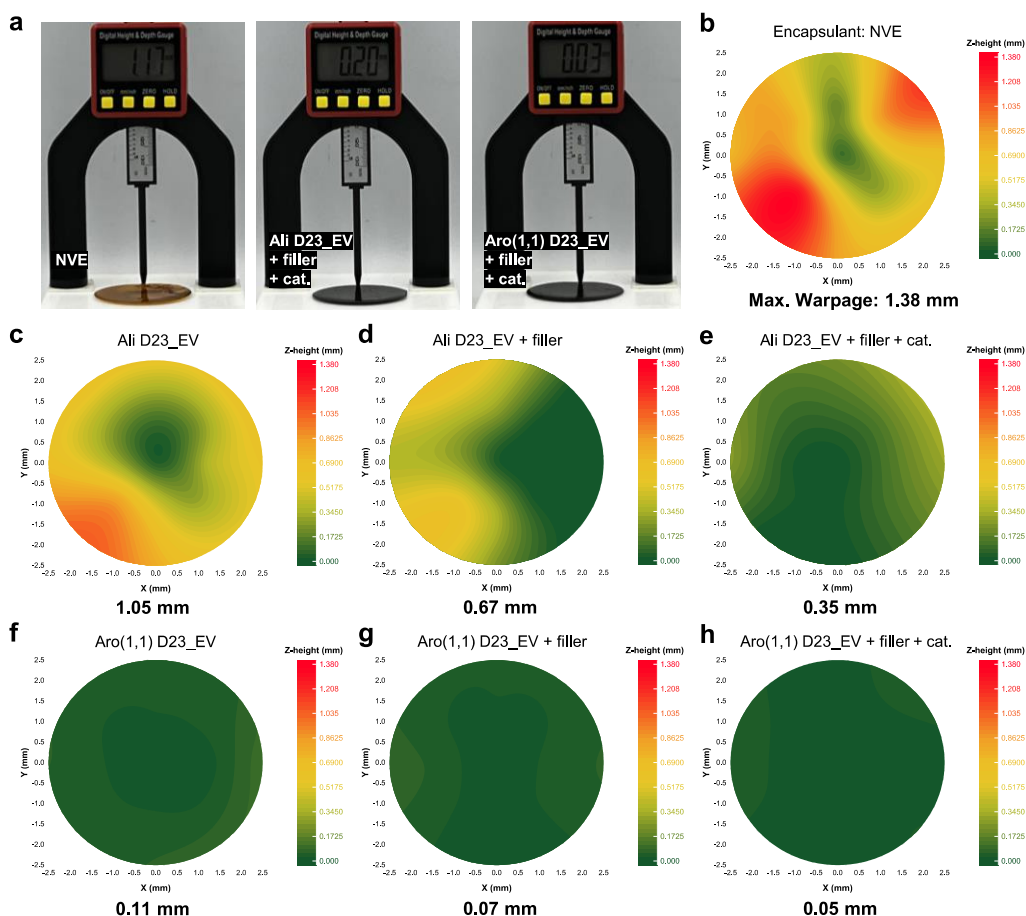
Figure 5-6. a Measuring warpage of silicon wafers (thickness = 0.3 mm) encapsulated with NVE, Ali D23_EV + filler + cat., and Aro(1,1) D23_EV + filler + cat. (**b-h**) Contour plots of warped silicon wafers, encapsulated by NVE and the epoxy vitrimers with and without filler or catalyst.

Likewise, we evaluated warpage in a glass wafer for the same encapsulants. As a frequently used RDL interposer, a glass wafer is required to maintain a low profile in FOWLP. The maximum warpage of the glass wafer using the NVE encapsulant was 1.27 mm, lower than the case of the silicon wafer using the same encapsulant. As predicted from the substrate's higher E' and thickness, the overall warpage values were lower than the value obtained from the silicon wafer coated with the same encapsulant. The effects of filler and catalyst addition also held true for the substrate. Just as in the silicon wafer, the Aro(1,1) D23_EV series also resulted in better warpage performance in the glass wafer.
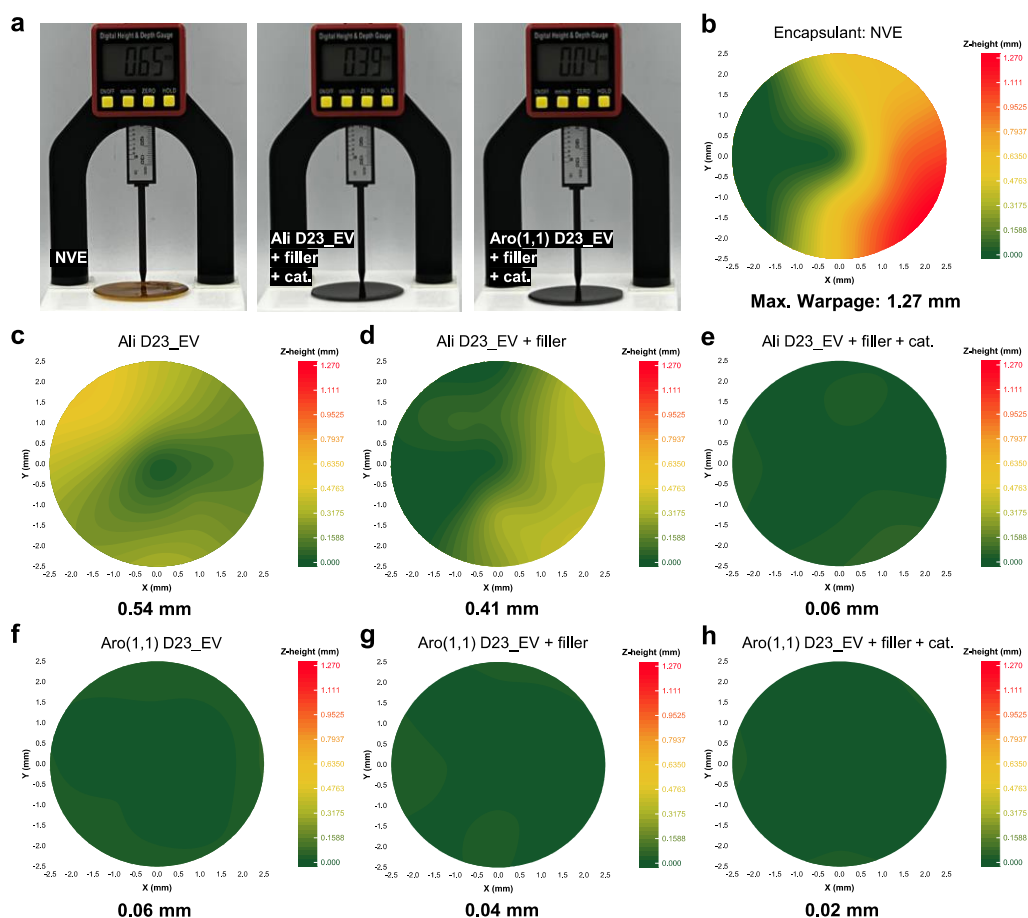
Figure 5-7. a Measuring warpage of glass wafers (thickness = 0.5 mm) encapsulated with NVE, Ali D23_EV + filler + cat., and Aro(1,1) D23_EV + filler + cat. (**b-h**) Contour plots of warped glass wafers, encapsulated by NVE and the epoxy vitrimers with and without filler or catalyst.

Lastly, we performed the same test on a polyimide film. Unlike the former substrates, the polyimide film spontaneously warps into a concave arc even without being touched due to its innate flexibility. Thus, the obtained warpage values were overestimated and are of little practical significance. Nonetheless, even for the polyimide substrate, the EV encapsulants were effective in reducing warpage. Additionally, the introduction of the catalyst had a positive effect on the substrate. However, the CTE reduction effect of the filler addition does not seem valid due to the relatively low CTE mismatch for the substrate.
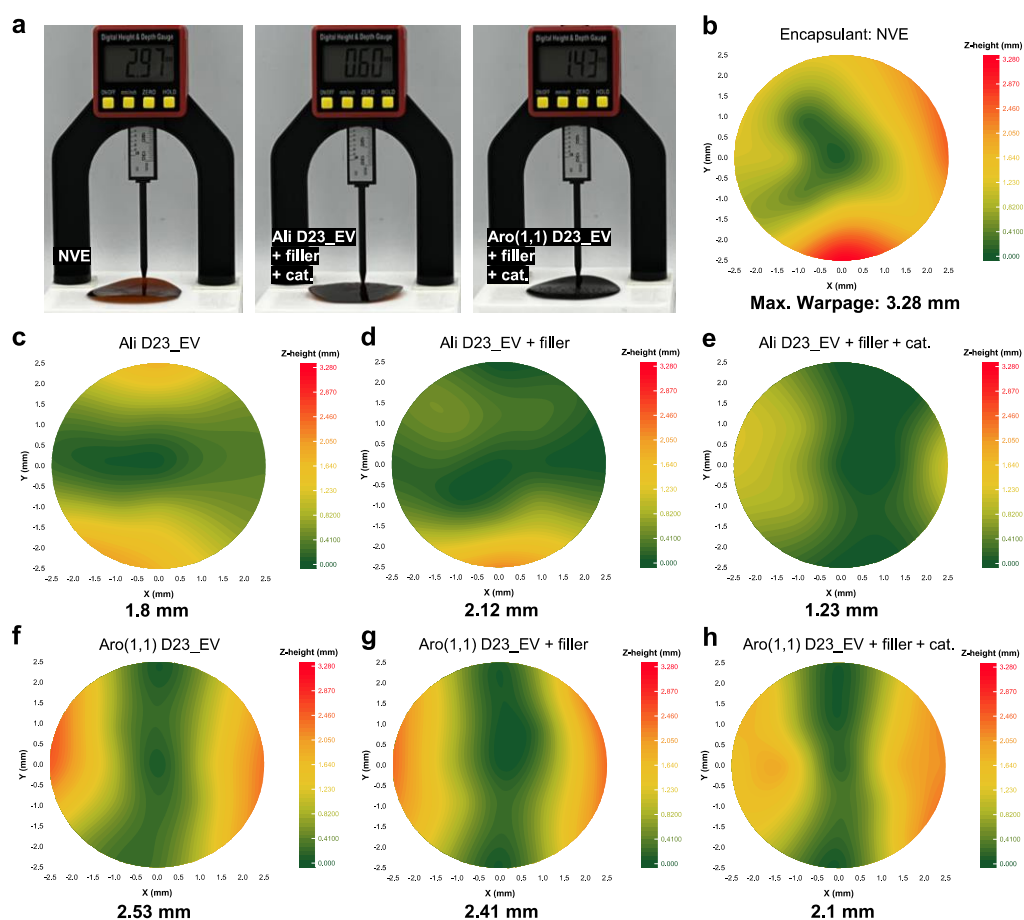
Figure 5-8. a Measuring warpage of the polyimide films encapsulated with NVE, Ali D23_EV + filler + cat., and Aro(1,1) D23_EV + filler + cat. (**b-h**) Contour plots of warped polyimide films, encapsulated by NVE and the epoxy vitrimers with and without filler or catalyst.
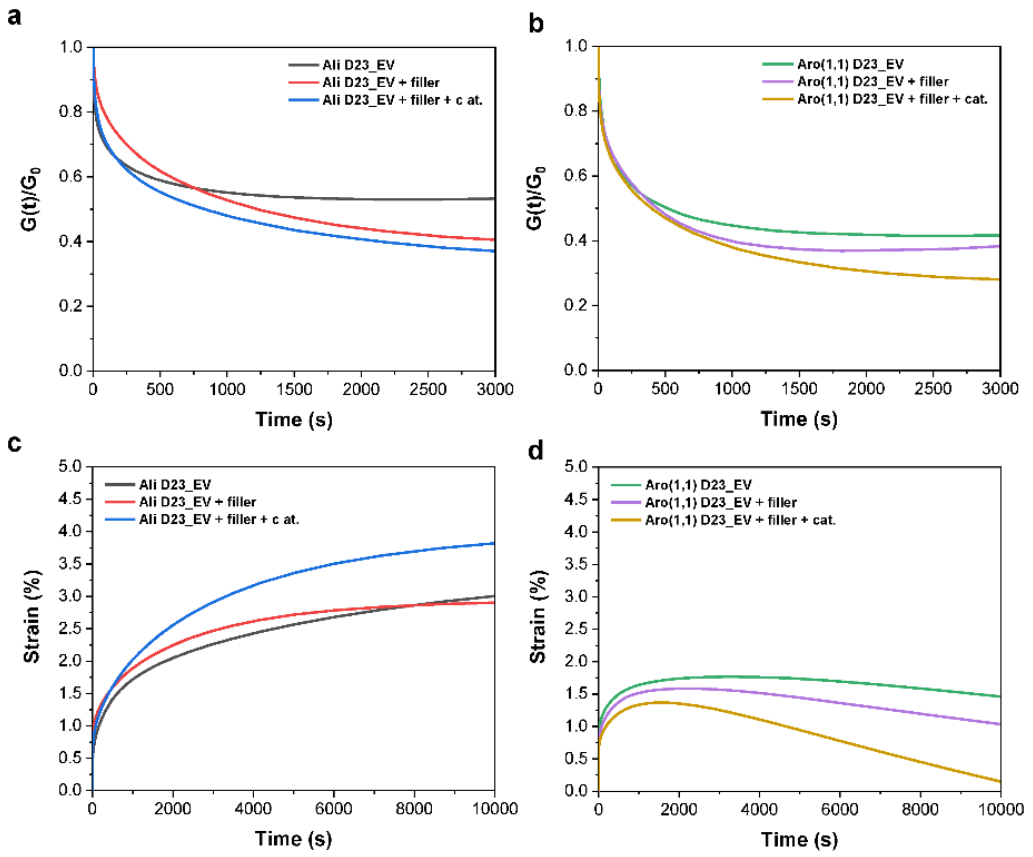
Figure 5-9. Stress-relaxation curves of **a** Ali D23_EV, Ali D23_EV + filler, and Ali D23_EV + filler + cat., and **b** Aro(1,1) D23_EV, Aro(1,1) D23_EV + filler, and Aro(1,1) D23_EV + filler, cat. Creep curves of **c** Ali D23_EV, Ali D23_EV + filler, and Ali D23_EV + filler + cat., and **d** Aro(1,1) D23_EV, Aro(1,1) D23_EV + filler, and Aro(1,1) D23_EV + filler + cat.

2.2.2 Stress Dissipation by the EV Encapsulants

What is most amazing about the warpage reduction by the EV encapsulant is that the material has CTE values of about 50 ppm °C^{-1} at 25°C and 150-200 ppm °C^{-1} at 150°C (**Figure 5-10**), which are almost 5-10 times greater than those of a commercial silica-filled epoxy molding compound (CTE 1 ~ 5 ppm °C^{-1}; CTE 2 ~ 50 ppm °C^{-1}). With this high CTE, the resulting CTE mismatch between an encapsulant and a substrate would impose an enormous stress build-up on an assembly, enough to induce warpage, as much as in the cases of using DICY-cured and NVE encapsulants. As stated in chapter 1, the stress build-up within a packaging assembly depends on many parameters, including E', CTE, T_g of the encapsulant and adherend, curing and operation conditions, and bondline thickness. We can adapt the equation 1-2 by excluding common parameters and substituting the proper parameters used in the test.

$$\sigma_{sub} = \varepsilon_{encap} \times E'_{encap} = \int_{T=25°C}^{T=180°C} [(\alpha_{encap} - \alpha_{sub}) \times E'_{encap}]\, dT \quad \text{(Equation 5-1)}$$

where σ_{sub} is the stress on a substrate, ε_{encap} is the strain of an encapsulant, E'$_{encap}$ is the storage modulus of an encapsulant, α_{encap} and α_{sub} are the CTE of an encapsulant and substrate, respectively, and dT is the temperature difference.

In the meantime, the residual bending stress applied on a substrate by the deformation of encapsulant can be reversely calculated from the obtained warpage by adapting the equation 1-1.

$$\sigma_{residual} = K \frac{E'_{encap}\, t_{encap}}{2\gamma R} \quad \text{(Equation 5-2)}$$

where $\sigma_{residual}$ is the residual bending stress of an assembly, t_{encap} is the thickness of an encapsulant, γ is Poisson's ratio, R is the radius of curvature, and K is the geometric parameter.

Merging the equations, we can obtain the dissipated stress by an encapsulant:

$$\sigma_{dissipated} = \sigma_{sub} - \sigma_{residual} \qquad \text{(Equation 5-3)}$$

The parameters related to the encapsulants and calculated stress values are presented in **Table 5-4** and **Table 5-5**.
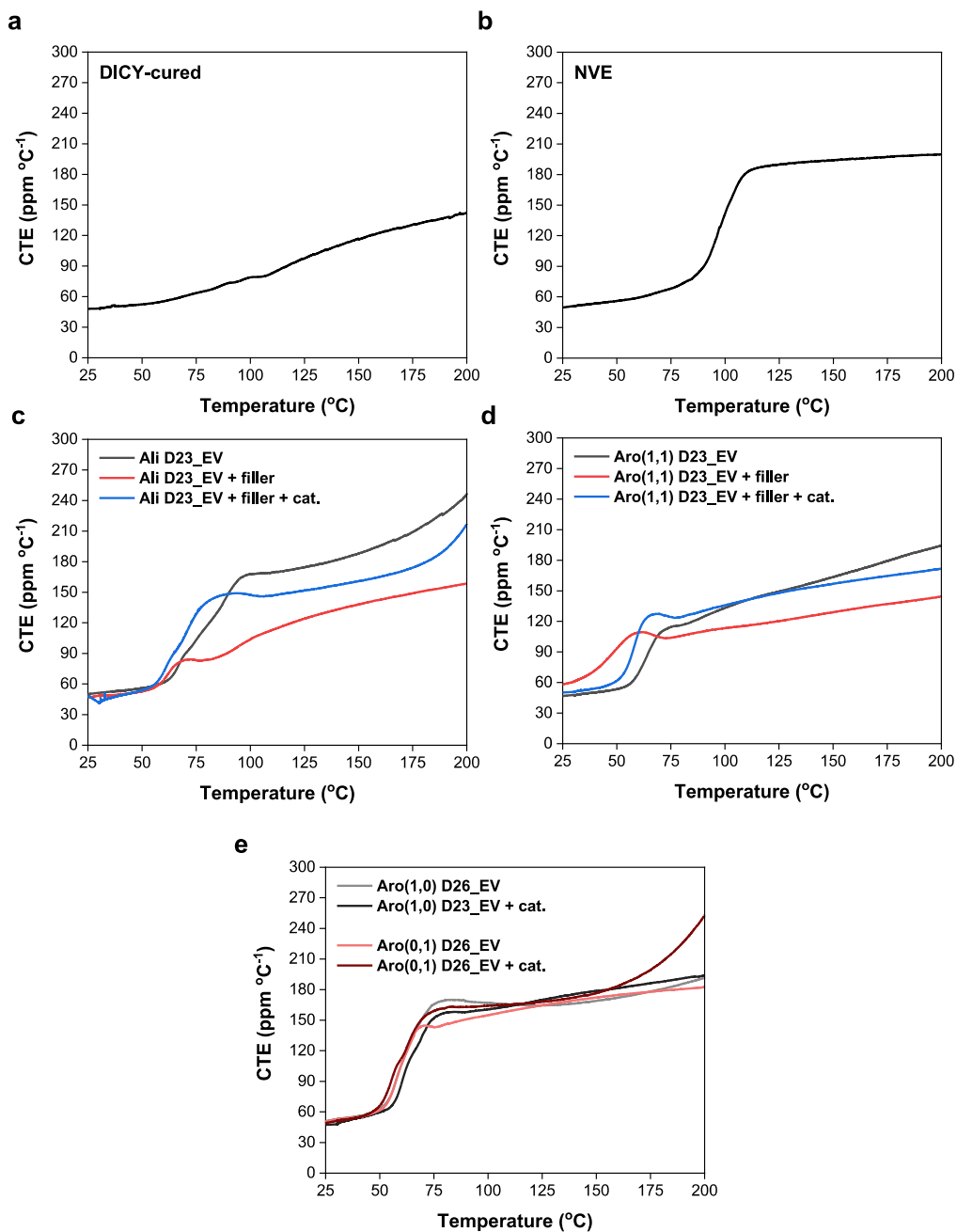
Figure 5-10. Thermal expansion curves of **a** NVE, **b** DICY-cured, **c** Ali D23_EVs, **d** Aro(1,1) D23_EVs, and **e** Aro(1,0) D26_EVs and Aro(0,1) D26_EVs.
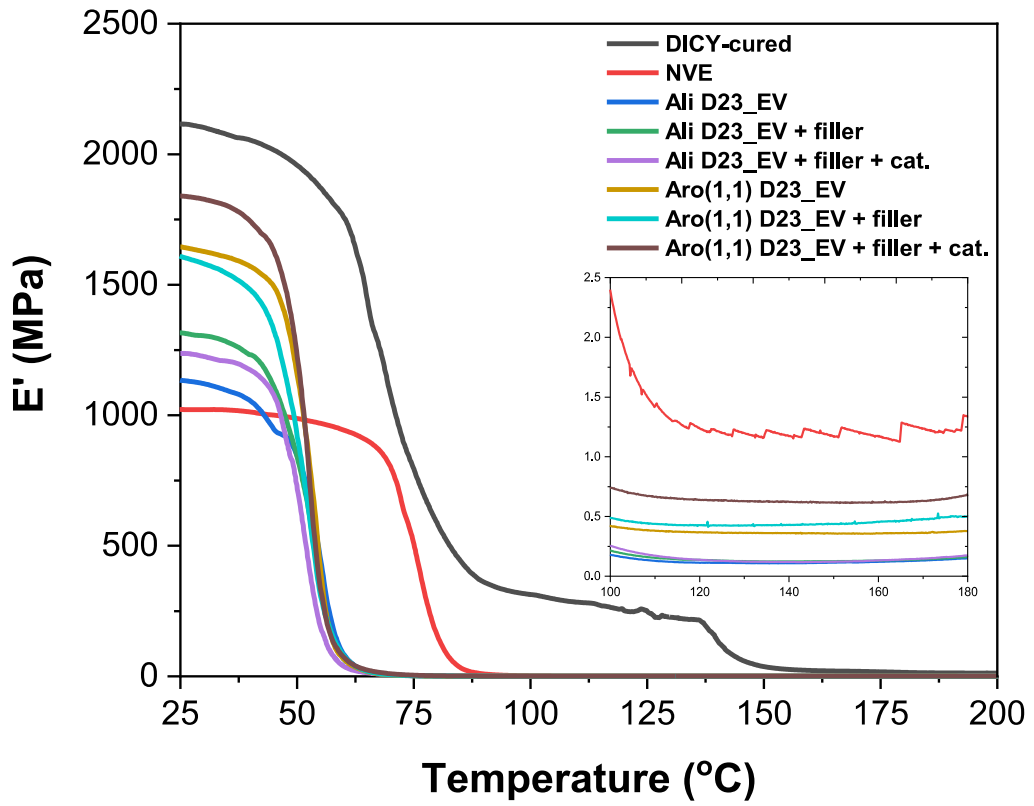
Figure 5-11. Elastic moduli of the encapsulants used in the warpage test.

Table 5-4. Parameters for calculating stress dissipation by encapsulants on silicon wafers.

	E' at 25°C [MPa]	CTE at 25°C [ppm °C⁻¹]	ΔT [°C]	σ_{sub} [MPa]	Film thickness [mm]	Poisson ratio	Radius of curvature [mm]	$\sigma_{residual}$ [MPa]	$\sigma_{dissipated}$ [MPa]
DICY-cured	2116	47.7		6.35	0.195		2.73	5.03	1.31
NVE	1022	49		2.72	0.185		2.95	2.13	0.59
Ali D23_EV	1133	49.7		1.60	0.189		3.5	0.87	0.73
Ali D23_EV + filler	1315	25		1.65	0.211		5.0	0.92	0.73
Ali D23_EV + filler + cat.	1236	48	155	1.47	0.206	0.5	9.1	0.56	0.91
Ali D23_EV	1645	53		2.4	0.201		28.5	0.23	2.18
Ali D23_EV + filler	1608	46		2.0	0.208		44.7	0.15	1.87
Ali D23_EV + filler + cat.	1839	49		2.7	0.205		62.5	0.12	2.55

Table 5-5. Parameters for calculating stress dissipation by encapsulants on glass wafers.

	E' at 25°C [MPa]	CTE at 25°C [ppm °C^{-1}]	ΔT [°C]	σ_{sub} [MPa]	Film thickness [mm]	Poisson ratio	Radius of curvature [mm]	$\sigma_{residual}$ [MPa]	$\sigma_{dissipated}$ [MPa]
DICY-cured	2116	47.7		5.55	0.224		3.09	5.10	0.45
NVE	1022	49		2.37	0.202		3.09	2.22	0.15
Ali D23_EV	1133	49.7		1.38	0.194		6.06	0.56	0.82
Ali D23_EV + filler	1315	25		1.41	0.197		7.83	0.66	0.75
Ali D23_EV + filler + cat.	1236	48	155	1.24	0.204	0.5	52.1	0.10	1.15
Ali D23_EV	1645	53		2.10	0.205		52.1	0.13	1.97
Ali D23_EV + filler	1608	46		1.73	0.207		78.1	0.09	1.65
Ali D23_EV + filler + cat.	1839	49		2.32	0.204		156.3	0.05	2.27

We calculated ratios of dissipated stress over total stress for the encapsulated substrates in the warpage test and compared them according to each encapsulant (**Figure 5-12**). The ratio is directly associated with the ability of an encapsulant to dissipate stress. As expectedly, the two species of non-vitrimer encapsulants (namely, DICY-cured and NVE) recorded ratios of about 20% and 8% for the silicon and glass wafers, respectively. It is noticeable that the encapsulants' abilities of stress dissipation are on par, regardless of their differences in CTE and E'. The adoption of the same DGEBA resin might be the reason for this.

On the contrary, the EV encapsulants displayed an enhanced ability of stress dissipation on both substrates. Thanks to their excellent stress-relaxation capability, the stress buildup within each assembly can be nullified. The Ali D23_EV series recorded a ratio between 40-60% on a silicon wafer and 50-90% on a glass wafer. It can be ascribed to the encapsulants' higher affinity ($\sigma_p \sim 7.1$ mJ m^{-2}) toward a polar glass substrate. On the other hand, the Aro(1,1) D23_EV series resulted in a much higher ratio, above 90%, irrespective of substrates, because they showed a good high adhesion on both substrates.

Additionally, the effects of additives are worthy of notice. Controversially, the addition of inorganic filler did not enhance the ability of stress dissipation as opposed to the expectation in industrial fields. The filler addition impacts the reduction in CTE and the increase in E', whose effects effectively cancel each other out, resulting in a negligible change or slight reduction in the encapsulant's ability to dissipate stress. On the contrary, the addition of SIL catalyst showed a linear proportional relation with the increment of the ratio for Ali D23_EV + filler and Aro(1,1) D23_EV + filler encapsulants. By incorporating the catalyst to accelerate the dynamic exchange reaction, the filled encapsulants restored their stress-relaxation capability, as depicted in **Figure 5-9**, which directly contributed to the stress dissipation within assemblies.
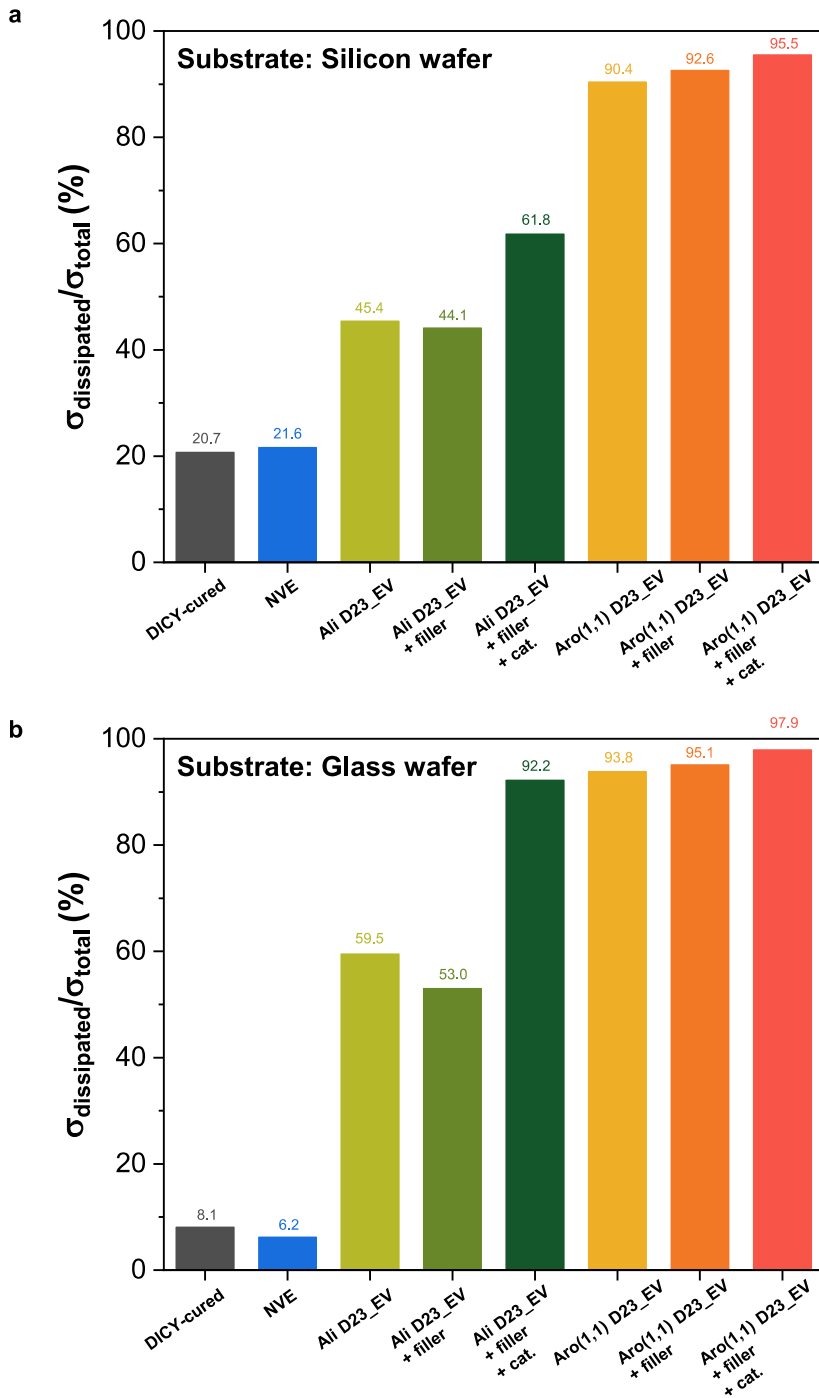
Figure 5-12. Ratios of dissipated stress over total stress of assemblies on **a** a silicon wafer and **b** a glass wafer.

2.3 Conformability of the Soft Epoxy Vitrimer Encapsulation

2.3.1 Deformation of Soft Encapsulants on a Polyimide Film

To confirm the applicability of the soft EV encapsulant in the CoF application, we prepared a structure consisting of an encapsulant and a polyimide substrate and conducted multiple deformation tests (bending and twisting). PDMS was selected as the reference encapsulant, while Aro(0,1) D26_EV, which recorded the highest adhesion strength toward the polyimide substrate, was selected as the soft EV encapsulant.

After 100 cycles of bending and stretching on a heating block at 160°C (**Figure 5-13a**), the PDMS encapsulant remained intact thanks to its softness (**Figure 5-13b**). Likewise, after 100 twists (**Figure 5-13e**), the PDMS-encapsulated polyimide substrate showed no particular defect and no warpage at both ends of the strip, indicating that the stress developed from the deformation had been completely dissipated (**Figure 5-13f**).

In contrast, the Aro(0,1) D26_EV encapsulant revealed a striking defect on its surface after the multiple bending test (**Figure 5-13c**). The wave pattern of the encapsulant developed due to the accumulated strain mismatch between the deformation of the encapsulant and the substrate during multiple deformations. When the material fails to dissipate the interfacial stress instantaneously, the residual stress applies to both the encapsulant and the substrate, resulting in local plastic deformation. For this reason, the Aro(1,0) D26_EV-encapsulated polyimide film showed a considerable amount of warpage after the twisting test (**Figure 5-13g**). On the other hand, with the small addition of SIL catalyst in the EV system, the surface defects and warpage issues were neatly resolved (**Figure 5-13d and h**).
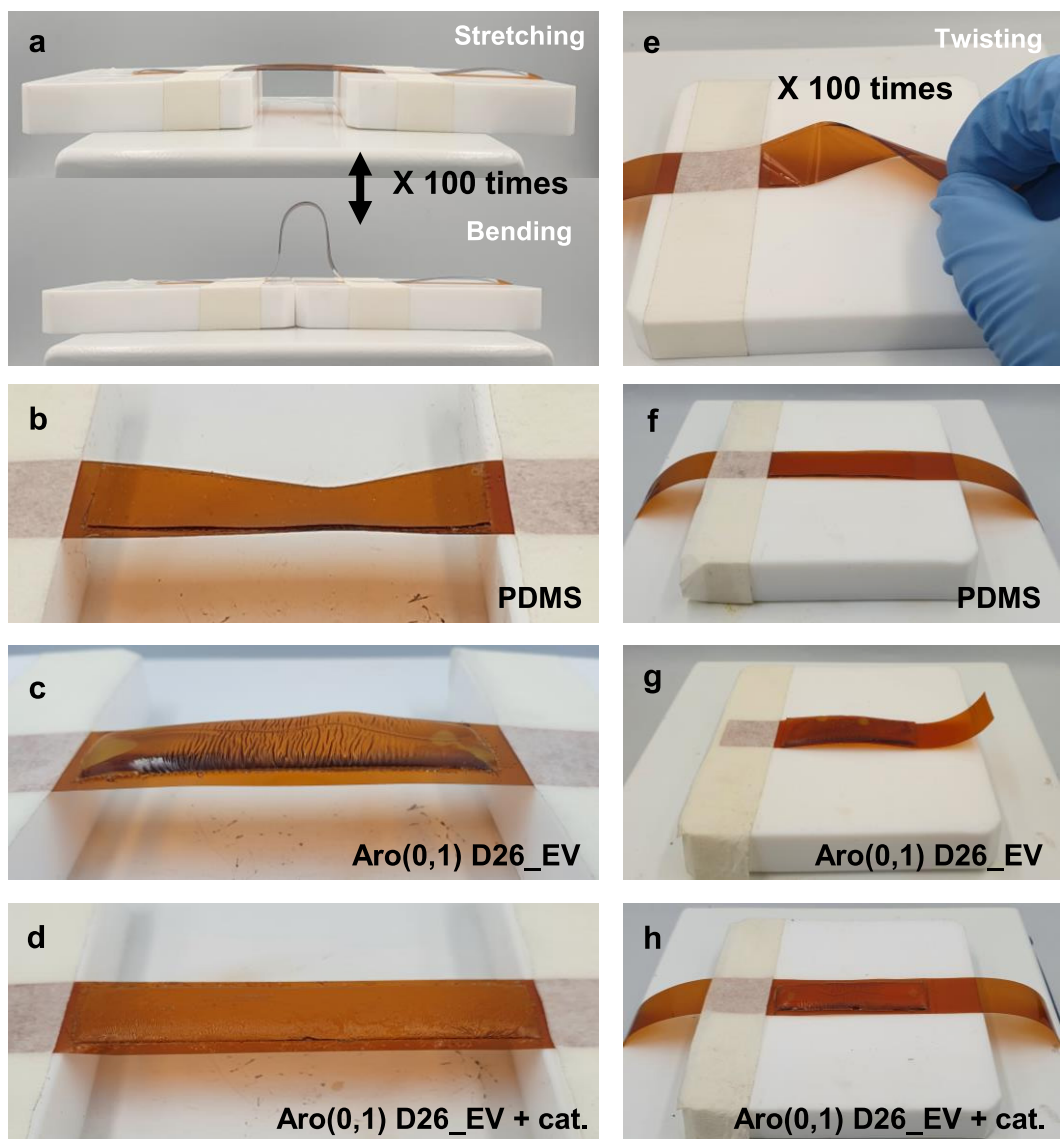
Figure 5-13. a A multiple bending test set and encapsulants after the test; **b** PDMS; **c** Aro(0,1) D26_EV; and **d** Aro(0,1) D26_EV + cat. **e** A multiple twisting test set and encapsulants after the test; **f** PDMS, **g** Aro(0,1) D26_EV, and **h** Aro(0,1) D26_EV + cat.

The effect of the SIL addition can be attributed to the accelerated dynamic exchange reaction within the crosslinked network of the EV encapsulant. This enhances the stress-relaxation characteristic of the material. For example, a much higher dosage of 2 mol% of [$Zn_{0.5}$(G4)]TFSI in the Aro(0,1) D26_EV system resulted in a drastic reduction in the characteristic relaxation time (τ^*) from 730 s to 20 s. The fast SR EV, i.e., the catalyzed encapsulant, survived 100 bending cycles and left no damage throughout the structure (**Figure 5-14**). In contrast, the slow SR EV, i.e., the uncatalyzed encapsulant, exhibited a bumpy layout and left ripple marks on its surface. The fast stress-relaxation afforded macroscopic topology rearrangements in series, contributing to the material's conformability to accommodate the repeating viscoelastic strain and stress at the interface between the encapsulant and substrate during the multiple deformations. In summary, for the CoF application, an encapsulant's stress-relaxation capability should be maximized via the addition of the SIL catalyst to cope with the rapid deformation of surroundings.
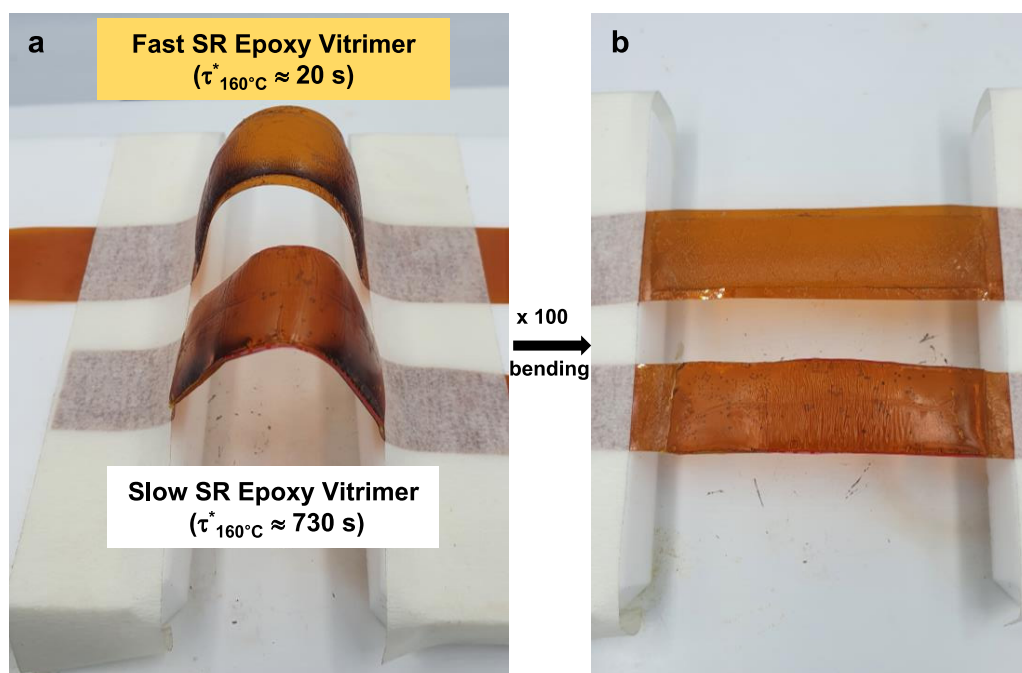
Figure 5-14. a Bending test on the fast SR and slow SR EV strips. **b** The samples after 100 times of bending.

In addition to the CoF application, we further applied the soft encapsulant on a flexible printed circuit board. A simply layered electronics package consisting of an encapsulant, an IC chip, and an FPCB was fabricated and integrated after epoxy curing. For the sake of comparison, three types of encapsulants were selected: NVE (a normal epoxy), PDMS (a reference soft encapsulant), and an EV containing 2 mol% of $[Zn_{0.5}(G4)]TFSI$. One end of the encapsulated substrate was taped to a fixed stage, and the other end was taped to a moving stage where the initial gap was 6 cm. Next, the specimen was pushed by a 500 g pendulum and held at the moved position. Finally, the specimen reverted to a relaxed state by removing the pendulum (**Figure 5-15a**). The heating plate at the bottom plane during the experiment was maintained at 100 °C to facilitate topology rearrangement.

At the bent state during the procedure, it is noteworthy that the specimen encapsulated with the EV bent greatly under pressure and yielded a radius curvature of 2.5 cm from the baseline close-up images of each encapsulant obtained (**Figure 5-15a, 2**). At this stage, close-up images of the deformed plane of each specimen exhibited definite differences in their reaction to compression (**Figure 5-15b**). A specimen encapsulated with NVE could not be retracted or deformed due to its high elastic modulus, which is generally anticipated for rigid epoxies. Only the edge of the polyimide strip, where no encapsulant had been applied, folded perpendicularly to the capped plane. On the contrary, the PDMS-encapsulated specimen was readily deformed upon stress. However, critical adhesive failure of PDMS on the FPCB surface occurred owing to its low effective modulus and weak adhesion. For the last group, the specimen, encapsulated with the EV + cat., successfully conformed to the deformation without adhesion failure, exhibiting a perfect encapsulation performance. Along with the supreme stress-relaxation capability, the strong adhesion property of the EV encapsulant to a PI substrate enabled the encapsulation even for the curved surface.
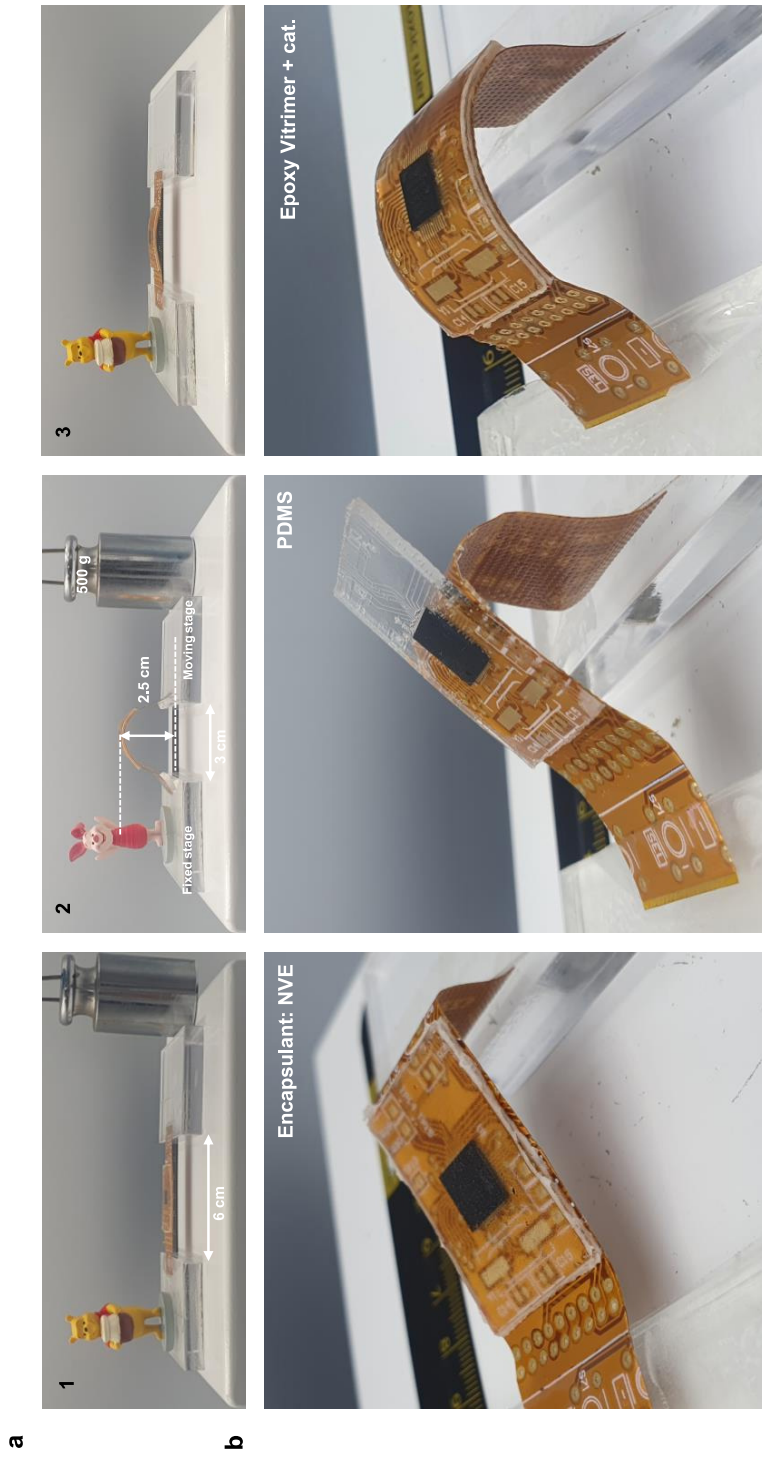
Figure 5-15. a Deformation test procedure: 1) Before test; 2) Deformation by pushing a pendulum; 3) Relaxation after removing the pendulum. **b** Bent state of the FPCB, encapsulated with NVE (left), PDMS (middle), and EV + cat. (right).

2.4 Selective Removal of the Epoxy Vitrimer Encapsulants

As a final benefit of an EV encapsulant, we demonstrated that it was able to selectively remove the encapsulants without damaging chip interconnections and the printed circuit boards (both flexible and rigid) underneath. While heating at 160°C, the softened encapsulants, Aro(0,1) D26_EV for an FPCB substrate and Aro(1,1) D23_EV + filler for a PCB substrate were manually scraped off, exhibiting adhesive failures with no residue (**Figure 5-15**). The rework feature has not been realized for rigid epoxy-based semiconductor packaging materials. As the production costs of chips, circuit boards, and packaging in surface mount devices have increased, the need for rework technology has also become highly desirable. The rework process requires specialized instruments and excessive heat above 250°C to weaken packaging materials and mechanically detach them (Yuchuan, *et al.*, 2015). Despite all the effort, however, vulnerable chips and circuit board surfaces are easily damaged in many ways (pad crater, solder ball missing, etc.) upon excessive heat and shear stress, indispensable for reducing the mechanical strengths of rigid epoxy encapsulants.

On the contrary, EV encapsulants showed their effectiveness in much milder rework conditions. Owing to the chain rearrangement of dynamic covalent linkages, the material becomes melt-processable, similar to a thermoplastic, at 160°C. In this state, the encapsulant can be removed by a manual scraper without the need for high-shear loading tools. After the removal, the chip-to-board interconnections and connection terminals on the FPCB and PCB substrates remained clean and undamaged. It should be emphasized that the removed encapsulants were also undamaged, so they can be reused elsewhere upon reprocessing (heating). This finding can promote the reuse of the expensive chip, board, and encapsulant, which would benefit the environment.

Figure 5-16. Rework tests for **a** Aro(0,1) D26_EV encapsulated flexible printed circuit board and **b** Aro(1,1) D23_EV + filler encapsulated rigid printed circuit board.
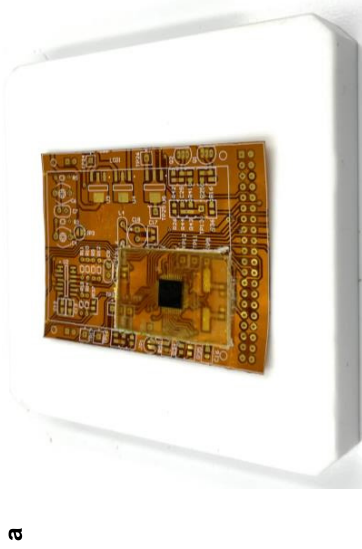
1. Encapsulated

2. Heating & Removal

3. After removal

a

b

200

In the meantime, the easily removable characteristic denotes the reduction of adhesion strength of EVs to the substrates. Above T_g (or T_v), the EVs turn into a viscoelastic solid, similar to a hot-melt adhesive. Thermoplastic-based adhesives exhibit time-and-temperature dependency on their adhesion strength, showing Barenblatt-like brittle cracks at low temperatures and high debonding speeds or Griffith-like ductile cracks at high temperatures and low debonding speeds (Luengo, *et al.*, 1998). Similarly, we contemplate that the EV encapsulant with dynamic linkages would form a blunt crack along the interphase due to the dissipation of debonding force while being transmitted through the bulk polymer. However, verifying this phenomenon requires further detailed investigation, which will be the subject of our future research.

2.5 Properties Related to Encapsulation

Lastly, we inspected the representative thermal, electrical, and packaging properties required in the qualification of electronics packages of all the encapsulants we have used so far to see if the developed materials conform to a certain quality within specified tolerance ranges. For comparison, we evaluated each performance of commercial products; Loctite EO7021 as a reference rigid encapsulant and Sylgard 184™ (PDMS) as a reference soft encapsulant.

2.5.1 Thermal Properties of the Encapsulants

The $T_{d5\%}$ value of the reference encapsulant was 315°C, while the values of prepared EV encapsulants were around 250-270°C. Note that Aro(1,1) D23_EVs have slightly higher $T_{d5\%}$ values than their counterpart of Ali D23_EVs, probably due to the higher content of aromatic compounds within the networks. Also, the addition of silica filler (10 wt%) has an effect of enhancing thermal stabilities of the epoxy encapsulants, increasing $T_{d5\%}$ by 15 to 20°C. On the contrary, the addition of the [$Zn_{0.5}$(G4)]TFSI SIL catalyst (0.5 mol%) resulted in a reduction of $T_{d5\%}$ by 7 to 15°C. Even though the thermal stability of the epoxy encapsulants was below that of the references, there is room for improvement through the choice of a thermally stable resin and the addition of inorganic fillers.

Table 5-6. Thermal stabilities of the epoxy encapsulants, measured by TGA.

Sample	$T_{d5\%}$ [°C]	Remaining weight percentage at 600°C [%]	Reduced weight percentage after 1 h isothermal at 160°C [%]
Loctite EO7021	315	80.2	0.06
NVE	265	9.5	0.25
Ali D23_EV	267	10.6	0.30
Ali D23_EV + filler	282	15.8	0.21
Ali D23_EV + filler + cat. (0.5 mol%)	273	24.0	0.28
Aro(1,1) D23_EV	267	10.7	0.18
Aro(1,1) D23_EV + filler	295	32.3	0.10
Aro(1,1) D23_EV + filler + cat. (0.5 mol%)	278	36.4	0.14
Sylgard™ 184	290	68	0.12
Aro(1,0) D26_EV	270	7.8	0.24
Aro(1,0) D26_EV + cat. (0.5 mol%)	253	10.6	0.28
Aro(0,1) D26_EV	261	8.2	0.31
Aro(0,1) D26_EV + cat. (0.5 mol%)	254	9.8	0.35

Additionally, we evaluated the long-term thermal stability of the encapsulants under the condition known as the burn-in test (125°C for 168 hours). The tendency was consistent with the results of the thermal stability measured by TGA. Nevertheless, the long-term stabilities of the EV encapsulants with the filler were comparable to those of the references.

Table 5-7. Mass loses of the epoxy encapsulants after a burn-in test condition.

Sample	Initial weight [g]	Final weight [g]	Mass loss [%]
Loctite EO7021	1.725	1.709	0.9
NVE	1.572	1.542	1.9
Ali D23_EV	1.658	1.605	3.2
Ali D23_EV+filler	1.592	1.569	1.5
Ali D23_EV+filler, cat. (0.5 mol%)	1.543	1.524	1.6
Aro(1,1) D23_EV	1.66	1.622	2.3
Aro(1,1) D23_EV+filler	1.547	1.521	1.7
Aro(1,1) D23_EV+filler+cat. (0.5 mol%)	1.58	1.555	1.6
Sylgard^{TM} 184	1.76	1.735	1.4
Aro(1,0) D26_EV	1.442	1.401	2.8
Aro(1,0) D26_EV+cat. (0.5 mol%)	1.526	1.489	2.4
Aro(0,1) D26_EV	1.479	1.425	3.4
Aro(0,1) D26_EV+cat. (0.5 mol%)	1.453	1.414	2.7

The thermal conductivities of the epoxy encapsulants were about 0.2 W m^{-1} K^{-1} which is within the range of thermal conductivity of unfilled insulative polymeric encapsulants (0.15 ~ 1.5 W m^{-1} K^{-1}).

Table 5-8. Thermal conductivities of the epoxy encapsulants.

Sample	Specific heat capacity [J g^{-1} K^{-1}]	Density [g cm^{-3}]	Thermal conductivity [W m^{-1} K^{-1}]
Loctite EO7021	-	1.19[a]	0.0005[a]
NVE	1.31	1.10	0.216
Ali D23_EV	1.33	1.12	0.231
Ali D23_EV+filler	1.33	1.17	0.216
Ali D23_EV+filler, cat. (0.5 mol%)	1.34	1.15	0.224
Aro(1,1) D23_EV	1.42	1.13	0.236
Aro(1,1) D23_EV+filler	1.42	1.17	0.214
Aro(1,1) D23_EV+filler+cat. (0.5 mol%)	1.45	1.14	0.228
Sylgard™ 184	-	-	0.27[b]
Aro(1,0) D26_EV	1.32	1.12	0.232
Aro(1,0) D26_EV+cat. (0.5 mol%)	1.36	1.09	0.249
Aro(0,1) D26_EV	1.31	1.11	0.226
Aro(0,1) D26_EV+cat. (0.5 mol%)	1.34	1.09	0.238

[a]Data from the technical data sheet (Loctite EO7021), Henkel, 2014.

[b]Data from the technical data sheet (SYLGARD™ 184 Silicone Elastomer), DOW, 2017

2.5.2 WVTR of the Encapsulants

As an encapsulant, its insulation performance against moisture is critical. Since no specific requirements are specified, we used the most common method for measuring the water vapor transmission rate of a film (ASTM F1249-2). It should be noted that the rigid epoxy encapsulants (Ali D23_EVs and Aro(1,1) D23_EVs) recorded higher WVTR values around $0.6 \sim 1.0$ g m^{-2} day^{-1} compared to their reference (0.2 g m^{-2} day^{-1}). In contrast, the soft epoxy encapsulants (Aro(1,0) D26_EVs and Aro(0,1) D26_EVs) recorded much smaller values around 1.2~1.7 when compared to their reference (232 g m^{-2} day^{-1}).

Table 5-9. Water vapor transmission rates of the cured encapsulants after 48 hr.

Sample	Thickness [mm]	Averaged WVTR [g m^{-2} day^{-1}]
Loctite EO7021	0.55	0.20 (± 0.05)
NVE	0.50	0.86 (± 0.12)
Ali D23_EV	0.49	0.94 (± 0.15)
Ali D23_EV+filler	0.53	0.75 (± 0.21)
Ali D23_EV+filler, cat. (0.5 mol%)	0.53	0.73 (± 0.18)
Aro(1,1) D23_EV	0.51	0.8 (± 0.10)
Aro(1,1) D23_EV+filler	0.50	0.65 (± 0.11)
Aro(1,1) D23_EV+filler+cat. (0.5 mol%)	0.46	0.63 (± 0.25)
Sylgard^{TM} 184	0.48	232 (± 11)
Aro(1,0) D26_EV	0.52	1.16 (± 0.32)
Aro(1,0) D26_EV+cat. (0.5 mol%)	0.47	1.21 (± 0.3)
Aro(0,1) D26_EV	0.50	1.54 (± 0.48)
Aro(0,1) D26_EV+cat. (0.5 mol%)	0.52	1.71 (± 0.28)

2.5.3 Volume Resistivity of the Encapsulants

Conforming to the NASA MSFC specification-592 for the qualification of die- and board-attach polymeric materials, the volume resistivity of the electrically insulative should be higher than $1.0 \times 10^{13}\,\Omega$ cm at 25°C. All the epoxy encapsulants fairly satisfy the criteria ($> 1.0 \times 10^{14}\,\Omega$ cm), even the ones with the catalyst.

Table 5-10. Volume resistivities of the cured epoxies w/ and w/o the [Zn$_{0.5}$(G4)]TFSI catalyst.

Sample	Thickness [mm]	Average Volume Resistivity [Ω cm]
Loctite EO7021	-	$2.0 \times 10^{17,\,a}$
NVE	0.52	6.2×10^{14} (CV[b] = 19.9 %)
Ali D23_EV	0.47	2.3×10^{15} (13.2 %)
Ali D23_EV + cat. (0.5 mol%)	0.55	2.0×10^{15} (7.3 %)
Aro(1,1) D23_EV	0.52	1.1×10^{15} (9.2 %)
Aro(1,1) D23_EV + cat. (0.5 mol%)	0.52	8.4×10^{14} (12.5 %)
Sylgard™ 184	-	$2.9 \times 10^{14,\,c}$
Aro(1,0) D26_EV	0.49	1.5×10^{15} (10.8 %)
Aro(1,0) D26_EV + cat. (0.5 mol%)	0.48	1.2×10^{15} (8.2 %)
Aro(0,1) D26_EV	0.52	1.8×10^{15} (14.2 %)
Aro(0,1) D26_EV + cat. (0.5 mol%)	0.51	1.4×10^{15} (7.5 %)

[a]Data from the technical data sheet (Loctite EO7021), Henkel, 2014.

[b]Coefficient of variation = (standard deviation / average) $\times$ 100

[c]Data from the technical data sheet (SYLGARD™ 184 Silicone Elastomer), DOW, 2017.

3 Conclusion

Here, we successfully applied the developed EV systems to both rigid and soft encapsulations through meticulous material selection and the addition of inorganic filler and SIL catalysts. Prior to application, we evaluated the surface properties of the EV encapsulants and substrates, namely a silicon wafer, a glass wafer, and a polyimide film, and measured the adhesion strength between them. Among the rigid encapsulants, the Aro(1,1) D23_EV encapsulant recorded much higher die shear strengths toward both a silicon wafer (12 N mm^{-2}, substrate failure) and a glass wafer (5 N mm^{-2}, adhesion failure) than those of the Ali D23_EV encapsulant. Among the soft encapsulants, the Aro(0,1) D26_EV encapsulant recorded a higher average peel strength toward a polyimide film (1.7 N mm^{-1}) than that of the Aro(1,0) D26_EV encapsulant (1.4 N mm^{-1}), with both values well above the adhesion strength of PDMS to a polyimide (0.08 N mm^{-1}).

For the rigid encapsulants, Ali D23_EV and Aro(1,1) D23_EV, we validated their effectiveness in reducing the warpage of encapsulated substrates. The effect was attributed to the materials' stress-relaxation capability, which dissipates stress buildup during curing and cooling shrinkage. Meanwhile, the addition of 10 wt% inorganic filler decreased the CTE value by about 20%, resulting in a reduction in warpage as well. Furthermore, adding 0.5 mol% of [Zn$_{0.5}$(G4)]TFSI into the filled system resulted in an encapsulant that induced almost zero warpage in silicon and glass wafers. The approach to resolve stress buildup within semiconductor packaging by adopting a stress-relaxable EV has never been reported and has enormous potential to be a game-changer in selecting a packaging material. All the rigid EV encapsulants showed comparable encapsulation properties to the commercial epoxy encapsulant.

For the soft encapsulant, Aro(0,1) D26_EV, we fabricated a hybrid flexible electronics assembly composed of a polyimide-based flexible printed circuit board and the EV encapsulant. The assembly outperformed its PDMS-encapsulated counterpart regarding adhesion performance, response to multiple deformations (bending and twisting), and

insulation properties. For the CoF application, a supreme stress-relaxation ability was required to dissipate the interfacial strain from substrate deformation instantly; otherwise, the encapsulant revealed defects on its surface. With the addition of 2 mol% of the SIL catalyst, the encapsulant survived 100 cycles of multiple deformations without any defects. All the soft EV encapsulants showed similar thermal stability and much better water vapor tightness than the reference PDMS encapsulant.

As a final benefit, the EV encapsulants (Aro(1,1) D23_EV + filler and Aro(0,1) D26_EV) allow for re-workability in both rigid and soft encapsulation applications. Due to their ability to become malleable at high temperatures, the encapsulants can be easily removed without damaging the chip interconnection or circuit board. This feature could encourage chip manufacturers to reuse valuable resources in line with eco-friendly initiatives.

The potential of these approaches is contingent upon the development of advanced packaging technology that utilizes large and thin wafers, expensive yet fragile components, and flexible substrates associated with future applications such as fan-out panel-level packaging for mobile devices, customized system-on-chip for the Internet of Things, and flexible electronics/packages for wearable devices.

Chapter 6
Overall Conclusion

1 Overall Conclusions

The objectives of the study were to:

1. Develop epoxy vitrimers (EVs) formulations with reasonable stress-relaxation and creep performances.

2. Accelerate the dynamic exchange reaction with the aid of soluble catalysts.

3. Apply the adjusted EV systems to semiconductor packaging.

The EVs studied in this research covered a wide range of mechanical properties, such as E' and tensile strength, stress-relaxation and creep performance, thermal properties (T_g, $T_{d5\%}$, and CTE), adhesion property, and deformability, depending on the composition, type of dynamic covalent bonds, and type and dose of SIL catalysts. The study provided a material selection guideline by combining stress-relaxation and creep characteristics for the variants. Additionally, the insufficient stress-relaxation capability of EVs with low fractions of dynamic linkage was enhanced without invoking serious increases in creep deformation with the aid of SIL catalysts. Finally, depending on their properties, the EV variants were successfully applied as hard or soft encapsulants for chip- or board-level semiconductor packaging. Consequently, the EV systems were expected to be a game-changer as a novel encapsulant in semiconductor packaging, gracefully coping with stress-induced defects and outperforming conventional materials in both rigid and soft encapsulations.

1.1 Formulating Epoxy Vitrimers with High Stress-relaxation & Low Creep

As a first step, we aimed to investigate the effects of substituents in DCAs and dynamic linkages in EV networks on material properties, including re-processability, E', T_g, and most importantly, stress-relaxation and creep performances. Guided by the adapted Flory-Stockmayer gelation theory, we prepared six EVs with different fractions of dynamic

linkages (D17~D34), which could be re-processed. As the dynamic fraction increased, the obtained vitrimer's E' and T_g decreased, while its stress-relaxation ability and creep strain increased accordingly. Meanwhile, substituting DCA with aromatic building blocks resulted in a significant acceleration of transamination and a reduction in activation energies for the reaction; E_a values were 51, 35, 26, and 45 kJ mol^{-1} for Ali D34-, Aro(1,0) D34-, Aro(0,1) D34-, and Aro(1,1) D34_EV, respectively. Surprisingly, this tendency was inconsistent with the result of creep deformations obtained from the same composition. The aromatic components of Aro DCAs appear to increase the matrix's viscosity, resulting in viscoelastic fluid deformation. Through our comprehensive efforts, we were able to obtain several practical formulations: Aro(0,1) D17-, Aro(1,1) D17, 23, 26, and 29_EV, demonstrating decent stress-relaxation ($G_{final}/G_0 < 0.7$) and low creep deformation (strain < 2%) at the same time.

1.2 Accelerating Stress-relaxation Capability of EVs with SIL Catalysts

As a stepping stone, we aimed to find a way to improve the dynamic exchange reaction and stress-relaxation in EVs with low dynamic fractions without compromising their mechanical strength. We synthesized four species of solvate ionic liquid catalysts perfectly soluble in the epoxy resin and Ali D23 DCA mixture. Interestingly, low dosages (0.5 and 2 mol%) of the soluble catalyst were sufficient to accelerate the transamination and reduce the activation energy for the reaction, thanks to its high solubility. The activation energy was reduced by 27 kJ mol^{-1} with 2 mol% of the [$Zn_{0.5}$(G4)]TFSI catalyst, as opposed to the uncatalyzed reaction with an activation energy of 71 kJ mol^{-1}. The catalyst induced a transition of reaction pathway into a metal-catalyzed one. Consequently, the catalyzed EV exhibited excellent stress-relaxation abilities and comparable tensile strength to those of uncatalyzed. The tensile strength was 72 MPa for the uncatalyzed EV and 74 MPa for the EV with 0.5 mol% of the [$Mg_{0.5}$(G4)]TFSI catalyst. Fortunately, the increase in creep deformation could be kept to a minimum by adding only low dosages of the catalyst to the EV systems. The creep strain

was 1.7% for Aro(1,1) D23_EV and 1.8% for Aro(1,1) D23_EV + 0.5 mol% of the [Zn0.5(G4)]TFSI catalyst.

1.3 Applying epoxy vitrimers both in Rigid and Soft Encapsulations

As the final landing, we validated the superior properties of the EVs when used for both rigid (CoW) and soft (CoF) encapsulation applications. We selected a few EVs based on their properties customized for each application. For rigid encapsulation, Ali D23- and Aro(1,1) D23_EV encapsulants were found to be highly effective in reducing warpage of silicon and glass wafers. Adding an inorganic filler (10 wt%) and a SIL catalyst (0.5 mol%) further reduced warpage to almost zero. For soft encapsulation, Aro(1,0) D26- and Aro(0,1) D26_EV were also effective in reducing warpage for a polyimide film substrate, outperforming the counter partner, PDMS, with respect to adhesion performance and response to multiple deformations (bending and twisting). A higher inclusion of SIL catalyst (2 mol%) was required to accommodate the rapid deformation from the flexible substrate. The EV encapsulants met a series of qualification criteria for a semiconductor packaging material. Furthermore, assemblies encapsulated with the EV encapsulants were reworkable at high temperatures without damaging the chip interconnection and substrates. In conclusion, the developed EV encapsulants outperformed conventional packaging materials regarding stress dissipation, warpage reduction, conformability, and reworkability, making them a game changer.

<u>References</u>

Allen, A. D. and Senoff, C. V., 1967, Preparation and infrared spectra of some ammine complexes of ruthenium(II) and ruthenium(III), *Canadian Journal of Chemistry*, **45** (12): 1337-1341

Altuna, F. I., Hoppe, C. E. and Williams, R. J. J., 2019, Epoxy vitrimers with a covalently bonded tertiary amine as catalyst of the transesterification reaction, *European Polymer Journal*, **113**: 297-304

Altuna, F. I., Casado, U., dell'Erba, I. E., Luna, L., Hoppe, C. E. and Williams, R. J. J., 2020, Epoxy vitrimers incorporating physical crosslinks produced by self-association of alkyl chains, *Polymer Chemistry*, **11** (7): 1337-1347

Austen Angell, C., Ansari, Y. and Zhao, Z., 2012, Ionic Liquids: Past, present and future, *Faraday Discussions*, **154** (0): 9-27

Bai, L. and Zheng, J., 2020, Robust, reprocessable and shape-memory vinylogous urethane vitrimer composites enhanced by sacrificial and self-catalysis Zn(II)–ligand bonds, *Composites Science and Technology*, **190**: 108062

Bakker, A., Gejji, S., Lindgren, J., Hermansson, K. and Probst, M. M., 1995, Contact ion pair formation and ether oxygen coordination in the polymer electrolytes $M[N(CF_3SO_2)_2]_2PEO_n$ for M = Mg, Ca, Sr and Ba, *Polymer*, **36** (23): 4371-4378

Balde, J. W., 3-D Assemblies of Stacked Chips and other Thin Packages, 2003, in *Foldable Flex and Thinned Silicon Multichip Packaging Technology*, Springer US, Boston, MA.

Brouillette, D., Irish, D. E., Taylor, N. J., Perron, G. r., Odziemkowski, M. and Desnoyers, J. E., 2002, Stable solvates in solution of lithium bis(trifluoromethylsulfone)imide in glymes and other aprotic solvents: Phase diagrams, crystallography and Raman spectroscopy, *Physical Chemistry Chemical Physics*, **4** (24): 6063-6071

Burattini, S., Greenland, B. W., Merino, D. H., Weng, W., Seppala, J., Colquhoun, H. M., Hayes, W., Mackay, M. E., Hamley, I. W. and Rowan, S. J., 2010, A Healable Supramolecular Polymer Blend Based on Aromatic π−π Stacking and Hydrogen-Bonding Interactions, *Journal of the American Chemical Society*, **132** (34): 12051-12058

Burgers, J., 1935, Mechanical considerations-model systems-phenomenological theories of relaxation and of viscosity, *First report on viscosity and plasticity*, **1**: 1

Capelot, M., Montarnal, D., Tournilhac, F. and Leibler, L., 2012, Metal-catalyzed transesterification for healing and assembling of thermosets, *Journal of the American Chemical Society*, **134** (18): 7664-7667

Capelot, M., Unterlass, M. M., Tournilhac, F. and Leibler, L., 2012, Catalytic Control of the Vitrimer Glass Transition, *ACS Macro Letters*, **1** (7): 789-792

Cash, J. J., Kubo, T., Dobbins, D. J. and Sumerlin, B. S., 2018, Maximizing the symbiosis of static and dynamic bonds in self-healing boronic ester networks, *Polymer Chemistry*, **9** (15): 2011-2020

Chanchani, R., 3D Integration Technologies – An Overview, 2009, in *Materials for Advanced*

Packaging, Springer US, Boston, MA.

Chen, C., Shekh, M. I., Cui, S. and Stadler, F. J., 2021, Rheological Behavior of Blends of Metallocene Catalyzed Long-Chain Branched Polyethylenes. Part I: Shear Rheological and Thermorheological Behavior, *Polymers*, **13** (3): 328

Chen, J. Y., Teng, S. Y., Hwang, S. J., Lee, H. H. and Huang, D. Y., 2006, Prediction of Process Induced Warpage of Electronic Package by P-V-T-C Equation and Taguchi Method, *2006 International Conference on Electronic Materials and Packaging*: 1-8

Cheng, H.-C. and Liu, Y.-C., 2019, Warpage Characterization of Molded Wafer for Fan-Out Wafer-Level Packaging, *Journal of Electronic Packaging*, **142** (1):011004

Chung, K., Dreier, G., Avery, E., Boyle, A., Koehn, W., Govaert, G. and Theunissen, D., 1990, Tack-free flexible film adhesives, **7**: 30-34

Cuminet, F., Caillol, S., Dantras, É., Leclerc, É. and Ladmiral, V., 2021, Neighboring Group Participation and Internal Catalysis Effects on Exchangeable Covalent Bonds: Application to the Thriving Field of Vitrimer Chemistry, *Macromolecules*, **54** (9): 3927-3961

Demongeot, A., Mougnier, S. J., Okada, S., Soulié-Ziakovic, C. and Tournilhac, F., 2016, Coordination and catalysis of Zn2+ in epoxy-based vitrimers, *Polymer Chemistry*, **7** (27): 4486-4493

Denissen, W., Rivero, G., Nicolaÿ, R., Leibler, L., Winne, J. M. and Du Prez, F. E., 2015, Vinylogous Urethane Vitrimers, *Advanced Functional Materials*, **25** (16): 2451-2457

Denissen, W., Winne, J. M. and Du Prez, F. E., 2016, Vitrimers: permanent organic networks with glass-like fluidity, *Chemical Science*, **7** (1): 30-38

Denissen, W., Droesbeke, M., Nicolay, R., Leibler, L., Winne, J. M. and Du Prez, F. E., 2017, Chemical control of the viscoelastic properties of vinylogous urethane vitrimers, *Nature Communications*, **8**: 14857

Emst, L. J., Jansen, K. M. B., Saraswat, M., Zhang, G. Q., Yang, D. G., Hof, C. v. t. and Bressers, H. J. L., 2006, Fully Cure-Dependent Modelling and Characterization of EMC's with Application to Package Warpage Simulation, *2006 11th International Symposium on Advanced Packaging Materials: Processes, Properties and Interface*: 23-27

Eyckens, D. J. and Henderson, L. C., 2019, A Review of Solvate Ionic Liquids: Physical Parameters and Synthetic Applications, *Frontier Chemistry*, **7**: 263

Fancey, K. S., 2005, A mechanical model for creep, recovery and stress relaxation in polymeric materials, *Journal of Materials Science*, **40** (18): 4827-4831

Fang, H., Ye, W., Ding, Y. and Winter, H. H., 2020, Rheology of the Critical Transition State of an Epoxy Vitrimer, *Macromolecules*, **53** (12): 4855-4862

Feldman, K. E., Kade, M. J., Meijer, E. W., Hawker, C. J. and Kramer, E. J., 2009, Model Transient

Networks from Strongly Hydrogen-Bonded Polymers, *Macromolecules*, **42** (22): 9072-9081

Flory, P. J., 1941, Molecular Size Distribution in Three Dimensional Polymers. I. Gelation1, *Journal of the American Chemical Society*, **63** (11): 3083-3090

Fortman, D. J., Brutman, J. P., Hillmyer, M. A. and Dichtel, W. R., 2017, Structural effects on the reprocessability and stress relaxation of crosslinked polyhydroxyurethanes, *Journal of Applied Polymer Science*, **134** (45): 44984

Fowkes, F. M., 1962, DETERMINATION OF INTERFACIAL TENSIONS, CONTACT ANGLES, AND DISPERSION FORCES IN SURFACES BY ASSUMING ADDITIVITY OF INTERMOLECULAR INTERACTIONS IN SURFACES, *The Journal of Physical Chemistry*, **66** (2): 382-382

Gao, H. and Liu, P., 2022, High-Temperature Encapsulation Materials for Power Modules: Technology and Future Development Trends, *IEEE Transactions on Components, Packaging and Manufacturing Technology*, **12** (11): 1867-1881

Giffin, G. A., Moretti, A., Jeong, S. and Passerini, S., 2014, Complex Nature of Ionic Coordination in Magnesium Ionic Liquid-Based Electrolytes: Solvates with Mobile Mg^{2+} Cations, *The Journal of Physical Chemistry C*, **118** (19): 9966-9973

Grondin, J., Lassègues, J.-C., Chami, M., Servant, L., Talaga, D. and Henderson, W. A., 2004, Raman study of tetraglyme–LiClO4solvate structures, *Physical Chemistry Chemical Physics*, **6** (17): 4260-4267

Gu, H., Gao, C., Du, A., Guo, Y., Zhou, H., Zhao, T., Naik, N. and Guo, Z., 2022, An overview of high-performance phthalonitrile resins: fabrication and electronic applications, *Journal of Materials Chemistry C*, **10** (8): 2925-2937

Guerre, M., Taplan, C., Nicolay, R., Winne, J. M. and Du Prez, F. E., 2018, Fluorinated Vitrimer Elastomers with a Dual Temperature Response, *Journal of the American Chemical Society*, **140** (41): 13272-13284

Guerre, M., Taplan, C., Winne, J. M. and Du Prez, F. E., 2020, Vitrimers: directing chemical reactivity to control material properties, *Chemical Science*, **11** (19): 4855-4870

Haida, P. and Abetz, V., 2020, Acid-Mediated Autocatalysis in Vinylogous Urethane Vitrimers, *Macromolecular Rapid Communications*, **41** (16): e2000273

Haleh Ardebili, M. G. P., Encapsulation technologies for electronic applications, 2009, 1st ed., Elsevier, MA.

Hameed, N., Eyckens, D. J., Long, B. M., Salim, N. V., Capricho, J. C., Servinis, L., De Souza, M., Perus, M. D., Varley, R. J. and Henderson, L. C., 2020, Rapid Cross-Linking of Epoxy Thermosets Induced by Solvate Ionic Liquids, *ACS Applied Polymer Materials*, **2** (7): 2651-2657

Hamzehlou, S. and Ruipérez, F., 2022, Computational study of the transamination reaction in vinylogous acyls: Paving the way to design vitrimers with controlled exchange kinetics, *Journal of*

Polymer Science, **60** (13): 1988-1999

Han, J., Liu, T., Hao, C., Zhang, S., Guo, B. and Zhang, J., 2018, A Catalyst-Free Epoxy Vitrimer System Based on Multifunctional Hyperbranched Polymer, *Macromolecules*, **51** (17): 6789-6799

Hao, M., Li, L., Wang, S., Sun, F., Bai, Y., Cao, Z., Qu, C. and Zhang, T., 2019, Stretchable, self-healing, transient macromolecular elastomeric gel for wearable electronics, *Microsystems & Nanoengineering*, **5** (1): 9

Hayashi, M., Noro, A. and Matsushita, Y., 2014, Viscoelastic properties of supramolecular soft materials with transient polymer network, *Journal of Polymer Science Part B: Polymer Physics*, **52** (11): 755-764

Henderson, W. A., Brooks, N. R., Brennessel, W. W. and Young, V. G., 2003, Triglyme−Li+ Cation Solvate Structures: Models for Amorphous Concentrated Liquid and Polymer Electrolytes (I), *Chemistry of Materials*, **15** (24): 4679-4684

Henderson, W. A., Brooks, N. R. and Young, V. G., 2003, Tetraglyme−Li+ Cation Solvate Structures: Models for Amorphous Concentrated Liquid and Polymer Electrolytes (II), *Chemistry of Materials*, **15** (24): 4685-4690

Henderson, W. A., 2006, Glyme−Lithium Salt Phase Behavior, *The Journal of Physical Chemistry B*, **110** (26): 13177-13183

Hoang, M. V., Chung, H.-J. and Elias, A. L., 2016, Irreversible bonding of polyimide and polydimethylsiloxane (PDMS) based on a thiol-epoxy click reaction, *Journal of Micromechanics and Microengineering*, **26** (10): 105019

James J. Licari, D. W. S., Adhesives technology for electronic applications, 2005, 1st ed., Elsevier, Norwich, NY.

Karkanas, P. I. and Partridge, I. K., 2000, Cure modeling and monitoring of epoxy/amine resin systems. II. Network formation and chemoviscosity modeling, *Journal of Applied Polymer Science*, **77** (10): 2178-2188

Kelly, G., Lyden, C., Lawton, W., Barrett, J., Saboui, A., Pape, H. and Peters, H. J. B., 1996, Importance of molding compound chemical shrinkage in the stress and warpage analysis of PQFPs, *IEEE Transactions on Components, Packaging, and Manufacturing Technology: Part B*, **19** (2): 296-300

Kelly, G., 1999, The Simulation of Thermomechanically Induced Stress in Plastic Encapsulated IC Packages: 1st ed. Springer, NY.

Kim, J., Kim, J., Kwon, K., Yong, Y., Kim, J., Lee, D., Kim, S. and Park, D., 2018, Large Area Encapsulation: Solid Type Epoxy Molding Compound, *2018 International Wafer Level Packaging Conference (IWLPC)*: 1-5

Kloxin, C. J. and Bowman, C. N., 2013, Covalent adaptable networks: smart, reconfigurable and

responsive network systems, *Chemical Society Reviews*, **42** (17): 7161-7173

Konarski, M. M., 1999, Effects of Tg and CTE on Semiconductor Encapsulants: Loctite Technical Paper

Landesberger, C., Klink, G., Schwinn, G. and Aschenbrenner, R., 2001, New dicing and thinning concept improves mechanical reliability of ultra thin silicon, *Proceedings International Symposium on Advanced Packaging Materials Processes, Properties and Interfaces (IEEE Cat. No.01TH8562)*: 92-97

Lau, J. H., Li, M., Tian, D., Fan, N., Kuah, E., Kai, W., Li, M., Hao, J., Cheung, Y. M., Li, Z., Tan, K. H., Beica, R., Taylor, T., Ko, C. T., Yang, H., Chen, Y. H., Lim, S. P., Lee, N. C., Ran, J., Xi, C., Wee, K. S. and Yong, Q., 2017, Warpage and Thermal Characterization of Fan-Out Wafer-Level Packaging, *IEEE Transactions on Components, Packaging and Manufacturing Technology*, **7** (10): 1729-1738

Lau, J. H., Li, M., Li, Q. M., Xu, I., Chen, T., Li, Z., Tan, K. H., Yong, Q. X., Cheng, Z., Wee, K. S., Beica, R., Ko, C. T., Lim, S. P., Fan, N., Kuah, E., Kai, W., Cheung, Y. M., Ng, E., Xi, C., Ran, J., Yang, H., Chen, Y. H., Lee, N. C., Tao, M., Lo, J. and Lee, R., 2018, Design, Materials, Process, Fabrication, and Reliability of Fan-Out Wafer-Level Packaging, *IEEE Transactions on Components, Packaging and Manufacturing Technology*, **8** (6): 991-1002

Lau, J. H., Li, M., Yang, L., Li, M., Xu, I., Chen, T., Chen, S., Yong, Q. X., Madhukumar, J. P., Kai, W., Fan, N., Kuah, E., Li, Z., Tan, K. H., Bao, W., Lim, S. P., Beica, R., Ko, C. T. and Xi, C., 2018, Warpage Measurements and Characterizations of Fan-Out Wafer-Level Packaging With Large Chips and Multiple Redistributed Layers, *IEEE Transactions on Components, Packaging and Manufacturing Technology*, **8** (10): 1729-1737

Lau, J. H., Semiconductor Advanced Packaging, 2020, 1st ed., Springer, Taiwan.

Lei, Q. L., Xia, X., Yang, J., Pica Ciamarra, M. and Ni, R., 2020, Entropy-controlled cross-linking in linker-mediated vitrimers, *Proceedings of the National Academy of Sciences of the United States of America*, **117** (44): 27111-27115

Lessard, J. J., Garcia, L. F., Easterling, C. P., Sims, M. B., Bentz, K. C., Arencibia, S., Savin, D. A. and Sumerlin, B. S., 2019, Catalyst-Free Vitrimers from Vinyl Polymers, *Macromolecules*, **52** (5): 2105-2111

Li, K., Cheng, X., Zhu, F., Li, L., Xie, Z., Luan, H., Wang, Z., Ji, Z., Wang, H., Liu, F., Xue, Y., Jiang, C., Feng, X., Li, L., Rogers, J. A., Huang, Y. and Zhang, Y., 2019, A Generic Soft Encapsulation Strategy for Stretchable Electronics, *Advanced Functional Materials*, **29** (8): 1806630

Li, L., Chen, X., Jin, K. and Torkelson, J. M., 2018, Vitrimers Designed Both To Strongly Suppress Creep and To Recover Original Cross-Link Density after Reprocessing: Quantitative Theory and Experiments, *Macromolecules*, **51** (15): 5537-5546

Liao, M.-C., Huang, P.-S., Lin, Y.-H., Tsai, M.-Y., Huang, C.-Y. and Huang, T.-C., 2017, Measurements of Thermally-Induced Curvatures and Warpages of Printed Circuit Board during a Solder Reflow Process Using Strain Gauges, *Applied Sciences*, **7** (7): 739

Licari, J. J. and Swanson, D. W., Chapter 3 - Chemistry, Formulation, and Properties of Adhesives, 2011, in *Adhesives Technology for Electronic Applications (Second Edition)*, William Andrew Publishing, Oxford.

Liu, F., Nair, C., Ito, H., DeProspo, B. H., Ravichandran, S., Akimaru, H., Hasegawa, K. and Tummala, R. R., 2019, Low-Cost 1- μ m Photolithography Technologies for Large-Body-Size, Low-Resistance Panel-Based RDL, *IEEE Transactions on Components, Packaging and Manufacturing Technology*, **9** (7): 1426-1433

Liu, H., Zhang, H., Wang, H., Huang, X., Huang, G. and Wu, J., 2019, Weldable, malleable and programmable epoxy vitrimers with high mechanical properties and water insensitivity, *Chemical Engineering Journal*, **368**: 61-70

Liu, T., Zhang, S., Hao, C., Verdi, C., Liu, W., Liu, H. and Zhang, J., 2019, Glycerol Induced Catalyst-Free Curing of Epoxy and Vitrimer Preparation, *Macromolecular Rapid Communications*, **40** (7): e1800889

Lu, X., Bao, C., Xie, P., Guo, Z. and Sun, J., 2021, Solution-Processable and Thermostable Super-Strong Poly(aryl ether ketone) Supramolecular Thermosets Cross-Linked with Dynamic Boroxines, *Advanced Functional Materials*, **31** (34): 2103061

Luengo, G., Pan, J., Heuberger, M. and Israelachvili, J. N., 1998, Temperature and Time Effects on the "Adhesion Dynamics" of Poly(butyl methacrylate) (PBMA) Surfaces, *Langmuir*, **14** (14): 3873-3881

Lv, G., Jensen, E., Shan, N., Evans, C. M. and Cahill, D. G., 2021, Effect of Aromatic/Aliphatic Structure and Cross-Linking Density on the Thermal Conductivity of Epoxy Resins, *ACS Applied Polymer Materials*, **3** (3): 1555-1562

Mandai, T., Nozawa, R., Tsuzuki, S., Yoshida, K., Ueno, K., Dokko, K. and Watanabe, M., 2013, Phase Diagrams and Solvate Structures of Binary Mixtures of Glymes and Na Salts, *The Journal of Physical Chemistry B*, **117** (48): 15072-15085

Mayer, U., Gutmann, V. and Gerger, W., 1975, The acceptor number — A quantitative empirical parameter for the electrophilic properties of solvents, *Monatshefte für Chemie / Chemical Monthly*, **106** (6): 1235-1257

Meng, F., Saed, M. O. and Terentjev, E. M., 2019, Elasticity and Relaxation in Full and Partial Vitrimer Networks, *Macromolecules*, **52** (19): 7423-7429

Montarnal, D., Capelot, M., Tournilhac, F. and Leibler, L., 2011, Silica-Like Malleable Materials from Permanent Organic Networks, *Science*, **334** (6058): 965-968

Monti, D., Jónsson, E., Palacín, M. R. and Johansson, P., 2014, Ionic liquid based electrolytes for sodium-ion batteries: Na$^+$ solvation and ionic conductivity, *Journal of Power Sources*, **245**: 630-636

Mori, T., 2019, Latest Technologies of Epoxy Molding Compound (EMC) for FO-WLP, *2019*

International Wafer Level Packaging Conference (IWLPC): 1-6

Nakano, T., 2010, Synthesis, structure and function of π-stacked polymers, *Polymer Journal*, **42** (2): 103-123

Nguyen, L. T., Gee, S. A. and Bogert, W. F. v. d., 1991, Effects of Configuration on Plastic Package Stresses, *Journal of Electronic Packaging*, **113** (4): 397-404
Nichetti, D. and Manas-Zloczower, I., 1998, Viscosity model for polydisperse polymer melts, *Journal of Rheology*, **42** (4): 951-969

Odashima, T., Susumago, Y., Nagata, S., Kino, H., Tanaka, T. and Fukushima, T., 2021, Wafer-Level Flexible 3D Corrugated Interconnect Formation for Scalable In-Mold Electronics with Embedded Chiplets, *2021 IEEE 71st Electronic Components and Technology Conference (ECTC)*: 494-499

Ouyang, G., Hanna, A., Benedict, S., Ezhilarasu, G., Alam, A., Irwin, R. W. and Iyer, S. S., 2022, Comprehensive Investigation of In-Plane and Out-of-Plane Die Shift in Flexible Fan-Out Wafer-Level Packaging Using Polydimethylsiloxane, *IEEE Transactions on Components, Packaging and Manufacturing Technology*, **12** (10): 1692-1701

Qi, D., Zhang, K., Tian, G., Jiang, B. and Huang, Y., 2021, Stretchable Electronics Based on PDMS Substrates, *Advanced Materials*, **33** (6): 2003155

Qin, F., Zhao, S., Dai, Y., Yang, M., Xiang, M. and Yu, D., 2020, Study of Warpage Evolution and Control for Six-Side Molded WLCSP in Different Packaging Processes, *IEEE Transactions on Components, Packaging and Manufacturing Technology*, **10** (4): 730-738

Reisinger, D., Kaiser, S., Rossegger, E., Alabiso, W., Rieger, B. and Schlogl, S., 2021, Introduction of Photolatent Bases for Locally Controlling Dynamic Exchange Reactions in Thermo-Activated Vitrimers, *Angewandte Chemie International Edition in English*, **60** (26): 14302-14306

Salunke, A., Sasidharan, S., Cherukattu Gopinathapanicker, J., Kandasubramanian, B. and Anand, A., 2021, Cyanate Ester—Epoxy Blends for Structural and Functional Composites, *Industrial & Engineering Chemistry Research*, **60** (8): 3260-3277

Seiffert, S., 2016, Effect of Supramolecular Interchain Sticking on the Low-Frequency Relaxation of Transient Polymer Networks, *Macromolecular Rapid Communications*, **37** (3): 257-264

Seneviratne, V., Frech, R., Furneaux, J. E. and Khan, M., 2004, Characterization of Crystalline and Solution Phases of Diglyme−LiSbF6, *The Journal of Physical Chemistry B*, **108** (24): 8124-8128

Shih, M., Chen, K., Lee, T., Tarng, D. and Hung, C. P., 2021, FE Simulation Model for Warpage Evaluation of Glass Interposer Substrate Packages, *IEEE Transactions on Components, Packaging and Manufacturing Technology*, **11** (4): 690-696
Shin, J. H., Yi, M. B., Lee, T. H. and Kim, H. J., 2022, Rapidly Deformable Vitrimer Epoxy System with Supreme Stress-Relaxation Capabilities via Coordination of Solvate Ionic Liquids, *Advanced Functional Materials*, **32** (51):2207329

Shterenberg, I., Salama, M., Yoo, H. D., Gofer, Y., Park, J.-B., Sun, Y.-K. and Aurbach, D., 2015,

Evaluation of (CF$_3$SO$_2$)$_2$N$^-$(TFSI) Based Electrolyte Solutions for Mg Batteries, *Journal of The Electrochemical Society*, **162** (13): A7118-A7128

Snyder, R. L., Fortman, D. J., De Hoe, G. X., Hillmyer, M. A. and Dichtel, W. R., 2018, Reprocessable Acid-Degradable Polycarbonate Vitrimers, *Macromolecules*, **51** (2): 389-397

Spiesschaert, Y., Guerre, M., De Baere, I., Van Paepegem, W., Winne, J. M. and Du Prez, F. E., 2020, Dynamic Curing Agents for Amine-Hardened Epoxy Vitrimers with Short (Re)processing Times, *Macromolecules*, **53** (7): 2485-2495

Stockmayer, W. H., 1944, Theory of Molecular Size Distribution and Gel Formation in Branched Polymers II. General Cross Linking, *The Journal of Chemical Physics*, **12** (4): 125-131

Taplan, C., Guerre, M., Winne, J. M. and Du Prez, F. E., 2020, Fast processing of highly crosslinked, low-viscosity vitrimers, *Materials Horizons*, **7** (1): 104-110

Tong, C., Substrate and Encapsulation Materials for Printed Flexible Electronics, 2022, in *Advanced Materials for Printed Flexible Electronics*, Springer International Publishing, Cham.

Tsuzuki, S., Shinoda, W., Matsugami, M., Umebayashi, Y., Ueno, K., Mandai, T., Seki, S., Dokko, K. and Watanabe, M., 2015, Structures of [Li(glyme)]$^+$ complexes and their interactions with anions in equimolar mixtures of glymes and Li[TFSA]: analysis by molecular dynamics simulations, *Physical Chemistry Chemical Physics*, **17** (1): 126-129

Ueno, K., Yoshida, K., Tsuchiya, M., Tachikawa, N., Dokko, K. and Watanabe, M., 2012, Glyme-lithium salt equimolar molten mixtures: concentrated solutions or solvate ionic liquids?, *The Journal of Physical Chemistry B*, **116** (36): 11323-11331

Ueno, K., Tatara, R., Tsuzuki, S., Saito, S., Doi, H., Yoshida, K., Mandai, T., Matsugami, M., Umebayashi, Y., Dokko, K. and Watanabe, M., 2015, Li+ solvation in glyme–Li salt solvate ionic liquids, *Physical Chemistry Chemical Physics*, **17** (12): 8248-8257

Van Lijsebetten, F., Spiesschaert, Y., Winne, J. M. and Du Prez, F. E., 2021, Reprocessing of Covalent Adaptable Polyamide Networks through Internal Catalysis and Ring-Size Effects, *Journal of the American Chemical Society*, **143** (38): 15834-15844

Van Lijsebetten, F., De Bruycker, K., Spiesschaert, Y., Winne, J. M. and Du Prez, F. E., 2022, Suppressing Creep and Promoting Fast Reprocessing of Vitrimers with Reversibly Trapped Amines, *Angewandte Chemie International Edition in English*, **61** (9): e202113872

Vidal, F., Gomezcoello, J., Lalancette, R. A. and Jäkle, F., 2019, Lewis Pairs as Highly Tunable Dynamic Cross-Links in Transient Polymer Networks, *Journal of the American Chemical Society*, **141** (40): 15963-15971

Wang, J., Yang, B., Lin, X., Gao, L., Liu, T., Lu, Y. and Wang, R., 2020, Research of TPU Materials for 3D Printing Aiming at Non-Pneumatic Tires by FDM Method, *Polymers*, **12** (11): 2492

Wang, L., Liu, Y., Qiao, Y., Wang, Y., Cui, Z., Zhu, S., Dong, F., Fang, S. and Du, A., 2022,

Molecularly engineered dual-crosslinked elastomer vitrimers with superior strength, improved creep resistance, and retained malleability, *Polymer Chemistry*, **13** (28): 4144-4153

Wang, S., Sun, Y., Sheng, C., Feng, Z., Li, R., Xue, L., Liu, J. and Liu, S., 2021, Warpage Analysis and Prediction of the Advanced Fan-Out Technology Based on Process Mechanics, *IEEE Transactions on Components, Packaging and Manufacturing Technology*, **11** (12): 2201-2213

Wang, W., Madsen, J., Genina, N., Hassager, O., Skov, A. L. and Huang, Q., 2021, Toward a Design for Flowable and Extensible Ionomers: An Example of Diamine-Neutralized Entangled Poly(styrene-co-4-vinylbenzoic acid) Ionomer Melts, *Macromolecules*, **54** (5): 2306-2315

Watanabe, A. O., Ali, M., Sayeed, S. Y. B., Tummala, R. R. and Pulugurtha, M. R., 2021, A Review of 5G Front-End Systems Package Integration, *IEEE Transactions on Components, Packaging and Manufacturing Technology*, **11** (1): 118-133

Watkins, T. and Buttry, D. A., 2015, Determination of Mg(2+) Speciation in a TFSI(-)-Based Ionic Liquid With and Without Chelating Ethers Using Raman Spectroscopy, *The Journal of Physical Chemistry B*, **119** (23): 7003-7014

Williams, G. and Watts, D. C., 1970, Non-symmetrical dielectric relaxation behaviour arising from a simple empirical decay function, *Transactions of the Faraday Society*, **66** (0): 80-85

Wu, M. L. and Lan, J. S., 2019, Simulation and Experimental Study of the Warpage of Fan-Out Wafer-Level Packaging: The Effect of the Manufacturing Process and Optimal Design, *IEEE Transactions on Components, Packaging and Manufacturing Technology*, **9** (7): 1396-1405

Wu, X., Yang, X., Yu, R., Zhao, X.-J., Zhang, Y. and Huang, W., 2018, A facile access to stiff epoxy vitrimers with excellent mechanical properties via siloxane equilibration, *Journal of Materials Chemistry A*, **6** (22): 10184-10188

Xu, K., Chen, M., Zhang, K. and Hu, J., 2004, Synthesis and characterization of novel epoxy resin bearing naphthyl and limonene moieties, and its cured polymer, *Polymer*, **45** (4): 1133-1140

Xu, R., Lee, J. W., Pan, T., Ma, S., Wang, J., Han, J. H., Ma, Y., Rogers, J. A. and Huang, Y., 2017, Designing Thin, Ultrastretchable Electronics with Stacked Circuits and Elastomeric Encapsulation Materials, *Advanced Functional Materials*, **27** (4): 1604545

Yang, D. G., Jansen, K. M. B., Ernst, L. J., Zhang, G. Q., Beijer, J. G. J. and Janssen, J. H. J., 2005, Experimental and numerical investigation on warpage of QFN packages induced during the array molding process, *2005 6th International Conference on Electronic Packaging Technology*: 94-98

Yao, Y., Lu, G. Q., Boroyevich, D. and Ngo, K. D. T., 2015, Survey of High-Temperature Polymeric Encapsulants for Power Electronics Packaging, *IEEE Transactions on Components, Packaging and Manufacturing Technology*, **5** (2): 168-181

Yeon, S., Park, J. and Lee, H.-J., 2016, Compensation Method for Die Shift Caused by Flow Drag Force in Wafer-Level Molding Process, *Micromachines*, **7** (6): 95

Yeon, S., Park, J. and Lee, H. J., 2016, Compensation Method for Die Shift Caused by Flow Drag Force in Wafer-Level Molding Process, *Micromachines (Basel)*, **7** (6): 95

Yepremyan, A., Osamudiamen, A., Brook, M. A. and Feinle, A., 2020, Dynamically tuning transient silicone polymer networks with hydrogen bonding, *Chemical Communications (Cambridge)*, **56** (88): 13555-13558

Yu, K., Taynton, P., Zhang, W., Dunn, M. L. and Qi, H. J., 2014, Influence of stoichiometry on the glass transition and bond exchange reactions in epoxy thermoset polymers, *RSC Advances*, **4** (89): 48682-48690

Yuchuan, W. and Qiang, C., 2015, Package on Package SMT rework technology, *2015 16th International Conference on Electronic Packaging Technology (ICEPT)*: 74-78

Yue, L., Guo, H., Kennedy, A., Patel, A., Gong, X., Ju, T., Gray, T. and Manas-Zloczower, I., 2020, Vitrimerization: Converting Thermoset Polymers into Vitrimers, *ACS Macro Letters*, **9** (6): 836-842

Yufeng Jin, Z. W., Jing Chen, Introduction to microsystem packaging technology, 2011, 1st Edition ed., CRC Press, Boca Raton.

Zhang, Z. and Wong, C. P., 2002, Study on the catalytic behavior of metal acetylacetonates for epoxy curing reactions, *Journal of Applied Polymer Science*, **86** (7): 1572-1579

List of Publications

This Ph.D. dissertation is based on the following publications.

I. Shin, J. H., Yi, M. B., Lee. T. H., Kim, H. J., 2022, Rapidly deformable vitrimer epoxy system with supreme stress-relaxation capabilities via coordination of solvate ionic liquids, *Advanced Functional Materials*. **32** (51): 2207329.

II. Shin, J. H. Kim, H. J., 2023, Warpage reduction in semiconductor packaging via epoxy vitrimer systems with a tailored stress dissipation characteristic, **in preparation**.

초록

팬아웃 웨이퍼 레벨 패키징, 3D 적층과 같은 첨단 패키징 기술의 등장으로 인하여, 공정, 패키징 디자인, 상호 연결 전략 및 재료 선택 등의 다양한 측면에서의 혁신이 요구되는 시대가 찾아왔다. 그러나 다른 분야의 눈부신 발전 속도와 비교해 볼 때, 반도체 포장재의 재료 자체의 혁신은 다소 부족한 것으로 보인다. 포장재는 일반적으로 고분자 재료로 구성되어 있으며, 패키징 내에서 조립품의 체결, 칩 또는 기판의 보호, 요소 간 상호 연결, 열 또는 응력의 방출 기능을 담당하고 있다. 오늘날에는 박형 기판, 취약 소자의 사용 및 복잡한 패키징 디자인 등으로 인해, 포장재의 응력을 분산시키는 역할이 더욱 중요해지고 있다. 만약 포장재가 스트레스 축적을 억제하지 못하게 되면 공정에서 다양한 종류의 문제가 발생할 수 있으며, 이는 품질과 생산성의 저해를 초래할 수 있다. 그 중에서도, 기판의 휨 현상은 뒤따르는 칩 조립 및 패키징의 후공정을 불가능하게 만들기 때문에, 공정의 연속성 또한 심각하게 훼손한다. 지금까지는 열팽창계수가 낮은 포장재를 채택하는 것으로 휨 현상을 억제하여 왔지만, 해당 방식에는 한계가 존재하므로 재료의 근본적인 측면에서 해결책이 필요한 상황이다. 또한, 유연전자재료 분야에서도 마찬가지로 강하면서 유연성을 갖는 재료에 대한 요구가 증대되고 있다. 두 상황에 대한 핵심적이면서 공통적인 해결책은 단단하면서도 응력을 효과적으로 발산할 수 있는 재료를 개발하는 것이다.

본 논문에서는, 비트리머라는 양면성을 갖는 재료를 적용함으로써 위 문제들에 대한 해결책을 제안한다. 비트리머는 가교 되어있는 구조체 내에서 동적인 교환 반응을 통하여, 재료의 위상을 재정렬할 수 있는 물질이다. 열 트리거에 의하여 위상이 재배열 되는 동안, 비트리머는 가교된 사슬들이 흐르면서 재료 스스로 스트레스를 완화하는 특징을 갖는다. 이러한 비트리머의 장점은 단단한 에폭시 소재와 결합하였을 때 더욱 빛이 난다. 따라서 우리는 목적에 맞는 특성을 가진 에폭시 비트리머를 개발하고, 재료 내부의 동적 교환 반응을 제어하여 응력 완화 능력을 향상시켰으며, 최종적으로 이들이 패키징 어플리케이션에 성공적으로 적용될 수 있음을 입증하였다.

먼저, 에폭시 비트리머는 열경화성 수지의 겔화 이론에 입각하여 다양한 혼합비를 갖

도록 제조하였다. 이때 상용 에폭시 수지와 동적 경화제라 불리는 합성 경화제를 배합하였다. 제조된 에폭시 비트리머는 모두 상온에서 매우 단단하였으며, 고온에서는 용융 가공이 가능하였다. 우리는 치환기 종류에 따라 4종의 동적 경화제를 합성하였으며, 경화물 조성 내에서 동적 교환 반응을 할 수 있는 사슬의 함량을 다르게 조절하여 이들이 에폭시 비트리머의 응력 완화 능력에 미치는 영향을 조사하였다. 방향족계 동적 경화제는 지방족계 동적경화제보다 더 높은 응력 완화 능력을 갖는 에폭시 비트리머를 제조하는데 일조하였다. 이는 방향족 인접기의 안정화 효과를 통한 빠른 아미노기 전이 반응 덕분인 것으로 확인하였다. 한편, 동적 교환 사슬의 함량이 높은 에폭시 비트리머는 더 높은 응력 완화 능력이 있음을 확인하였다. 그러나, 해당 특성은 기계적 강도와 장기 치수 변형 안정성의 감소를 야기할 수 있으므로, 적절한 수준을 갖는 조성을 채택하는 것이 필요하였다

두 번째로, 우리는 새로운 종류의 용융 금속 복합체인 용액화 이온 액체 촉매를 합성하였고, 이를 동적 교환 반응을 가속하기 위한 촉매로서 에폭시 비트리머에 도입했다. 용액화 이온성 액체 촉매는 기존의 금속 분말과 달리 0.5~2 mol% 수준의 용량만으로도 에폭시 비트리머의 응력 완화 특성을 크게 향상시킬 수 있었다. 이는 해당 화합물이 에폭시에 대해 높은 혼화성과 루이스 산성 특성을 가지기 때문인 것으로 확인하였다. 우리는 적절한 촉매 투여를 통하여 상온에서는 매우 높은 저장탄성률 (10^9 Pa 이상)을 가지면서도 160°C에서는 매우 짧은 응력 완화 시간 (약 수 초)을 갖는 고성능의 에폭시 비트리머를 제조할 수 있었다. 이러한 촉진 효과 덕분에, 기계적 특성 (저장 탄성률 및 인장 강도)과 점탄성 성능 (크립 변형)을 손상시키지 않으면서, 응력 분산 능력만을 더욱 집중적으로 향상시킬 수 있었다.

마지막으로, 우리는 개발된 에폭시 비트리머 시스템을 칩 온 웨이퍼 와 칩 온 필름 어플리케이션들에 각각 적용하였다. 이를 위해, 각 애플리케이션에 잘 맞는 특성 (탄성계수, 응력 완화, 크립 등)을 갖는 에폭시 비트리머를 선정하였다. 강도가 높은 포장재가 필요한 패키징 어플리케이션에서, 에폭시 비트리머 포장재는 실리콘과 유리 웨이퍼에서 발생하는 휨 현상을 감소시키는데 매우 효과적인 것으로 확인되었다. 또한 무기 충전제와 용액화 이온성 액체 촉매의 첨가를 통해 휨 현상을 완전히 억제할 수 있었다. 강도가 낮은 포장재를 사용하는 플렉시블 어플리케이션에서는, 에폭시 비트리머 포장재

가 폴리이미드 기판의 휘어짐을 효과적으로 감소시키면서도 PDMS 기반 포장재보다 우수한 접착성과 변형성을 가짐을 입증하였다. 추가적으로, 에폭시 비트리머 포장재를 사용한 패키징 결합체를 고온으로 가열함에 따라, 칩 상호 연결 및 기판의 손상 없이, 포장재 만을 선택적으로 제거할 수 있었다.

결과적으로, 위 연구들은 에폭시 비트리머의 (1) 가교 결합 내의 동적 교환 반응을 제어하였고, (2) 응력 분산 능력만을 향상시켰으며, 이를 (3) 반도체 패키징 어플리케이션 등에서, 휨 현상을 억제하는 동시에 유연기판에도 적용될 수 있음을 보여주었다.

키워드: 비트리머, 에폭시, 동적 교환 반응, 용액화 이온 액체, 응력 완화, 응력 해소, 휨 현상, 반도체 패키징, 패키징 포장재.